UNIVERSITY OF SOUTHAMPTON

Faculty of Engineering and Physical Sciences
School of Engineering

Theoretical Methods to Predict the Interaction of Aero-engine Fan Tone Radiation with the Fuselage and its Boundary Layer

by

Dionysios Marios Rouvas

Master of Engineering

ORCiD: https://orcid.org/0009-0001-6646-4444

A thesis for the degree of
Doctor of Philosophy

21st June 2023

University of Southampton

Abstract

Faculty of Engineering and Physical Sciences
School of Engineering

Doctor of Philosophy

Theoretical Methods to Predict the Interaction of Aero-engine Fan Tone Radiation with the Fuselage and its Boundary Layer

by Dionysios Marios Rouvas

The work in this thesis is focused on the acoustic installation effects of an aero-engine fan noise source adjacent to a cylindrical fuselage with a boundary layer running down its length. The main scope of this work is the development of theoretical methods to quantify scattering/diffraction by the fuselage and the refraction effect due to the presence of the boundary layer. The aim is to provide a faster and less computationally demanding alternative to high-fidelity numerical methods. The acoustic near-field of an installed fan noise source has been investigated before with the use of numerical methods to solve the problem of sound propagation through the shear layer. Therefore, in this work analytic expressions are derived that describe the acoustic pressure both in the near-field, in the form of a Fourier series and a Fourier integral, and in the far-field, in the form of a Fourier series. The use of numerical methods is avoided by utilising an asymptotic method for thin linear boundary-layer profiles. Additionally, a rudimentary step-function profile is investigated that avoids the solution to the Pridmore-Brown equation altogether. The capability of the two profiles to approximate the effects of more complex boundary layer profiles such as the quarter-sine and the 1/7th power-law profile is investigated. The analytic expressions are validated by comparing theoretical results to existing numerical results for the pressure on the fuselage surface. The two equivalent simplified profiles prove to be able to approximate the same effects as more realistic profiles especially for thin boundary layers. The linear profile accurately predicts shielding effects for thin boundary layers, but the step-function profile retains its accuracy regardless of the boundary-layer thickness. Both theoretical approaches are able to capture the pressure contour pattern and amplitude of shielding on the fuselage surface. The main advantage of this novel theoretical approach is the speed at which it can produce reliable results since there is no need for numerical schemes. Therefore, a multi-mode parametric study is conducted that identifies shielding trends on the fuselage surface and far-field directivity trends in various stages of flight. Multiple flow and source characteristics are examined with flight Mach number, cut-off ratio of the modal output of the fan, and boundary-layer thickness standing out as the major factors that affect shielding on the fuselage surface and directivity phase shifts in the far-field. The results of the multi-mode parameteric study highlight the capability of this novel theoretical approach to produce quick and reliable results that can serve as a preliminary analysis to a more in-depth numerical analysis.

Contents

List of Figures

List of Tables

Declaration of Authorship

I declare that this thesis and the work presented in it is my own and has been generated by me as the result of my own original research.

I confirm that:

1. This work was done wholly or mainly while in candidature for a research degree at this University;
2. Where any part of this thesis has previously been submitted for a degree or any other qualification at this University or any other institution, this has been clearly stated;
3. Where I have consulted the published work of others, this is always clearly attributed;
4. Where I have quoted from the work of others, the source is always given. With the exception of such quotations, this thesis is entirely my own work;
5. I have acknowledged all main sources of help;
6. Where the thesis is based on work done by myself jointly with others, I have made clear exactly what was done by others and what I have contributed myself;
7. Parts of this work have been published as:
   D-M. Rouvas and A. McAlpine. Theoretical methods for the prediction of near-field and far-field dound radiation of fan tones scattered by a cylindrical fuselage. *Proceedings of the AIAA Aviation 2021*, AIAA 2021-2300, 2021.

   D-M. Rouvas and A. McAlpine. Prediction of fan tone radiation scattered by a cylindrical fuselage. *Proceedings of the 11th EASN Conference*, 1226(012050), 2022b.

   D-M. Rouvas and A. McAlpine. An analytical model of sound refraction by the fuselage boundary-layer for fan tone radiation from a turbofan aero-engine. *Proceedings of the 28th AIAA/CEAS Aeroacoustics Conference*, AIAA 2022-3059, 2022a.

Signed:..... Date:.....

Acknowledgements

My principal thanks go to Alan McAlpine. His guidance and support were instrumental in the carrying out of the research that is presented in this thesis. He was always very willing to share his technical expertise and sit and go through challenging mathematics for the satisfaction of my self-affirmation.

I am also grateful to Matthew, Suresh and Alan for checking and turning on my computer while I was away due to the pandemic. Without you guys I wouldn't be able to complete a crucial part of my work. I would also like to thank Rod and Lorna for their help in spell checking the thesis.

The work in this thesis is part of the ARTEM project. This project has received funding from the European Union's Horizon 2020 research and innovation programme under grant No. 769 350. ARTEM and other projects within the MG1-2-2017 call 'Reducing Aviation Noise' were initiated by the EREA 'Future Sky' initiative. I would also like to acknowledge the financial contribution from the EPSRC via the University of Southampton's Doctoral Training Grant.

Also I would like to extend my appreciation to the continuing support provided by Rolls–Royce plc through the University Technology Centre in Propulsion Systems Noise at the Institute of Sound and Vibration Research, especially Dr Christoph Richter (Rolls-Royce Deutschland) for his input and recommendations that are now part of this thesis.

To my parents, Thanasis and Christiana, who always supported me, and my professor Penelope Menounou who helped me discover my true calling.

Definitions and Abbreviations

a	duct radius, m
a_0	fuselage radius, m
b	distance between the centreline of the fuselage and centreline of the intake duct, m
c_0	speed of sound, $\mathrm{m{\cdot}s^{-1}}$
D_n	coefficient for the step-function boundary layer expressions
E_n	Fourier coefficient for the near-field incident pressure
F_n	coefficient for the far-field incident pressure
G	bracketed term used in linear boundary layer analysis
$\mathrm{H}_m^{(2)}$	Hankel function of the second kind, order m
I	denotes an integral
J_m	Bessel function of the first kind, order m
K	non-dimensional axial wavenumber
k_0	freespace wavenumber, $\mathrm{rad{\cdot}m^{-1}}$
k_z	axial wavenumber, $\mathrm{rad{\cdot}m^{-1}}$
k_{zlq}	axial wavenumber, mode (l,q), $\mathrm{rad{\cdot}m^{-1}}$
l	azimuthal order of mode
M_∞	free-stream Mach number
M_w	Mach number at the fuselage surface for linear boundary layer
M_0	internal Mach number for step-function boundary layer
P_{lq}	pressure amplitude of mode (l,q), Pa
p'	acoustic pressure, Pa
q	radial order of mode
R	bracketed term used in boundary layer analysis
(r,ϕ,z)	cylindrical coordinate system centered on the intake duct (or disc source)
$(\bar{r},\bar{\phi},\bar{z})$	cylindrical coordinate system centered on the fuselage
$(\bar{R},\bar{\theta},\bar{\phi})$	spherical polar coordinate system centered on the fuselage
S_n	bracketed term used in linear boundary layer analysis
t	time, s
W_{lq}	sound power of mode (l,q), Watt
W_t	total sound power of source, Watt
Y_n	bracketed term used in step-function boundary layer analysis
Γ	radial wavenumber, $\mathrm{rad{\cdot}m^{-1}}$
γ	alternative form of radial wavenumber, $\mathrm{rad{\cdot}m^{-1}}$
Δ	wavenumber in real space used in far-field analysis, dependent on $\bar{\theta}$, $\mathrm{rad{\cdot}m^{-1}}$
Δ_{bl}	difference between sound pressure level with and without the presence of a

	boundary layer, dB
Δ_{source}	difference between sound pressure level due to different sources, dB
δ	boundary layer thickness, m
ϵ	non-dimensional error metric
ε	non-dimensional boundary-layer thickness
ζ	non-dimensional radial coordinate used to denote location within the linear boundary layer
κ_{lq}	modal eigenvalue, mode (l, q), rad·m^{-1}
φ	Mach number distribution inside the linear boundary layer, dependent on ζ
ω_0	angular frequency, rad·s^{-1}
$\mathfrak{L}$	bracketed term used in linear boundary layer far-field pressure expression
$\mathfrak{S}$	bracketed term used in linear boundary layer far-field pressure expression
Subscripts	
L	denotes quantity of linear boundary layer
SF	denotes quantity of step-function boundary layer
ff	denotes far-field quantity
i	denotes incident field
in	denotes field inside the linear boundary layer
n	denotes quantity is a Fourier–Bessel harmonic
∞	denotes field outside the boundary layer or free-stream value
s	denotes scattered field
t	denotes total field
0	denotes field inside the step-function boundary layer
Superscripts	
(lbl)	denotes Fourier transform integral in the linear boundary layer near-field pressure expression
(sbl)	denotes Fourier transform integral in the step-function boundary layer near-field pressure expression
$'$	denotes differentiation with respect to a function's argument
ee	denotes source with equal energy per mode
10	denotes rotor-locked source with dominant mode's sound power 10 dB higher than all other cut-on modes
20	denotes rotor-locked source with dominant mode's sound power 20 dB higher than all other cut-on modes
30	denotes rotor-locked source with dominant mode's sound power 30 dB higher than all other cut-on modes
20, 10	denotes rotor-locked source with second radial order rotor-locked mode
Symbol	
$\bar{\ }$	denotes Fourier transformed quantity

Chapter 1

Introduction

With the introduction of the turbojet engine in the 1950s, commercial aviation entered an era of unprecedented growth. This new radical development enabled international travel to become mainstream thus improving the quality of life across the planet. However, as it is the case with many technological advancements, this rapidly growing industry introduced new problems and challenges along with its many benefits. Increased CO_2 emissions and levels of noise pollution instantly became issues that needed resolving due to their harmful impact on our health. These harmful emissions are expected to become an even bigger problem according to Airbus (2019) and Boeing (2019), which predict an increase in air traffic by 5% per year around the world and even 6.5% for some regions in Asia until 2037. With the number of flights and passengers per year constantly increasing, it is no wonder that intense efforts for maintaining the levels of noise pollution to a minimum are of utmost importance.

Over the years, organisations around the world, for example the International Civil Aviation Organisation (2008) and the American Federal Aviation Administration, have introduced rules and regulations that dictate certain standards regarding noise produced by aircrafts. These standards serve the ultimate goal of maintaining low noise pollution levels even though the frequency of flights keeps on increasing. It is clear that in order for the industry to meet these standards, the use of accurate noise prediction methods is required. The Council of ICAO has introduced the balanced approach in order to resolve the problem. This approach is based on understanding the four key elements of aircraft noise management (International Civil Aviation Organisation (2008), International Coordinating Council of Aerospace Industries Associations (2004)): reduction of noise at source, land use planning and management, noise abatement operational procedures and operating restrictions. Obviously, for the air travel industry the first element is the important one as it effectively means producing quieter aircraft.

Since the 1960s, the noise produced by aircraft has been greatly reduced. This reduction is the equivalent of 20dB or in other terms, aircraft have become 75% quieter (International Coordinating Council of Aerospace Industries Associations (2004)). This is largely due to the optimisation of the components of the turbofan engine. Specifically, the introduction of the high bypass ratio turbofan reduced significantly the jet noise which at the time was the dominant noise source (International Coordinating Council of Aerospace

Industries Associations (2004) and Astley (2014)). Also, improvements in the sweeping of the rotors and stators have had an important impact on the noise produced by the fan. The most important noise control feature found in modern engines is probably the acoustic liners. By installing an acoustic liner in the fan's intake and bypass duct system, the modal noise component is reduced significantly, a fact that has lead to a very comprehensive research on liners in recent years.

Despite these efforts over the years, new local limitations are constantly being introduced since the impact on communities near airports is everchanging due to the increase of air traffic. The certification standards set forth by the Council of ICAO aim to encourage the manufacturers to comply with all the limitations. The certification levels are determined using the Effective Perceived Noise Level (EPNL) which is unique for every aircraft and is measured in EPNLdB (Chapter 4 of International Civil Aviation Organisation (2008)). The EPNL is scaled to include exposure duration and tonal content. These effective noise levels are measured in three different positions along the flight path for three different operating conditions. These three positions are: Approach, Sideline and Cutback or Flyover and are shown in Fig.(1.1).

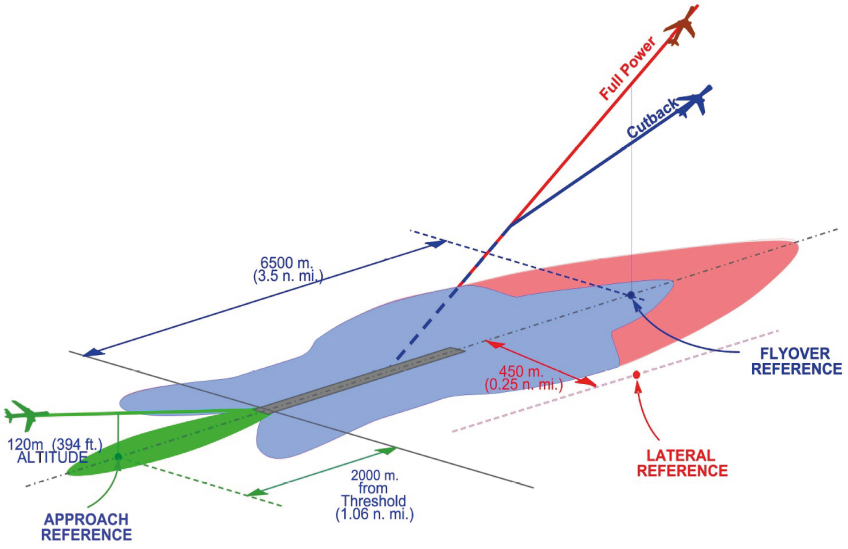

FIGURE 1.1: ICAO Aircraft Certification Reference Conditions. Taken from International Civil Aviation Organisation (2008).

Back in 2001 ACARE (2001) set a collection of goals to be achieved by 2020 with the ultimate aim to maintain a competitive air travel industry whilst reducing the environmental impact to a minimum. One of these goals was to eliminate noise nuisance. This translated to a reduction of 50%, but there were no specific details given on how this goal was to be achieved (Astley (2014)). The goals set forth by ACARE were updated by the European Commission (2011) to 65% reduction of perceived noise emission by 2050, which means a cumulative reduction of 45 EPNLdB for the three operating conditions (Astley (2014)). As stated by Astley (2014), the European Commission recognised the need for a balanced approach, not only in the sense expressed by ICAO, but also in a more practical way, meaning that all the noise sources on the aircraft must be reduced in a uniform way if a cumulative reduction of perceived noise is to be achieved. This balanced approach requires the ability to predict how the noise sources on the aircraft interact with each other. Following this approach, this thesis focuses on the interaction of fan noise, generated by the turbofan, with the adjacent fuselage. The alterations of the

sound field due to interactions of the noise source with components of the aircraft are called installation effects and are the main focus of this thesis.

1.1 Aircraft Noise Sources

The most important noise sources can be categorised into three broad groups. Engine noise, jet noise and airframe noise. The distribution, strength and directivity of these sources depend on the configuration of the aircraft. The engine position, engine model, fuselage and wing configuration are all factors to be taken into consideration when one attempts to calculate the contribution of each source. However, for the commonly used tube-wing configuration, the noise sources are laid out as shown in Fig.(1.2).

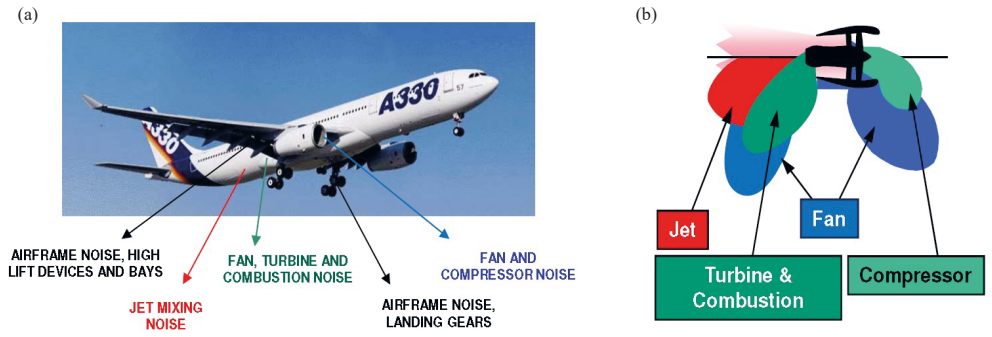

FIGURE 1.2: **[(a)]** Aircraft noise sources and **[(b)]** directivities of engine sources. Taken from Astley (2014).

Engine noise is usually split into other subcategories. That happens because of the complexity of the turbojet engine and specifically the turbofan engine. As can be seen in Fig.(1.2), the engine generates fan and compressor noise from the intake, turbine and combustion noise from the exhaust outlet and also jet noise is generated when the hot exhaust gases mix with the usually much cooler ambient fluid (Astley (2014)). Furthermore, airframe noise is always present. Airframe noise is generated when high-speed unsteady flow impinges on the components of the airframe (Astley (2014)). Generally, the smoother the airframe geometry the less noise is generated. Consequently, the main contributors of airframe noise are landing gear, high-lift devices and trailing edge sources (Lilley (2001)). Generally landing gear noise is dominant, although according to Smith (1989) the discontinuities on the wing's geometry such as flaps and slats can cause a significant increase in the EPNL.

The work in this thesis focuses on the installation effects of fan noise for the following reasons. The most commonly used turbofan engine ingests air which it then splits into two streams. The core stream is directed through the compressor into the combustor where it is mixed with fuel and then burned. After the combustion, the jet of exhaust gases are accelerated and expanded through the turbine and exits the rear of the engine where it is mixed with the ambient air and the air of the outer stream. The outer stream of air is directed around the core through a bypass duct and is accelerated by a fan and then propelled out of the rear of the engine. The outer stream of air is cooler than the core stream and its speed is considerably smaller. This difference in conditions leads to the mixing of those two streams to generate jet noise. The

bigger the discrepancies between the two streams the more noise is generated, leading to jet noise being the dominant engine noise source over the fan noise, which is the noise generated by the fan and propagated out of the intake, the bypass and the exhaust duct. Modern high bypass ratio turbofan engines direct the largest percentage of the air ingested around the core. This means that the desired thrust is achieved at slower jet velocity. It has been proven by Lighthill (a)-Lighthill (b), that the intensity of jet noise is scaled by u^8, meaning that a reduction in jet velocity leads to significant reduction in jet noise. As a result, modern engines tend to generate much less jet noise, effectively making the fan noise the dominant source.

Apart from the jet itself, there are a couple of mechanisms involving the jet that can lead to potentially powerful noise sources on the aircraft. Experimental studies by Mead and Strange (1998) revealed that the two main jet noise installation effects are reflection by the wing, which tends to affect higher frequencies, and interaction between the jet and the wing and its high-lift devices and/or its trailing edge, which tends to affect lower frequencies. These installation effects are projected to cause an increase in noise over 2 dB. The jet-wing interaction noise sources usually resemble the radiation by a dipole with its axis perpendicular to the wing axis, meaning that the effect is negligible at locations close to the wing axis. One such location is the fuselage, therefore jet-wing interaction noise sources do not affect the pressure levels that reach the fuselage. However, more recent publications (Mayoral and Papamoschou (2013), Bychkov et al. (2016), Bychkov and Faranosov (2018)) point out that this might be misleading in more modern configurations. Modern configurations incorporate larger engines and therefore the jet is closer to the wing, exacerbating this effect.

Further theoretical and computational studies on jet-wing interaction sources (Mayoral and Papamoschou (2013), Bychkov et al. (2016), Bychkov and Faranosov (2018)) have repeatedly revealed that this phenomenon is largely dominant in the rear arc. Quantitative results show that propagation in the rear arc is far more pronounced than in the forward arc, with 10 dB minimum difference. It is important to note that this is true for both near- and far-field cases. The airframe surfaces that are more likely to be affected by the jet-wing interaction sources are located downstream of the jet. Jet-wing interaction noise sources have also been investigated for flight conditions although only in qualitative terms. These qualitative studies (Mead and Strange (1998), Mayoral and Papamoschou (2013), Bychkov et al. (2016), Bychkov and Faranosov (2018)) have indicated that higher flight Mach numbers tend to alleviate the effects especially in the rear arc by compacting the affected area. Therefore, since in this work the focus is the upstream area (forward arc) and the fuselage surface pressure during flight, it is deemed that the jet-wing interaction noise sources are relatively small compared to the fan noise sources.

Apart from the general configuration of the aircraft and its engine, another significant factor that affects the noise signature of the sources is the operating condition of the aircraft. Figure (1.3) shows the distribution of the noise sources at the three designated operating conditions as set forth by the council of ICAO for an aircraft with a high bypass ratio turbofan engine. Jet noise is dominant only at the sideline position. During the approach, even though the engine is on idle, fan noise is still a significant contributing factor to the total aircraft EPNL, although airframe noise is the dominant source. On the other hand, during take-off (or cutback) fan noise is undoubtedly the dominant noise source. This persistent presence of fan noise is another reason for its inclusion in this thesis as the main noise source.

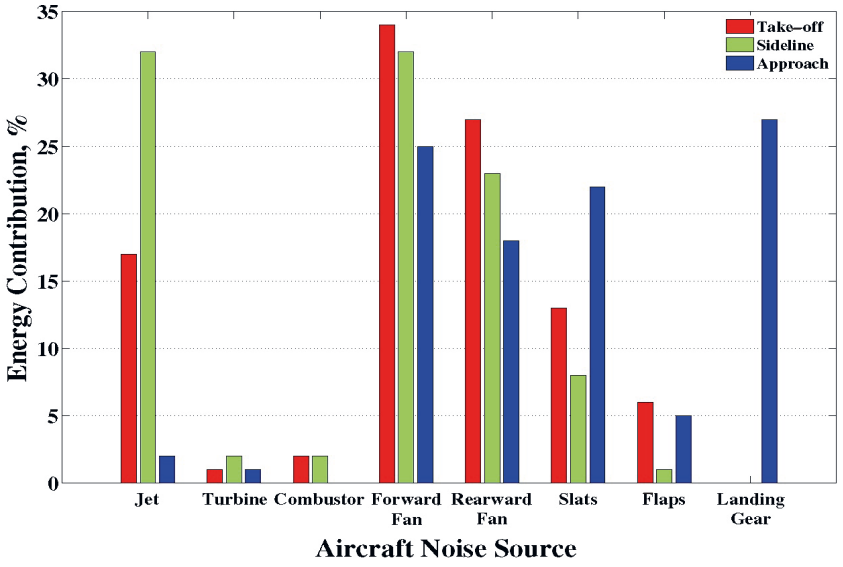

FIGURE 1.3: Noise source distribution. Taken from Lawrence (2014).

Since fan noise appears to be dominant, this thesis will investigate how this noise interacts with the adjacent aircraft components. The primary aim of the thesis will be the scattering and refraction of fan noise by the fuselage and its boundary layer. Fan noise includes strong tonal components, thus the analysis in this thesis will be done using time-harmonic spinning modes exiting the intake of the engine. Of course, fan noise propagates to the rear of the engine but the focus of this work will be on sound radiation from the intake duct. The fan broadband noise problem is by itself a complicated one. It is generated by the interaction between the fan and turbulence. This interaction leads to the generation of broadband noise that propagates towards the exhaust of the engine. This mechanism is far too complex to be modeled using analytic methods and so it is out of the scope of the work presented here.

1.2 Installation Effects

As stated previously the noise generated by the sources on the aircraft will interact with the rest of the aircraft's components. These various interactions lead to substantial alterations in the acoustic field compared with the same source in free space. Alterations are expected both for the near- and the far-field. For that reason it is misleading to calculate only the free-field response of the noise source, its interactions must be included. Installation effects are of utmost importance for the industry since the EPNL measured includes these effects and the community experiences the noise generated by the aircraft as a whole.

More specifically, the aim of this work is to develop and validate analytic expressions that describe the acoustic near- and far-field from an installed fan noise source adjacent to a cylindrical fuselage. This model replicates the real-life situation of a turbofan engine mounted under the wing with its intake duct next to the fuselage. The derived expressions aim to simulate the predicted scattering on the fuselage and the predicted refraction due to the presence of a boundary layer on the fuselage. In this work, the term scattering will refer to reflection and diffraction around a cylindrical fuselage. The primary noise source will be a

distributed disc source which aims to simulate an acoustic mode exiting the fan duct. This mode then radiates and impinges on the fuselage or is refracted as it propagates through the boundary layer on the fuselage. The total field is calculated in the near- and far-field with the ultimate goal of providing some insight on the actual acoustic field that the community experiences.

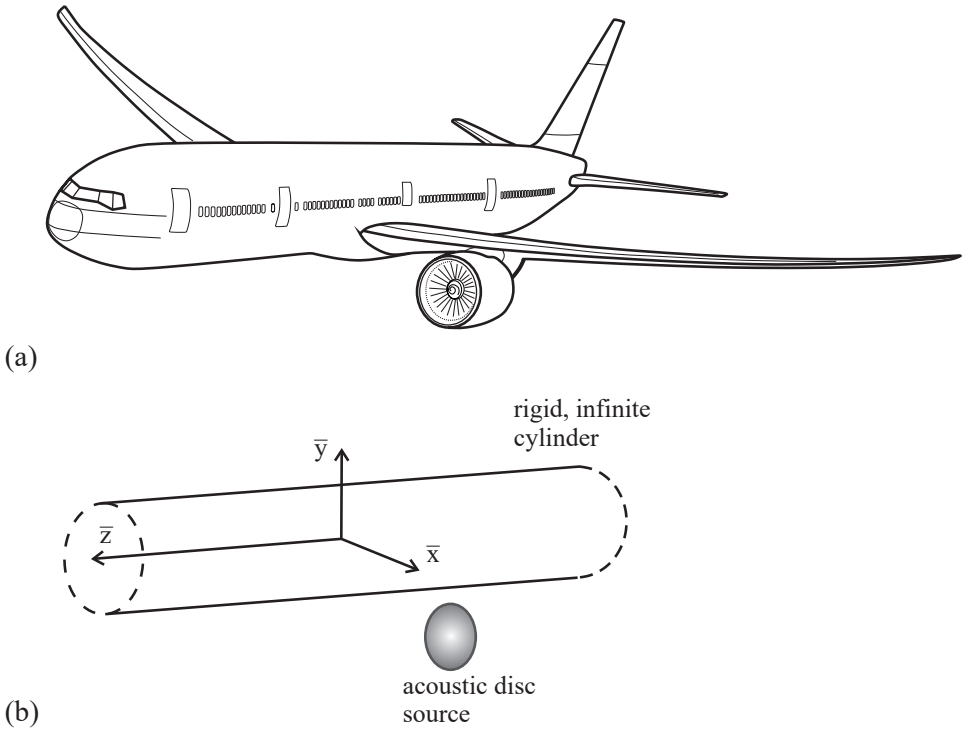

FIGURE 1.4: Sketch of an installed turbofan aero-engine. Taken from McAlpine et al. (2015).

1.3 Aim and Objectives

The main aim of this work is to develop theoretical methods to predict the acoustic installation effects for an advanced ultra high bypass ratio turbofan engine. The ultimate goal of this thesis is to propose alternative methods that avoid the use of high-fidelity numerical methods. These numerical methods often prove to be costly and time-consuming. Theoretical methods, on the other hand, are capable of providing quick and accurate results that facilitate the identification of trends. More specifically, the work focuses on the scattering of a fan noise source by an

adjacent cylindrical fuselage, and more importantly on the refraction of sound due to the boundary layer on the fuselage. The objectives that have been achieved during the course of this PhD project are:

1. Derive a disc source model that describes the incident pressure in the near- and far-field radiated from the intake of an Ultra High By-Pass Ratio Turbofan engine. The model will be based on the previous work of spinning modes exiting an intake duct.
2. Derive analytical expressions for the total pressure on the fuselage surface and in the far-field after scattering by an adjacent cylindrical fuselage with no boundary layer (only scattering on the fuselage is considered without a refraction effect).
3. Derive analytical expressions for the total pressure on the fuselage surface and in the far-field after scattering and refraction by an adjacent cylindrical fuselage with a rudimentary step-function boundary layer velocity profile.
4. Derive analytical expressions for the total pressure on the fuselage surface and in the far-field after scattering and refraction by an adjacent cylindrical fuselage with a more complex linear boundary layer velocity profile.
5. Validate the expressions analytically and then numerically.
6. Investigate an appropriate method to approximate the effects of a more complex and realistic boundary layer profile, such as the 1/7th power-law profile which resembles a turbulent boundary layer, by using the simplified step-function or linear profiles.
7. Conduct a parametric multimodal study in which the pressure on the fuselage surface and in the far-field is calculated for realistic aircraft dimensions and varying flight parameters:
    - Dominant mode's cut-off ratio.
    - Flight altitude.
    - Flight Mach number.
    - Fan rpm or frequency.
    - Boundary-layer thickness.

1.4 Original Contributions

Most previous work on acoustic installation effects has been focused on the scattering and refraction of a propeller noise source by a cylindrical fuselage. Since propeller aircraft are on the decline for the last 30 years and turbofan engines are now the most commonly used propulsion system it is pertinent to investigate installation effects for fan noise sources. The scattering of a fan noise source has only very recently been investigated by McAlpine et al. (2015). Their work focused on the near-field, specifically on the pressure on the fuselage surface. This thesis will use the same disc source as derived in McAlpine et al. (2015). However, unlike in McAlpine et al. (2015), this thesis will also focus on both the near- the

far-field pressure, giving an insight into the installation effects that impact the community. The acoustic far-field for an installed engine has been investigated before but only for a propeller noise source (Lu (1990)). So far, that far-field problem has never been applied to fan noise. Therefore, the derivation of an expression that describes the acoustic far-field when a fan noise source is scattered on an adjacent cylindrical fuselage (with and without a boundary layer) is an original contribution.

This thesis also aims to develop analytic methods to solve the boundary layer problem. So far, in order to investigate the refraction effect of the fuselage boundary layer, previous researchers have utilised numerical methods. Given that a realistically thin boundary layer allows the use of asymptotic methods and the fact that high-fidelity numerical methods can be time-consuming, it is beneficial to develop a fully analytic approach. That is why the ultimate goal of this thesis is to develop methods that are analytic and avoid the use of more complex and costly hybrid approaches that combine low- and high-fidelity methods that have already been used in previous work. Therefore, another original contribution of this thesis is the development of theoretical methods to solve the problem of sound propagation through a shear layer. This is performed by using simplified velocity profiles: either a step-function profile or a linear profile.

In the case of the rudimentary step-function velocity profile, the analysis is split into two solutions: inside and outside of the boundary layer. Both these regions are governed by the Helmholtz equation, thus the two solutions are matched at the edge of the boundary layer to obtain the total installed field. This procedure has been proposed by Hanson (1984) who used a propeller noise source and assumed no flow inside the boundary layer. The novel contribution of this thesis is the use of a fan noise source and a generalisation of the step-function profile to include any constant arbitrary Mach number inside the boundary layer. The novel solution is then extended to include expressions for both the pressure on the fuselage surface and on the far-field.

In the case of the linear velocity profile, the analysis is again split into two solutions inside and outside the boundary layer. The challenge and original contribution here is solving analytically the Pridmore-Brown equation (Pridmore-Brown (1958)), which governs the sound propagation inside the shear layer. All previous work resorted to using numerical methods to solve the Pridmore-Brown equation. The novel work in this thesis proposes using an asymptotic method used in duct acoustics by Eversman and Beckemeyer (1972), in order to solve the equation analytically. The two solutions are then matched at the edge of the boundary layer to obtain the total installed field. The novel final solution is then extended to include expressions for both the pressure on the fuselage surface and in the far-field.

Another original contribution in this thesis is the investigation of the optimal method to utilise a simplified profile (linear or step-function) that approximates the same refraction effect as a more complex boundary-layer profile, such as the 1/7th power-law profile which resembles a turbulent boundary layer. To the best of the author's knowledge, the methods presented have not been considered before.

Finally, since the methods proposed here are theoretical and avoid the use of costly numerical methods, a parametric multimodal study is conducted that allows a wide range of varying parameters to be tested. This study produces results on the fuselage surface and far-field

pressure for different stages of flight allowing for quick, accurate and realistic trends to be identified. Such a wide range of results represents the validation of an original and novel theoretical tool that can be very useful in future applications.

A part of the results and derivations presented in this thesis has been presented before in the published papers, Rouvas and McAlpine (2021), Rouvas and McAlpine (2022b), Rouvas and McAlpine (2022a).

1.5 Layout of the Thesis

Every objective mentioned above is fulfilled in the chapters that follow.
Chapter 2: Literature Review. In this chapter, the literature on installation effects, fan tone propagation and sound propagation through a shear layer is studied and presented. By studying the various publications on the subject of installation acoustics the potential research areas are identified.
Chapter 3: Theoretical Analysis. As mentioned before, the focus of the work in this thesis is the development of theoretical methods. In this chapter, expressions for the far-field and near-field acoustic pressure around the cylindrical fuselage are derived. Firstly, the analysis is conducted assuming no boundary layer on the fuselage. The second section includes the analysis with the presence of a step-function boundary layer profile on the fuselage. The third section includes the analysis with the presence of a linear boundary layer profile on the fuselage. The expressions are validated analytically by reducing them to known solutions.
Chapter 4: Code Development. The derived expressions are coded and their convergence rate is investigated. Numerical problems are encountered and solved using approximations.
Chapter 5: Validation. The generated code is used to produce results that will further prove the validity of the derived expressions. This is done by comparing the results with equivalent results generated using numerical methods. Parameters such as frequency, Mach number and boundary-layer thickness are investigated. The limitations of the theoretical methods are investigated.
Chapter 6: Parametric Study Results. The layout of the parametric study is presented and the flight parameters to be used are presented. The key results and conclusions are presented. Useful trends are identified.
Chapter 7: Discussion of the Results. The parametric study results are revisited in order to gain perspective and insight into the trends that have been revealed. Also, a comparison between the results generated using a step-function profile and the results generated using a linear profile is conducted.
Chapter 8: Conclusion. The key results and conclusions presented in this thesis are summarised and suggestions for future work are proposed.

Chapter 2

Literature Review

In the following chapter, a review of the key publications on acoustic installation effects is presented. The purpose of this chapter is to identify the gaps in knowledge concerning installation effects so that realistic objectives can be set and original contributions can be made. The papers reviewed here deal with installation effects caused by the fuselage, namely scattering around the fuselage. By the end of this chapter it will be shown that research on installation effects only recently included a fan noise source. Previously, all the work regarding acoustic installation effects used propeller noise sources or other elementary sources. As explained in the introduction, in recent decades the turbofan engine has surpassed in popularity all other means of propulsion, meaning that a deeper understanding of the scattering of a fan noise source by the fuselage is desirable. The review starts by giving a background on fan-tone radiation. Then the simplest case of noise scattering around the fuselage without a boundary layer is presented. Due to the importance of the presence of a boundary layer on the fuselage, a comprehensive background is presented on sound propagation through a shear layer. Lastly, a thorough review is given on how the boundary layer affects the scattering around the fuselage.

2.1 Fan-tone Radiation

Since the work described in this report concerns mainly the acoustic installation effects of a turbofan engine, it would be helpful to describe its basic functions and provide some insight on how it generates and radiates sound. A turbofan engine works on the basic principle of compressing air, combusting it and then propelling it backwards from the rear of the engine. Firstly, a large portion of the air ingested by the engine is compressed through the fan. This compressed bypassed air is accelerated to the rear outlet of the engine thus producing thrust. A smaller portion of the air ingested is directed into a compressor located behind the fan. There, the air is gradually compressed before it reaches the next component of the engine which is the combustion chambers. At these chambers the compressed air is mixed with fuel and then burned. The resulting exhaust fumes expand and accelerate towards the rear outlet of the engine while passing through a turbine. After exiting the turbine, the exhaust fumes are propelled out of the rear outlet of the engine in the form of a jet. All these complex rotating

mechanisms generate sound which propagates to the front and rear of the engine where it ultimately radiates to the open space. A very comprehensive study on fan noise generation and propagation was conducted by Tyler and Sofrin (1962) and their findings are presented below.

Tyler and Sofrin (1962) firstly described the generating mechanisms of noise inside a turbofan engine. They focused their research on rotor noise and rotor-stator noise, meaning the noise generated by the rotation of the blades of the rotor or their interaction with the vanes of the stator, since the two most significant generating mechanisms are the steady aerodynamic blade loading and blade thickness. Additionally, the authors focused on the importance of the blade passing frequency since it is the dominant frequency in the spectrum of turbofan noise. The significance of these factors was verified with experimental tests, which revealed that the pressure field for rotor only configurations consisted of a group of lobed patterns rotating at the same speed as the rotor. Also, the number of lobes on each pattern was related to the BPF or its harmonics, meaning that the first pattern (associated with the first BPF) had as many lobes as the blades, while the second pattern (associated with the second harmonic of the BPF) had twice as many lobes. The amplitude of the lobes was found to be dependent on the aerodynamic characteristics of the blades. It became clear that the pressure pattern will always be rotor-locked no matter the characteristics of the blade. It was noted that this was not the case for rotor-stator interaction.

Tyler and Sofrin modeled the transmission of these lobed patterns along the inlet duct of the turbofan engine. They firstly assumed a rectangular duct and came to the conclusion that the transmission of the pressure patterns depends on the driving frequency. When the driving frequency is above or below a certain value, called cut-off, the transmission behaves very differently. In the mathematical analysis, the transmission or propagation of the pressure pattern depends on an exponent with imaginary argument. When the frequency is below a certain value the argument of the exponent becomes real and so the expression for the pressure becomes exponentially decaying. On the other hand, when the frequency is above this critical value, the exponent's argument is imaginary and so it describes a harmonic fluctuation. The authors actually concluded that the exponential decay is greater when the frequency is well below the cut-off frequency. It became clear that only certain frequencies and modes can propagate inside a duct.

The same physical properties were observed for an annular duct, although the expressions were different. The main difference in the mathematical analysis between the cylindrical and the rectangular duct is the presence of Bessel functions in the expression for the eigenmodes. In an annular duct, the sound waves behave like standing waves in the radial direction and their shape is described by a Bessel function. The argument of the Bessel function is dependent on the radius of the duct and its boundary condition. This boundary condition refers to the inner wall of the duct. By changing this boundary condition the pressure field can be altered and attenuated. This boundary condition can be altered by placing liners on the inside of the duct's walls. The authors came to the same conclusion as in the case of the rectangular duct that the propagation of the pressure pattern depends on the driving frequency. In the case of the annular duct, the factor which determines the propagation or not of the pressure field is the circumferential Mach number. This is the Mach number at which the pressure pattern sweeps the duct's walls and is controlled by the value of the frequency.

A very important observation made by Tyler and Sofrin (1962) was that concerning the rotor-stator interaction. A rotor will produce a single lobed pattern for a single frequency, speed and number of blades. A rotor-stator structure will produce for the same characteristics various lobed patterns rotating at various speeds. Once again, the lobed patterns are a product of the periodic interaction of the blade wakes from the rotor and the stator vanes, meaning that only their amplitude is dependent on the geometric and aerodynamic characteristics of the blades and vanes. In fact there are an infinite number of possible patterns or modes but only a finite number of them propagate and those modes can be determined using the number of blades and vanes. This has been a very important discovery because by selecting the number of blades and vanes it can be determined which modes will propagate while all the others will be cut-off and exponentially decay.

Lastly, Tyler and Sofrin modeled the radiation of these lobes out of the duct. These "spinning modes" can be used to model a distributed source at the face of the duct termination. The acoustic axial particle velocity can be obtained from the pressure pattern of the mode. The particle velocity can be used to formulate a Raleigh integral which will yield a distribution of monopoles on the area of the duct termination. The authors used this distributed source to model the radiation of the spinning modes out of the duct termination. Their results were presented in the form of polar directivity plots. The common characteristic of these plots was that, apart from the case of the plane wave, all other modes had zero pressure at the duct's centerline. Another trend discovered was the dependency on frequency and order of the mode. The higher the frequency or the order of the mode, the more secondary lobes appear on the directivity plot. Also, at high frequencies the principal lobe tends to be closer to the duct's centerline. Finally, the authors pointed out that due to the complexity of the fan noise directivity, in comparison to the jet noise, it is very important that atmospheric turbulence and temperature gradient be taken into account when one attempts to calculate the far-field radiation of the fan modes.

More recent work in fan tone radiation and propagation has been conducted by Schwaller et al. (1997). During their work, noise measurements were taken in the intake and in the far-field of a fan test rig which had three configurations regarding the intake geometry, ranging from a simple intake to a more complex droop intake. The purpose of this work was to determine the influence of the intake geometry on the modal output of the fan engine. The droop intake geometry will introduce distortion in the flow which will interact with the fan and produce propagating modes. Their findings provide insight into the modal breakdown of a fan engine which was possible with the use of a rotating microphone array. The rotor-locked or rotor-alone mode that occurs when the fan tip speed becomes supersonic proves to be very important as it dominates the other modes when it is cut-on by 10 dB or more. Another conclusion by Schwaller et al. (1997) is that the intake distortion tends to offset the sound energy towards the previous azimuthal order mode compared to the rotor-locked mode, highlighting the importance of the rotor-locked mode.

Similar work was later conducted by Schwaller et al. (2006). Once again, a test rig was constructed that was 1/3rd scale model of an actual fan engine. The purpose of the work presented in this paper was to prove the effectiveness of a scale model and its ability to produce results that are very similar to that of a full scale engine model. As in Schwaller et al. (1997), the configuration had a droop intake which greatly influences the noise measurements.

Results revealed a good agreement between the test rig and the full scale engine measurements except at low frequencies where jet noise tends to dominate fan noise. An interesting conclusion is the difference between the measured broadband and buzz-saw noise. In the case of the broadband noise, the levels were higher when the droop intake was pointed towards the observer whereas the opposite was true for the buzz-saw noise. That stems from the fact that buzz-saw noise is dominated by the rotor-locked mode which is characterised by low cut-off ratio. Furthermore, as in Schwaller et al. (1997), the importance of the rotor-locked mode is exhibited and the distortion modes created by the droop intake. The distortion modes are on either azimuthal side of the rotor-locked mode and exhibit the same increase in noise levels of up to 20 dB compared with the rest of the modes detected.

Important work on mode detection and radiation has also been conducted by Achunche et al. (2009). In this work, a prediction method for fan tone radiation and propagation is proposed based on finite element (FE) methods and the results are compared with noise measurements from a 1/3rd scale model of a fan. The conclusions are remarkably similar to previous papers on mode detection, meaning that the equal energy per mode assumption is valid until supersonic fan tip speeds. Once the tip velocities are supersonic, the rotor-locked mode dominates over the other modes by at least 20 dB.

2.2 Scattering By the Fuselage Without a Boundary Layer

Research on purely scattering effects without the inclusion of a boundary layer on the fuselage has been conducted with interesting results. It is important to note that earlier publications considered propeller noise sources due to the popularity of the propeller against the fan engine at the time. Initially, Fuller (1989) developed a mathematical formulation to calculate a correction factor which can be used to correct the free-field pressure when there is a cylindrical fuselage present. Fuller's model was fairly simple as it did not include a mean flow so it focused solely on scattering effects and not refraction effects caused by the boundary layer. Fuller (1989) used both monopole and dipole sources in an attempt to simulate more accurately a propeller noise source. The obtained correction factor was simply the ratio of the free-field to the total acoustic pressure. The analysis used the Graf's addition theorem the same way it had been done for previous publications. There was no need for a Frobenius method since there is no flow hence no boundary layer. Fuller (1989) chose to present the results in terms of varying frequency and source location. The results reveal that frequency plays a very important role even without a boundary layer. More specifically, the higher the frequency the clearer the shadow zone behind the cylindrical fuselage. This can be explained due to the fact that lower frequencies tend to diffract around the cylinder more than higher frequencies meaning that at low frequencies the shadow zone tends to shrink due to more creeping waves arriving at this location. Also, Fuller observed that by moving the source away from the cylinder the correction factor was increased at the front of the cylinder. This happened because when the source is far away from the surface, the incidence angle approaches normal incidence in which case reflection is stronger than diffraction around the cylinder. Fuller (1989) also conducted some calculations using a dipole as a source. The main difference between the dipole and the monopole results was that the dipole results were more oscillatory, a fact that is attributed to the highly directional nature of the dipole. Finally, Fuller

constructed a rudimentary model for a propeller noise source using a rotating dipole. The results revealed that the correction factor is highly sensitive to the position of the blade or the dipole due to the directional nature of the source.

Another significant work on the scattering effect of the fuselage without a boundary layer was done by McAlpine and Kingan (2012). In their paper, they focused on the far-field radiation of an installed open rotor using distributed sources of rotating monopoles and dipoles to simulate a realistic propeller noise source. The methodology used in that work was similar to previous publications. The incident field was derived centered on the propeller and later shifted to another coordinate system centered on the cylindrical fuselage, whilst the scattered field is expressed as cylindrical outgoing waves. The expressions for the far-field obtained by McAlpine and Kingan were consistent with far-field analysis, such as the strong dependence on Bessel and Hankel functions. However, due to the added complexity of the propeller noise sources used, the expressions included multiple summations which led to the authors conducting a convergence study. They concluded that convergence is dependent to the "relative" Mach number which depends on the flight speed and the rotation speed of the propeller. Illustrative results were provided in the form of azimuthal directivity plots. These plots showed the distinctive shadow zone behind the fuselage and also revealed that the far-field pressure is dependent on geometrical characteristics such as the propeller's radius or its distance from the cylindrical fuselage. McAlpine and Kingan also extended the model to include predictions for unsteady loading on the installed rotor. They used an impulsive excitation which resembles the sound field produced when the wake from a pylon interacts with the rotor's blade. Once again, the azuimuthal directivity plot revealed that the far-field pressure is dependent on the location of the fuselage and the rotor.

As mentioned before, the turbofan engine is much more widely used these days which led to the work of McAlpine et al. (2015). This paper's main distinctive feature was the introduction of a fan noise source as opposed to a propeller noise source which had been used previously. To model the fan noise source, the Rayleigh integral was used as suggested by Tyler and Sofrin (1962). The axial particle velocity of a spinning mode is used to obtain a distribution of monopoles on a disc source located at the face of the inlet duct. This method was first introduced by Tyler and Sofrin (1962). This distributed disc source is used to obtain the incident field caused by the spinning mode exiting the fan inlet. Then, the methodology applied is the same as in McAlpine and Kingan (2012). It is important to note that initially no boundary layer is included in the model by McAlpine et al. (2015). The near-field expression derived by McAlpine *et al.* bears similarities with the near-field expression of McAlpine and Kingan (2012), but with key differences relating to the source terms. McAlpine *et al.* did not extend the model to the far-field. Since the use of this distributed source was new to the field of acoustic installation effects, a validation study was performed to assess whether the distributed source could accurately model a spinning mode exiting than fan inlet. As expected, the distributed source was able to model accurately the spinning mode up to 75^{o} polar angles at which point the diffraction on the duct lip became dominant and was not modeled by the distributed disc source. The diffraction around the duct's lip can be modeled using the Wiener-Hopf method as will be seen later. In order to validate the scattered field expression, the results were compared to the results by Fuller (1989). This meant that the derived expression had to be reduced to a stationary monopole, but nevertheless the

comparison showed very good agreement. Once again, a convergence study was required since, as in all previous work, the pressure is expressed in terms of Fourier series. The convergence results showed that for relatively high frequency, more that 150 harmonics are required for the series to converge. Finally, some illustrative results were presented. In that paper the focus was on the near-field pressure, more specifically the pressure on the surface of the fuselage. The results once again showed a clear shadow zone at the side of the fuselage away from the source, whereas on the side of the source a doubling of pressure was observed corresponding to a near normal incidence and reflection on the surface of the fuselage. Another interesting observation was that the maximum pressure level was not predicted in the plane of the source but further upstream of it. That was because the principal lobes of the spinning modes considered were not directed at 90^o since at that point diffraction would play a far more important role.

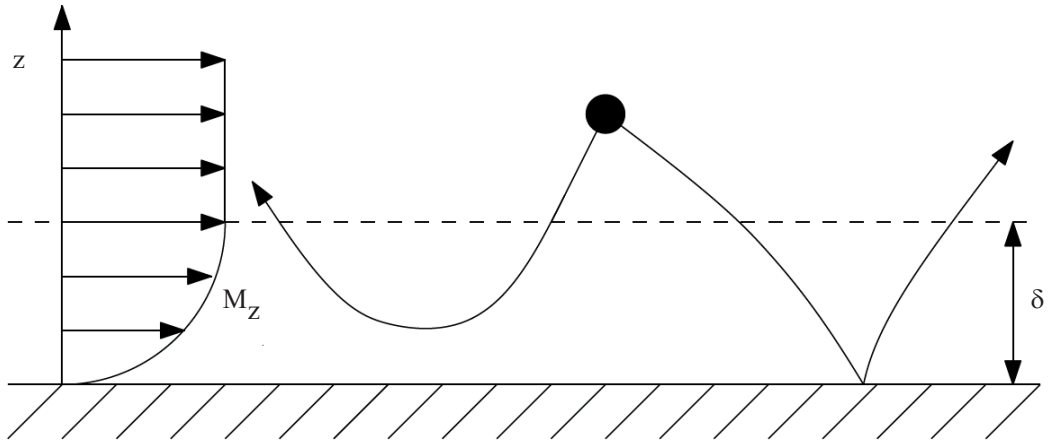

FIGURE 2.1: Sketch of refracted rays downstream and upstream of the source. Taken from Gaffney (2016).

All publications that did not include a boundary layer recognised this omission. Indeed, those solutions failed to predict accurately the noise levels on the fuselage since experimental results showed considerably lower noise levels than the predicted ones (as shown in McAninch (1983) and Hanson and Magliozzi (1985) which will be discussed in depth). This apparent shielding is due to the refraction of sound upstream of the source, see Fig. (2.1). Therefore, the following section thoroughly reviews previous research that aimed to model how sound propagation is altered when a shear layer is present in the flow. Subsequently, a section follows that explains how the sound propagation through a shear layer is applied to the fuselage scattering problem.

2.3 Sound Propagation Through Shear Layers

The problem of sound propagation through a shear layer is governed by the Pridmore-Brown equation. Since the scope of the present work is to highlight and use different and novel methods, mainly analytic, it is deemed necessary to provide a review of additional techniques used to overcome the difficulty of solving the Pridmore-Brown equation. These techniques are

used mainly in duct and liner acoustics when the flow in the duct includes shear boundary layers at the duct walls. A lot of focus should be given in the use of asymptotic methods since they provide an analytic solution to the problem without sacrificing too much accuracy. However, as will be seen in later sections, many recent publications treat the problem of sound passing through a shear layer mainly by employing numerical methods and bridging the singularity present in the Pridmore-Brown equation using the Frobenius method. A thorough review of these methods and how they apply on the fuselage scattering problem will follow in section 2.3.2.

Pridmore-Brown (1958) was the first to attempt to solve the differential equation which was later named after him. In his paper he simplified the problem by only considering two-dimensional flow over a simple plane wall. This flow develops a shear layer above the wall and he proceeded in studying the effects of that shear in the downstream propagating acoustic plane wave. In the paper, two velocity profiles were investigated, a simplified linear and a more realistic 1/7th power law turbulent layer profile. Firstly, the two-dimensional differential equation is solved for a linear profile using an approximate method proposed by Langer (1937). This allows an analytic solution to the problem as long as the Mach gradient in the shear is sufficiently small. Then the problem is reduced to a simple eigenvalue problem. Pridmore-Brown (1958) produced results for a medium and small velocity gradient, which revealed that the shear affects the higher frequencies more than it does the lower ones. The same technique was used to solve the equation for the turbulent layer. In this case the approximate solution proposed by Langer (1937) breaks down at the wall, but this singularity is bridged using a Laurent series. The turbulent layer results revealed the same trends as the linear case, leading the author to suggest that a very good estimate for the realistic turbulent layer can be achieved by using an equivalent linear boundary layer profile. Pridmore-Brown (1958) also produced some results for acoustically soft walls, which revealed that the change of the attenuation due to the lining of the wall is minimal when the boundary layer thickness is comparable to the wavelength of the acoustic wave. That was expected since in that case the refraction effect is very small compared to higher frequencies.

The work by Pridmore-Brown (1958) inspired a lot of subsequent research on the subject. Mungur and Gladwell (1969) were the first ones to improve on Pridmore-Brown's work. Their analysis was also confined to two dimensions but they included viscosity terms in order to investigate its effects on the propagation through the shear, although certain assumptions were made, namely the temperature gradient being constant across the duct. Firstly, Mungur and Gladwell (1969) validated the expression by investigating the inviscid case and comparing it to the results by Pridmore-Brown (1958). The expression successfully reduces to the two-dimensional Pridmore-Brown equation when viscosity is set to zero. In terms of solving the equation, Mungur and Gladwell (1969) employed a fourth order Runge-Kutta scheme assuming a power law profile. By doing so they eliminated the singularity at the wall present in Pridmore-Brown's paper, while the numerical results were very close to Pridmore-Brown's results. They also proceeded to solve the problem that included a finite impedance on the walls. The complexity of the analysis was increased in that case but the results were more realistic since the Pridmore-Brown method assumed the same pressure distribution across the duct for both rigid and soft walls.

Mungur and Plumblee (1969) extended the analysis of Mungur and Gladwell (1969) to investigate the effects of wall impedance in an annular duct. They also assumed a duct with finite length and introduced reflection at the duct termination. They begun by deriving the Pridmore-Brown equation for cylindrical coordinates and employed the nondimensionalisation that all subsequent papers on the subject used. This nondimensionalisation can be applied to any circular duct. They initially validated the expression by reducing the shear to a uniform flow and recovered the Bessel equation. Further validation was performed by investigating the uniform flow case both for rigid and nonrigid walls. The general inviscid case with finite wall impedance was then solved by employing an extended version of the Runge-Kutta scheme used in Mungur and Gladwell (1969). The paper presented an extensive parametric study with parameters like effects of sheared flow on mode shapes and propagation and attenuation constants, with focus given especially on the effects of shear on the attenuation. The boundary layer thickness varied from 1.5% to 12.5% of the annular radius while the profile chosen was a quarter sine. The results indicated that with increasing boundary layer thickness the attenuation was increased downstream because sound was refracted towards the walls. Also, Mungur and Plumblee (1969) concluded that the differences in attenuation are too large to ignore the shear effects. Another interesting conclusion reached in this study was that it is inaccurate to use measurements from a rectangular duct to predict the attenuation of an annular duct.

A different technique was used by Shankar (1971). Shankar (1971) addressed an issue that had not been addressed before. He did not make any assumptions regarding the form of the solution and instead used a perturbation scheme to obtain a solution. By doing so, the solution was expressed in terms of a given sound pressure distribution which was determined by the source. By using an initial plane wave perturbation, the solution could be written in a power series form. Then the large time solution could be obtained which would give the pressure distribution long after initial perturbation has passed and the transient effects have dissipated. The results showed that refraction is dependent on the relation between the wavelength and the duct width. Furthermore, Shankar (1971) concluded that upstream sound was refracted away from the wall, and with increasing frequency and Mach number the effects of the shear were also increased as expected. Shankar (1971) also pointed out that this method is confined by the limitations of the perturbation scheme, meaning that when the shear effects become too large they can no longer be treated as a small perturbation.

Mariano (1971) was another researcher who investigated the effect of shear layer in the attenuation of a lined duct. He employed a finite difference scheme to solve the Pridmore-Brown equation in a three-dimensional rectangular duct with lined walls with viscosity and temperature effects neglected. The aim of this work was to calculate the attenuation spectra along the duct. Mariano's work was also focused on investigating the practicality of using a linear velocity profile. More specifically he performed simulations both for the 1/7th power law profile and an equivalent linear profile with half the thickness and the results were indeed very close. This led to establishing a practical law that allows any turbulent boundary layer profile to be replaced with an equivalent linear without sacrificing accuracy. This was also suggested by Pridmore-Brown (1958). In order to estimate the value for a typical boundary layer thickness, Mariano (1971) used flat plate theory to evaluate the growth of the turbulent layer. He assumed a constant value of the boundary layer thickness

calculated at the center of the duct. Results were presented in a range of parameters, such as Mach number, boundary layer thickness and the effect of slip on the wall. The boundary layer thickness varied from 0.1% to 13.8% of the duct width and once again it largely affects the attenuation spectra. As in previous publications the larger the boundary layer thickness the larger the attenuation upstream. Also, it was reported that the cases with no slip at the wall demonstrated larger decrease in attenuation. One distinctive feature of Mariano's paper is the comparison with experimental results. Measurements of the attenuation spectra were obtained from three different materials. The comparison with the theoretical prediction revealed that the prediction is very accurate on the upstream but slightly worse on the downstream. Mariano (1971) concluded that the effect of the shear is much more important and pronounced in the upstream than in downstream, and that the slip on the wall decreased the effect.

Ko (1972) also studied the effect of shear on the attenuation spectra. More specifically he studied a circular duct and focused on the effect the shear has on the effectiveness of the liner. Like Mariano (1971), he also used a finite difference scheme, specifically the central difference formula along different radial stations of the duct and the liner. Ko (1972) proceeded to conduct a thorough parametric study focused on the characteristics of the flow as well as the characteristics of the liner. He investigated the effect on the attenuation of boundary layer thickness, Mach number, frequency of the facing sheet, lining thickness and duct length. He also compared some results with experimental measurements. He concluded that contrary to popular belief, the fundamental mode might not be the least attenuated and that is because there is a wide range of parameters that determine the attenuation and very important amongst them is the boundary layer thickness. As expected, increased boundary layer thickness led to considerable decrease in the attenuation upstream. Once again, Ko (1972) underlines the importance of the presence of the shear for the upstream since the downstream effects are negligible.

Another researcher that attempted to investigate the effect of boundary layer on the attenuation of a lined circular duct was Eversman (1970). His motive was the discrepancies between the uniform flow predictions and the actual experimental measurements. The method used by Eversman (1970) is based on Mungur and Plumblee's work with suitable modifications since contrary to Mungur and Plumblee's case where the duct was annular, now the duct is circular which means there is a singularity at its center. As mentioned above, Eversman (1970) uses the same Runge-Kutta technique to solve the problem but in order to bridge the singularity at the center of the duct, he introduces a power series solution near the center. Eversman (1970) investigated three different boundary layer thicknesses ranging from 0% to 10% of the duct radius. The conclusions he drew are very similar to the conclusions that were reached by other researchers mentioned above. First of all, the downstream effects are negligible while the upstream effects are quite pronounced. Secondly, larger boundary layer thickness leads to a reduction in the attenuation upstream since more and more sound is refracted away from the wall. These conclusions led Eversman (1970) to suggest that liner performance is better downstream.

Eversman and Beckemeyer (1972) recognised that a Runge-Kutta method will always suffer from high computational cost as all numerical methods do. They decided to introduce an asymptotic method to solve the Pridmore-Brown equation. For thin boundary layers the solution inside the boundary layer can be asymptotically expressed as a power series. That

allows the solution to be in terms of integrals that can be solved analytically especially for simpler profiles like the linear profile or the quarter-sine profile. Of course this method, being an asymptotic solution, is valid only for sufficiently small boundary layer thicknesses compared to the radius of the circular duct. It is evident then, that a validation study is in order. Some initial results were presented by Eversman and Beckemeyer (1972) that involved comparison with an exact Runge-Kutta solution. The comparison revealed that the approximate solution is remarkably close to the exact one. However, this initial study was for a very thin boundary layer (just 0.5% of the duct radius) and a very small Helmholtz number; conditions that do not constitute a realistic example.

Eversman (1972) published shortly after Eversman and Beckemeyer (1972) the validation study needed for the asymptotic expansion method. In this more recent paper, Eversman (1972) presented comparisons with the Runge-Kutta method but this time for boundary layer thicknesses up to 10% of the duct radius. Also, the Helmholtz numbers this time were higher although still considered medium to low. The results revealed that the approximate method is reliable even for very thick boundary layers. Of course, the accuracy tends to decrease with larger boundary layer thicknesses but the error is less than 20% for thick boundary layers which according to Eversman (1972) is acceptable for many practical applications. One unexpected conclusion reached by Eversman (1972) is that there is deviation in the lower frequencies from the exact solution. According to him, this is because of the impedance on the walls which is very sensitive to change in low frequencies.

Finally, Goldstein and Rice (1973) introduced an entirely new method of solving the problem analytically. In their paper they attempt to evaluate an effective wall impedance that will replace the boundary layer as a boundary condition in a two-dimensional duct. Goldstein and Rice (1973) assumed a linear boundary layer profile. By making that assumption and with an elaborate change of variable the equation reduces to Weber's equation which has a known analytic solution expressed in Parabolic Cylinder Functions (PCFs). These PCFs allow the two-dimensional problem to be solved entirely analytically. In addition, Goldstein and Rice's method does not appear to have a strict restriction regarding the thickness of the boundary layer although they do mention that a very thick boundary layer compared to the wavelength may present complications. Unfortunately, Goldstein and Rice (1973) did not present any results of a more practical interest that would facilitate the validation of that method.

It was not until Scott (1979) used this technique to evaluate the far-field effect when sound passes through a linear shear. Scott's objective was to produce polar directivity plots for multipole sources either close or inside the shear. He used line sources comprised by monopoles, dipoles and quadrupoles. His governing equation was two-dimensional as in Goldstein and Rice (1973). The differential equation is solved using the analysis proposed by Goldstein and Rice (1973) which meant that the expressions are dependent on PCFs. Scott (1979) derived not only exact expressions for the far-field directivity but approximate ones for low and high frequency. This corresponds to small and large argument approximations for the PCFs. Once again it was revealed that the boundary layer thickness is paramount in determining the shear effect on sound. Scott's work also revealed the difficult nature of PCFs, since their computation poses certain challenges. More specifically, the code used for the exact calculation of the PCFs struggled at high frequencies, although at that point the large argument approximation could reliably replace the exact expression. In addition, a lot of

difficulties were encountered at the calculation of the directivity at certain polar angles either because of singular points or because of inability of the code to compute the PCFs. Despite these difficulties, Scott (1979) concluded that this method is reliable for the evaluation of the polar directivity.

2.3.1 Two-dimensional Problem

In more recent publications several attempts have been made to analytically solve the problem of sound propagation through a shear layer. These publications are characterised by the simplicity of the boundary layer, which is usually two-dimensional, and the simplicity of the source, point or line sources.

Jones (1977) was one of the first researchers to examine the problem of sound travelling through a two-dimensional linear shear. The source used was a simple time-harmonic line source. The sound would then propagate through the two-dimensional layer from lower Mach number to the flow above it where the free stream value of the Mach number is achieved. The main objective by Jones (1977) was to determine a limit of the layer thickness over which the layer can no longer be simplified by a vortex sheet. Jones (1977) concluded that the vortex sheet assumption is only valid for very thin layers. This is a conclusion reached by future researchers too. Around the same time Amiet (1978) focused on the refraction of sound by a shear layer. His scope was to determine which parameters are important when one considers an open jet wind tunnel shear layer correction. Amiet (1978) found that the layer thickness is not important at the high Mach numbers achieved in open jet tunnels. On the contrary, he concluded that the shear layer shape can be more important in determining the correction factor. It should be noted that the analytical expressions developed by Amiet (1978) assume either an infinitesimally small or infinitely large shear layer thickness.

Campos et al. (1999), proposed linearly independent solutions based around the critical layer that occurs in a linear shear. The critical layer is the layer on which the Pridmore-Brown equation is singular and therefore is no longer valid. Physically the critical layer corresponds to a point at which the phase velocity of pressure perturbation equals the local velocity of the free stream. By moving the critical layer at the wall boundary and using the Frobenius method, a final solution can be obtained for an incident wave that has the form of an acoustic perturbation inside the boundary layer. The Frobenius solution and its advantages are discussed in section 2.3.2. Campos and Serrao (1998) extended the theory to include an exponential velocity profile and focused on the same effects, namely the ability of the critical layer to act as an absorption mechanism for sound.

Campos and Kobayashi (Campos and Kobayashi (2000), Campos (2000)), explored a more realistic example phenomenon of a shear with finite thickness between two free stream flows. This phenomenon is usually present at flow separation in high Mach number flows. They used hyperbolic tangent velocity profiles and examined the reflected and transmitted waves through the transitioning flows. Campos and Kobayashi (2000) performed several examples including varying shear layer thickness compared to the wavelength and angle of incidence. They concluded that contrary to previous findings (Miles (1958)), the thickness of the shear layer is very important. Only for thicknesses considerably smaller than the wavelength can the

assumption of a vortex sheet be used. For thicker layers, the sound flow interaction must be considered.

Campos and Kobayashi (2009) continued their work and introduced temperature gradients inside the shear that are associated with the varying sound speed inside the shear. They assumed constant enthalpy in order to create the temperature profile inside the shear. The challenge in Campos and Kobayashi (2009) was the fact that the critical layers present on the problem are now two instead of one. There is the critical layer associated with the flow, where the Doppler shifted frequency vanishes which has been investigated in previous work (Campos and Kobayashi (2000)), and the layer where the speed of sound vanishes which creates another regular singularity. The three profiles used in the analysis were the linear, exponential and the hyperbolic tangent. Campos and Kobayashi (2010) also placed a rudimentary line source outside the boundary layer in order to model the refraction and reflection of the shear layer. They concluded that the temperature gradient only affects the refraction levels when the Mach number is supersonic. When the Mach number is subsonic, the velocity profile is the one that plays the major role on the refraction behavior.

2.3.2 Frobenius Series Solution

It is the author's opinion that the Frobenius solution to the problem of sound refraction by a shear boundary layer merits its own section since it proved to be very influential and has commonly been used to solve the Pridmore-Brown equation. Furthermore, as will be seen later, this solution is used consistently in problems involving scattering by the fuselage and its boundary layer for both propeller and fan noise sources.

McAninch (1983) was the first one to attempt to explain the apparent shielding effect caused by the boundary layer. As mentioned before in section 2.2, experimental results (McAninch (1983), Hanson and Magliozzi (1985)) showed that there is a discrepancy between the theoretical predictions that omit the boundary layer and the actual measurements on the fuselage surface upstream of the source. Since the microphones were mounted beneath the boundary layer, it became obvious that its effect could not be neglected. McAninch (1983) proposed a theoretical solution using a more realistic Pohlhausen velocity profile rather than a simplified one which was used by current analytical models. The major mathematical challenge with the proposed solution was a singularity occurring at a "critical" point inside the boundary layer. At that critical point, the Pridmore-Brown equation presents a singularity and is no longer valid. McAninch (1983) suggested using a Frobenius series method to bridge this singularity around the critical point. The solution around the critical point is then matched to the known solution at the edge of the boundary layer thus obtaining the full analytical solution for sound waves travelling through a boundary layer. The Frobenius series used by McAninch (1983) was inspired by the specific method proposed by Tam and Morris (1980). Tam and Morris bridged the singularity present in Pridmore-Brown equation using a Frobenius series in a two-dimensional plane. McAninch concluded that this refraction effect of the boundary layer caused significant shielding, especially for propagating angles close to being parallel to the axis of the fuselage, and that it is sensitive to frequency and Mach number.

2.4 Propeller Noise Scattering by the Fuselage and Refraction by its Boundary Layer

The Frobenius series solution has proved to be successful in being used alongside high-fidelity numerical methods, such as Runge-Kutta routines. This section is dedicated to the problem of propeller noise scattering by the fuselage and the refraction effect caused by the inclusion of a boundary layer on the fuselage. As will be seen, the papers presented here use high-fidelity numerical methods alongside the Frobenius solution to give estimates of the fuselage surface pressure and the far-field pressure.

Hanson (1984) understood the need for an analytical model to describe propagation inside a shear layer. The motivation for Hanson's work was similar to McAninch's in that he was trying to explain the discrepancies between experimental measurements and the analytical results. More specifically, Hanson (1984) based his work on a Prop-Fan scale model. The experimental results of the model revealed much lower fuselage pressure levels than the predicted doubling of 6dB. Hanson's initial analytical model was simplified, meaning the velocity profile was a simple step profile and the flow is two-dimensional. This simplification eliminates the singularity present in McAninch's model since the resulting equation is not the Pridmore-Brown equation. Hanson's model included scattering waves by the fuselage which were not part of McAninch's analysis. As usual the scattered waves take the form of the scattering surface. In this simplified case the scattering surface was a flat plate, so both scattered and incident waves are in the form of plane waves. Similar to McAninch (1983) the pressure outside and inside the boundary layer is matched at the edge through continuity of pressure and fluid particle displacement.

The results produced from Hanson's analytical model revealed the significance of the role the boundary layer plays in sound propagation. The shielding or refraction effect occurs mainly upstream of the source, and is virtually negligible downstream of it with only the doubling of 6dB due to reflection being visible. Hanson concluded that forward of the source the refraction effect is sensitive to Mach number and wavelength. In fact the lower the Mach number the weaker the effect. On the other hand the smaller the wavelength the stronger the attenuation. This can be explained by the fact that when the wavelength is much shorter than the boundary layer thickness, multiple cycles of refraction will occur within the boundary layer. Another conclusion from this work was that the attenuation effect would reduce at larger scale models. This fact is closely related to the wavelength effect. Although this model was very simplified (scattering by a flat plate, plane incident waves, step-function velocity profile) it revealed the importance of the boundary layer and it became the basis for all the subsequent analytical models.

The paper by Hanson and Magliozzi (1985) is probably one of the most important publications regarding acoustic installation effects. It was the first example of a realistic prediction method with minimal simplifications. This work was based on the initial model by Hanson (1984) but it was extended to include a solution in three dimensions, a more complex boundary layer profile and a more realistically shaped fuselage. In this case, the fuselage is represented by an infinitely long, rigid cylinder while the boundary layer's thickness is constant along and around the fuselage. Another extension of the model was the inclusion of a realistic propeller

source based on a previous model developed by Hanson (1985). That model was developed to describe the acoustic near-field of a propeller using thickness loading and quadrupole sources. In the case of Hanson and Magliozzi (1985) the propeller noise source is modeled using this similar kind of distributed, rotating source.

The analysis performed by Hanson and Magliozzi (1985) formed the mathematical framework for all future analytical work in acoustic installation effects. They focused on the calculation of the near-field pressure and more specifically on the pressure on the fuselage since their results were ultimately compared to measurements taken from the same experimental model as in Hanson (1984) which had an array of microphones distributed along the fuselage. The pressure was expressed in terms of a Fourier series since in this form it is easier to examine the frequency and Mach number dependency. The cylindrical coordinate system for the incident pressure field was naturally centered on the propeller axis as in Hanson (1985), but the coordinate system used for the derivation of the scattered field needs to be centered on the cylindrical fuselage because, as mentioned before, the scattered waves take the shape of the scattering surface. Hanson and Magliozzi (1985) proposed using the Graf's addition theorem (Abramowitz and Stegun (1965)) to shift the incident coordinate system to the center of the fuselage, thus facilitating the summation of the two fields into one total field. This methodology has been proven to be very effective and popular for the topic of fuselage scattering and it will be used in the work presented in this report. However, inside the boundary layer the situation is more complicated stemming from the fact that the velocity profile is arbitrary and not simplified. This means that the equation that needs solving is the Pridmore-Brown equation which has the singularity mentioned in McAninch (1983). As in McAninch (1983), Hanson and Magliozzi used the Frobenius method to bridge the singularity as proposed by Tam and Morris (1980). Tam and Morris bridged the singularity using a Frobenius series in a two-dimensional plane. That is why Hanson and Magliozzi choose to unravel the cylindrical coordinate system into a two-dimensional plane, an approximation that is valid since the thickness of the boundary layer is significantly smaller than the radius of the cylindrical fuselage. Finally, the solution is matched with the free-stream one at the edge of the boundary layer.

This analytical model proved to be very successful and confirmed the trends shown in the experimental measurements. The model could provide an accurate picture of the fuselage scattering effects. A distinctive shadow zone was visible behind the fuselage which was expected, whereas on the source's side of the fuselage there was almost full pressure doubling. Once again, it was clear that the shielding was greater when the wavelength was shorter, or when the frequencies were higher harmonics of the BPF. As concluded by Hanson (1984), the refraction effect upstream of the source became stronger with increasing Mach number. The results presented by Hanson and Magliozzi emphasise the fact that the scale of the model plays an important role. They concluded that maximum shielding is achieved when complete refraction occurs which is dependent on Mach number and frequency. Overall, the model proved to be very accurate in predicting the acoustic installation effects by a cylindrical fuselage even though the source model was reduced to a rather simplified one, meaning that in the future efforts need to be made for more accurate representations of the source.

Although this model proved to be accurate, Lu (1990) proposed some extensions to improve it. Lu's model did not simplify the problem by assuming a thin and isothermal boundary layer.

Lu (1990) also used asymptotic approximations to calculate the acoustic far-field as well as the fuselage surface pressure. Furthermore, the thin boundary layer assumption made by Hanson and Magliozzi (1985) is not present in Lu's work. In that case the arbitrary boundary layer has a constant thickness but it does not need to be much smaller than the radius of the fuselage. Also, the boundary layer exhibits temperature variations in order to examine the dependency of the installation effect on the boundary layer's temperature profile. The source used in the analysis was a rotating monopole to simulate a propeller source and the results were compared to experimental measurements of a counter-rotating model propeller.

The analysis proposed by Lu is very similar to that used by Hanson and Magliozzi (1985). The pressure is expressed in terms of a Fourier series and the Frobenius method is used to bridge the singularity inside the boundary layer. Just like in Hanson and Magliozzi (1985), the Graf's addition theorem is used to shift the coordinate system from the monopole source to the centre of the fuselage, thus obtaining the total pressure field in terms of Bessel and Hankel functions. Moreover, an asymptotic approximation is used to calculate the far-field which will enable the calculation of community noise. Results confirmed the trends predicted by Hanson and Magliozzi (1985). The distinctive shadow zone behind the fuselage was again clear and the monopole pressure distribution along the fuselage seemed to be shifted aft of the plane of the source. This shifting is caused by the refraction effect and is observed in the paper by Hanson and Magliozzi (1985). Also, the shielding effect is clearly visible upstream of the source as was the case for all the previous work. Once again the dependency on Mach number and frequency is presented. The higher the Mach number the stronger the shielding upstream with the same happening for higher frequencies. Very similar trends are observed for the cases of varying boundary layer thickness and varying azimuthal angle. The thicker the boundary layer the stronger the shielding which is explained, as mentioned before, by the scale effect meaning that the thicker the layer the more refracted the waves will become since they will be subject to multiple cycles of refraction. By changing the azimuthal angle from zero, the distance travelled by the wave is increased effectively strengthening the refraction effect. Another conclusion reached by Lu (1990) is that the boundary layer velocity profile does not have a strong effect on the sound attenuation. The same was observed for varying temperature. Different temperatures of the boundary layer caused little to no change in the fuselage pressure levels. On the other hand, the far-field pressure proved to be very sensitive to the boundary layer effect. The installed far-field exhibited up to 4 dB difference than the free-field due to the inclusion of the fuselage and its boundary layer. According to Lu (1990) the thickness of the boundary layer plays a very important role in the directivity pattern of the far-field pressure. Finally, comparison with the experimental measurements showed good agreement as far as the trends are concerned but there were considerable discrepancies up to 5 dB. Lu attributed these discrepancies mainly to the unrealistic monopole source used in the analysis, meaning that a more complex source must be used that better resembles a propeller noise source

Two papers by Brambley et al. (Brambley et al. (2011), Brambley et al. (2012)) investigated the use of the Frobenius series method to bridge the singularity around the critical point as suggested by McAninch (1983) and Tam and Morris (1980). The focus of this work was to investigate the impact of the critical layer and whether its inclusion in the analysis affects the results. Brambley et al. (Brambley et al. (2011), Brambley et al. (2012)) highlighted the benefits of the Frobenius series, namely its ability to facilitate accurate numerical solutions inside the

shear layer. Brambley et al. concluded that when the source is outside the flow, the effects of the critical layer decay rapidly along the duct where the sheared flow is located, therefore it is not necessary to include the critical layer in the analysis. However, there are some instances where the critical layer should be considered. According to Brambley et al., in some high frequency examples the critical layer creates instabilities in the solution.

Research on the far-field propeller noise has also been performed by Belyaev (2012). The techniques used to solve the problem of sound propagation through the boundary layer are the same as previous publications, but there are differences in the modeling of the propeller noise source. Belyaev (2012) proposed a more realistic and representative propeller noise source, in contrast to point sources that had been used so far in previous work. This decision was made due to the findings of Papamoschou (2012) and Ostrikov (2012) who proved that the source distribution plays a vital role in scattering both in jet noise and bluff body interactions. Therefore, Belyaev sought to model a more complex propeller noise source based on thickness noise as proposed in Hanson (1985). Belyaev only examined the far-field and presented polar directivity plots. These plots presented the far-field pressure for a variety of varying parameters. These parameters were the free stream Mach number, boundary-layer velocity profile and boundary-layer thickness among others. The conclusion reached by Belyaev was that the far-field effect can be significant and it is recommended that it is not omitted. Also, parameters such as boundary-layer thickness or free stream Mach number play a major role in the far-field pressure and can greatly affect the results.

Brouwer (2016) also investigated both the near- and far-field of an installed open rotor adjacent to a cylindrical fuselage. He derived analytical solutions for the incident field produced by a single-rotor propeller and a contra-rotating propeller. Brouwer (2016) derived these expressions using a lifting-line model which simulates very well the effect of a single-rotor propeller and it closely approximates the effect of the contra-rotating open rotor although not as well as the single-rotor. Like Lu (1990), far-field approximations are used for distances away from the fuselage. Brouwer (2016) focused on the azimuthal directivity plots and highlighted the importance of the asymptotic solution for the far-field and how it reduces the computational cost compared to high-fidelity numerical solutions. As for the near-field, the same conclusions have been reached as in previous research. Namely, the refraction due to the presence of the boundary layer is substantial upstream of the source.

2.5 Fan Noise Scattering by the Fuselage and Refraction by its Boundary Layer

As is evident, the research on installation effects over many years has been focused on propeller noise. The first attempt to model fan noise installation effects was made by McAlpine et al. (2015) (see its review in section 2.2), who did not include a boundary layer on the fuselage. In this section, the few recent publications are reviewed that attempt to solve the problem of fan noise scattering by the fuselage and its refraction due to the presence of a boundary layer on the fuselage. It is important to note that the solutions presented here use high-fidelity numerical methods as was the case in section 2.4.

Gaffney and McAlpine (2017) extended the same distributed source model introduced in McAlpine et al. (2015) to include a boundary layer around the fuselage. The incident and scattered near-field expressions outside the boundary layer are the same as in McAlpine et al. (2015). For the solution inside the boundary layer, the Pridmore-Brown equation must be solved. As mentioned in previous publications (McAninch (1983), Hanson and Magliozzi (1985), Lu (1990)), the singularity present in the Pridmore-Brown equation can be bridged using a Frobenius method. The same technique is applied by Gaffney and McAlpine (2017). As in previous publications, the solution inside the boundary layer is matched with the solution outside at the layer's edge. The Pridmore-Brown equation has no known analytical solution, so a numerical Runge-Kutta solver was employed. The ODE solver is applied around the "critical layer" which is the radial location at which the singularity is located. In close proximity of this layer, the Frobenius method is used and it is matched to the surrounding solution provided by the ODE solver. Further calculations were needed due to the fact that the expressions are in the form of an inverse Fourier z-transform. Thus, a rigorous verification and convergence investigation was conducted by Gaffney and McAlpine (2017). The code was verified by setting the shear layer's Mach number distribution equal to the free stream constant Mach number. The results were compared with the free stream only solution and showed good agreement, effectively verifying the code. A convergence study was also conducted which investigated the effect of the width of the "critical layer" that needs to be used for the Frobenius method to be accurate. For further validation of the method, it was compared to the method proposed in Lu (1990) by reducing the disc source's radius to resemble a monopole source. The comparison revealed that although the solution in Gaffney and McAlpine (2017) did predict substantial shielding upstream of the source, it did not agree with the rapid increase in shielding that Lu had predicted. Gaffney and McAlpine (2017) produced illustrative results for the pressure on the surface of the fuselage for varying flow characteristics, such as boundary layer profile, and varying source characteristics, such as the spinning mode exiting the fan duct. A shielding coefficient was introduced which corresponds to the amount of acoustic energy refracted away from the surface of the fuselage. The results revealed similar patterns as in previous publications (Hanson and Magliozzi (1985), Lu (1990), Fuller (1989)). More specifically it was observed that higher frequencies were susceptible to more shielding and that the thicker the boundary layer the more shielding it produced. Also, refraction was more significant further upstream of the source since the incidence angle becomes shallower meaning that waves are refracted more easily. It was also revealed that the profile shape plays an important role in the shielding effect, with the power law mean-flow profile producing less shielding than other profiles tested. This is due to the fact that the power-law profile generally has a smaller gradient than other profiles, such as the quarter-sine profile. Steeper gradients generally lead to more refraction. Gaffney and McAlpine (2017) also concluded that refraction is more effective for well cut-on modes because their principal lobes impinge on the fuselage at shallower incidence angles making them more susceptible to refraction.

Finally, Gaffney and McAlpine (2018) extended the model even further to include a more realistic source. Using the Wiener-Hopf method the diffraction around the duct's lip can be modeled giving a more realistic incident field which is valid for higher polar angles. Although this method gives good results for high polar angles there are limitations, since at even higher polar angles or even further downstream, other sources start to become dominant such as

propagation from the bypass. The methodology used by Gaffney and McAlpine (2018) is the same as in Gaffney and McAlpine (2017) with the main difference being the derivation of the incident field. The incident field is no longer a disc source but rather the sum of the spinning mode exiting the duct exit and its diffraction field. The scattered field and the propagation inside the boundary layer are modeled exactly as in Gaffney and McAlpine (2017).
Preliminary results revealed that further upstream of the source, the pressure levels on the surface of the fuselage are almost identical to the case of the disc source. However, closer to the source's plane the discrepancies become larger since the angle of incidence increases and the Wiener-Hopf method becomes more accurate than the disc source. Gaffney and McAlpine (2018) concluded that the maximum angle at which the disc source can be used to little loss of accuracy is around 70^o as concluded in other previous works. The results were once again presented in the form of the shielding coefficient, and showed once more the shielding effect of the boundary layer upstream of the source. The nature of the new Wiener-Hopf source enabled rapid calculations of multi-mode simulations which gave a more realistic radiation pattern for a turbofan engine. A slight increase of pressure levels is observed downstream of the source since in this region the sound is refracted towards the surface. The conclusion was that the shape of the boundary layer profile is not as significant as its thickness.

2.6 Computational and Experimental Methods

The following section presents a brief review of literature that exists concerning numerical and experimental methods used for the prediction of installation effects. As will be seen, the literature on these methods is not very comprehensive compared to theoretical methods due to the computational requirements of the problem that needs to be solved. It should be pointed out that the review that follows does not go into detail about the methods, but rather it focuses on the results and conclusions.

One of the most popular numerical methods that are used in acoustics is ray-tracing. Atalla and Glegg (1991) were the first to find an application for ray-tracing in predicting acoustic installation effects. Atalla and Glegg (1991) used the theory of geometrical acoustics. This allowed them to extend the ray-tracing algorithm to include bodies of arbitrary shape and an arbitrary moving medium. This gives an advantage over analytic solutions since they are dependent on simplifications. Of course, geometrical acoustics theory has other limitations such as the requirement that the moving medium must have smoothly varying characteristics or problems associated with the presence of singular points. Atalla and Glegg use rotating sources since they are interested in rotor noise and they validate their method by running simple examples that have analytic solutions and then comparing the results. A couple of those examples are the case of a plane wave impinging on a sphere and a point source impinging on a cylinder. The method proved to be very accurate except for the shadow zone region where its performance deteriorates. Atalla and Glegg (1991) concluded that the scattering effects cannot be neglected especially for highly directive sources. Also, the effect of flow proved to be very important at high Mach numbers since it displaces the lobes and the shadow zone. It should be noted that no shear layer was included in the analysis.

Ray-tracing has been used more recently by Agarwal et al. (2007). In this paper the geometrical theory of diffraction is used to predict the acoustic shielding from the "silent aircraft" airframe. This flying wing configuration allows the engines to be mounted on top of the blended wing body, thus allowing sound to propagate to the ground only through diffraction by the edges of the body. The analysis in the paper is limited to low Mach number homentropic flow, but unlike Atalla and Glegg (1991) it involves a more robust diffraction theory. Once again, the method is validated by comparing the results for a simple problem of diffraction around a cylinder. Moreover, the work by Agarwal et al. (2007) included small-scale experimental measurements. The ray-tracing method produced results with good agreement with the measurements, as long as the dimensions of the object are sufficiently larger that the wavelength. It is also important to point out that the flow was assumed to be low-Mach and with no boundary layer. It was concluded that the inclusion of a shear in the flow would complicate the problem and would render the method too expensive to use.

Another computational approach to modeling installation effects was by Stanescu et al. (2002). The work by Stanescu et al. (2002) involves the use of a spectral method to compute the field around a configuration with fuselage and wing. The source used in this work was a spinning mode simulating a fan noise source. Stanescu et al. (2002) used parallel processing to reduce the computational cost of the problem, but the cost for a realistic range of frequencies is still very high. Furthermore, the results in this work were for a stationary medium. The results with the inclusion of a fuselage adjacent to the source revealed differences that are too important to neglect. The field was greatly altered due to reflections on the fuselage. Another example was the inclusion of a wing below the source. This led to significantly reduced noise levels below the wing because of the expected reflection of sound upwards. It was concluded that with the inclusion of fuselage and wing the sound pressure levels on the surface of the fuselage were significantly increased.

Wang and Zhou (1998) used a boundary element method based on the acoustic analogy to model the effects of the presence of the fuselage adjacent to a propeller noise source. The novelty in this paper was the inclusion of a non-rigid boundary condition on the fuselage surface. Once again, refractive effects of the boundary layer are neglected by assuming a low Mach number. The analysis was based on the Ffowcs Williams-Hawkings analogy. The validation was carried out by reducing the fuselage to a vibrating sphere both in a stationary and a moving medium, which has an analytic solution. The results showed good agreement with the error being less than 0.1 dB. This method can be applied for arbitrary shapes of the fuselage and it showed that the convective effects of the flow cannot be neglected even for low Mach numbers.

Experimental work in installation effects is primarily focused on the shielding and mainly turbulence scattering that occurs when sound propagates through a turbulent shear layer. The work by Candel et al. (Candel et al. (1975), Candel et al. (1976)) investigated the sound propagation and frequency scattering through a turbulent jet layer experimentally. Their conclusion on shielding was that the layer thickness plays a very important role in the shielding. Also, they noticed the phenomenon of total reflection at higher angles of observation or rather at upstream regions. The most significant result on frequency scattering was that the large scale structure of the turbulent jet layer determine the scattering process, namely the scattered sound waves follow the same pattern as the turbulent structures.

This phenomenon of haystacking or broadening of the far-field noise spectra was further more investigated by Ewert et al. (2009). By using Computational AeroAcoustics methods, they developed a prediction model for haystacking and compared the results with the experimental measurements by Candel etal. (Candel et al. (1975), Candel et al. (1976)). As stated in Candel et al. (Candel et al. (1975), Candel et al. (1976)), this haystacking effect is the result of fan tones interacting with the turbulence inside a shear layer. The broadening of the spectra leads to a reduction of the noise peaks in the far-field which means, as proposed by Ewert et al. (2009), that this broadening can be used to attenuate sound peaks. In the work by Ewert et al. (2009), the turbulent shear layer is calculated using a RANS code and CAA methods are used to calculate the propagation of sound inside the shear layer. The numerical predictions showed good agreement with the measurements performed by Candel et al..

Another very important computational work on the subject was done by Siefert and Delfs (2011) who focused on high Mach number scattering rather than low Mach number as in the work by Dittmar and Hall (1990). They used a RANS simulation to calculate the flow field and they included turbulent fluctuations in the boundary layer to model the scattering inside the layer. In this paper, the fuselage was simplified to a flat plate and the source to a monopole due to the increased complexity of the problem. Siefert and Delfs (2011) highlight the importance of the refraction due to the presence of the boundary layer which is prevalent in their results. Furthermore, they concluded that refraction is more pronounced in higher frequencies. Siefert and Delfs (2011) also modeled the frequency scattering inside the layer due to turbulent fluctuations in the shear. These results revealed sound does transmit in the shadow zone due to scattering and it can lead to significant alterations of the sound field. The authors concluded that this effect might be misleading in certain regions because the fluctuations become comparable to the numerical error far upstream of the source where the refraction is dominant owing to the shallowness of the incidence angle.

Significant work on turbulence scattering by the fuselage boundary layer has also been conducted by Dierke et al. (2013). The model used in this paper is more realistic and resembles an aircraft with a rear-mounted fan engine. The purpose of the work was to investigate the refraction and scattering effect of the turbulent boundary layer on the fuselage upstream of the engine intake. The calculation of the boundary layer development and growth was conducted with a RANS code that yielded a layer thickness of about 0.1m to 0.2m. The calculation of the incident wave was conducted with the finite element code ACTRAN with azimuthal order modes of 20 or 24 which correspond to rotor-locked modes. Finally, the propagation of the sound waves was calculated with the CAA code PIANO. The conclusion reached by the authors was that the refraction effect is substantial even for steep angles of incidence. Also, the turbulence scattering effect does not play a significant role in the shadow zone but its substantial effect on the frequency shift towards higher frequencies cannot be ignored.

Finally, a notable paper on experimental work was published by Burd and Eversman (2007). The focus of the work was on measuring the interior noise of a business jet with twin turbojet engines mounted at the rear of the plane. Both ground and flight tests were conducted. One of the main conclusions of the experiment was that the inlet noise is dominant not very far upstream of the engine. In fact, the further upstream the more dominant the boundary layer excitation becomes, making it the main contributor to interior noise. The findings allowed for a theoretical design of the optimal acoustic treatment for the engine inlet. Furthermore, a

simplified method was developed for the prediction of the effect of the liner on the interior noise.

Before moving on to the analysis, it is beneficial to sum up the extensive literature review presented in the previous sections. It is clear that in the past, research focused on propeller noise. Specifically, the installation effects of noise scattering and refraction by the fuselage and its boundary layer were investigated extensively using propeller noise sources. The presence of the boundary layer proves to be an extremely important factor in predicting the noise levels on the fuselage surface. The refraction upstream of the source due to the boundary layer leads to significant shielding in the upstream area of the fuselage. Furthermore, this literature review revealed that high-fidelity numerical methods have been used extensively in installation effects analysis. Theoretical methods are more widely used in simpler problems that use rudimentary sources and two dimensions only. Therefore, the work in this thesis aims to fill these gaps in knowledge. Namely, as explained in the introduction, the generation of theoretical methods that describe the fan noise scattering by the fuselage and refraction by its boundary layer.

Chapter 3

Analysis

The ultimate goal of this thesis is to propose analytical methods to solve the problem of fan noise refraction and scattering by an adjacent cylindrical fuselage and its boundary layer. In order to develop such analytical methods, simplified boundary layer profiles will be used. Thus, the derivation of theoretical methods is facilitated. The advantage of theoretical or analytical methods is the low computational cost. By utilising such approaches one can avoid the use of costly and time-consuming high-fidelity numerical methods. Research so far, has relied on the use of such methods to solve the problem of sound propagation through a shear layer in the flow. That trend has been established due to the presence of the Pridmore-Brown equation (Pridmore-Brown (1958)) which has no known analytical solution.

It is the scope of this thesis to provide such an analytical solution, albeit subject to certain restrictions and simplifications. Despite the assumptions the theoretical methods proposed here rely on, they prove to be accurate enough in order to provide quick trends and predictions. This ability to produce quick and accurate trends is very important for the industry as it facilitates parametric studies to be conducted in a timely manner.

This chapter describes the theoretical formulations that have been conducted in order to solve the problem in question. The layout of the chapter is:

1. *Uniform flow analysis*. Although the problem of the uniform flow has already been developed and discussed in McAlpine and Kingan (2012), McAlpine et al. (2015), Gaffney (2016), it is deemed important to iterate it here. The uniform flow solution is important because it gives a baseline and a means to measure the shielding that will occur when there is a boundary layer present on the fuselage. An original piece of work in this section will be the derivation of a far-field pressure expression, which has not been investigated before for that type of fan noise source.

2. *Step-function boundary layer profile analysis*. In this section a rudimentary step-function velocity profile is introduced on the fuselage. This simple profile avoids the need to solve the Pridmore-Brown equation since there is no shear in the flow. Original and novel expressions both for the fuselage surface pressure and the far-field pressure are derived and presented.

3. *Linear boundary layer profile analysis*. In this section a more complex and more representative linear velocity profile is introduced on the fuselage. This more complex profile requires an asymptotic solution to the Pridmore-Brown equation. This more realistic velocity profile will provide more accuracy to the results. Original and novel expressions both for the fuselage surface pressure and the far-field pressure are derived and presented.

3.1 Uniform Flow Analysis

The aim of this analysis is the development of a model that can predict the acoustic near-field and far-field produced when a distributed source is scattered by an adjacent cylindrical fuselage. In this model the cylindrical fuselage will be represented by a rigid cylinder while the distributed source will take the form of a disc source. The objective is that this model will simulate the scattering that occurs when the noise exiting from the fan duct, represented here by the distributed disc source, impinges on the nearby fuselage, represented here by the rigid cylinder.

As stated before, the same problem has been investigated before using propeller noise sources, see Refs. Hanson and Magliozzi (1985), Lu (1990), Belyaev (2012), Brouwer (2016). Even simpler models have been proposed that utilise rudimentary point sources that can simulate an open rotor noise source, see Refs. Hanson (1984), Tam and Morris (1980), Fuller (1989). The theoretical formulation presented in this thesis has similarities with the propeller noise source analysis presented in those previous publications. It is clear that one significant difference between the current work and previous work is the nature of the source, since the source derived here represents a fan noise source and not a propeller noise source. Therefore, it is reasonable to expect differences between the expressions derived here and in previous publications. More specifically, these differences are manifested in the source terms. That is readily understood considering the fact that a propeller noise source is typically modeled using rotating point sources (monopoles to simulate thickness noise and dipoles to simulate loading noise, McAlpine and Kingan (2012)), whereas in this work the fan noise source is represented by a distribution of stationary monopoles. Other than this difference, the rest of the uniform flow mathematical formulation is similar to previous propeller noise source models that do not include a boundary layer.

The mathematical formulation will consist of the following steps. Firstly, the incident field produced by the distributed source, originally in terms of the cylindrical coordinate system centered around the disc source ((r, ϕ, z) in Fig. (3.1)), will be transformed to a cylindrical coordinate system centered on the cylindrical fuselage, $(\bar{r}, \bar{\phi}, \bar{z})$ in Fig. (3.1). By doing so, the total field can be easily calculated by simply summing the scattered and incident field. This shifting of the coordinate system is important since the scattered field will be by definition centered around the cylindrical fuselage (Hanson and Magliozzi (1985)). Once the Fourier-transformed total field is obtained, the next step will be to solve the inverse Fourier z-transform of the total field to obtain the acoustic pressure field in real space. Lastly, a validation of the approach is presented by reducing the disc source to a monopole source and comparing the result to a known reference solution.

The analysis begins by considering a cylindrical ducted fan with radius a. The original coordinate system that is used is a cylindrical one where the z-axis coincides with the duct centerline. Also there is a subsonic mean flow, Mach number $M_z = U_z/c_0$, directed in the negative z-direction outside and inside the duct as shown in Fig.(3.1). The sound field generated by the fan within the duct is modeled using "spinning modes" (Tyler and Sofrin (1962)). To avoid any confusion, it is stated that in the following analysis the convention that will be used is $\exp[+\mathrm{i}\omega_0 t]$. A time-harmonic mode with azimuthal order l and radial order q has acoustic pressure and axial particle velocity given by (eqs.(1) through (4) in McAlpine et al. (2015))

$$\hat{p}_{lq} = P_{lq}\mathrm{J}_l(\kappa_{lq}r)\mathrm{e}^{\mathrm{i}(-l\phi - k_{zlq}z)}, \tag{3.1}$$

$$\hat{u}_{zlq} = \frac{\xi_{lq}}{\rho_0 c_0} P_{lq}\mathrm{J}_l(\kappa_{lq}r)\mathrm{e}^{\mathrm{i}(-l\phi - k_{zlq}z)}, \tag{3.2}$$

where P_{lq} is the modal amplitude,

$$\xi_{lq} = \frac{k_{zlq}}{(k_0 + k_{zlq}M_z)}, \tag{3.3}$$

while the dispersion relationship is given by

$$k_{zlq}^2 + \kappa_{lq}^2 = (k_0 + k_{zlq}M_z)^2. \tag{3.4}$$

The Bessel function of the first kind and order l is denoted by J_l. Also, κ_{lq} is the set of the eigenvalues which satisfy $\mathrm{J}_l'(\kappa_{lq}a) = 0$, k_{zlq} is the axial wavenumber of mode (l, q), c_0 is the speed of sound, ρ_0 is the mean density of the air inside the duct and $k_0 = \omega_0/c_0$. The cylindrical coordinates are (r, ϕ, z).

3.1.1 Incident field

According to McAlpine et al. (2015) the acoustic pressure generated by a fan tone exiting a duct can be modeled by integrating a distribution of monopole sources over the cross-section of the duct termination. The derivation of the incident field is described in McAlpine et al. (2015) and in appendices A and B. Here only a review of the process is presented. The governing equation that describes the incident field due to the presence of a rotating monopole in uniform flow is the non-homogeneous convected wave equation,

$$\left(\nabla^2 - \frac{1}{c_0^2}\frac{\mathrm{D}^2}{\mathrm{D}t^2}\right)p' = -\rho_0\frac{\mathrm{D}q}{\mathrm{D}t}, \tag{3.5}$$

which written in full in cylindrical polar coordinates is,

$$\frac{\partial^2 p_i'}{\partial r^2} + \frac{1}{r}\frac{\partial p_i'}{\partial r} + \frac{1}{r^2}\frac{\partial^2 p_i'}{\partial \phi^2} + \frac{\partial^2 p_i'}{\partial z^2} - \frac{1}{c_0^2}\left(\frac{\partial}{\partial t} - U\frac{\partial}{\partial z}\right)^2 p_i' = -\rho_0\left(\frac{\partial}{\partial t} - U\frac{\partial}{\partial z}\right)q, \tag{3.6}$$

where

$$q(r, \phi, z, t) = Q_0\mathrm{e}^{\mathrm{i}\omega_0 t}\frac{\delta(r-a)}{r}\left(\sum_{n=-\infty}^{\infty}\delta(\phi - \Omega t - 2\pi n)\right)\delta(z), \tag{3.7}$$

with Q_0 being the volume velocity of the monopole and Ω is the rotational velocity of the monopole, see appendix A. Note that the process so far is typical of the derivation of a rotating monopole source described in McAlpine and Kingan (2012), which is the most efficient way of modeling the thickness noise produced by a propeller. Also in McAlpine and Kingan (2012), the same process is repeated for a rotating dipole, giving an alternative for loading noise for a propeller noise source. It is important to note that the difference between the two rotating point sources is that a monopole is specified in terms of its volume velocity Q_0 whereas a dipole is characterised in terms of force per unit volume $\mathfrak{F}$. By taking the Fourier transform of eq.(3.6) the resulting equation can be solved using the method of variation of parameters, see appendix A. The Fourier transform involves Fourier transforms in z and t and the Fourier series in ϕ as follows:

$$\overline{p'_{im}}\,(r,k_z,\omega) = \int_{-\infty}^{\infty}\int_{-\pi}^{\pi}\int_{-\infty}^{\infty} p'_i(r,\phi,z,t)\mathrm{e}^{\mathrm{i}(k_z z+m\phi-\omega t)}\mathrm{d}z\mathrm{d}\phi\mathrm{d}t, \tag{3.8}$$

$$\Rightarrow p'_i(r,\phi,z,t) = \frac{1}{(2\pi)^3}\sum_{m=-\infty}^{\infty}\left(\int_{-\infty}^{\infty}\int_{-\infty}^{\infty}\overline{p'_{im}}\,(r,k_z,\omega)\mathrm{e}^{-\mathrm{i}(k_z z-\omega t)}\mathrm{d}k_z\mathrm{d}\omega\right)\mathrm{e}^{-\mathrm{i}m\phi}. \tag{3.9}$$

This transforms the derivatives as follows:

$$\frac{\partial}{\partial z}\rightarrow -\mathrm{i}k_z,\quad \frac{\partial}{\partial\phi}\rightarrow -\mathrm{i}m\quad\text{and}\quad \frac{\partial}{\partial t}\rightarrow \mathrm{i}\omega. \tag{3.10}$$

Also, in this case the monopole is stationary so $\Omega = 0$. By doing so the Fourier transformed pressure due to a single monopole s is,

$$\overline{p'_{im}}\,(r,k_z) = \frac{\pi}{2}Q^{(s)}\rho_0 c_0(k_0+k_z M_z)\mathrm{H}_m^{(2)}(\Gamma_z r_>)\mathrm{J}_m(\Gamma_z r_<), \tag{3.11}$$

where $\Gamma_z^2 = (k_0+k_z M_z)^2 - k_z^2$ is a radial wavenumber. Note that the radial wavenumber has the same subscript z as the Mach number M_z. Generally, in the following analysis the radial wavenumber will bear the same subscript as the Mach number with which it is involved. By specifying the source strength as,

$$Q^{(s)} = \frac{\xi_{lq}P_{lq}}{\rho_0 c_0}\mathrm{J}_l(\kappa_{lq}\eta)\mathrm{e}^{-\mathrm{i}ls\psi}\delta A, \tag{3.12}$$

where δA is an elementary area occupied by a monopole on the surface of the disc source (which is located at $z=0$), η is the radial distance between the center of the disc source to the monopole on its surface and ψ is the azimuthal angle on the disc source where the monopole lies, see Fig. (B.1) in appendix B. Also, the variable $r_>$ is defined as r when $r>\eta$ and as η when $r<\eta$. Accordingly, $r_<$ is defined as η when $r>\eta$ and as r when $r<\eta$. By integrating over the surface of the disc source, the incident field is obtained as in eq.(20) from McAlpine et al. (2015):

$$p'_i\,(r,\phi,z,t) \;=\; \frac{\xi_{lq}P_{lq}}{4}\int_{-\infty}^{\infty}(k_0+k_z M_z)\,\Psi_{lq}\,\mathrm{H}_l^{(2)}\,(\Gamma_z r)\,\mathrm{e}^{-\mathrm{i}k_z z}\,\mathrm{d}k_z\,\mathrm{e}^{-\mathrm{i}l\phi}\,\mathrm{e}^{\mathrm{i}\omega_0 t}. \tag{3.13}$$

More details can be found in appendix B. The function Ψ_{lq} is given by

$$\Psi_{lq} = \frac{\Gamma_z a}{\kappa_{lq}^2 - \Gamma_z^2} \mathrm{J}_l(\kappa_{lq} a) \mathrm{J}_l'(\Gamma_z a), \quad \Gamma_z \neq \kappa_{lq}, \tag{3.14}$$

$$\Psi_{lq} = \frac{1}{2}\left(a^2 - \frac{l^2}{\kappa_{lq}^2}\right) \mathrm{J}_l^2(\kappa_{lq} a), \quad \Gamma_z = \kappa_{lq}. \tag{3.15}$$

Equation (3.13) is remarkably similar to the same result obtained in McAlpine and Kingan (2012) for a rotating point source, representative of a propeller noise source. In fact the only differences are in the source terms. Namely, terms ξ_{lq}, P_{lq}, Ψ_{lq} and l that refer to the spinning mode are replaced by the point source strength Q_0 and its rotational velocity Ω.

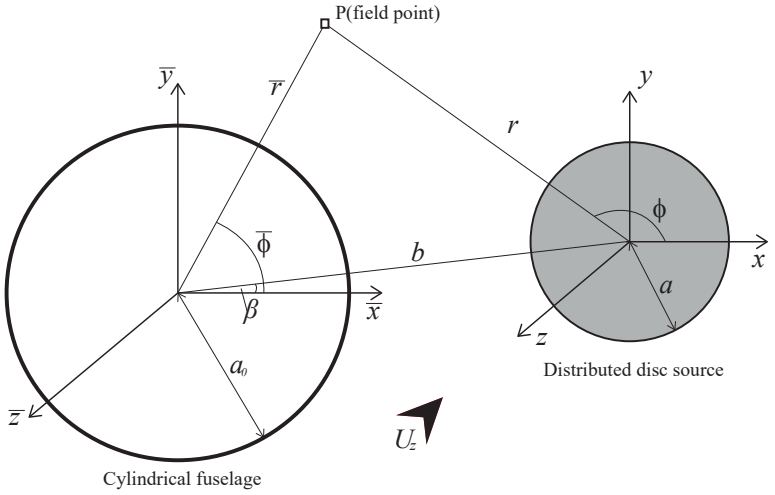

FIGURE 3.1: Coordinate systems for the source and the cylinder.

3.1.1.1 Shifting the Coordinate System

Graf's Addition Theorem is used to shift the coordinate system from the duct's centreline, (r, ϕ, z), to the adjacent cylinder's centreline,$(\bar{r}, \bar{\phi}, \bar{z})$. This must be done before the scattered field is introduced because the scattered field will be based on the cylinder's coordinate system. Graf's theorem according to Abramowitz and Stegun (1965),

$$\zeta_m(w)\mathrm{e}^{\mathrm{i}\chi} = \sum_{n=-\infty}^{\infty} \zeta_{m+n}(u)\mathrm{J}_n(v)\mathrm{e}^{\mathrm{i}n\alpha}, \tag{3.16}$$

where ζ can be any of the Bessel functions or linear combinations thereof. Also the condition $|u| > |ve^{\pm \mathrm{i}\alpha}|$ applies. The lengths w, u and v, and angles α and χ are part of the triangle shown in Fig.(3.2). Direct application of Graf's Theorem gives (triangle flipped taking $w = \Gamma_z r,\ v = \Gamma_z b$ and $u = \Gamma_z \bar{r}$, while $\alpha = \bar{\phi} - \beta$ and $\chi = \phi - \bar{\phi}$)

$$\mathrm{H}_l^{(2)}(\Gamma_z r)\,\mathrm{e}^{\mathrm{i}l\chi} = \sum_{n=-\infty}^{\infty} \mathrm{H}_{l+n}^{(2)}(\Gamma_z \bar{r})\,\mathrm{J}_n(\Gamma_z b)\,\mathrm{e}^{\mathrm{i}n\alpha}. \tag{3.17}$$

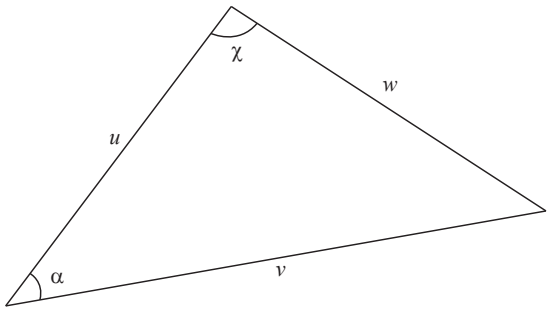

FIGURE 3.2: Graf's Addition theorem.

Note that by using the far-field assumption, $\bar{r} >> b$, the theorem's condition, $|u| > |v|$, is satisfied. By setting $l \to -l$ and $n \to -n$

$$\mathrm{H}_{-l}^{(2)}\left(\Gamma_z r\right)\mathrm{e}^{-\mathrm{i}l(\phi-\bar{\phi})} = \sum_{n=-\infty}^{\infty}\mathrm{H}_{-l-n}^{(2)}\left(\Gamma_z \bar{r}\right)\mathrm{J}_{-n}\left(\Gamma_z b\right)\mathrm{e}^{-\mathrm{i}n(\bar{\phi}-\beta)}, \tag{3.18}$$

which becomes

$$\mathrm{H}_{l}^{(2)}\left(\Gamma_z r\right)\mathrm{e}^{-\mathrm{i}l\phi} = \sum_{n=-\infty}^{\infty}\mathrm{H}_{l+n}^{(2)}\left(\Gamma_z \bar{r}\right)\mathrm{J}_{n}\left(\Gamma_z b\right)\mathrm{e}^{-\mathrm{i}(l+n)\bar{\phi}}\,\mathrm{e}^{\mathrm{i}n\beta}. \tag{3.19}$$

Renaming $l+n \to m$ so that $n = m-l$

$$\mathrm{H}_{l}^{(2)}\left(\Gamma_z r\right)\mathrm{e}^{-\mathrm{i}l\phi} = \sum_{m-l=-\infty}^{\infty}\mathrm{H}_{m}^{(2)}\left(\Gamma_z \bar{r}\right)\mathrm{J}_{m-l}\left(\Gamma_z b\right)\mathrm{e}^{-\mathrm{i}m\bar{\phi}}\,\mathrm{e}^{\mathrm{i}(m-l)\beta}. \tag{3.20}$$

The l on the summation can be dropped since it is considered a constant in comparison to the m which runs from $-\infty$ to ∞, and so eq.(3.20) becomes

$$\mathrm{H}_{l}^{(2)}\left(\Gamma_z r\right)\mathrm{e}^{-\mathrm{i}l\phi} = \sum_{m=-\infty}^{\infty}\mathrm{H}_{m}^{(2)}\left(\Gamma_z \bar{r}\right)\mathrm{J}_{m-l}\left(\Gamma_z b\right)\mathrm{e}^{-\mathrm{i}m\bar{\phi}}\,\mathrm{e}^{\mathrm{i}(m-l)\beta}. \tag{3.21}$$

Substitution on eq.(20) from McAlpine et al. (2015) and renaming $m \to n$

$$\begin{aligned} p_i'\left(\bar{r},\bar{\phi},\bar{z},t\right) = \frac{1}{(2\pi)^2}\sum_{n=-\infty}^{\infty}\int_{-\infty}^{\infty}\pi^2\xi_{lq}P_{lq}\left(k_0+k_z M_z\right)\Psi_{lq}\,\mathrm{e}^{\mathrm{i}(n-l)\beta}\,\mathrm{J}_{n-l}\left(\Gamma_z b\right)\times \\ \mathrm{H}_{n}^{(2)}\left(\Gamma_z \bar{r}\right)\mathrm{e}^{\mathrm{i}\omega_0 t}\,\mathrm{e}^{-\mathrm{i}k_z\bar{z}}\,\mathrm{d}k_z\,\mathrm{e}^{-\mathrm{i}n\bar{\phi}}, \end{aligned} \tag{3.22}$$

or

$$p_i'\left(\bar{r},\bar{\phi},\bar{z},t\right) = \frac{1}{(2\pi)^2}\sum_{n=-\infty}^{\infty}\int_{-\infty}^{\infty}\overline{p_{in}'}\left(\bar{r},k_z,t\right)\mathrm{e}^{-\mathrm{i}k_z\bar{z}}\,\mathrm{d}k_z\,\mathrm{e}^{-\mathrm{i}n\bar{\phi}}, \tag{3.23}$$

where

$$\overline{p'_{in}}\,(\bar{r},k_z,t) \;=\; \pi^2\xi_{lq}P_{lq}\,(k_0+k_zM_z)\,\Psi_{lq}\,\mathrm{e}^{\mathrm{i}(n-l)\beta}\,\mathrm{J}_{n-l}\,(\Gamma_z b)\,\mathrm{H}_n^{(2)}\,(\Gamma_z\bar{r})\,\mathrm{e}^{\mathrm{i}\omega_0 t}. \tag{3.24}$$

On the other hand, by taking the near-field assumption $\bar{r} < b$ and flipping the triangle again (so that $u = \Gamma_z b$, $v = \Gamma_z \bar{r}$, $w = \Gamma_z r$ and $\alpha = \bar{\phi} - \beta$, $\chi = \pi + \beta - \phi$) the incident field for the near-field is recovered:

$$\overline{p'_{in}}\,(\bar{r},k_z,t) \;=\; \pi^2\xi_{lq}P_{lq}(-1)^{l+n}(k_0+k_zM_z)\,\Psi_{lq}\,\mathrm{e}^{-\mathrm{i}(l-n)\beta}\,\mathrm{H}_{l-n}^{(2)}\,(\Gamma_z b)\,\mathrm{J}_n\,(\Gamma_z\bar{r})\,\mathrm{e}^{\mathrm{i}\omega_0 t}. \tag{3.25}$$

Note the change in $\bar{r}$ dependence between the near- and far-field expressions. As shown by Lu (1990), the far-field should be dependent on $\bar{r}$ through a Hankel function contrary to the near-field where the dependence is through a Bessel function. It is also important to highlight the difference between the expressions derived here for a fan noise source (involving a spinning mode) and a typical propeller noise source expression (involving rotating point sources), such as the ones derived in McAlpine and Kingan (2012). The expressions are very similar with the sole differences contained in the source terms. More specifically, terms that would involve spinning mode characteristics (subscript lq, or more specifically ξ_{lq}, P_{lq} and Ψ_{lq}), in the case of a propeller noise source they instead involve the point source strength Q_0 (or $\mathfrak{F}$ in the case of a rotating dipole) and the rotational velocity Ω.

The key result of this section is the fact that by shifting the coordinate system, the incident field in eq.(3.13) is written in a Fourier series form, eqs. (3.23), (3.24) and (3.25). This will enable the derivation of a Fourier-transformed total field once the Fourier-transformed scattered field is derived in the next section, since the Fourier-transformed incident field is given in eq.(3.24) or (3.25).

3.1.2 Scattered and Total Field

The scattered field is basically the solution to the homogeneous convected wave equation expressed in cylindrical coordinates around the cylindrical fuselage,

$$\frac{\partial^2 p'_i}{\partial\bar{r}^2} + \frac{1}{\bar{r}}\frac{\partial p'_i}{\partial\bar{r}} + \frac{1}{\bar{r}^2}\frac{\partial^2 p'_i}{\partial\bar{\phi}^2} + \frac{\partial^2 p'_i}{\partial\bar{z}^2} - \frac{1}{c_0^2}\left(\frac{\partial}{\partial t} - U\frac{\partial}{\partial\bar{z}}\right)^2 p'_i \;=\; 0, \tag{3.26}$$

and since the scattered waves need to be outward propagating cylindrical waves, then the Fourier transformed scattered field will be expressed in terms of a Hankel function,

$$\overline{p'_{sn}}\,(\bar{r},k_z,t) = \frac{1}{2\pi}\int_{-\infty}^{\infty} a_n(k_z,\omega)\mathrm{H}_n^{(2)}\,(\Gamma_z\bar{r})\mathrm{e}^{\mathrm{i}\omega t}\mathrm{d}\omega, \tag{3.27}$$

or

$$\overline{p'_{sn}}\,(\bar{r},k_z,t) \;=\; \frac{1}{2\pi}b_n(k_z,\omega_0)\mathrm{H}_n^{(2)}\,(\Gamma_z\bar{r})\,\mathrm{e}^{\mathrm{i}\omega_0 t}, \tag{3.28}$$

if coefficient a_n can be rewritten $a_n(k_z,\omega) = b_n(k_z,\omega)\delta(\omega-\omega_0)$. By taking the total Fourier transformed pressure field given by the sum of the incident and the scattered fields,

$$\overline{p'_{tn}}\,(\bar{r},k_z,t) \;=\; \overline{p'_{in}}\,(\bar{r},k_z,t) \;+\; \overline{p'_{sn}}\,(\bar{r},k_z,t), \tag{3.29}$$

and by employing a rigid hard-wall boundary condition at the fuselage surface,

$$\frac{\partial \overline{p'_{tn}}}{\partial \bar{r}} = \frac{\partial \overline{p'_{in}}}{\partial \bar{r}} + \frac{\partial \overline{p'_{sn}}}{\partial \bar{r}} = 0 \quad \text{at} \quad \bar{r} = a_0, \tag{3.30}$$

where $\overline{p'_{in}}$ is the near-field expression given by eq.(3.25) since the fuselage surface lies in the near-field ($a_0 < b$), one can solve for the coefficient $b_n(k_z, \omega_0)$,

$$b_n(k_z, \omega_0) = -2\pi^3 \xi_{lq} P_{lq} (-1)^{l+n} \, \mathrm{e}^{-\mathrm{i}(l-n)\beta} \, (k_0 + k_z M_z) \, \Psi_{lq} \, \mathrm{H}^{(2)}_{l-n}(\Gamma_z b) \, \frac{\mathrm{J}'_n(\Gamma_z a_0)}{\mathrm{H}^{(2)\prime}_n(\Gamma_z a_0)}. \tag{3.31}$$

By substituting eq.(3.31) into eq.(3.28), the Fourier-transformed scattered field is obtained,

$$\overline{p'_{sn}}(\bar{r}, k_z, t) = -\pi^2 \xi_{lq} P_{lq} (-1)^{l+n} \, \mathrm{e}^{-\mathrm{i}(l-n)\beta} \, (k_0 + k_z M_z) \, \Psi_{lq} \, \mathrm{H}^{(2)}_{l-n}(\Gamma_z b) \, \mathrm{H}^{(2)}_n(\Gamma_z \bar{r}) \, \frac{\mathrm{J}'_n(\Gamma_z a_0)}{\mathrm{H}^{(2)\prime}_n(\Gamma_z a_0)} \, \mathrm{e}^{\mathrm{i}\omega_0 t}. \tag{3.32}$$

Finally, the Fourier-transformed total field is found by summing the incident field and the scattered field, either in the near-field in which case eqs. (3.25) and (3.32) are summed together, or in the far-field in which case eqs. (3.24) and (3.32) are summed together. The total field in real space is found by performing an inverse Fourier z-transform

$$p'_t(\bar{r}, \bar{\phi}, \bar{z}, t) = \frac{1}{(2\pi)^2} \sum_{n=-\infty}^{\infty} \int_{-\infty}^{\infty} \overline{p'_{tn}}(\bar{r}, k_z, t) \, \mathrm{e}^{-\mathrm{i}k_z \bar{z}} \, \mathrm{d}k_z \, \mathrm{e}^{-\mathrm{i}n\bar{\phi}}. \tag{3.33}$$

3.1.3 Fuselage Surface Pressure

The near-field case is of interest on setting $\bar{r} = a_0$ since it describes the pressure on the fuselage surface. By setting $\bar{r} = a_0$ and using eq.(3.29) with the Fourier-transformed incident field given by eq.(3.25) and scattered field given by eq.(3.32),

$$\begin{aligned} \overline{p'_{tn}}(a_0, k_z, t) = {} & \pi^2 \xi_{lq} P_{lq} \, (-1)^{l+n} \, \mathrm{e}^{-\mathrm{i}(l-n)\beta} \, (k_0 + k_z M_z) \, \Psi_{lq} \, \mathrm{H}^{(2)}_{l-n}(\Gamma_z b) \times \\ & \left[\frac{\mathrm{J}_n(\Gamma_z a_0) \mathrm{H}^{(2)\prime}_n(\Gamma_z a_0) - \mathrm{J}'_n(\Gamma_z a_0) \, \mathrm{H}^{(2)}_n(\Gamma_z a_0)}{\mathrm{H}^{(2)\prime}_n(\Gamma_z a_0)} \right] \mathrm{e}^{\mathrm{i}\omega_0 t}. \end{aligned} \tag{3.34}$$

Then by using the Wronskian formula,

$$\mathrm{J}_n(x) \, \mathrm{H}^{(2)\prime}_n(x) - \mathrm{J}'_n(x) \, \mathrm{H}^{(2)}_n(x) = -\mathrm{i}\left(\frac{2}{\pi x} \right), \tag{3.35}$$

the following is obtained,

$$\begin{aligned} \overline{p'_{tn}}(a_0, k_z, t) = {} & \pi^2 \xi_{lq} P_{lq} \, (-1)^{l+n} \, \mathrm{e}^{-\mathrm{i}(l-n)\beta} \, (k_0 + k_z M_z) \, \Psi_{lq} \, \mathrm{H}^{(2)}_{l-n}(\Gamma_z b) \times \\ & \left[\Big(-\mathrm{i}(2/\pi\Gamma_z a_0) \Big) / \mathrm{H}^{(2)\prime}_n(\Gamma_z a_0) \right] \mathrm{e}^{\mathrm{i}\omega_0 t}. \end{aligned} \tag{3.36}$$

Finally, the total pressure in real space is given by eq.(3.33) substituting $\overline{p'_{tn}}\,(\bar{r}, k_z, t)$ with $\overline{p'_{tn}}\,(a_0, k_z, t)$ from eq.(3.36),

$$p'_t\,(a_0, \bar{\phi}, \bar{z}, t) \;=\; \frac{\xi_{lq} P_{lq}}{4}\,(-1)^l\,\mathrm{e}^{-\mathrm{i}l\beta}\,\mathrm{e}^{\mathrm{i}\omega_0 t}\sum_{n=-\infty}^{\infty}\left\{(-1)^n\,I_n\,(a_0, \bar{z})\,\mathrm{e}^{-\mathrm{i}n(\bar{\phi}-\beta)}\right\}, \tag{3.37}$$

where

$$I_n\,(a_0, \bar{z}) = \int_{-\infty}^{\infty}(k_0 + k_z M_z)\,\Psi_{lq}\,\mathrm{H}^{(2)}_{l-n}\,(\Gamma_z b)\left[\left(-\mathrm{i}(2/\pi\Gamma_z a_0)\right)/\mathrm{H}^{(2)\prime}_n\,(\Gamma_z a_0)\right]\mathrm{e}^{-\mathrm{i}k_z\bar{z}}\,\mathrm{d}k_z. \tag{3.38}$$

This integral cannot be solved analytically and therefore a numerical integration routine will be employed. That will raise certain difficulties as will be seen later regarding certain numerical singularities on the integration domain. Equations (3.37) and (3.38) are the key results of this section and they give the pressure on the surface of the fuselage which is relevant for the assessment of cabin noise. The previous sections and the pressure on the cylinder are presented in more detail in McAlpine et al. (2015) and in Rouvas and McAlpine (2021). The work by McAlpine et al. (2015) did not present any solutions for the far field. The next section will deal with the derivation of the far-field pressure which was presented in the paper by Rouvas and McAlpine (2021).

3.1.4 Total Far-Field

The same process is followed for the far-field case. Once again, the Fourier-transformed total field is described by eq.(3.29):

$$\overline{p'_{tn}}\,(\bar{r}, k_z, t) \;=\; \overline{p'_{in}}\,(\bar{r}, k_z, t) \;+\; \overline{p'_{sn}}\,(\bar{r}, k_z, t). \tag{3.39}$$

The Fourier-transformed scattered field is given by eq.(3.32) as in the near-field case. However, for the far-field case the Fourier-transformed incidence field in eq.(3.29) is given by eq.(3.24). These substitutions into eq.(3.39) yield

$$\begin{aligned}\overline{p'_{t_{nff}}}\,(\bar{r}, k_z, t) \;=\;& \pi^2\xi_{lq}P_{lq}\,(k_0 + k_z M_z)\,\Psi_{lq}\,\mathrm{e}^{\mathrm{i}(n-l)\beta}\,\mathrm{J}_{n-l}\,(\Gamma_z b)\,\mathrm{H}^{(2)}_n\,(\Gamma_z\bar{r})\,\mathrm{e}^{\mathrm{i}\omega_0 t}\\ &-\left[\pi^2\xi_{lq}P_{lq}(-1)^{l+n}\,\mathrm{e}^{-\mathrm{i}(l-n)\beta}\,(k_0 + k_z M_z)\,\Psi_{lq}\,\mathrm{H}^{(2)}_{l-n}\,(\Gamma_z b)\times\right.\\ &\left.\mathrm{H}^{(2)}_n\,(\Gamma_z\bar{r})\,\frac{\mathrm{J}'_n\,(\Gamma_z a_0)}{\mathrm{H}^{(2)\prime}_n\,(\Gamma_z a_0)}\,\mathrm{e}^{\mathrm{i}\omega_0 t}\right],\end{aligned} \tag{3.40}$$

which can be rewritten

$$\begin{aligned}\overline{p'_{t_{nff}}}\,(\bar{r}, k_z, t) \;=\;& \pi^2\xi_{lq}P_{lq}\,\mathrm{e}^{\mathrm{i}(n-l)\beta}\,(k_0 + k_z M_z)\,\Psi_{lq}\,\mathrm{H}^{(2)}_n\,(\Gamma_z\bar{r})\,\mathrm{e}^{\mathrm{i}\omega_0 t}\times\\ &\left[\frac{\mathrm{J}_{n-l}\,(\Gamma_z b)\mathrm{H}^{(2)\prime}_n\,(\Gamma_z a_0) - \mathrm{H}^{(2)}_{n-l}\,(\Gamma_z b)\,\mathrm{J}'_n\,(\Gamma_z a_0)}{\mathrm{H}^{(2)\prime}_n\,(\Gamma_z a_0)}\right].\end{aligned} \tag{3.41}$$

Notice the change in notation with the subscript ff that denotes *far-field* quantity. Finally the total far-field in real space is obtained by

$$p'_{t_{ff}}(\bar{r},\bar{\phi},\bar{z},t) \;=\; \frac{1}{(2\pi)^2}\sum_{n=-\infty}^{\infty}\int_{-\infty}^{\infty}\overline{p'_{t_{nff}}}(\bar{r},k_z,t)\,\mathrm{e}^{-\mathrm{i}k_z\bar{z}}\,\mathrm{d}k_z\,\mathrm{e}^{-\mathrm{i}n\bar{\phi}}. \tag{3.42}$$

The resulting inverse Fourier z-transform integral in eq.(3.42) can be solved asymptotically by employing spherical polar coordinates and a large argument approximation for the Hankel function term which is dependent on $\bar{r}$. This expresses the integral in an appropriate form to be solved by applying the method of stationary phase, as shown in the appendix of Rouvas and McAlpine (2021).

3.1.4.1 Asymptotic Evaluation of the Integral with the Method of Stationary Phase

In order to solve eq.(3.42), first the inverse Fourier z-transform must be determined

$$I_n \;=\; \frac{1}{2\pi}\int_{-\infty}^{\infty}\overline{p'_{t_{nff}}}(\bar{r},k_z,t)\,\mathrm{e}^{-\mathrm{i}k_z\bar{z}}\,\mathrm{d}k_z. \tag{3.43}$$

The integral can be evaluated using the method of stationary phase which is given by Self (2005) (chapter 4, eqs.(50) and (53))

$$I(x) \;=\; \int_a^b f(t)\mathrm{e}^{\mathrm{i}x\phi(t)}\mathrm{d}t, \quad \text{as } x\to\infty. \tag{3.44}$$

Then, if there is a single point $a\le c\le b$ such that $\phi'(c)=0$, provided that $\phi''(c)\neq 0$, then

$$I(x) \;\sim\; f(c)\left(\frac{2\pi}{x|\phi''(c)|}\right)^{1/2}\mathrm{e}^{\mathrm{i}x\phi(c)\pm\mathrm{i}\pi/4}, \quad \text{as } x\to\infty. \tag{3.45}$$

Since the aim is the evaluation of the far-field pressure, spherical polar coordinates are employed $(\bar{R},\bar{\theta},\bar{\phi})$. The integral will be calculated in the limit as $\bar{R}\to\infty$. The substitutions are

$$\bar{r} \;=\; \bar{R}\sin\bar{\theta} \quad \text{and} \quad \bar{z} \;=\; \bar{R}\cos\bar{\theta} \tag{3.46}$$

The dependence of the function $\overline{p'_{tn}}(\bar{r},k_z,t)$ on $\bar{r}$ is through the Hankel function which for large $\bar{R}$ can be replaced by its asymptotic form

$$\mathrm{H}_n^{(2)}(\Gamma_z\bar{r}) \;=\; \mathrm{H}_n^{(2)}(\Gamma_z\bar{R}\sin\bar{\theta}) \;\sim\; \sqrt{\frac{2}{\pi\Gamma_z\bar{R}\sin\bar{\theta}}}\,\mathrm{e}^{\frac{1}{2}n\pi\mathrm{i}}\,\mathrm{e}^{\frac{1}{4}\pi\mathrm{i}}\,\mathrm{e}^{-\mathrm{i}\Gamma_z\bar{R}\sin\bar{\theta}} \quad \text{as} \quad \bar{R}\to\infty. \tag{3.47}$$

Also, $\exp(-\mathrm{i}k_z\bar{z})\to\exp(-\mathrm{i}k_z\bar{R}\cos\bar{\theta})$ so the integral in eq.(3.43) can be expressed in the form

$$I_n \;\sim\; \frac{1}{2\pi}\int_{-\infty}^{\infty}f_n(k_z,\bar{R},\bar{\theta})\,\mathrm{e}^{-\mathrm{i}\bar{R}(\Gamma_z\sin\bar{\theta}+k_z\cos\bar{\theta})}\,\mathrm{d}k_z \quad \text{as} \quad \bar{R}\to\infty, \tag{3.48}$$

where

$$f_n(k_z,\bar{R},\bar{\theta}) = \pi^2\xi_{lq}P_{lq}\,\mathrm{e}^{\mathrm{i}(n-l)\beta}\,(k_0+k_zM_z)\,\Psi_{lq}\sqrt{\frac{2}{\pi\Gamma_z\bar{R}\sin\bar{\theta}}}\,\mathrm{e}^{\frac{1}{2}n\pi\mathrm{i}}\,\mathrm{e}^{\frac{1}{4}\pi\mathrm{i}}\times \left[\frac{\mathrm{J}_{n-l}\,(\Gamma_z b)\mathrm{H}_n^{(2)\prime}\,(\Gamma_z a_0)-\mathrm{H}_{n-l}^{(2)}\,(\Gamma_z b)\,\mathrm{J}_n'\,(\Gamma_z a_0)}{\mathrm{H}_n^{(2)\prime}\,(\Gamma_z a_0)}\right]\mathrm{e}^{\mathrm{i}\omega_0 t}. \tag{3.49}$$

By introducing the similarity variables as in Chapman (2000)

$$\sigma^2 = 1-M_z^2, \tag{3.50}$$

$$\hat{R} = \frac{\bar{R}}{\sigma}(1-M_z^2\sin^2\bar{\theta})^{1/2}, \tag{3.51}$$

$$\cos\hat{\theta} = \frac{\cos\bar{\theta}}{(1-M_z^2\sin^2\bar{\theta})^{1/2}}, \tag{3.52}$$

$$\sin\hat{\theta} = \frac{\sigma\sin\bar{\theta}}{(1-M_z^2\sin^2\bar{\theta})^{1/2}}, \tag{3.53}$$

$$\tau = \sigma^2\frac{k_z}{k_0}-M_z, \tag{3.54}$$

$$\Gamma_z = \frac{k_0}{\sigma}(1-\tau^2)^{1/2}, \tag{3.55}$$

$$k_z = \frac{k_0}{\sigma^2}(\tau+M_z), \tag{3.56}$$

$$\mathrm{d}k_z = \frac{k_0}{\sigma^2}\mathrm{d}\tau, \tag{3.57}$$

the integral I_n in eq.(3.48) can be rewritten in the form

$$I_n \sim \frac{1}{2\pi}\int_{-\infty}^{\infty} g_n(k_z,\hat{R},\hat{\theta})\,\mathrm{e}^{\mathrm{i}\hat{R}\hat{\phi}(\tau)}\,\mathrm{d}\tau \quad \text{as} \quad \hat{R}\to\infty, \tag{3.58}$$

where

$$\hat{\phi}(\tau) = -\left(\frac{k_0}{\sigma}(1-\tau^2)^{1/2}\,\sin\hat{\theta}+\frac{k_0}{\sigma}(\tau+M_z)\,\cos\hat{\theta}\right), \tag{3.59}$$

and

$$g_n(\tau,\hat{R},\hat{\theta}) = \pi^2\xi_{lq}P_{lq}\,\mathrm{e}^{\mathrm{i}(n-l)\beta}\,\left(k_0+\frac{k_0}{\sigma^2}(\tau+M_z)M_z\right)\Psi_{lq}(\frac{k_0}{\sigma}(1-\tau^2)^{1/2}) \sqrt{\frac{2}{\pi\frac{k_0}{\sigma}(1-\tau^2)^{1/2}\hat{R}\sin\hat{\theta}}}\,\mathrm{e}^{\frac{1}{2}n\pi\mathrm{i}}\,\mathrm{e}^{\frac{1}{4}\pi\mathrm{i}}\,\mathrm{e}^{\mathrm{i}\omega_0 t}\,\frac{k_0}{\sigma^2}\times \left[\frac{\mathrm{J}_{n-l}\,(\frac{k_0}{\sigma}(1-\tau^2)^{1/2}b)\mathrm{H}_n^{(2)\prime}\,(\frac{k_0}{\sigma}(1-\tau^2)^{1/2}a_0)-\mathrm{H}_{n-l}^{(2)}\,(\frac{k_0}{\sigma}(1-\tau^2)^{1/2}b)\,\mathrm{J}_n'\,(\frac{k_0}{\sigma}(1-\tau^2)^{1/2}a_0)}{\mathrm{H}_n^{(2)\prime}\,(\frac{k_0}{\sigma}(1-\tau^2)^{1/2}a_0)}\right]. \tag{3.60}$$

The equation $\phi'(c)=0$ yields $c=\cos\hat{\theta}$. Also, when $|\tau|>1$, Γ_z becomes imaginary, so the integrand will become exponentially small as $\hat{R}\to\infty$. That means the limits of the integral can

be replaced by $(-1, 1)$. With this substitution, the integral in eq.(3.58) becomes

$$I_n \;=\; \frac{1}{2\pi}\, g_n(c) \left(\frac{2\pi}{\hat{R}|\hat{\phi}''(c)|} \right)^{1/2} \; \mathrm{e}^{\mathrm{i}\hat{R}\hat{\phi}(c)+\mathrm{i}\pi/4}, \quad \text{as } \hat{R} \to \infty. \tag{3.61}$$

where

$$\hat{\phi}(c) \;=\; -\frac{k_0}{\sigma}(1 + M_z \cos\hat{\theta}), \tag{3.62}$$

$$\hat{\phi}''(c) \;=\; \frac{k_0}{\sigma \sin^2\hat{\theta}}. \tag{3.63}$$

$$\begin{aligned} I_n \;=\; & \frac{1}{2\pi}\pi^2 \xi_{lq} P_{lq}\, \mathrm{e}^{\mathrm{i}(n-l)\beta} \left(k_0 + \frac{k_0}{\sigma^2}(\cos\hat{\theta} + M_z)M_z\right) \Psi_{lq}(\tfrac{k_0}{\sigma}\sin\hat{\theta}) \sqrt{\frac{2}{\pi \frac{k_0}{\sigma}\hat{R}\sin^2\hat{\theta}}}\, \mathrm{e}^{\frac{1}{2}n\pi\mathrm{i}}\, \mathrm{e}^{\frac{1}{4}\pi\mathrm{i}} \times \\ & \mathrm{e}^{\mathrm{i}\omega_0 t}\, \frac{k_0}{\sigma^2} \left[\frac{\mathrm{J}_{n-l}\,(\frac{k_0}{\sigma}\sin\hat{\theta}b)\mathrm{H}_n^{(2)\prime}\,(\frac{k_0}{\sigma}\sin\hat{\theta}a_0) - \mathrm{H}_{n-l}^{(2)}\,(\frac{k_0}{\sigma}\sin\hat{\theta}b)\,\mathrm{J}_n'\,(\frac{k_0}{\sigma}\sin\hat{\theta}a_0)}{\mathrm{H}_n^{(2)\prime}\,(\frac{k_0}{\sigma}\sin\hat{\theta}a_0)} \right] \times \\ & \sqrt{\frac{2\pi}{\hat{R}\frac{k_0}{\sigma\sin^2\hat{\theta}}}}\, \mathrm{e}^{-\mathrm{i}\hat{R}\frac{k_0}{\sigma}(1+M_z\cos\hat{\theta})+\mathrm{i}\pi/4}, \end{aligned} \tag{3.64}$$

where $\Psi_{lq}(\frac{k_0}{\sigma}\sin\hat{\theta})$ is Ψ_{lq} as defined in eq.(3.14) calculated taking $\Gamma_{zc} = \frac{k_0}{\sigma}\sin\hat{\theta}$. Then returning to the original coordinates using eqs. (3.51)-(3.57), and setting $\Delta_z = \frac{k_0 \sin\bar{\theta}}{(1-M_z^2\sin^2\bar{\theta})^{1/2}}$ and $S(\bar{\theta}) = \frac{((1-M_z^2\sin^2\bar{\theta})^{1/2}+M_z\cos\bar{\theta})}{\sigma^2}$, the following is obtained

$$\begin{aligned} I_n \;=\; & \frac{\mathrm{i}\pi\xi_{lq}P_{lq}k_0}{\bar{R}}\, \mathrm{e}^{\mathrm{i}(n-l)\beta}\, \frac{S(\bar{\theta})}{(1-M_z^2\sin^2\bar{\theta})}\, \Psi_{lq}(\Delta_z) \times \\ & \left[\frac{\mathrm{J}_{n-l}\,(\Delta_z b)\mathrm{H}_n^{(2)\prime}\,(\Delta_z a_0) - \mathrm{H}_{n-l}^{(2)}\,(\Delta_z b)\,\mathrm{J}_n'\,(\Delta_z a_0)}{\mathrm{H}_n^{(2)\prime}\,(\Delta_z a_0)} \right] \mathrm{e}^{\frac{1}{2}n\pi\mathrm{i}}\, \mathrm{e}^{\mathrm{i}\omega_0 t}\, \mathrm{e}^{-\mathrm{i}k_0\bar{R}S(\bar{\theta})}. \end{aligned} \tag{3.65}$$

So from eqs.(3.42) and (3.43)

$$p'_{t_{ff}}\,(\bar{R}, \bar{\theta}, \bar{\phi}, t) \;=\; \frac{1}{(2\pi)} \sum_{n=-\infty}^{\infty} I_n\, \mathrm{e}^{-\mathrm{i}n\bar{\phi}}, \tag{3.66}$$

or

$$\begin{aligned} p'_{t_{ff}}\,(\bar{R}, \bar{\theta}, \bar{\phi}, t) = & \frac{\mathrm{i}\xi_{lq}P_{lq}k_0}{2\bar{R}}\, \Psi_{lq}(\Delta_z)\, \frac{S(\bar{\theta})}{(1-M_z^2\sin^2\bar{\theta})} \sum_{n=-\infty}^{\infty} \mathrm{e}^{\mathrm{i}(n-l)\beta}\, \mathrm{e}^{\frac{1}{2}n\pi\mathrm{i}}\, \mathrm{e}^{\mathrm{i}\omega_0 t} \times \\ & \mathrm{e}^{-\mathrm{i}k_0\bar{R}S(\bar{\theta})}\, \mathrm{e}^{-\mathrm{i}n\bar{\phi}} \left[\frac{\mathrm{J}_{n-l}\,(\Delta_z b)\mathrm{H}_n^{(2)\prime}\,(\Delta_z a_0) - \mathrm{H}_{n-l}^{(2)}\,(\Delta_z b)\,\mathrm{J}_n'\,(\Delta_z a_0)}{\mathrm{H}_n^{(2)\prime}\,(\Delta_z a_0)} \right]. \end{aligned} \tag{3.67}$$

Equation (3.67) is the final expression that gives the pressure in the far-field. This far-field expression is expressed in terms of a Fourier series and has been validated by reducing the disc source to a point source. When this is performed, after considerable algebraic manipulation, eq.(3.67) reduces to the known solution for a stationary monopole adjacent to a cylinder given by Bowman (page 127, eq.(2.149) from Ref. Bowman et al. (1969)). The validation process is outlined in detail in appendix C.

Once again, attention should be drawn to the similarities between the expression derived here (for a fan noise source) and the equivalent expressions for a propeller noise source derived in

Lu (1990) and McAlpine and Kingan (2012). The expressions are very similar apart from the source terms. Fan noise source terms ξ_{lq}, P_{lq} and Ψ_{lq} are instead replaced by rotating point source terms, such as volume velocity Q_0 and rotational velocity Ω. A concluding analogy could be made at this point. Amplitude terms, such as ξ_{lq} and P_{lq}, have equivalent counterparts in propeller noise source cases. These equivalent terms are the volume velocity Q_0 or force per unit volume $\mathfrak{F}$ in a rotating dipole case. On the other hand, more nuanced terms, such as Ψ_{lq} which generally are involved in directivity, are more related to the rotational velocity Ω in the propeller noise case.

3.1.5 Section Summary

The aim of summing up this chapter is to highlight the key expressions derived and presented in this part of the analysis. The first derived expression that will be used to produce uniform flow results is the fuselage surface pressure expression in eqs.(3.37) and (3.38). Although, the derivation of this expression is the result of previous work (see McAlpine et al. (2015)), it is deemed important for the process to be revisited and presented again for clarity. Equations (3.37) and (3.38) will be used to calculate the acoustic pressure on the fuselage surface when there is no boundary layer on the fuselage.

The novel work presented in this chapter is the derivation of the uniform flow far-field expression in eq.(3.67). The disc source analysis of the problem that had been proposed by McAlpine et al. (2015) did not include the far-field. The far-field derivation presented here aims to fill that gap. Equation (3.67) will be used to calculate the far-field pressure when there is no boundary layer present on the fuselage.

3.2 Step-Function Boundary Layer Profile Analysis

As explained in the literature review, the assumption of uniform flow can no longer be considered accurate, see McAninch (1983) through Hanson (1985), and Gaffney and McAlpine (2017), Gaffney and McAlpine (2018). Therefore, the presence of the boundary layer on the fuselage must be taken into account in order to capture the realistic refraction effect of the boundary layer. In this thesis, two simplified boundary layer velocity profiles will be investigated that enable an analytical solution, thus working towards the ultimate goal of the work in this thesis: avoid the use of high-fidelity numerical methods. The two velocity profiles are the step-function velocity profile, whose analysis will be detailed in the following sections, and the more complex linear velocity profile, whose analysis will be detailed later on.

The first and most rudimentary approximation of a boundary layer velocity profile is the step-function profile. Its advantage over the linear profile is the fact that it requires no solution to the Pridmore-Brown equation (Pridmore-Brown (1958)) because there is no shear in the flow. The problem of fan noise refraction due to the presence of a step-function boundary layer on the fuselage has not been addressed analytically before to the best of the author's knowledge. Therefore, the derivations that follow are a novel work.

The process that is followed is a simple matching procedure. Since there is no shear, the solutions inside and outside the boundary layer are the solutions to the uniform flow problem. These two solutions are matched at the edge of the boundary layer to obtain the total field. The boundary layer profile $M(z)$ with thickness δ is replaced with a simple step-function profile with effective thickness δ_{SF}. The effective thickness δ_{SF} is usually the displacement thickness (Hanson (1984) and Hanson (1985)) and thus is smaller than the actual boundary layer thickness δ. Inside the boundary layer, $a_0 < \bar{r} < a_0 + \delta_{SF}$, the flow has a Mach number M_0 which is smaller than the free stream Mach number M_∞ outside the boundary layer, $\bar{r} > a_0 + \delta_{SF}$. The analysis is also outlined briefly in the paper by Rouvas and McAlpine (2022a).

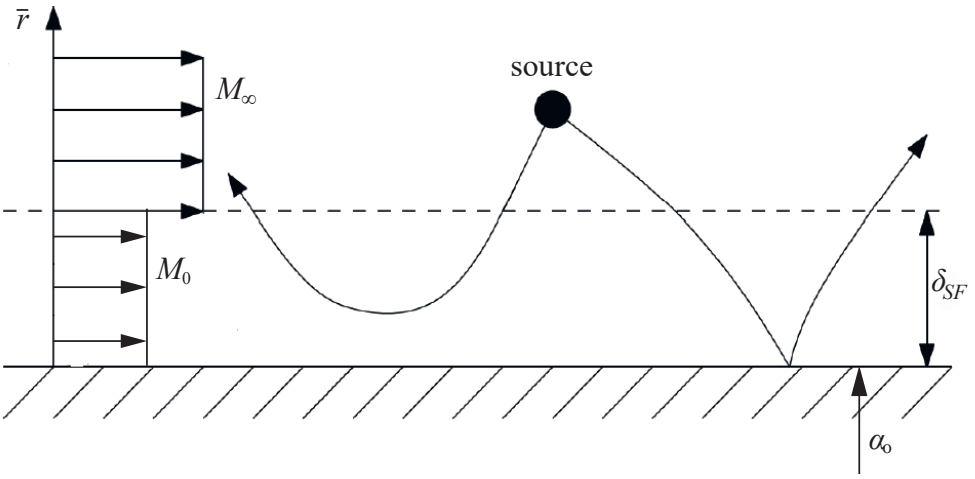

FIGURE 3.3: Boundary layer with step-function velocity profile.

3.2.1 Inside the Boundary Layer

As explained before, due to the simple form of the step-function profile, a solution to the Pridmore-Brown equation is avoided. That is because there is no shear in the flow. Essentially, the problem consists of two uniform flows on top of each other as seen in Fig. (3.3). The total field inside the boundary layer, $a_0 < \bar{r} < a_0 + \delta_{SF}$, is the solution of the homogeneous

convected wave equation expressed in the cylinder's polar coordinates since the scattering object is a cylinder (McAlpine and Kingan (2012)),

$$\frac{\partial^2 p'_{t0}}{\partial \bar{r}^2} + \frac{1}{\bar{r}}\frac{\partial p'_{t0}}{\partial \bar{r}} + \frac{1}{\bar{r}^2}\frac{\partial^2 p'_{t0}}{\partial \bar{\phi}^2} + \frac{\partial^2 p'_{t0}}{\partial \bar{z}^2} - \frac{1}{c_0^2}\left(\frac{\partial}{\partial t} - U_0\frac{\partial}{\partial \bar{z}}\right)^2 p'_{t0} = 0, \tag{3.68}$$

where U_0 is the flow velocity inside the boundary layer, denoted by the subscript 0. By taking the Fourier transform of eq.(3.68) and following the procedure outlined in McAlpine and Kingan (2012) and in section 3.1, an appropriate solution is obtained of the form,

$$\overline{p'_{t0_n}}(\bar{r}, k_z, t) = \frac{1}{2\pi}\int_{-\infty}^{\infty}\left(\widetilde{A}_n(k_z,\omega)\,\mathrm{J}_n(\Gamma\bar{r}) + \widetilde{B}_n(k_z,\omega)\,\mathrm{H}_n^{(2)}(\Gamma\bar{r})\right)\mathrm{e}^{\mathrm{i}\omega t}\,\mathrm{d}\omega, \tag{3.69}$$

where $\Gamma^2 = (k + k_z M_0)^2 - k_z^2$ as shown in section 3.1. Also as before,
$\widetilde{A}_n(k_z,\omega) = A_n(k_z,\omega)\,\delta(\omega-\omega_0)$ and $\widetilde{B}_n(k_z,\omega) = B_n(k_z,\omega)\,\delta(\omega-\omega_0)$. In the absence of a boundary layer, the term $\widetilde{A}_n(k_z,\omega)$ would be set to zero so when $\bar{r}\to\infty$ the solution would represent an outward propagating wave, as demonstrated in McAlpine and Kingan (2012). However, in the presence of the boundary layer, the range of $\bar{r}$ is confined inside the boundary layer, thus both the Bessel and the Hankel function terms in eq.(3.69) are retained.
The total pressure must satisfy the rigid wall boundary condition on the surface of the cylinder, since the cylinder is considered acoustically hard

$$\frac{\partial p'_{t0}}{\partial \bar{r}} = 0 \quad \text{at} \quad \bar{r} = a_0. \tag{3.70}$$

On taking the Fourier transform, the condition becomes

$$\frac{\partial \overline{p'_{t0_n}}}{\partial \bar{r}} = 0 \quad \text{at} \quad \bar{r} = a_0. \tag{3.71}$$

By substituting eq.(3.69) into the boundary condition and taking into account the Dirac-delta functions, the following is obtained

$$\frac{1}{2\pi}A_n(k_z,\omega_0)\,\Gamma_0\,\mathrm{J}'_n(\Gamma_0 a_0)\,\mathrm{e}^{\mathrm{i}\omega_0 t} + \frac{1}{2\pi}B_n(k_z,\omega_0)\,\Gamma_0\,\mathrm{H}_n^{(2)\prime}(\Gamma_0 a_0)\,\mathrm{e}^{\mathrm{i}\omega_0 t} = 0, \tag{3.72}$$

which becomes

$$A_n(k_z,\omega_0)\mathrm{J}'_n(\Gamma_0 a_0) + B_n(k_z,\omega_0)\mathrm{H}_n^{(2)\prime}(\Gamma_0 a_0) = 0, \tag{3.73}$$

where $\Gamma_0^2 = (k_0 + k_z M_0)^2 - k_z^2$. Note that the "radial" wavenumber bears the same subscript as the Mach number it refers to as explained in section 3.1. In this case since the wavenumber refers to the inside Mach number it bears the subscript 0 as in M_0.

3.2.2 Outside the Boundary Layer

Outside of the boundary layer but still in the near-field, $a_0 + \delta_{SF} < \bar{r} < b$, the incident field is described by eq.(27) in McAlpine et al. (2015) and eq.(3.25) in section 3.1. Note the change in notation from Γ_z to Γ_∞, where $\Gamma_\infty^2 = (k_0 + k_z M_\infty)^2 - k_z^2$ because the incident field refers to the region outside the boundary layer where the Mach number is equal to the free stream Mach

number M_∞. From eq.(3.25),

$$\overline{p'_{i\infty_n}}\left(\bar{r},k_z,t\right) \;=\; E_n\left(k_z,\omega_0\right)\mathrm{J}_n\left(\Gamma_\infty\bar{r}\right)\mathrm{e}^{\mathrm{i}\omega_0 t} \quad \text{for} \quad a_0+\delta_{SF}<\bar{r}<b, \tag{3.74}$$

where $E_n\left(k_z,\omega_0\right) \;=\; \pi^2\xi_{lq}P_{lq}\left(-1\right)^{(l+n)}\mathrm{e}^{-\mathrm{i}(l-n)\beta}\left(k_0+k_zM_\infty\right)\Psi_{lq}\,\mathrm{H}^{(2)}_{l-n}\left(\Gamma_\infty b\right)$, and Ψ_{lq} is dependent on Γ_∞ as shown in McAlpine et al. (2015) or in section 3.1.
The scattered field outside the boundary layer is once again the solution to the convected wave equation (eq.(3.68)), only this time the Bessel function term is discarded because it does not satisfy the outward propagating wave condition at infinity. Therefore, as in McAlpine et al. (2015),

$$\overline{p'_{s\infty_n}}\left(\bar{r},k_z,t\right) \;=\; \frac{1}{2\pi}\int_{-\infty}^{\infty}\widetilde{C}_n\left(k_z,\omega\right)\mathrm{H}^{(2)}_n\left(\Gamma\bar{r}\right)\mathrm{e}^{\mathrm{i}\omega t}\,\mathrm{d}\omega, \tag{3.75}$$

where $\widetilde{C}_n\left(k_z,\omega\right)=C_n\left(k_z,\omega\right)\delta\left(\omega-\omega_0\right)$ and Γ is defined now as $\Gamma^2=\left(k+k_zM_\infty\right)^2-k_z^2$ since it refers to the free stream Mach number outside the boundary layer. Taking into consideration the Dirac delta function, eq.(3.75) can be rewritten as

$$\overline{p'_{s\infty_n}}\left(\bar{r},k_z,t\right) \;=\; \frac{1}{2\pi}C_n\left(k_z,\omega_0\right)\mathrm{H}^{(2)}_n\left(\Gamma_\infty\bar{r}\right)\mathrm{e}^{\mathrm{i}\omega_0 t}, \tag{3.76}$$

where $\Gamma_\infty^2=\left(k_0+k_zM_\infty\right)^2-k_z^2$.
Before moving on further with the analysis, it is important to mention again some important practices regarding the "radial" wavenumbers Γ_∞ and Γ_0. As explained in McAlpine et al. (2015) and in appendix B there is a range of k_z in which the wavenumbers are real and positive. Outside this range these wavenumbers become imaginary and are modified accordingly in order to represent an outgoing wave,

$$\begin{aligned}
&\Gamma_\infty=\sqrt{\left(k_0+k_zM_\infty\right)^2-k_z^2}, && \text{when}\;\; \left(k_0+k_zM_\infty\right)^2>k_z^2\\
&\Gamma_\infty=-\mathrm{i}\gamma_\infty,\;\text{where}\;\gamma_\infty=\sqrt{k_z^2-\left(k_0+k_zM_\infty\right)^2}, && \text{when}\;\; \left(k_0+k_zM_\infty\right)^2<k_z^2,
\end{aligned} \tag{3.77}$$

and

$$\begin{aligned}
&\Gamma_0=\sqrt{\left(k_0+k_zM_0\right)^2-k_z^2}, && \text{when}\;\; \left(k_0+k_zM_0\right)^2>k_z^2\\
&\Gamma_0=-\mathrm{i}\gamma_0,\;\text{where}\;\gamma_0=\sqrt{k_z^2-\left(k_0+k_zM_0\right)^2}, && \text{when}\;\; \left(k_0+k_zM_0\right)^2<k_z^2.
\end{aligned} \tag{3.78}$$

In those cases, γ_∞ and γ_0 are always real and positive. Figure (3.4) demonstrates the different regions on the k_z-axis where these transitions from real to imaginary numbers occur. Note that there are also two points along the k_z-axis at which $\Psi_{lq}(\Gamma_\infty)$ is singular. These points are called k_{z1} and k_{z2} and will always lie between the two points where Γ_∞ becomes 0. Figure (3.4) shows the only two combinations that can occur between the transition points of Γ and the singular points of Ψ_{lq} along the k_z-axis. The importance of these regions and these singular points will become apparent during the numerical integration of the inverse Fourier z-transform that will be shown at the end of this chapter.

3.2.3 Matching of the Two Solutions

The pressure expressions outside and inside the boundary layer involve three unknown coefficients, $A_n\left(k_z,\omega_0\right)$, $B_n\left(k_z,\omega_0\right)$ and $C_n\left(k_z,\omega_0\right)$, that must be evaluated. Therefore, three

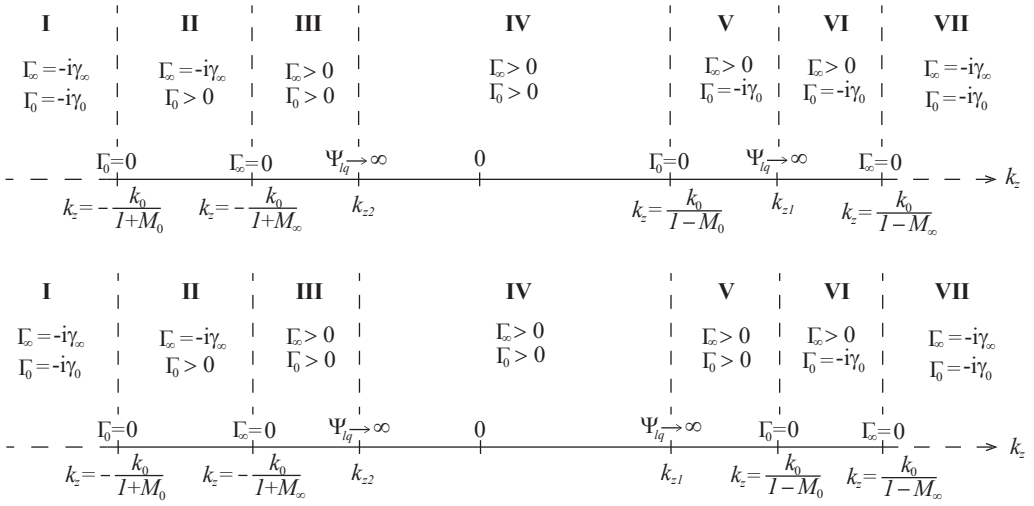

FIGURE 3.4: Transition of Γ values along the k_z-axis, **[top]** $k_{z1} > \frac{k_0}{1-M_0}$, **[bottom]** $k_{z1} < \frac{k_0}{1-M_0}$.

equations are needed in order to evaluate the coefficients and describe the entire pressure field. One such equation is eq.(3.73) which has been derived using the boundary condition on the wall of the cylinder. The remaining two equations will be obtained by employing a matching of the two solutions at the edge of the boundary layer.
The two solutions are matched at the edge of the boundary layer, $\bar{r} = a_0 + \delta_{SF}$. The first matching condition is that of pressure continuity. The pressure inside the boundary layer must be the same as the pressure outside the boundary layer at the edge. This is expressed as follows:

$$\overline{p'_{t0_n}} = \overline{p'_{t\infty_n}} \quad \text{at} \quad \bar{r} = a_0 + \delta_{SF}, \tag{3.79}$$

which can be rewritten as

$$\overline{p'_{t0_n}} = \overline{p'_{i\infty_n}} + \overline{p'_{s\infty_n}} \quad \text{at} \quad \bar{r} = a_0 + \delta_{SF}, \tag{3.80}$$

since outside the boundary layer, the sum of the incident and scattered field equals the total field in that region. By substituting equations (3.69), (3.74) and (3.76) into eq.(3.80), the following is obtained:

$$\begin{aligned} &\frac{1}{2\pi} A_n(k_z, \omega_0) \mathrm{J}_n(\Gamma_0(a_0 + \delta_{SF})) + \frac{1}{2\pi} B_n(k_z, \omega_0) \mathrm{H}_n^{(2)}(\Gamma_0(a_0 + \delta_{SF})) = \\ &= E_n(k_z, \omega_0) \mathrm{J}_n(\Gamma_\infty(a_0 + \delta_{SF})) + \frac{1}{2\pi} C_n(k_z, \omega_0) \mathrm{H}_n^{(2)}(\Gamma_\infty(a_0 + \delta_{SF})). \end{aligned} \tag{3.81}$$

By substituting $A_n\left(k_z,\omega_0\right)$ in accordance with eq.(3.73), the $C_n\left(k_z,\omega_0\right)$ coefficient can be expressed in terms of the $B_n\left(k_z,\omega_0\right)$ coefficient:

$$\begin{aligned} C_n\left(k_z,\omega_0\right) =& \frac{B_n\left(k_z,\omega_0\right)}{\mathrm{H}_n^{(2)}\left(\Gamma_\infty(a_0+\delta_{SF})\right)}\left[\mathrm{H}_n^{(2)}\left(\Gamma_0(a_0+\delta_{SF})\right)-\mathrm{J}_n\left(\Gamma_0(a_0+\delta_{SF})\right)\frac{\mathrm{H}_n^{(2)\prime}\left(\Gamma_0 a_0\right)}{\mathrm{J}_n'\left(\Gamma_0 a_0\right)}\right] \\ & -2\pi\, E_n\left(k_z,\omega_0\right)\frac{\mathrm{J}_n\left(\Gamma_\infty(a_0+\delta_{SF})\right)}{\mathrm{H}_n^{(2)}\left(\Gamma_\infty(a_0+\delta_{SF})\right)}. \end{aligned} \tag{3.82}$$

The second matching condition is the displacement continuity condition. According to this condition, the fluid particles on either side of the interface at the edge of the boundary layer have the same displacement as explained by Hanson (1984). The displacement condition is more physically representative than the simpler pressure gradient continuity condition and it is recommended by Hanson (1984) and others (Mariano (1971), Ko (1972), Eversman (1970), Eversman (1972)) for problems involving sound transmitting through shear layers.
The analysis for the displacement condition starts with the linearised momentum equation:

$$\rho_0\frac{D_0 u}{Dt}=-\nabla p', \tag{3.83}$$

where $\frac{D_0}{Dt}=\frac{\partial}{\partial t}+U\cdot\nabla$ and $U=-U_0\hat{z}$ since flow velocity is directed towards the negative z-axis. Using these relations eq.(3.83) can be rewritten as

$$\rho_0\frac{\partial u}{\partial t}-\rho_0 U_0\frac{\partial u}{\partial z}=-\nabla p'. \tag{3.84}$$

Taking only the $\bar{r}$-axis components, since the displacement condition applies to the axis perpendicular to the edge of the boundary layer,

$$\rho_0\frac{\partial u_{\bar{r}}}{\partial t}-\rho_0 U_0\frac{\partial u_{\bar{r}}}{\partial z}=-\frac{\partial p'}{\partial \bar{r}}. \tag{3.85}$$

The displacement η is found by integrating eq.(3.85) as in Hanson (1984) by using the definition of the radial velocity $u_{\bar{r}}=\frac{D_0\eta}{Dt}$. By substituting this relation into eq.(3.85), the following is obtained:

$$\rho_0 c_0^2\left(\frac{1}{c_0}\frac{\partial}{\partial t}-\frac{U_0}{c_0}\frac{\partial}{\partial z}\right)^2\eta=-\frac{\partial p'}{\partial \bar{r}}. \tag{3.86}$$

Finally, by taking into consideration the following definitions, $M=U_0/c_0$, $k_0=\omega_0/c_0$, and taking the Fourier transforms, $\frac{\partial}{\partial z}\rightarrow -\mathrm{i}k_z$, $\frac{\partial}{\partial t}\rightarrow \mathrm{i}\omega_0$,

$$\rho_0 c_0^2\left(k_0+Mk_z\right)^2\overline{\eta}=\frac{\partial\overline{p'}}{\partial\bar{r}}. \tag{3.87}$$

Using eq.(3.87) the displacement condition can be expressed as follows:

$$\overline{\eta_0}=\overline{\eta_\infty}\quad\text{at}\quad \bar{r}=a_0+\delta_{SF}, \tag{3.88}$$

or

$$\frac{\partial\overline{p'_{t0_n}}}{\partial\bar{r}}\,\frac{1}{\left(k_0+k_zM_0\right)^2}=\frac{\partial\overline{p'_{t\infty_n}}}{\partial\bar{r}}\,\frac{1}{\left(k_0+k_zM_\infty\right)^2}\quad\text{at}\quad \bar{r}=a_0+\delta_{SF}, \tag{3.89}$$

and finally

$$\frac{\partial \overline{p'_{t0_n}}}{\partial \bar{r}} \frac{1}{\left(k_0 + k_z M_0\right)^2} = \left(\frac{\partial \overline{p'_{i\infty_n}}}{\partial \bar{r}} + \frac{\partial \overline{p'_{s\infty_n}}}{\partial \bar{r}} \right) \frac{1}{\left(k_0 + k_z M_\infty\right)^2} \quad \text{at} \quad \bar{r} = a_0 + \delta_{SF}. \tag{3.90}$$

By substituting equations (3.69), (3.74) and (3.76) into eq.(3.90) the following is obtained:

$$\begin{aligned} &\left[\frac{1}{2\pi} A_n\left(k_z, \omega_0\right) \Gamma_0 \mathrm{J}'_n\left(\Gamma_0(a_0 + \delta_{SF})\right) + \frac{1}{2\pi} B_n\left(k_z, \omega_0\right) \Gamma_0 \mathrm{H}^{(2)\prime}_n\left(\Gamma_0(a_0 + \delta_{SF})\right) \right] \frac{1}{\left(k_0 + k_z M_0\right)^2} = \\ &= \left[E_n\left(k_z, \omega_0\right) \Gamma_\infty \mathrm{J}'_n\left(\Gamma_\infty(a_0 + \delta_{SF})\right) + \frac{1}{2\pi} C_n\left(k_z, \omega_0\right) \Gamma_\infty \mathrm{H}^{(2)\prime}_n\left(\Gamma_\infty(a_0 + \delta_{SF})\right) \right] \frac{1}{\left(k_0 + k_z M_\infty\right)^2}. \end{aligned} \tag{3.91}$$

Furthermore, by substituting the coefficient $A_n\left(k_z, \omega_0\right)$ using eq.(3.73) and the coefficient $C_n\left(k_z, \omega_0\right)$ using eq.(3.82), and solving for $B_n\left(k_z, \omega_0\right)$, eq.(3.91) becomes

$$\begin{aligned} B_n\left(k_z, \omega_0\right) = &\frac{\left[\mathrm{J}'_n\left(\Gamma_\infty(a_0 + \delta_{SF})\right) - \mathrm{H}^{(2)\prime}_n\left(\Gamma_\infty(a_0 + \delta_{SF})\right) \frac{\mathrm{J}_n\left(\Gamma_\infty(a_0+\delta_{SF})\right)}{\mathrm{H}^{(2)}_n\left(\Gamma_\infty(a_0+\delta_{SF})\right)} \right]}{D_n\left(k_z, \omega_0\right)} \\ &\times 2\pi E_n\left(k_z, \omega_0\right) \frac{\Gamma_\infty}{\left(k_0 + k_z M_\infty\right)^2}, \end{aligned} \tag{3.92}$$

where the coefficient $D_n\left(k_z, \omega_0\right)$ is defined as

$$\begin{aligned} D_n\left(k_z, \omega_0\right) = &\left[\mathrm{H}^{(2)\prime}_n\left(\Gamma_0(a_0 + \delta_{SF})\right) - \mathrm{J}'_n\left(\Gamma_0(a_0 + \delta_{SF})\right) \frac{\mathrm{H}^{(2)\prime}_n\left(\Gamma_0 a_0\right)}{\mathrm{J}'_n\left(\Gamma_0 a_0\right)} \right] \frac{\Gamma_0}{\left(k_0 + k_z M_0\right)^2} \\ &- \left[\mathrm{H}^{(2)}_n\left(\Gamma_0(a_0 + \delta_{SF})\right) - \mathrm{J}_n\left(\Gamma_0(a_0 + \delta_{SF})\right) \frac{\mathrm{H}^{(2)\prime}_n\left(\Gamma_0 a_0\right)}{\mathrm{J}'_n\left(\Gamma_0 a_0\right)} \right] \\ &\times \frac{\Gamma_\infty}{\left(k_0 + k_z M_\infty\right)^2} \frac{\mathrm{H}^{(2)\prime}_n\left(\Gamma_\infty(a_0 + \delta_{SF})\right)}{\mathrm{H}^{(2)}_n\left(\Gamma_\infty(a_0 + \delta_{SF})\right)}. \end{aligned} \tag{3.93}$$

The expression for the coefficient $B_n\left(k_z, \omega_0\right)$ can be simplified by using the Wronskian formula

$$\mathrm{J}'_n\left(x\right) \mathrm{H}^{(2)}_n\left(x\right) - \mathrm{J}_n\left(x\right) \mathrm{H}^{(2)\prime}_n\left(x\right) = \mathrm{i}\left(\frac{2}{\pi x}\right), \tag{3.94}$$

which when introduced, modifies eq.(3.92) to give

$$B_n\left(k_z, \omega_0\right) = \frac{4\mathrm{i}\, E_n\left(k_z, \omega_0\right)}{\left(a_0 + \delta_{SF}\right)\left(k_0 + k_z M_\infty\right)^2 D_n\left(k_z, \omega_0\right) \mathrm{H}^{(2)}_n\left(\Gamma_\infty(a_0 + \delta_{SF})\right)}. \tag{3.95}$$

Coefficient $A_n\left(k_z, \omega_0\right)$ now can also be evaluated using eqs.(3.73) and (3.95),

$$A_n\left(k_z, \omega_0\right) = -\frac{4\mathrm{i}\, E_n\left(k_z, \omega_0\right) \mathrm{H}^{(2)\prime}_n\left(\Gamma_0 a_0\right)}{\left(a_0 + \delta_{SF}\right)\left(k_0 + k_z M_\infty\right)^2 D_n\left(k_z, \omega_0\right) \mathrm{H}^{(2)}_n\left(\Gamma_\infty(a_0 + \delta_{SF})\right) \mathrm{J}'_n\left(\Gamma_0 a_0\right)}, \tag{3.96}$$

and coefficient $C_n\left(k_z, \omega_0\right)$ using eqs.(3.82) and (3.95).
With all of the coefficients known, expressions for the acoustic pressure both inside and outside the boundary layer can be derived. Since the areas of interest are the surface of the

cylindrical fuselage (for the evaluation of cabin noise levels) and the far-field (for the evaluation of community noise), the next sections are dedicated to the evaluation of those expressions.

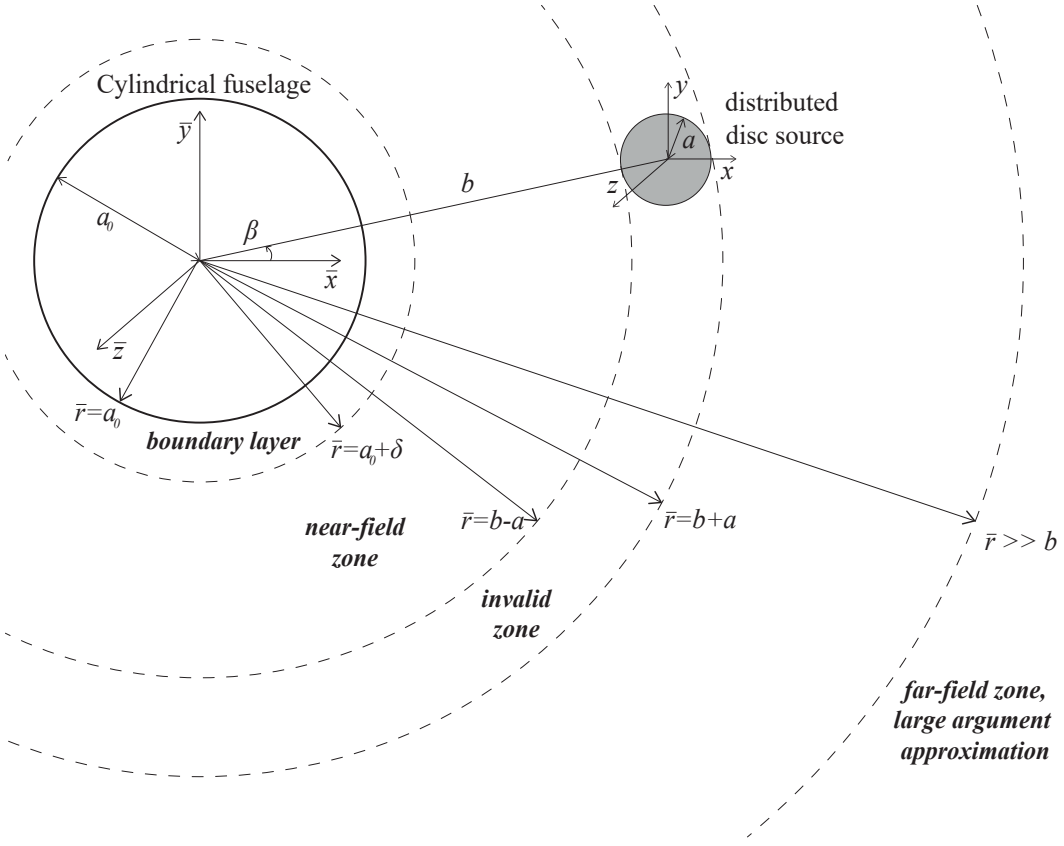

FIGURE 3.5: Sketch showing the zones where near and far field solutions are valid.

3.2.4 Fuselage Surface Pressure

The fuselage surface is inside the boundary layer. With the coefficients $A_n\left(k_z,\omega_0\right)$ and $B_n\left(k_z,\omega_0\right)$ known, an expression for the pressure inside the boundary layer can be written by using eq.(3.69)

$$\overline{p'_{t0_n}}\left(\bar{r},k_z\right) = \frac{A_n\left(k_z,\omega_0\right)}{2\pi}\mathrm{J}_n\left(\Gamma_0\bar{r}\right) + \frac{B_n\left(k_z,\omega_0\right)}{2\pi}\mathrm{H}_n^{(2)}\left(\Gamma_0\bar{r}\right), \tag{3.97}$$

and by replacing the coefficients $A_n\left(k_z,\omega_0\right)$ and $B_n\left(k_z,\omega_0\right)$ with their expressions according to eqs. (3.96) and (3.95) respectively:

$$\begin{aligned}\overline{p'_{t0_n}}\left(\bar{r},k_z\right) =& \frac{2\mathrm{i}\,E_n\left(k_z,\omega_0\right)}{\pi(a_0+\delta_{SF})\left(k_0+k_zM_\infty\right)^2 D_n\left(k_z,\omega_0\right)\mathrm{H}_n^{(2)}\left(\Gamma_\infty(a_0+\delta_{SF})\right)} \\ &\times\left[\mathrm{H}_n^{(2)}\left(\Gamma_0\bar{r}\right)-\mathrm{J}_n\left(\Gamma_0\bar{r}\right)\frac{\mathrm{H}_n^{(2)\prime}\left(\Gamma_0a_0\right)}{\mathrm{J}'_n\left(\Gamma_0a_0\right)}\right].\end{aligned} \tag{3.98}$$

By setting $\bar{r} = a_0$ and using the Wronskian formula as in eq.(3.94), the surface pressure expression is recovered:

$$\overline{p'_{t0_n}}\,(a_0, k_z) = \frac{-4\,E_n\,(k_z, \omega_0)}{\pi^2 \Gamma_0\, a_0 (a_0 + \delta_{SF})\,\left(k_0 + k_z M_\infty\right)^2 D_n\,(k_z, \omega_0)\,\mathrm{H}_n^{(2)}\,(\Gamma_\infty (a_0 + \delta_{SF}))\,\mathrm{J}'_n\,(\Gamma_0 a_0)}. \tag{3.99}$$

Equation (3.99) represents the Fourier-transformed total field on the surface of the cylindrical fuselage. In order to acquire the total field in real space an inverse Fourier transform integration must be carried out. The dependence on $\bar{\phi}$ is represented as always, in the form of a Fourier series:

$$p'_{t0}\,(a_0, \bar{\phi}, \bar{z}, t) \;=\; \frac{1}{(2\pi)^2} \sum_{n=-\infty}^{\infty} \int_{-\infty}^{\infty} \overline{p'_{t0_n}}\,(a_0, k_z)\,\mathrm{e}^{-\mathrm{i}k_z \bar{z}}\,\mathrm{d}k_z\,\mathrm{e}^{-\mathrm{i}n\bar{\phi}}\,\mathrm{e}^{\mathrm{i}\omega_0 t}, \tag{3.100}$$

which becomes, using eq.(3.99),

$$p'_{t0}\,(a_0, \bar{\phi}, \bar{z}, t) \;=\; \frac{\xi_{lq} P_{lq}}{4}\,(-1)^l\,\mathrm{e}^{-\mathrm{i}l\beta} \sum_{n=-\infty}^{\infty} (-1)^n\,\mathrm{e}^{\mathrm{i}n\beta}\,I_n^{(sbl)}(a_0, \bar{z})\,\mathrm{e}^{-\mathrm{i}n\bar{\phi}}\,\mathrm{e}^{\mathrm{i}\omega_0 t} \tag{3.101}$$

where the inverse Fourier integral is given by:

$$I_n^{(sbl)}(a_0, \bar{z}) = \int_{-\infty}^{\infty} -\frac{\left(k_0 + k_z M_\infty\right)\Psi_{lq}\,\mathrm{H}_{l-n}^{(2)}\,(\Gamma_\infty b)}{\frac{\pi^2}{4}\Gamma_0\, a_0 (a_0 + \delta_{SF})\,\left(k_0 + k_z M_\infty\right)^2 D_n\,(k_z, \omega_0)\,\mathrm{H}_n^{(2)}\,(\Gamma_\infty (a_0 + \delta_{SF}))\,\mathrm{J}'_n\,(\Gamma_0 a_0)} \times \mathrm{e}^{-\mathrm{i}k_z \bar{z}}\,\mathrm{d}k_z, \tag{3.102}$$

where *sbl* stands for *step boundary layer*. Equations (3.101) and (3.102) are the essential results of this section. The integral $I_n^{(sbl)}(a_0, \bar{z})$ cannot be solved analytically so it is evaluated numerically. As will be demonstrated in later chapters, the numerical evaluation of this integral will pose certain difficulties since the integrand has singular points along the k_z-axis of integration, as shown in Fig.(3.4). It is also worth noting that eqs. (3.37) and (3.101) are exactly the same apart from the integral, which contains the terms that have to do with the interaction between the two flow regions, outside and inside the boundary layer.

3.2.5 Near-field Validation

For clarity and validation purposes, this section also describes the evaluation process for the total field outside the boundary layer but still in the near-field zone, see Fig.(3.5). The total field outside the boundary layer in that region, $a_0 + \delta_{SF} < \bar{r} < b - a$, is the sum of the incident and scattered field:

$$\overline{p'_{t\infty_n}} \;=\; \overline{p'_{i\infty_n}} + \overline{p'_{s\infty_n}}. \tag{3.103}$$

The incident and scattered fields are given from eqs. (3.74) and (3.76) respectively,

$$\overline{p'_{t\infty_n}}\,(\bar{r}, k_z) = \; E_n\,(k_z, \omega_0)\,\mathrm{J}_n\,(\Gamma_\infty \bar{r}) + \frac{1}{2\pi}\,C_n\,(k_z, \omega_0)\,\mathrm{H}_n^{(2)}\,(\Gamma_\infty \bar{r}) \quad \text{for} \quad a_0 + \delta_{SF} < \bar{r} < b - a, \tag{3.104}$$

and by substituting the coefficient $C_n\left(k_z,\omega_0\right)$ using eqs. (3.82) and (3.95), eq.(3.104) becomes

$$\begin{aligned}\overline{p'_{t\infty_n}}\left(\bar{r},k_z\right) =& E_n\left(k_z,\omega_0\right)\Bigg[\mathrm{J}_n\left(\Gamma_\infty\bar{r}\right)+\frac{2\mathrm{i}}{\pi(a_0+\delta_{SF})\left(k_0+k_zM_\infty\right)^2 D_n\left(k_z,\omega_0\right)\mathrm{H}_n^{(2)}\left(\Gamma_\infty(a_0+\delta_{SF})\right)}\times\\ &\times\left[\mathrm{H}_n^{(2)}\left(\Gamma_0(a_0+\delta_{SF})\right)-\mathrm{J}_n\left(\Gamma_0(a_0+\delta_{SF})\right)\frac{\mathrm{H}_n^{(2)\prime}\left(\Gamma_0a_0\right)}{\mathrm{J}'_n\left(\Gamma_0a_0\right)}\right]\frac{\mathrm{H}_n^{(2)}\left(\Gamma_\infty\bar{r}\right)}{\mathrm{H}_n^{(2)}\left(\Gamma_\infty(a_0+\delta_{SF})\right)}\\ &-\frac{\mathrm{J}_n\left(\Gamma_\infty(a_0+\delta_{SF})\right)}{\mathrm{H}_n^{(2)}\left(\Gamma_\infty(a_0+\delta_{SF})\right)}\mathrm{H}_n^{(2)}\left(\Gamma_\infty\bar{r}\right)\Bigg].\end{aligned} \tag{3.105}$$

The initial analytic validation carried out in this section, serves the purpose of ensuring the robustness of the analytical process. At this point of the analysis the only validation process that can be used, is to reduce the boundary layer profile to a uniform flow and check whether the reduced solution converges towards a known analytic solution for uniform flow. A benchmark solution for the uniform flow problem is the one presented by McAlpine et al. (2015), which has been described in earlier sections of this thesis.

Assuming that the methods used in this chapter are correctly implemented, when the two Mach numbers inside and outside the boundary layer are equal, the derived solution described by eqs. (3.98)-(3.102) must reduce to the uniform flow solution given by McAlpine et al. (2015) and described in section 3.1. The same must be true for the solution for the pressure outside the boundary layer. Both expressions must reduce to the same known uniform flow solution. For the derived solution to be analytically valid the following needs to be true: eqs. (3.98) and (3.105) converge to eq.(39) in McAlpine et al. (2015) (which is the Fourier-transformed uniform flow solution) when $M_0\rightarrow M_\infty$.
When $M_0\rightarrow M_\infty$, it immediately follows that $\Gamma_0\rightarrow\Gamma_\infty$ and the coefficient $D_n\left(k_z,\omega_0\right)$ from eq.(3.93) is reduced as follows

$$\begin{aligned}D_n\left(k_z,\omega_0\right) =& -\frac{\Gamma_\infty}{\left(k_0+k_zM_\infty\right)^2}\frac{\mathrm{H}_n^{(2)\prime}\left(\Gamma_\infty a_0\right)}{\mathrm{J}'_n\left(\Gamma_\infty a_0\right)}\\ &\times\left[\mathrm{J}'_n\left(\Gamma_\infty(a_0+\delta_{SF})\right)-\mathrm{J}_n\left(\Gamma_\infty(a_0+\delta_{SF})\right)\frac{\mathrm{H}_n^{(2)\prime}\left(\Gamma_\infty(a_0+\delta_{SF})\right)}{\mathrm{H}_n^{(2)}\left(\Gamma_\infty(a_0+\delta_{SF})\right)}\right],\end{aligned} \tag{3.106}$$

and using the Wronskian formula from eq.(3.94),

$$D_n\left(k_z,\omega_0\right) = -\frac{\mathrm{H}_n^{(2)\prime}\left(\Gamma_\infty a_0\right)}{\mathrm{J}'_n\left(\Gamma_\infty a_0\right)}\frac{2\mathrm{i}}{\pi\left(a_0+\delta_{SF}\right)\left(k_0+k_zM_\infty\right)^2\mathrm{H}_n^{(2)}\left(\Gamma_\infty(a_0+\delta_{SF})\right)}. \tag{3.107}$$

Therefore, eq.(3.105) can be reduced using the new form of $D_n\left(k_z,\omega_0\right)$ from eq.(3.107) and setting $\Gamma_0 \to \Gamma_\infty$,

$$\begin{aligned}\overline{p'_{t\infty_n}}\left(\bar{r},k_z\right) =& E_n\left(k_z,\omega_0\right)\Bigg[\mathrm{J}_n\left(\Gamma_\infty\bar{r}\right) - \frac{\mathrm{J}'_n\left(\Gamma_\infty a_0\right)}{\mathrm{H}_n^{(2)\prime}\left(\Gamma_\infty a_0\right)}\times \\ &\times\left[\mathrm{H}_n^{(2)}\left(\Gamma_\infty(a_0+\delta_{SF})\right) - \mathrm{J}_n\left(\Gamma_\infty(a_0+\delta_{SF})\right)\frac{\mathrm{H}_n^{(2)\prime}\left(\Gamma_\infty a_0\right)}{\mathrm{J}'_n\left(\Gamma_\infty a_0\right)}\right]\frac{\mathrm{H}_n^{(2)}\left(\Gamma_\infty\bar{r}\right)}{\mathrm{H}_n^{(2)}\left(\Gamma_\infty(a_0+\delta_{SF})\right)} \\ &- \frac{\mathrm{J}_n\left(\Gamma_\infty(a_0+\delta_{SF})\right)}{\mathrm{H}_n^{(2)}\left(\Gamma_\infty(a_0+\delta_{SF})\right)}\mathrm{H}_n^{(2)}\left(\Gamma_\infty\bar{r}\right)\Bigg],\end{aligned} \tag{3.108}$$

which finally becomes

$$\overline{p'_{t\infty_n}}\left(\bar{r},k_z\right) = E_n\left(k_z,\omega_0\right)\left[\mathrm{J}_n\left(\Gamma_\infty\bar{r}\right) - \frac{\mathrm{J}'_n\left(\Gamma_\infty a_0\right)}{\mathrm{H}_n^{(2)\prime}\left(\Gamma_\infty a_0\right)}\mathrm{H}_n^{(2)}\left(\Gamma_\infty\bar{r}\right)\right], \tag{3.109}$$

which is exactly the same as eq.(39) in McAlpine et al. (2015), proving that the total pressure field outside the boundary is successfully reduced to a uniform flow solution in the absence of a boundary layer.

The same can be proven for the total pressure field inside the boundary layer in eq.(3.98) following the same procedure by setting $\Gamma_0 \to \Gamma_\infty$ and substituting $D_n\left(k_z,\omega_0\right)$ with its reduced form as in eq.(3.107),

$$\begin{aligned}\overline{p'_{t0_n}}\left(\bar{r},k_z\right) =& -\frac{2\mathrm{i}\,E_n\left(k_z,\omega_0\right)}{\pi(a_0+\delta_{SF})\left(k_0+k_zM_\infty\right)^2\frac{\mathrm{H}_n^{(2)\prime}\left(\Gamma_\infty a_0\right)}{\mathrm{J}'_n\left(\Gamma_\infty a_0\right)}\frac{2\mathrm{i}\mathrm{H}_n^{(2)}\left(\Gamma_\infty(a_0+\delta_{SF})\right)}{\pi\left(a_0+\delta_{SF}\right)\left(k_0+k_zM_\infty\right)^2\mathrm{H}_n^{(2)}\left(\Gamma_\infty(a_0+\delta_{SF})\right)}} \\ &\times\left[\mathrm{H}_n^{(2)}\left(\Gamma_\infty\bar{r}\right) - \mathrm{J}_n\left(\Gamma_\infty\bar{r}\right)\frac{\mathrm{H}_n^{(2)\prime}\left(\Gamma_\infty a_0\right)}{\mathrm{J}'_n\left(\Gamma_\infty a_0\right)}\right],\end{aligned} \tag{3.110}$$

which becomes

$$\overline{p'_{t0_n}}\left(\bar{r},k_z\right) = E_n\left(k_z,\omega_0\right)\left[\mathrm{J}_n\left(\Gamma_\infty\bar{r}\right) - \frac{\mathrm{J}'_n\left(\Gamma_\infty a_0\right)}{\mathrm{H}_n^{(2)\prime}\left(\Gamma_\infty a_0\right)}\mathrm{H}_n^{(2)}\left(\Gamma_\infty\bar{r}\right)\right], \tag{3.111}$$

which is exactly the same as eq.(39) in McAlpine et al. (2015).

3.2.6 Total Far-field

As demonstrated in the case of the uniform flow in section 3.1, extra care must be taken for the derivation of the far-field pressure expression due to the difference in the incident field expression when $\bar{r} > b + a$. As explained before, the far-field region (see Fig.(3.5)) requires a flip in the triangle of the Graf's Addition theorem. So for the far-field, eq.(3.74) cannot be used to describe the incident field. The correct expression for the incident field when $\bar{r} > b + a$ is

given in eq.(3.24) in section 3.1,

$$\overline{p'_{i\infty_n}}\left(\bar{r},k_z\right)=\pi^2\xi_{lq}P_{lq}\,\mathrm{e}^{-\mathrm{i}(l-n)\beta}\left(k_0+k_zM_\infty\right)\Psi_{lq}\,\mathrm{J}_{n-l}\left(\Gamma_\infty b\right)\mathrm{H}_n^{(2)}\left(\Gamma_\infty\bar{r}\right)\quad\text{for}\quad\bar{r}>b+a. \tag{3.112}$$

With the incident field known, the total field can be obtained since the scattered field $\overline{p'_{s\infty_n}}$ is known from eq.(3.76),

$$\begin{aligned}&\overline{p'_{t\infty_n}}=\overline{p'_{i\infty_n}}+\overline{p'_{s\infty_n}}\Rightarrow\\&\overline{p'_{t\infty_n}}=\pi^2\xi_{lq}P_{lq}\,\mathrm{e}^{-\mathrm{i}(l-n)\beta}\left(k_0+k_zM_\infty\right)\Psi_{lq}\,\mathrm{J}_{n-l}\left(\Gamma_\infty b\right)\mathrm{H}_n^{(2)}\left(\Gamma_\infty\bar{r}\right)+\frac{1}{2\pi}\,C_n\left(k_z,\omega_0\right)\mathrm{H}_n^{(2)}\left(\Gamma_\infty\bar{r}\right),\end{aligned} \tag{3.113}$$

or

$$\begin{aligned}&\overline{p'_{t_{nff}}}=\pi^2\xi_{lq}P_{lq}\,\mathrm{e}^{-\mathrm{i}(l-n)\beta}\left(k_0+k_zM_\infty\right)\Psi_{lq}\,\mathrm{J}_{n-l}\left(\Gamma_\infty b\right)\mathrm{H}_n^{(2)}\left(\Gamma_\infty\bar{r}\right)\\&+\frac{B_n\left(k_z,\omega_0\right)}{2\pi\mathrm{H}_n^{(2)}\left(\Gamma_\infty(a_0+\delta_{SF})\right)}\left[\mathrm{H}_n^{(2)}\left(\Gamma_0(a_0+\delta_{SF})\right)-\mathrm{J}_n\left(\Gamma_0(a_0+\delta_{SF})\right)\frac{\mathrm{H}_n^{(2)\prime}\left(\Gamma_0a_0\right)}{\mathrm{J}'_n\left(\Gamma_0a_0\right)}\right]\mathrm{H}_n^{(2)}\left(\Gamma_\infty\bar{r}\right)\\&-E_n\left(k_z,\omega_0\right)\frac{\mathrm{J}_n\left(\Gamma_\infty(a_0+\delta_{SF})\right)}{\mathrm{H}_n^{(2)}\left(\Gamma_\infty(a_0+\delta_{SF})\right)}\,\mathrm{H}_n^{(2)}\left(\Gamma_\infty\bar{r}\right).\end{aligned} \tag{3.114}$$

By substituting $B_n\left(k_z,\omega_0\right)$ and $E_n\left(k_z,\omega_0\right)$ with their expressions according to eq.(3.95),

$$\begin{aligned}&\overline{p'_{t_{nff}}}=\pi^2\xi_{lq}P_{lq}\,\mathrm{e}^{-\mathrm{i}(l-n)\beta}\left(k_0+k_zM_\infty\right)\Psi_{lq}\,\mathrm{J}_{n-l}\left(\Gamma_\infty b\right)\mathrm{H}_n^{(2)}\left(\Gamma_\infty\bar{r}\right)\\&+\frac{4\mathrm{i}\,\pi^2\xi_{lq}P_{lq}\left(-1\right)^{(l+n)}\mathrm{e}^{-\mathrm{i}(l-n)\beta}\left(k_0+k_zM_\infty\right)\Psi_{lq}\,\mathrm{H}_{l-n}^{(2)}\left(\Gamma_\infty b\right)}{2\pi\mathrm{H}_n^{(2)}\left(\Gamma_\infty(a_0+\delta_{SF})\right)(a_0+\delta_{SF})\left(k_0+k_zM_\infty\right)^2D_n\left(k_z,\omega_0\right)\mathrm{H}_n^{(2)}\left(\Gamma_\infty(a_0+\delta_{SF})\right)}\\&\times\left[\mathrm{H}_n^{(2)}\left(\Gamma_0(a_0+\delta_{SF})\right)-\mathrm{J}_n\left(\Gamma_0(a_0+\delta_{SF})\right)\frac{\mathrm{H}_n^{(2)\prime}\left(\Gamma_0a_0\right)}{\mathrm{J}'_n\left(\Gamma_0a_0\right)}\right]\mathrm{H}_n^{(2)}\left(\Gamma_\infty\bar{r}\right)\\&-\pi^2\xi_{lq}P_{lq}\left(-1\right)^{(l+n)}\mathrm{e}^{-\mathrm{i}(l-n)\beta}\left(k_0+k_zM_\infty\right)\Psi_{lq}\,\mathrm{H}_{l-n}^{(2)}\left(\Gamma_\infty b\right)\frac{\mathrm{J}_n\left(\Gamma_\infty(a_0+\delta_{SF})\right)}{\mathrm{H}_n^{(2)}\left(\Gamma_\infty(a_0+\delta_{SF})\right)}\,\mathrm{H}_n^{(2)}\left(\Gamma_\infty\bar{r}\right).\end{aligned} \tag{3.115}$$

Before continuing further, certain terms must be introduced for the sake of brevity. By setting

$$F_n\left(k_z,\omega_0\right)=\pi^2\xi_{lq}P_{lq}\,\mathrm{e}^{-\mathrm{i}(l-n)\beta}\left(k_0+k_zM_\infty\right)\Psi_{lq}, \tag{3.116}$$

and the term in the square brackets

$$Y_n\left(\Gamma_0\right)=\left[\mathrm{H}_n^{(2)}\left(\Gamma_0(a_0+\delta_{SF})\right)-\mathrm{J}_n\left(\Gamma_0(a_0+\delta_{SF})\right)\frac{\mathrm{H}_n^{(2)\prime}\left(\Gamma_0a_0\right)}{\mathrm{J}'_n\left(\Gamma_0a_0\right)}\right], \tag{3.117}$$

and finally by considering the following property of the Hankel function

$$\left(-1\right)^{(l+n)}\mathrm{H}_{l-n}^{(2)}\left(\Gamma_\infty b\right)=\left(-1\right)^{(l+n)}\left(-1\right)^{(n-l)}\mathrm{H}_{n-l}^{(2)}\left(\Gamma_\infty b\right)=\mathrm{H}_{n-l}^{(2)}\left(\Gamma_\infty b\right), \tag{3.118}$$

eq.(3.115) can be rewritten as:

$$\begin{aligned}\overline{p'_{t_{nff}}}\left(\bar{r},k_z\right) =& F_n\left(k_z,\omega_0\right)\Bigg[\mathrm{J}_{n-l}\left(\Gamma_\infty b\right)\\ &+\Bigg[\frac{2\mathrm{i}\,Y_n\left(\Gamma_0\right)}{\pi(a_0+\delta_{SF})\,\mathrm{H}_n^{(2)}\left(\Gamma_\infty(a_0+\delta_{SF})\right)\left(k_0+k_zM_\infty\right)^2 D_n\left(k_z,\omega_0\right)}\\ &-\mathrm{J}_n\left(\Gamma_\infty(a_0+\delta_{SF})\right)\Bigg]\frac{\mathrm{H}_{n-l}^{(2)}\left(\Gamma_\infty b\right)}{\mathrm{H}_n^{(2)}\left(\Gamma_\infty(a_0+\delta_{SF})\right)}\Bigg]\mathrm{H}_n^{(2)}\left(\Gamma_\infty\bar{r}\right).\end{aligned} \tag{3.119}$$

Following the same procedure as in the near-field case, an inverse Fourier z-transform must be performed in order to obtain the total field in real space. Also, a Fourier series is introduced for the dependence on $\bar{\phi}$ as in the case of the near-field,

$$p'_{t_{ff}}\left(\bar{r},\bar{\phi},\bar{z},t\right) = \frac{1}{(2\pi)^2}\sum_{n=-\infty}^{\infty}\int_{-\infty}^{\infty}\overline{p'_{t_{nff}}}\left(\bar{r},k_z\right)\mathrm{e}^{-\mathrm{i}k_z\bar{z}}\,\mathrm{d}k_z\,\mathrm{e}^{-\mathrm{i}n\bar{\phi}}\,\mathrm{e}^{\mathrm{i}\omega_0 t}. \tag{3.120}$$

As in the uniform flow case, this inverse Fourier z-transform can be solved analytically using the method of stationary phase. The process is very similar to the uniform flow case in section 3.1.4.1 and is presented in appendix D. Here, only the key results are shown:

$$\begin{aligned}p'_{t_{ff}}\left(\bar{R},\bar{\phi},\bar{\theta},t\right) =& \frac{\mathrm{i}\xi_{lq}P_{lq}\,k_0\,\Psi_{lq}(\Delta_\infty)}{2\bar{R}}\,\frac{S\left(\bar{\theta}\right)}{\left(1-M_\infty^2\sin^2\bar{\theta}\right)}\,\mathrm{e}^{-\mathrm{i}k_0\bar{R}S(\bar{\theta})}\\ &\times\sum_{n=-\infty}^{\infty}\mathfrak{S}_n(\bar{\theta})\,\mathrm{e}^{\frac{1}{2}n\pi\mathrm{i}}\,\mathrm{e}^{\mathrm{i}(n-l)\beta}\,\mathrm{e}^{-\mathrm{i}n\bar{\phi}}\,\mathrm{e}^{\mathrm{i}\omega_0 t},\end{aligned} \tag{3.121}$$

where

$$\begin{aligned}\mathfrak{S}_n(\bar{\theta}) =& \Bigg[\mathrm{J}_{n-l}\left(\Delta_\infty b\right)+\Bigg[\frac{2\mathrm{i}\left(1-M_\infty^2\sin^2\bar{\theta}\right)Y_n\left(\Delta_0\right)}{\pi(a_0+\delta_{SF})\,\mathrm{H}_n^{(2)}\left(\Delta_\infty(a_0+\delta_{SF})\right)k_0^2\,S^2\left(\bar{\theta}\right)D_n\left(\Delta_\infty,\Delta_0\right)}\\ &-\mathrm{J}_n\left(\Delta_\infty(a_0+\delta_{SF})\right)\Bigg]\frac{\mathrm{H}_{n-l}^{(2)}\left(\Delta_\infty b\right)}{\mathrm{H}_n^{(2)}\left(\Delta_\infty(a_0+\delta_{SF})\right)}\Bigg].\end{aligned} \tag{3.122}$$

The rest of the terms are

$$\begin{aligned}D_n\left(\Delta_\infty,\Delta_0\right) =& \Bigg[\mathrm{H}_n^{(2)\prime}\left(\Delta_0(a_0+\delta_{SF})\right)-\mathrm{J}_n'\left(\Delta_0(a_0+\delta_{SF})\right)\frac{\mathrm{H}_n^{(2)\prime}\left(\Delta_0 a_0\right)}{\mathrm{J}_n'\left(\Delta_0 a_0\right)}\Bigg]\\ &\times\frac{\Delta_0}{k_0^2\left(1+\frac{C\left(\bar{\theta}\right)M_0}{\left(1-M_\infty^2\sin^2\bar{\theta}\right)^{1/2}}\right)^2}\\ &-\Bigg[\mathrm{H}_n^{(2)}\left(\Delta_0(a_0+\delta_{SF})\right)-\mathrm{J}_n\left(\Delta_0(a_0+\delta_{SF})\right)\frac{\mathrm{H}_n^{(2)\prime}\left(\Delta_0 a_0\right)}{\mathrm{J}_n'\left(\Delta_0 a_0\right)}\Bigg]\\ &\times\frac{\sin\bar{\theta}(1-M_\infty^2\sin^2\bar{\theta})^{1/2}}{k_0\,S^2\left(\bar{\theta}\right)}\,\frac{\mathrm{H}_n^{(2)\prime}\left(\Delta_\infty(a_0+\delta_{SF})\right)}{\mathrm{H}_n^{(2)}\left(\Delta_\infty(a_0+\delta_{SF})\right)},\end{aligned} \tag{3.123}$$

with $\Delta_\infty = \frac{k_0 \sin\bar{\theta}}{(1-M_\infty^2 \sin^2\bar{\theta})^{1/2}}$ and

$$\Delta_0 = \frac{k_0}{(1-M_\infty^2 \sin^2\bar{\theta})^{1/2}} \sqrt{(1-M_\infty^2 \sin^2\bar{\theta}) + C(\bar{\theta})[2M_0(1-M_\infty^2 \sin^2\bar{\theta})^{1/2} - C(\bar{\theta})\sigma_0^2]}. \quad (3.124)$$

Finally, $S(\bar{\theta}) = \frac{(1-M_\infty^2 \sin^2\bar{\theta})^{1/2} + M_\infty \cos\bar{\theta}}{\sigma_\infty^2}$, $C(\bar{\theta}) = \frac{\cos\bar{\theta} + (1-M_\infty^2 \sin^2\bar{\theta})^{1/2} M_\infty}{\sigma_\infty^2}$, $\sigma_\infty^2 = 1 - M_\infty^2$ and $\sigma_0^2 = 1 - M_0^2$. Equation (3.121) is the essential conclusion of this section. It describes the acoustic pressure in the far-field around the fuselage using spherical polar coordinates centered on the cylindrical fuselage, while taking into account the step-function boundary layer on the surface of the fuselage.

While the method of stationary phase is preferred in far-field approximations (see Lu (1990)), the presence of multiple branch cuts along the integration domain gives rise to an issue that should be addressed. The presence of branch cuts implies that the integrand close to those branch points (see Fig. (3.4) may be significant and the method of stationary phase may ignore its impactful contribution. Therefore, the method of steepest descent is employed as in Gabard (2008). This method is more robust than the method of stationary phase because, unlike the stationary phase method which integrates along the real k_z-axis, the steepest descent method deforms the integration path onto the complex plane avoiding the branch points but retaining the impactful contribution of the integrand around those points. The solution of the integral in eq.(3.120) with the method of steepest descent is carried out in appendix E.

The final expression in appendix E is exactly the same as in eq.(3.121). This essentially means that the method of steepest descent yields the same result as the method of stationary phase. This is also demonstrated in appendices D and E where it is proven that the point of stationary phase is the same as the saddle point in the steepest descent method. The method of stationary phase only takes into account the contribution of the integrand around the point of stationary phase. On the other hand, the method of steepest descent only takes into account the contribution of the integrand around the saddle point along the steepest descent deformed integration contour. Therefore, if the point of stationary phase is the same as the saddle point, the integration should yield the same result for both methods. Thus, it is proven that in this case the presence of branch points along the integration domain does not affect the overall result. For that reason, a deformation of the integration contour onto the complex plane is not necessary and therefore the method of stationary phase is capable of producing a mathematically robust solution.

3.2.7 Far-field Validation

As in the case of the near-field, the analytical validation process involves reducing the step-function boundary layer to a uniform flow. Assuming that the analytical methods used in the previous section are valid, when the two Mach numbers inside and outside the boundary layer are equal, the derived solution described by eq.(3.121) must reduce to the uniform flow far-field solution given by eq.(3.67). For the derived solution to be analytically valid the following needs to be true: eq.(3.121) converges to eq.(3.67) when $M_0 \to M_\infty$.

When $M_0 \to M_\infty$ it immediately follows that $\sigma_0 \to \sigma_\infty$. It must also follow that $\Delta_0 \to \Delta_\infty$,

$$\begin{aligned}\Delta_0 &= \frac{k_0}{(1-M_\infty^2\sin^2\bar{\theta})^{1/2}}\sqrt{(1-M_\infty^2\sin^2\bar{\theta})+C\,(\bar{\theta})[2M_\infty(1-M_\infty^2\sin^2\bar{\theta})^{1/2}-C\,(\bar{\theta})\sigma_\infty^2]}\\ &= \frac{k_0\sin\bar{\theta}}{(1-M_\infty^2\sin^2\bar{\theta})^{1/2}} = \Delta_\infty.\end{aligned} \tag{3.125}$$

The term $D_n\,(\Delta_\infty,\Delta_0)$ will also reduce to the form of $D_n\,(\Delta_\infty)$,

$$\begin{aligned}D_n\,(\Delta_\infty,\Delta_0) =& \left[\mathrm{H}_n^{(2)\prime}\,(\Delta_\infty(a_0+\delta_{SF})) - \mathrm{J}_n'\,(\Delta_\infty(a_0+\delta_{SF}))\,\frac{\mathrm{H}_n^{(2)\prime}\,(\Delta_\infty a_0)}{\mathrm{J}_n'\,(\Delta_\infty a_0)}\right]\\ &\times\frac{\sin\bar{\theta}(1-M_\infty^2\sin^2\bar{\theta})^{1/2}}{k_0S^2(\bar{\theta})}\\ &-\left[\mathrm{H}_n^{(2)}\,(\Delta_\infty(a_0+\delta_{SF})) - \mathrm{J}_n\,(\Delta_\infty(a_0+\delta_{SF}))\,\frac{\mathrm{H}_n^{(2)\prime}\,(\Delta_\infty a_0)}{\mathrm{J}_n'\,(\Delta_\infty a_0)}\right]\\ &\times\frac{\sin\bar{\theta}(1-M_\infty^2\sin^2\bar{\theta})^{1/2}}{k_0\,S^2\,(\bar{\theta})}\,\frac{\mathrm{H}_n^{(2)\prime}\,(\Delta_\infty(a_0+\delta_{SF}))}{\mathrm{H}_n^{(2)}\,(\Delta_\infty(a_0+\delta_{SF}))}.\end{aligned} \tag{3.126}$$

This expression can be simplified,

$$\begin{aligned}D_n\,(\Delta_\infty) =& -\frac{\sin\bar{\theta}(1-M_\infty^2\sin^2\bar{\theta})^{1/2}}{k_0S^2(\bar{\theta})}\,\frac{\mathrm{H}_n^{(2)\prime}\,(\Delta_\infty a_0)}{\mathrm{J}_n'\,(\Delta_\infty a_0)}\\ &\times\left[\mathrm{J}_n'\,(\Delta_\infty(a_0+\delta_{SF})) - \mathrm{H}_n^{(2)\prime}\,(\Delta_\infty(a_0+\delta_{SF}))\frac{\mathrm{J}_n\,(\Delta_\infty(a_0+\delta_{SF}))}{\mathrm{H}_n^{(2)}\,(\Delta_\infty(a_0+\delta_{SF}))}\right],\end{aligned} \tag{3.127}$$

and by using the Wronskian formula from eq.(3.94),

$$D_n(\Delta_\infty) = -\frac{\sin\bar{\theta}(1-M_\infty^2\sin^2\bar{\theta})^{1/2}}{k_0S^2(\bar{\theta})}\,\frac{\mathrm{H}_n^{(2)\prime}\,(\Delta_\infty a_0)}{\mathrm{J}_n'\,(\Delta_\infty a_0)}\,\frac{2\mathrm{i}}{\pi\Delta_\infty(a_0+\delta_{SF})\mathrm{H}_n^{(2)}\,(\Delta_\infty(a_0+\delta_{SF}))}. \tag{3.128}$$

Finally the reduced form of the $\mathfrak{S}_n(\bar{\theta})$ term in eq.(3.121) can be evaluated,

$$\begin{aligned}\mathfrak{S}_n(\bar{\theta}) =& \left[\mathrm{J}_{n-l}\,(\Delta_\infty b)\right.\\ &+\left[\frac{-2\mathrm{i}\,(1-M_\infty^2\sin^2\bar{\theta})\,Y_n\,(\Delta_\infty)}{\pi(a_0+\delta_{SF})\,\mathrm{H}_n^{(2)}\,(\Delta_\infty(a_0+\delta_{SF}))\,k_0^2\,S^2\,(\bar{\theta})\,\frac{\sin\bar{\theta}(1-M_\infty^2\sin^2\bar{\theta})^{1/2}}{k_0S^2(\bar{\theta})}\,\frac{\mathrm{H}_n^{(2)\prime}\,(\Delta_\infty a_0)}{\mathrm{J}_n'\,(\Delta_\infty a_0)}\,\frac{2\mathrm{i}}{\pi\Delta_\infty(a_0+\delta_{SF})\mathrm{H}_n^{(2)}\,(\Delta_\infty(a_0+\delta_{SF}))}}\right.\\ &\left.\left.-\,\mathrm{J}_n\,(\Delta_\infty(a_0+\delta_{SF}))\right]\frac{\mathrm{H}_{n-l}^{(2)}\,(\Delta_\infty b)}{\mathrm{H}_n^{(2)}\,(\Delta_\infty(a_0+\delta_{SF}))}\right]\\ =& \left[\mathrm{J}_{n-l}\,(\Delta_\infty b) + \left[-Y_n\,(\Delta_\infty)\frac{\mathrm{J}_n'\,(\Delta_\infty a_0)}{\mathrm{H}_n^{(2)\prime}\,(\Delta_\infty a_0)} - \mathrm{J}_n\,(\Delta_\infty(a_0+\delta_{SF}))\right]\frac{\mathrm{H}_{n-l}^{(2)}\,(\Delta_\infty b)}{\mathrm{H}_n^{(2)}\,(\Delta_\infty(a_0+\delta_{SF}))}\right],\end{aligned} \tag{3.129}$$

and since from eq.(3.117),

$$Y_n\left(\Delta_\infty\right) = \left[\mathrm{H}_n^{(2)}\left(\Delta_\infty(a_0+\delta_{SF})\right) - \mathrm{J}_n\left(\Delta_\infty(a_0+\delta_{SF})\right)\frac{\mathrm{H}_n^{(2)\prime}\left(\Delta_\infty a_0\right)}{\mathrm{J}_n'\left(\Delta_\infty a_0\right)}\right], \tag{3.130}$$

eq.(3.129) can be further simplified,

$$\begin{aligned}\mathfrak{S}_n(\bar{\theta}) = &\left[\mathrm{J}_{n-l}\left(\Delta_\infty b\right) + \left[-\mathrm{H}_n^{(2)}\left(\Delta_\infty(a_0+\delta_{SF})\right)\frac{\mathrm{J}_n'\left(\Delta_\infty a_0\right)}{\mathrm{H}_n^{(2)\prime}\left(\Delta_\infty a_0\right)}\right.\right.\\ &\left.\left.+\mathrm{J}_n\left(\Delta_\infty(a_0+\delta_{SF})\right)\frac{\mathrm{H}_n^{(2)\prime}\left(\Delta_\infty a_0\right)}{\mathrm{J}_n'\left(\Delta_\infty a_0\right)}\frac{\mathrm{J}_n'\left(\Delta_\infty a_0\right)}{\mathrm{H}_n^{(2)\prime}\left(\Delta_\infty a_0\right)} - \mathrm{J}_n\left(\Delta_\infty(a_0+\delta_{SF})\right)\right]\frac{\mathrm{H}_{n-l}^{(2)}\left(\Delta_\infty b\right)}{\mathrm{H}_n^{(2)}\left(\Delta_\infty(a_0+\delta_{SF})\right)}\right]\\ =&\left[\mathrm{J}_{n-l}\left(\Delta_\infty b\right) - \mathrm{H}_{n-l}^{(2)}\left(\Delta_\infty b\right)\frac{\mathrm{J}_n'\left(\Delta_\infty a_0\right)}{\mathrm{H}_n^{(2)\prime}\left(\Delta_\infty a_0\right)}\right].\end{aligned} \tag{3.131}$$

The final form of eq.(3.131) is identical to the bracket term in eq.(3.67) for the uniform flow case. The rest of the terms in eq.(3.121) cannot be further reduced or simplified since they are not dependent on M_0 in any way. This leads to the reduced form of eq.(3.121),

$$\begin{aligned}p'_{t_{ff}}\left(\bar{R},\bar{\phi},\bar{\theta},t\right) =& \frac{\mathrm{i}\xi_{lq}P_{lq}\,k_0\,\Psi_{lq}(\Delta_\infty)}{2\bar{R}}\,\frac{S\left(\bar{\theta}\right)}{\left(1-M_\infty^2\sin^2\bar{\theta}\right)}\,\mathrm{e}^{-\mathrm{i}k_0\bar{R}S(\bar{\theta})}\\ &\times\sum_{n=-\infty}^{\infty}\left[\mathrm{J}_{n-l}\left(\Delta_\infty b\right) - \mathrm{H}_{n-l}^{(2)}\left(\Delta_\infty b\right)\frac{\mathrm{J}_n'\left(\Delta_\infty a_0\right)}{\mathrm{H}_n^{(2)\prime}\left(\Delta_\infty a_0\right)}\right]\mathrm{e}^{\frac{1}{2}n\pi\mathrm{i}}\,\mathrm{e}^{\mathrm{i}(n-l)\beta}\,\mathrm{e}^{-\mathrm{i}n\bar{\phi}}\,\mathrm{e}^{\mathrm{i}\omega_0 t},\end{aligned} \tag{3.132}$$

which is exactly the same as the uniform flow expression in eq.(3.67). Note the difference in notation, since in the uniform flow case there was only one Mach number M_z and one Δ_z term which can arbitrarily be renamed M_∞ and Δ_∞ since their definitions are exactly the same as in the step-function boundary layer case.

3.2.8 Section Summary

The aim of this chapter was to derive some key expressions and equations that will be used to produce pressure calculations when there is a step-function boundary layer profile present on the surface of the fuselage. Specifically, the first of these expressions describe the pressure on the fuselage surface in eqs. (3.101) and (3.102). The far-field solution for the same problem is also derived and presented in this chapter. Equation (3.121) gives the pressure in the far-field of the fuselage when there is a step-function boundary layer on it. The main advantage of using such a simple profile that has no shear, is to avoid solving the Pridmore-Brown equation.

As stated before, the step-function boundary layer profile may not seem realistic enough in order to produce results that closely match those of a more representative profile but it provides plenty of insight into the refraction problem as will be seen later. Furthermore, as will be seen later, the simplicity of the step-function profile will lead to certain advantages over other methods. The results in this chapter represent a novel work of an analytical

solution of fan noise refraction by a step-function boundary layer that has not been presented before to the best of the author's knowledge.

3.3 Linear Boundary Layer Profile Analysis

The step-function boundary layer profile is a good initial approximation for a more complex boundary layer. The next stage of the analysis will include an even more realistic velocity profile. This profile is chosen to be the linear profile because it is still relatively simple and enables an analytical solution. As stated before, the challenge of having a shear layer in the flow is the necessity to solve the Pridmore-Brown equation (Pridmore-Brown (1958)),

$$\frac{\mathrm{D}_0}{\mathrm{D}t}\left(\frac{\mathrm{D}_0{}^2 p}{\mathrm{D}t^2} - \nabla^2 p\right) - 2M' \frac{\partial^2 p}{\partial \bar{r}\partial \bar{z}} = 0, \tag{3.133}$$

where $M' = \mathrm{d}M/\mathrm{d}\bar{r}$ is the Mach number gradient. All previous work on fuselage boundary layer refraction relied on numerical methods to solve the Pridmore-Brown equation, namely Runge-Kutta routines (Hanson and Magliozzi (1985), Lu (1990), Brambley et al. (2011), Brambley et al. (2012), Gaffney and McAlpine (2017), Gaffney and McAlpine (2018), Campos et al. (1999)).

The key novel contribution of this thesis is the use of an asymptotic analytical approach to solve the Pridmore-Brown equation. This solution has been proposed by Eversman and Beckemeyer (1972) who used it in order to calculate the sound propagation through a shear layer that develops on the walls of a duct. Eversman (1972) concluded that the solution is valid and accurate for sufficiently thin boundary layers. Therefore, in this thesis this analytical method will be used to solve the problem of sound propagation through a shear layer that develops on the wall of the fuselage. A simple linear shear will be used in order to simplify the calculations and facilitate quicker results in contrary to previous numerical work. Also, by allowing a slip velocity at the wall, the linear profile can be used to simulate other profiles such as the quarter-sine or the $1/7$th power law. These results are also available in the paper by Rouvas and McAlpine (2021).

The process that is followed is once again a matching procedure. The solution inside the boundary layer (the solution to the Pridmore-Brown equation) is matched to the solution outside the boundary layer (which is a simple uniform flow problem as described in previous sections) at the edge of the boundary layer in order to obtain the total field. The boundary layer profile $M(z)$ with thickness δ is replaced with a linear velocity profile with effective thickness δ_L. Inside the boundary layer, $a_0 < \bar{r} < a_0 + \delta_L$, the flow exhibits a linear shear layer with a Mach number at the wall M_w which is smaller than the free stream Mach number M_∞ outside the boundary layer, $\bar{r} > a_0 + \delta_L$. The importance of allowing a slip at the wall has already been described in Rouvas and McAlpine (2021) and will be shown later in this thesis in more detail. The analysis is also outlined briefly in the paper by Rouvas and McAlpine (2021).

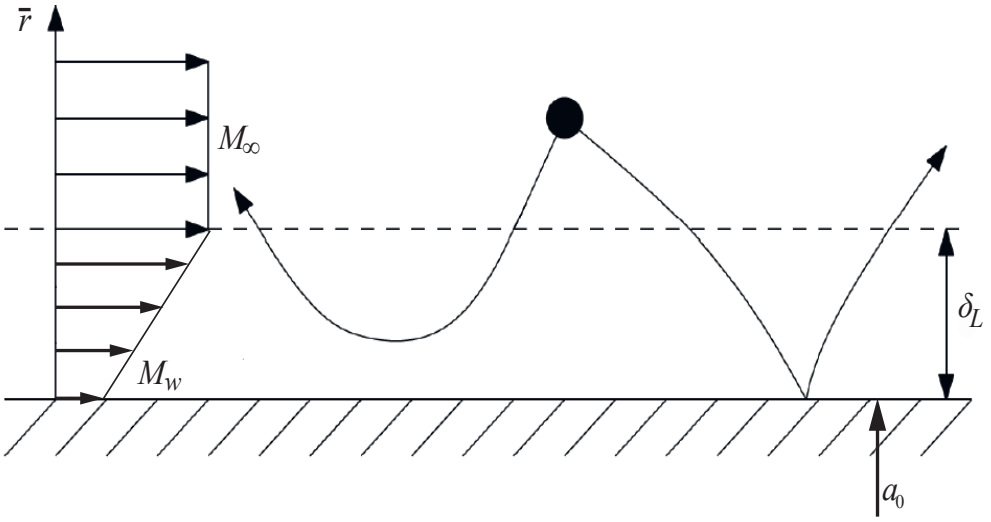

FIGURE 3.6: Boundary layer with linear velocity profile.

3.3.1 Inside the Boundary Layer

Inside the boundary layer the sound propagation is governed by the Pridmore-Brown equation. The analysis begins with the Fourier-transformed Pridmore-Brown equation expressed in cylindrical polar coordinates, given in Gaffney (2016) eq.(5.1.13), which describes the total field inside a linear boundary layer with slip on the wall M_w and free stream Mach number M_∞,

$$\frac{\mathrm{d}^2\overline{p'_{t_{in_n}}}}{\mathrm{d}\bar{r}^2} + \left(\frac{1}{\bar{r}} - \frac{2k_zM'}{k_0+k_zM}\right)\frac{\mathrm{d}\overline{p'_{t_{in_n}}}}{\mathrm{d}\bar{r}} + \left[(k_0+k_zM)^2 - k_z^2 - \frac{n^2}{\bar{r}^2}\right]\overline{p'_{t_{in_n}}} = 0. \tag{3.134}$$

The initial part of the analysis is to change variables firstly to $y = \frac{\bar{r}-a_0}{a_0}$, and then to $\zeta = \frac{y}{\varepsilon}$, with the parameter

$$\varepsilon = \frac{\delta_L}{a_0}, \tag{3.135}$$

as the non-dimensional boundary-layer thickness. Essentially, this change of variables is done in order to perform an inner expansion inside the boundary layer. Thus, the limits of the boundary layer are shifted from $a_0 < \bar{r} < a_0 + \delta_L$ to $0 < \zeta < 1$. With these changes, eq.(3.134) becomes

$$\begin{aligned}&\frac{\mathrm{d}^2\overline{p'_{t_{in_n}}}}{\mathrm{d}\zeta^2} + \left(\frac{\varepsilon}{\varepsilon\zeta+1} - \frac{2KM_\infty}{1+KM}\frac{\mathrm{d}\varphi}{\mathrm{d}\zeta}\right)\frac{\mathrm{d}\overline{p'_{t_{in_n}}}}{\mathrm{d}\zeta}\\ &+\varepsilon^2\left\{(k_0a_0)^2\left[(1+KM)^2-K^2\right] - \frac{n^2}{(\varepsilon\zeta+1)^2}\right\}\overline{p'_{t_{in_n}}} = 0,\end{aligned} \tag{3.136}$$

where $K = k_z/k_0$. The boundary condition at the fuselage surface is a rigid hard-wall boundary condition as before, which means

$$\frac{\mathrm{d}\overline{p'_{t_{in_n}}}}{\mathrm{d}\zeta} = 0 \ \text{ at } \ \zeta = 0, \tag{3.137}$$

because $\bar{r} = a_0 \Rightarrow \zeta = 0$ by definition. Also, the Mach number profile inside the linear boundary layer is defined as

$$M = M_\infty \varphi(\zeta) = M_\infty \left(\zeta \frac{M_\infty - M_w}{M_\infty} + \frac{M_w}{M_\infty} \right). \tag{3.138}$$

3.3.1.1 Power Series Solution

Following Eversman and Beckemeyer (1972), eq.(3.136) can be solved using a power series solution in ε of the form,

$$\overline{p'_{t_{in_n}}}(\zeta) = \overline{p'_0}(\zeta) + \varepsilon \overline{p'_1}(\zeta) + \varepsilon^2 \overline{p'_2}(\zeta) + \varepsilon^3 \overline{p'_3}(\zeta) + \dots. \tag{3.139}$$

Note that for convenience and brevity the arguments k_z and t are omitted from the Fourier-transformed pressure $\overline{p'_{t_{in_n}}}$. Before moving any further it is important to highlight the fact that this is a power series solution, which means that it is valid for sufficiently thin boundary layers. This fact is also investigated by Eversman (1972), who concluded that the solution is indeed valid for fairly thick boundary layers but its use there should be avoided. The validity bounds of the proposed solution will be thoroughly investigated in later chapters of this thesis.

The next step is to substitute the power series solution in eq.(3.139) into eqs. (3.136) and (3.137). By doing so and equating the terms that are of the same order of ε from the left hand side with the same order from the right hand side, differential equations and their respective boundary conditions can be obtained for each of the terms in the power series.

Zeroth order term:

$$\frac{\mathrm{d}^2 \overline{p'_0}}{\mathrm{d}\zeta^2} - \frac{2KM_\infty}{1 + KM_\infty \varphi} \frac{\mathrm{d}\varphi}{\mathrm{d}\zeta} \frac{\mathrm{d}\overline{p'_0}}{\mathrm{d}\zeta} = 0, \tag{3.140}$$

$$\frac{\mathrm{d}\overline{p'_0}}{\mathrm{d}\zeta}(\zeta = 0) = 0. \tag{3.141}$$

For the first order term

$$2\zeta \frac{\mathrm{d}^2 \overline{p'_0}}{\mathrm{d}\zeta^2} + \frac{\mathrm{d}^2 \overline{p'_1}}{\mathrm{d}\zeta^2} + \frac{\mathrm{d}\overline{p'_0}}{\mathrm{d}\zeta} - \frac{4\zeta KM_\infty}{1 + KM_\infty \varphi} \frac{\mathrm{d}\varphi}{\mathrm{d}\zeta} \frac{\mathrm{d}\overline{p'_0}}{\mathrm{d}\zeta} - \frac{2KM_\infty}{1 + KM_\infty \varphi} \frac{\mathrm{d}\varphi}{\mathrm{d}\zeta} \frac{\mathrm{d}\overline{p'_1}}{\mathrm{d}\zeta} = 0, \tag{3.142}$$

which, by using eq.(3.140), will become

$$\frac{\mathrm{d}^2 \overline{p'_1}}{\mathrm{d}\zeta^2} - \frac{2KM_\infty}{1 + KM_\infty \varphi} \frac{\mathrm{d}\varphi}{\mathrm{d}\zeta} \frac{\mathrm{d}\overline{p'_1}}{\mathrm{d}\zeta} = -\frac{\mathrm{d}\overline{p'_0}}{\mathrm{d}\zeta}, \tag{3.143}$$

$$\frac{\mathrm{d}\overline{p'_1}}{\mathrm{d}\zeta}(\zeta = 0) = 0. \tag{3.144}$$

For the second order term

$$\begin{aligned}&\zeta^2\frac{\mathrm{d}^2\overline{p_0'}}{\mathrm{d}\zeta^2}+2\zeta\frac{\mathrm{d}^2\overline{p_1'}}{\mathrm{d}\zeta^2}+\frac{\mathrm{d}^2\overline{p_2'}}{\mathrm{d}\zeta^2}+\zeta\frac{\mathrm{d}\overline{p_0'}}{\mathrm{d}\zeta}+\frac{\mathrm{d}\overline{p_1'}}{\mathrm{d}\zeta}\\&-\frac{\zeta^2 2KM_\infty}{1+KM_\infty\varphi}\frac{\mathrm{d}\varphi}{\mathrm{d}\zeta}\frac{\mathrm{d}\overline{p_0'}}{\mathrm{d}\zeta}-\frac{4\zeta KM_\infty}{1+KM_\infty\varphi}\frac{\mathrm{d}\varphi}{\mathrm{d}\zeta}\frac{\mathrm{d}\overline{p_1'}}{\mathrm{d}\zeta}-\frac{2KM_\infty}{1+KM_\infty\varphi}\frac{\mathrm{d}\varphi}{\mathrm{d}\zeta}\frac{\mathrm{d}\overline{p_2'}}{\mathrm{d}\zeta}\\&+X\overline{p_0'}-n^2\overline{p_0'}=0,\end{aligned}\tag{3.145}$$

which, by using eqs. (3.140) and (3.143), will become

$$\frac{\mathrm{d}^2\overline{p_2'}}{\mathrm{d}\zeta^2}-\frac{2KM_\infty}{1+KM_\infty\varphi}\frac{\mathrm{d}\varphi}{\mathrm{d}\zeta}\frac{\mathrm{d}\overline{p_2'}}{\mathrm{d}\zeta}=-\frac{\mathrm{d}\overline{p_1'}}{\mathrm{d}\zeta}+\zeta\frac{\mathrm{d}\overline{p_0'}}{\mathrm{d}\zeta}-X\overline{p_0'}+n^2\overline{p_0'},\quad X=(k_0a_0)^2\Big[(1+KM_\infty\varphi)^2-K^2\Big],\tag{3.146}$$

$$\frac{\mathrm{d}\overline{p_2'}}{\mathrm{d}\zeta}(\zeta=0)=0.\tag{3.147}$$

For the third order term

$$\begin{aligned}&\zeta^2\frac{\mathrm{d}^2\overline{p_1'}}{\mathrm{d}\zeta^2}+2\zeta\frac{\mathrm{d}^2\overline{p_2'}}{\mathrm{d}\zeta^2}+\frac{\mathrm{d}^2\overline{p_3'}}{\mathrm{d}\zeta^2}+\zeta\frac{\mathrm{d}\overline{p_1'}}{\mathrm{d}\zeta}+\frac{\mathrm{d}\overline{p_2'}}{\mathrm{d}\zeta}\\&-\frac{\zeta^2 2KM_\infty}{1+KM_\infty\varphi}\frac{\mathrm{d}\varphi}{\mathrm{d}\zeta}\frac{\mathrm{d}\overline{p_1'}}{\mathrm{d}\zeta}-\frac{4\zeta KM_\infty}{1+KM_\infty\varphi}\frac{\mathrm{d}\varphi}{\mathrm{d}\zeta}\frac{\mathrm{d}\overline{p_2'}}{\mathrm{d}\zeta}-\frac{2KM_\infty}{1+KM_\infty\varphi}\frac{\mathrm{d}\varphi}{\mathrm{d}\zeta}\frac{\mathrm{d}\overline{p_3'}}{\mathrm{d}\zeta}\\&+2\zeta X\overline{p_0'}+X\overline{p_1'}-n^2\overline{p_1'}=0,\end{aligned}\tag{3.148}$$

which, by using eqs. (3.143) and (3.146), will become

$$\frac{\mathrm{d}^2\overline{p_3'}}{\mathrm{d}\zeta^2}-\frac{2KM_\infty}{1+KM_\infty\varphi}\frac{\mathrm{d}\varphi}{\mathrm{d}\zeta}\frac{\mathrm{d}\overline{p_3'}}{\mathrm{d}\zeta}=-\frac{\mathrm{d}\overline{p_2'}}{\mathrm{d}\zeta}+\zeta\frac{\mathrm{d}\overline{p_1'}}{\mathrm{d}\zeta}-\zeta^2\frac{\mathrm{d}\overline{p_0'}}{\mathrm{d}\zeta}-X\overline{p_1'}+n^2\overline{p_1'}-2\zeta n^2\overline{p_0'},\tag{3.149}$$

$$\frac{\mathrm{d}\overline{p_3'}}{\mathrm{d}\zeta}(\zeta=0)=0.\tag{3.150}$$

As per Eversman and Beckemeyer (1972), by arbitrarily specifying the pressure at the wall, for the zeroth term,

$$\overline{p_0'}(\zeta=0)=\overline{p'_{t_{in_n}}}(0),\tag{3.151}$$

then the rest of the higher-order terms

$$\begin{aligned}&\overline{p_1'}(\zeta=0)=0,\\&\overline{p_2'}(\zeta=0)=0\quad\text{etc.}\end{aligned}\tag{3.152}$$

Equations (3.140)-(3.150) are second order differential equations that can be solved by reducing them to first order differential equations. By doing so the method of separation of variables can be used along with the integrating factor method in order to yield expressions for the pressure terms in the power series of eq.(3.139). Equation (3.140) is solved by setting $\frac{\mathrm{d}\overline{p_0'}}{\mathrm{d}\zeta}=q$. By doing so, the equation is transformed into a first order differential equation,

$$\frac{\mathrm{d}q}{\mathrm{d}\zeta}-\frac{2KM_\infty}{1+KM_\infty\varphi}\frac{\mathrm{d}\varphi}{\mathrm{d}\zeta}q=0.\tag{3.153}$$

By separating the variables, this leads to

$$q = c(1 + KM_\infty\varphi)^2 \Rightarrow \frac{\mathrm{d}\overline{p_0'}}{\mathrm{d}\zeta} = c(1 + KM_\infty\varphi)^2, \tag{3.154}$$

where c is the integrating constant. This simple differential equation is easily solved by using the boundary condition in eq.(3.141)

$$\frac{\mathrm{d}\overline{p_0'}}{\mathrm{d}\zeta}(\zeta = 0) = 0 \Rightarrow c(1 + KM_\infty\varphi(0))^2 = 0 \Rightarrow c(1 + KM_w)^2 = 0. \tag{3.155}$$

It immediately follows that either $c = 0$ or $k_z = -\frac{k_0}{M_w}$. The solution $k_z = -\frac{k_0}{M_w}$ represents a special case where the critical layer occurs at the wall. This special solution will not be investigated here. The more general solution is $c = 0$, which gives the solution for the zeroth order term of the power series, because if $c = 0$ then it follows from eq.(3.154),

$$\begin{aligned} \frac{\mathrm{d}\overline{p_0'}}{\mathrm{d}\zeta} = 0 \qquad &\Rightarrow \qquad \overline{p_0'}(\zeta) = \text{constant}, \\ &\Rightarrow \qquad \overline{p_0'}(\zeta) = \overline{p_{t_{in_n}}'}(0). \end{aligned} \tag{3.156}$$

where $\overline{p_{t_{in_n}}'}(0)$ is the arbitrarily specified pressure at the fuselage wall $\overline{p_{t_{in}}'}(\zeta = 0)$ as in eq.(3.151).

Equation (3.143) is solved the same way, by setting $\frac{\mathrm{d}\overline{p_1'}}{\mathrm{d}\zeta} = q$. Also, by using eq.(3.156), eq.(3.143) is transformed into

$$\frac{\mathrm{d}q}{\mathrm{d}\zeta} - \frac{2KM_\infty}{1 + KM_\infty\varphi}\frac{\mathrm{d}\varphi}{\mathrm{d}\zeta}q = 0, \tag{3.157}$$

which is the same as eq.(3.153). Also, since the boundary condition in eq.(3.144) is the same as in the zeroth order term case (eq.(3.141)), it follows that the first order term will have the same solution as the zeroth order term in eq.(3.156),

$$\begin{aligned} \frac{\mathrm{d}\overline{p_1'}}{\mathrm{d}\zeta} = 0 \qquad &\Rightarrow \qquad \overline{p_1'}(\zeta) = \text{constant}, \\ &\Rightarrow \qquad \overline{p_1'}(\zeta) = \overline{p_1'}(\zeta = 0) = 0. \end{aligned} \tag{3.158}$$

Moving on to the solution for the second order term. This is eq.(3.146) and once again it is solved by setting $\frac{\mathrm{d}\overline{p_2'}}{\mathrm{d}\zeta} = q$. Also following from the solutions of the zeroth and first terms, eqs. (3.156) and (3.158) respectively, eq.(3.146) is transformed into

$$\frac{\mathrm{d}q}{\mathrm{d}\zeta} - \frac{2KM_\infty}{1 + KM_\infty\varphi}\frac{\mathrm{d}\varphi}{\mathrm{d}\zeta}q = -X\overline{p_{t_{in_n}}'}(0) + n^2\overline{p_{t_{in_n}}'}(0), \tag{3.159}$$

which becomes

$$\frac{\mathrm{d}q}{\mathrm{d}\zeta} - \frac{2KM_\infty}{1 + KM_\infty\varphi}\frac{\mathrm{d}\varphi}{\mathrm{d}\zeta}q = \left[\mu - \nu(1 + KM_\infty\varphi)^2\right]\overline{p_{t_{in_n}}'}(0), \tag{3.160}$$

where

$$\nu = (k_0a_0)^2 \quad \text{and} \quad \mu = (k_0a_0)^2K^2 + n^2. \tag{3.161}$$

Equation (3.160) can be solved with the method of the integrating factor. Let the integrating factor be

$$u(\zeta) = (1 + KM_\infty\varphi)^{-2}. \tag{3.162}$$

So the solution to eq.(3.160), according to the integrating factor method, will be

$$q = \frac{\int u(\zeta)\left[\mu - \nu(1 + KM_\infty\varphi)^2\right]\overline{p'_{t_{in}}}(0)\mathrm{d}\zeta + c}{u(\zeta)}, \tag{3.163}$$

where c is the integrating constant. By using a dummy variable,

$$\frac{\mathrm{d}\overline{p'_2}}{\mathrm{d}\zeta} = \mu\overline{p'_{t_{in}}}(0)(1 + KM_\infty\varphi)^2\int_0^\zeta \frac{\mathrm{d}\eta}{(1 + KM_\infty\varphi(\eta))^2} - \nu\overline{p'_{t_{in_n}}}(0)\zeta(1 + KM_\infty\varphi)^2 + c(1 + KM_\infty\varphi)^2. \tag{3.164}$$

Once again, this simple differential equation can be solved by utilising the boundary condition in eq.(3.147). Indeed by setting $\zeta = 0$ in eq.(3.164) yields

$$c(1 + KM_w)^2 = 0, \tag{3.165}$$

and as before the general solution $c = 0$ is chosen. With c known, an expression for $\frac{\mathrm{d}\overline{p'_2}}{\mathrm{d}\zeta}$ can be recovered from eq.(3.164) and by integrating an expression for $\overline{p'_2}$ can also be recovered,

$$\frac{\mathrm{d}\overline{p'_2}}{\mathrm{d}\zeta} = \overline{p'_{t_{in_n}}}(0)(1 + KM_\infty\varphi)^2\left[\mu\int_0^\zeta \frac{\mathrm{d}\eta}{(1 + KM_\infty\varphi(\eta))^2} - \nu\zeta\right], \tag{3.166}$$

$$\Rightarrow \quad \overline{p'_2}(\zeta) = \overline{p'_{t_{in_n}}}(0)\int_0^\zeta\left\{(1 + KM_\infty\varphi(\sigma))^2\left[\mu\int_0^\sigma \frac{\mathrm{d}\eta}{(1 + KM_\infty\varphi(\eta))^2} - \nu\sigma\right]\right\}\mathrm{d}\sigma \tag{3.167}$$

The same process is followed for the third order term. By integrating using the integrating factor method, the solution for the third order term is recovered,

$$\frac{\mathrm{d}\overline{p'_3}}{\mathrm{d}\zeta} = -\overline{p'_{t_{in_n}}}(0)(1 + KM_\infty\varphi)^2\Big\{\int_0^\zeta\left[\mu\int_0^\xi \frac{\mathrm{d}\eta}{(1 + KM_\infty\varphi(\eta))^2} - \nu\xi\right]\mathrm{d}\xi + 2\int_0^\zeta \frac{mn^2}{(1 + KM_\infty\varphi(m))^2}\mathrm{d}m\Big\}, \tag{3.168}$$

$$\Rightarrow \quad \overline{p'_3}(\zeta) = -\overline{p'_{t_{in_n}}}(0)\int_0^\zeta(1 + KM_\infty\varphi(\sigma))^2\Big\{\int_0^\sigma\left[\mu\int_0^\xi \frac{\mathrm{d}\eta}{(1 + KM_\infty\varphi(\eta))^2} - \nu\xi\right]\mathrm{d}\xi + 2\int_0^\sigma \frac{mn^2}{(1 + KM_\infty\varphi(m))^2}\mathrm{d}m\Big\}\mathrm{d}\sigma. \tag{3.169}$$

3.3.1.2 Total Field

With these terms known, the power series expression can be evaluated that describes the total field inside the boundary layer. For the pressure, up to the second order terms are retained in order to have an error of $O(\varepsilon^3)$,

$$\overline{p'_{t_{in_n}}}(\zeta) = \overline{p'_0}(\zeta) + \varepsilon\overline{p'_1}(\zeta) + \varepsilon^2\overline{p'_2}(\zeta). \tag{3.170}$$

Substituting eqs. (3.156), (3.158) and (3.167) into eq. (3.170) gives

$$\overline{p'_{t_{in_n}}}(\zeta) = \overline{p'_{t_{in_n}}}(0)\left\{1 + \varepsilon^2 \int_0^\zeta \left[(1 + KM_\infty\varphi(\sigma))^2\left[\mu \int_0^\sigma \frac{\mathrm{d}\eta}{(1 + KM_\infty\varphi(\eta))^2} - \nu\sigma\right]\right]\mathrm{d}\sigma\right\}. \quad (3.171)$$

In order to retain comparative relative error, following Eversman and Beckemeyer (1972), the expression for the pressure derivative is carried to within an error of $O(\varepsilon^4)$,

$$\frac{\mathrm{d}\overline{p'_{t_{in_n}}}}{\mathrm{d}\zeta}(\zeta) = \frac{\mathrm{d}\overline{p'_0}}{\mathrm{d}\zeta}(\zeta) + \varepsilon\frac{\mathrm{d}\overline{p'_1}}{\mathrm{d}\zeta}(\zeta) + \varepsilon^2\frac{\mathrm{d}\overline{p'_2}}{\mathrm{d}\zeta}(\zeta) + \varepsilon^3\frac{\mathrm{d}\overline{p'_3}}{\mathrm{d}\zeta}(\zeta). \quad (3.172)$$

Substituting the terms from eqs. (3.156), (3.158), (3.166) and (3.168) into eq. (3.172) gives,

$$\begin{aligned}\frac{\mathrm{d}\overline{p'_{t_{in_n}}}}{\mathrm{d}\zeta}(\zeta) =& \varepsilon^2\overline{p'_{t_{in_n}}}(0)(1 + KM_\infty\varphi)^2\left\{\left[\mu\int_0^\zeta \frac{\mathrm{d}\eta}{(1 + KM_\infty\varphi(\eta))^2} - \nu\zeta\right]\right. \\ &\left. - \varepsilon\left[\int_0^\zeta\left[\mu\int_0^\xi \frac{\mathrm{d}\eta}{(1 + KM_\infty\varphi(\eta))^2} - \nu\xi\right]\mathrm{d}\xi + 2n^2\int_0^\zeta \frac{m}{(1 + KM_\infty\varphi(m))^2}\mathrm{d}m\right]\right\}.\end{aligned} \quad (3.173)$$

The integrals in eqs. (3.171) and (3.173) need to be evaluated in order to obtain expressions for the pressure and its derivative as a function of ζ.

Before the integrals are evaluated, the following quantities are introduced to facilitate the integrations and also for brevity. These quantities are

$$s = K(M_\infty - M_w), \quad (3.174)$$

and

$$g = K(M_\infty - M_w)(1 + KM_w) = s(1 + KM_w). \quad (3.175)$$

This will transform the term $(1 + KM_\infty\varphi)^2$ into

$$(1 + KM_\infty\varphi)^2 = (1 + K\zeta(M_\infty - M_w) + KM_w)^2 = (g/s + \zeta s)^2. \quad (3.176)$$

Then solving the integrals in eq.(3.171) leads to the power series Fourier-transformed pressure as a function of ζ to within an error of $O(\varepsilon^3)$,

$$\overline{p'_{t_{in_n}}}(\zeta) = \overline{p'_{t_{in_n}}}(0)\left\{1 + \varepsilon^2\left[-\nu s^2\frac{\zeta^4}{4} + \frac{\zeta^3}{3}\left(\frac{s^2\mu}{g} - 2\nu g\right) + \frac{\zeta^2}{2}\left(\mu - \nu\frac{g^2}{s^2}\right)\right]\right\}. \quad (3.177)$$

Additionally, solving the integrals in eq.(3.173) leads to the power series Fourier-transformed pressure derivative as a function of ζ to within an error of $O(\varepsilon^4)$,

$$\begin{aligned}\frac{\mathrm{d}\overline{p'_{t_{in_n}}}}{\mathrm{d}\zeta}(\zeta) = \varepsilon^2\overline{p'_{t_{in_n}}}(0)\Bigg\{&-\nu s^2\zeta^3 + \zeta^2(\mu\frac{s^2}{g} - 2\nu g) + \zeta(\mu - \nu g^2/s^2)\\ &-\varepsilon\Bigg[(2n^2-\mu)\Big[(\zeta + g/s^2)^2\ln\Big(\frac{s^2\zeta}{g}+1\Big) - \zeta\frac{g}{s^2}\Big]\\ &-\nu s^2\frac{\zeta^4}{2} + \zeta^3(\mu\frac{s^2}{g} - \nu g) - \zeta^2\Big[2(n^2-\mu) + \frac{\nu}{2}\frac{g^2}{s^2}\Big]\Bigg]\Bigg\}.\end{aligned} \tag{3.178}$$

3.3.2 Matching of the Two Solutions

In order to match the two solutions at the edge of the boundary layer, $\bar{r} = a_0 + \delta_L$ or equivalently $\zeta = 1$, the pressure and its derivative at that point must be known. Therefore, $\overline{p'_{t_{in_n}}}$ and $\frac{\mathrm{d}\overline{p'_{t_{in_n}}}}{\mathrm{d}\bar{r}}$ in eqs. (3.177) and (3.178) are evaluated at $\zeta = 1$.

$$\overline{p'_{t_{in_n}}}(\zeta = 1, k_z, t) = \overline{p'_{t_{in_n}}}(0)\Bigg\{1 + \varepsilon^2\Bigg[\mu\Big(\frac{s^2}{3g} + \frac{1}{2}\Big) - \nu\Big(\frac{s^2}{4} + \frac{2}{3}g + \frac{1}{2}\frac{g^2}{s^2}\Big)\Bigg]\Bigg\}\mathrm{e}^{\mathrm{i}\omega_0 t}. \tag{3.179}$$

$$\begin{aligned}\frac{\mathrm{d}\overline{p'_{t_{in_n}}}}{\mathrm{d}\bar{r}}(\zeta = 1, k_z, t) = &\frac{\varepsilon}{a_0}\overline{p'_{t_{in_n}}}(0)(1 + KM_\infty)^2\Bigg\{\mu\Big(\frac{1}{g} - \frac{1}{(s^2+g)}\Big) - \nu\\ &-\varepsilon\Bigg[\frac{(2n^2-\mu)}{s^2}\ln\Big(\frac{s^2+g}{g}\Big) - \frac{2n^2}{s^2+g} + \frac{\mu}{g} - \frac{\nu}{2}\Bigg]\Bigg\}\mathrm{e}^{\mathrm{i}\omega_0 t}.\end{aligned} \tag{3.180}$$

Outside the boundary layer the mean flow is uniform and thus the total field can be expressed in terms of an incident and scattered field derived previously in section 3.1. The Fourier-transformed incident field is given in eq.(3.25)

$$\overline{p'_{i\infty_n}}(\bar{r}, k_z, t) \;=\; E_n(k_z, \omega_0)\mathrm{J}_n(\Gamma_\infty\bar{r})\,\mathrm{e}^{\mathrm{i}\omega_0 t}, \tag{3.181}$$

where

$$E_n(k_z, \omega_0) = \pi^2\xi_{lq}P_{lq}(-1)^{l+n}(k_0 + k_z M_\infty)\,\Psi_{lq}\,\mathrm{e}^{-\mathrm{i}(l-n)\beta}\,\mathrm{H}^{(2)}_{l-n}(\Gamma_\infty b). \tag{3.182}$$

Also, according to the uniform flow theory (see section 3.1), the Fourier-transformed scattered field will be in terms of a Hankel function, because outward propagating cylindrical waves are required,

$$\overline{p'_{s\infty_n}}(\bar{r}, k_z, t) \;=\; \frac{1}{2\pi}C^L_n(k_z, \omega_0)\mathrm{H}^{(2)}_n(\Gamma_\infty\bar{r})\,\mathrm{e}^{\mathrm{i}\omega_0 t}, \tag{3.183}$$

where Γ_∞ exhibits the behaviour outlined in section 3.2. Inside the boundary layer, the Fourier transformed total field is described in eqs. (3.177) and (3.178). The matching of the two solutions is essential in order to determine the two unknowns of the problem, namely the Fourier-transformed pressure at the fuselage wall $\overline{p'_{t_{in_n}}}(0)$ in eqs. (3.177) and (3.178), and the coefficient $C^L_n(k_z, \omega_0)$ in eq.(3.183). The evaluation of $\overline{p'_{t_{in_n}}}(0)$ is one of the key results of the analysis in this section since it specifies the pressure at the wall which is practically the most important part of the near-field solution.

The matching is performed by using two boundary conditions at the edge of the boundary layer, $\bar{r} = a_0 + \delta_L$ or equivalently $\zeta = 1$. The pressure continuity condition,

$$\overline{p'_{t_{in_n}}}(\zeta = 1) = \overline{p'_{t\infty_n}}(\bar{r} = a_0 + \delta_L), \tag{3.184}$$

and the particle displacement continuity condition, as previously in section 3.2. After all, this is the nominal continuity condition as explained in Hanson (1984). However, in the linear profile case this reduces to a pressure gradient continuity condition. This is evident from eqs. (3.87) through (3.89), where in the linear profile case the internal Mach number is the same as the external Mach number at the edge of the boundary layer ($M_0 = M_\infty$). Therefore, the continuity condition reduces to

$$\frac{\mathrm{d}\overline{p'_{t_{in_n}}}}{\mathrm{d}\bar{r}}(\zeta = 1) = \frac{\mathrm{d}\overline{p'_{t\infty_n}}}{\mathrm{d}\bar{r}}(\bar{r} = a_0 + \delta_L). \tag{3.185}$$

Since the total Fourier-transformed field outside the layer is the sum of the incident and the scattered field, the pressure continuity condition is expressed as

$$\overline{p'_{t_{in_n}}}(\zeta = 1) = \overline{p'_{i\infty_n}}(\bar{r} = a_0 + \delta_L) + \overline{p'_{s\infty_n}}(\bar{r} = a_0 + \delta_L), \tag{3.186}$$

and by substituting eqs. (3.179), (3.181) and (3.183) into eq.(3.186),

$$\begin{aligned}&\overline{p'_{t_{in_n}}}(0)\left\{1 + \varepsilon^2\left[\mu\left(\frac{s^2}{3g} + \frac{1}{2}\right) - \nu\left(\frac{s^2}{4} + \frac{2}{3}g + \frac{1}{2}\frac{g^2}{s^2}\right)\right]\right\} \\ &= E_n(k_z, \omega_0)\mathrm{J}_n\left(\Gamma_\infty(a_0 + \delta_L)\right) + \frac{1}{2\pi}C_n^L(k_z, \omega_0)\mathrm{H}_n^{(2)}\left(\Gamma_\infty(a_0 + \delta_L)\right).\end{aligned} \tag{3.187}$$

The same procedure is followed for the pressure gradient continuity condition,

$$\frac{\mathrm{d}\overline{p'_{t_{in_n}}}}{\mathrm{d}\bar{r}}(\zeta = 1) = \frac{\mathrm{d}\overline{p'_{i\infty_n}}}{\mathrm{d}\bar{r}}(\bar{r} = a_0 + \delta_L) + \frac{\mathrm{d}\overline{p'_{s\infty_n}}}{\mathrm{d}\bar{r}}(\bar{r} = a_0 + \delta_L), \tag{3.188}$$

and substituting eq.(3.180), (3.181) and (3.183) into eq.(3.188),

$$\begin{aligned}&\frac{\varepsilon}{a_0}\overline{p'_{t_{in_n}}}(0)(1 + KM_\infty)^2\left\{\mu\left(\frac{1}{g} - \frac{1}{(s^2 + g)}\right) - \nu - \varepsilon\left[\frac{(2n^2 - \mu)}{s^2}\ln\left(\frac{s^2 + g}{g}\right) - \frac{2n^2}{s^2 + g} + \frac{\mu}{g} - \frac{\nu}{2}\right]\right\} \\ &= E_n(k_z, \omega_0)\Gamma_\infty\mathrm{J}'_n\left(\Gamma_\infty(a_0 + \delta_L)\right) + \frac{1}{2\pi}C_n^L(k_z, \omega_0)\Gamma_\infty\mathrm{H}_n^{(2)\prime}\left(\Gamma_\infty(a_0 + \delta_L)\right),\end{aligned} \tag{3.189}$$

Using eqs. (3.187) and (3.189), solving for $\overline{p'_{t_{in_n}}}(0)$ and $C_n^L(k_z, \omega_0)$ leads to

$$\begin{aligned}\overline{p'_{t_{in_n}}}(0) = \frac{E_n(k_z, \omega_0)}{G}\Bigg[&\mathrm{J}_n\left(\Gamma_\infty(a_0 + \delta_L)\right) \\ &+ \frac{\left[\mathrm{J}'_n\left(\Gamma_\infty(a_0 + \delta_L)\right) - \frac{R}{G}\frac{\varepsilon}{\Gamma_\infty a_0}(1 + KM_\infty)^2\mathrm{J}_n\left(\Gamma_\infty(a_0 + \delta_L)\right)\right]}{\left[\frac{R}{G}\frac{\varepsilon}{\Gamma_\infty a_0}(1 + KM_\infty)^2\mathrm{H}_n^{(2)}\left(\Gamma_\infty(a_0 + \delta_L)\right) - \mathrm{H}_n^{(2)\prime}\left(\Gamma_\infty(a_0 + \delta_L)\right)\right]}\mathrm{H}_n^{(2)}\left(\Gamma_\infty(a_0 + \delta_L)\right)\Bigg],\end{aligned} \tag{3.190}$$

where

$$G = \left\{1 + \varepsilon^2 \left[\mu\left(\frac{s^2}{3g} + \frac{1}{2}\right) - \nu\left(\frac{s^2}{4} + \frac{2}{3}g + \frac{1}{2}\frac{g^2}{s^2}\right)\right]\right\}, \tag{3.191}$$

and

$$R = \left\{\mu\left(\frac{1}{g} - \frac{1}{(s^2+g)}\right) - \nu - \varepsilon\left[\frac{(2n^2-\mu)}{s^2}\ln\left(\frac{s^2+g}{g}\right) - \frac{2n^2}{s^2+g} + \frac{\mu}{g} - \frac{\nu}{2}\right]\right\}. \tag{3.192}$$

The evaluation of $\overline{p'_{t_{in_n}}}(0)$ is a key result of this part of the work, since it represents the Fourier-transformed pressure on the surface of the fuselage. However, it is important to mention the other quantities that can be determined. The Fourier-transformed scattered field is essential for the evaluation of the far-field case. The coefficient $C_n^L(k_z, \omega_0)$ is

$$C_n^L(k_z,\omega_0) = \frac{2\pi E_n(k_z,\omega_0)\left[\mathrm{J}'_n\left(\Gamma_\infty(a_0+\delta_L)\right) - \frac{R}{G}\frac{\varepsilon}{\Gamma_\infty a_0}(1+KM_\infty)^2\mathrm{J}_n\left(\Gamma_\infty(a_0+\delta_L)\right)\right]}{\left[\frac{R}{G}\frac{\varepsilon}{\Gamma_\infty a_0}(1+KM_\infty)^2\mathrm{H}_n^{(2)}\left(\Gamma_\infty(a_0+\delta_L)\right) - \mathrm{H}_n^{(2)\prime}\left(\Gamma_\infty(a_0+\delta_L)\right)\right]}. \tag{3.193}$$

Thus, the Fourier-transformed scattered field is given from eq.(3.183) upon substituting $C_n^L(k_z, \omega_0)$ with its expression from eq.(3.193),

$$\overline{p'_{s_{\infty_n}}}(\bar{r}, k_z, t) = \frac{E_n(k_z,\omega_0)\left[\mathrm{J}'_n\left(\Gamma_\infty(a_0+\delta_L)\right) - \frac{R}{G}\frac{\varepsilon}{\Gamma_\infty a_0}(1+KM_\infty)^2\mathrm{J}_n\left(\Gamma_\infty(a_0+\delta_L)\right)\right]}{\left[\frac{R}{G}\frac{\varepsilon}{\Gamma_\infty a_0}(1+KM_\infty)^2\mathrm{H}_n^{(2)}\left(\Gamma_\infty(a_0+\delta_L)\right) - \mathrm{H}_n^{(2)\prime}\left(\Gamma_\infty(a_0+\delta_L)\right)\right]}\mathrm{H}_n^{(2)}\left(\Gamma_\infty\bar{r}\right)\mathrm{e}^{\mathrm{i}\omega_0 t}. \tag{3.194}$$

3.3.3 Near-Field Validation

Before moving on, an initial validation can be performed at this point by taking the limit as $\delta_L \to 0$ in eqs. (3.190) and (3.194). When the boundary layer vanishes then the expressions should reduce to the uniform flow expressions given by McAlpine et al. (2015) and outlined in section 3.1. Therefore, it is expected that when $\delta_L \to 0$, eq.(3.190) reduces to eq.(3.36). Also, eq.(3.194) will reduce to eq.(3.32) which is the scattered field for uniform flow.

Firstly, the bracketed terms G and R are evaluated in the limit as $\delta_L \to 0$. Considering that $\delta_L \to 0$ also means that $\varepsilon \to 0$, by definition

$$\lim_{\varepsilon\to 0} G = 1, \tag{3.195}$$

and

$$\lim_{\varepsilon\to 0} R = \left\{\mu\left(\frac{1}{g} - \frac{1}{(s^2+g)}\right) - \nu\right\}. \tag{3.196}$$

Therefore, when $\delta_L \to 0$ or $\varepsilon \to 0$, eq.(3.190) will become

$$\overline{p'_{t_{in_n}}}(\bar{r}=a_0,k_z) = E_n(k_z,\omega_0)\Bigg[\mathrm{J}_n\left(\Gamma_\infty a_0\right) + \frac{\left[\mathrm{J}'_n\left(\Gamma_\infty a_0\right) - \left(\mu\left(\frac{1}{g}-\frac{1}{(s^2+g)}\right)-\nu\right)\frac{0}{\Gamma_\infty a_0}(1+KM_\infty)^2\mathrm{J}_n\left(\Gamma_\infty a_0\right)\right]}{\left[\left(\mu\left(\frac{1}{g}-\frac{1}{(s^2+g)}\right)-\nu\right)\frac{0}{\Gamma_\infty a_0}(1+KM_\infty)^2\mathrm{H}_n^{(2)}\left(\Gamma_\infty a_0\right) - \mathrm{H}_n^{(2)\prime}\left(\Gamma_\infty a_0\right)\right]}\mathrm{H}_n^{(2)}\left(\Gamma_\infty a_0\right)\Bigg], \tag{3.197}$$

or

$$\overline{p'_{t_{in_n}}}(\bar{r}=a_0,k_z) = E_n(k_z,\omega_0)\left[\mathrm{J}_n\left(\Gamma_\infty a_0\right) + \frac{\mathrm{J}'_n\left(\Gamma_\infty a_0\right)}{-\mathrm{H}_n^{(2)\prime}\left(\Gamma_\infty a_0\right)}\mathrm{H}_n^{(2)}\left(\Gamma_\infty a_0\right)\right], \tag{3.198}$$

which becomes, by using the Wronskian formula $\mathrm{J}'_n(x)\,\mathrm{H}_n^{(2)}(x) - \mathrm{J}_n(x)\,\mathrm{H}_n^{(2)\prime}(x) = \mathrm{i}\left(\frac{2}{\pi x}\right)$,

$$\overline{p'_{t_{in_n}}}(\bar{r}=a_0,k_z) = E_n(k_z,\omega_0)\left[\frac{-\mathrm{i}2}{\pi\Gamma_\infty a_0\mathrm{H}_n^{(2)\prime}\left(\Gamma_\infty a_0\right)}\right], \tag{3.199}$$

which is the same as eq.(41) in McAlpine et al. (2015) or eq.(3.36) in section 3.1 of this thesis.

On the other hand, by taking eq.(3.194) when $\delta_L \to 0$ or $\varepsilon \to 0$,

$$\overline{p'_{s_{\infty_n}}}(\bar{r},k_z) = E_n(k_z,\omega_0) \times \frac{\left[\mathrm{J}'_n\left(\Gamma_\infty a_0\right) - \left(\mu\left(\frac{1}{g}-\frac{1}{(s^2+g)}\right)-\nu\right)\frac{0}{\Gamma_\infty a_0}(1+KM_\infty)^2\mathrm{J}_n\left(\Gamma_\infty a_0\right)\right]}{\left[\left(\mu\left(\frac{1}{g}-\frac{1}{(s^2+g)}\right)-\nu\right)\frac{0}{\Gamma_\infty a_0}(1+KM_\infty)^2\mathrm{H}_n^{(2)}\left(\Gamma_\infty a_0\right) - \mathrm{H}_n^{(2)\prime}\left(\Gamma_\infty a_0\right)\right]}\mathrm{H}_n^{(2)}\left(\Gamma_\infty \bar{r}\right), \tag{3.200}$$

or

$$\overline{p'_{s_{\infty_n}}}(\bar{r},k_z) = -E_n(k_z,\omega_0)\frac{\mathrm{J}'_n\left(\Gamma_\infty a_0\right)}{\mathrm{H}_n^{(2)\prime}\left(\Gamma_\infty a_0\right)}\mathrm{H}_n^{(2)}\left(\Gamma_\infty \bar{r}\right), \tag{3.201}$$

which is exactly the same as in eq.(36) in McAlpine et al. (2015) or eq.(3.32) in section 3.1 of this thesis.

3.3.4 Fuselage Surface Pressure

Equation (3.190) represents the Fourier-transformed pressure on the fuselage surface. In order to obtain the pressure in real space an inverse Fourier z-transform must be performed. The dependence on $\bar{\phi}$ is represented as always, in the form of a Fourier series. Thus, following from eq.(3.33), the pressure on the fuselage surface is

$$p'_{t_{in}}(a_0,\bar{\phi},\bar{z},t) = \frac{1}{(2\pi)^2}\sum_{n=-\infty}^{\infty}\int_{-\infty}^{\infty}\overline{p'_{t_{in_n}}}(a_0,k_z)\,\mathrm{e}^{-\mathrm{i}k_z\bar{z}}\,\mathrm{d}k_z\,\mathrm{e}^{-\mathrm{i}n\bar{\phi}}\,\mathrm{e}^{\mathrm{i}\omega_0 t}, \tag{3.202}$$

which becomes, using eq.(3.190),

$$p'_{t_{in}}(a_0,\bar{\phi},\bar{z},t) = \frac{1}{(2\pi)^2}\sum_{n=-\infty}^{\infty}\int_{-\infty}^{\infty} E_n(k_z,\omega_0)\left[\mathrm{J}_n\left(\Gamma_\infty(a_0+\delta_L)\right)\frac{1}{G}\right.$$
$$\left. + \frac{\left[\mathrm{J}'_n\left(\Gamma_\infty(a_0+\delta_L)\right) - \frac{R}{G}\frac{\varepsilon}{\Gamma_\infty a_0}(1+KM_\infty)^2\mathrm{J}_n\left(\Gamma_\infty(a_0+\delta_L)\right)\right]}{\left[\frac{R}{G}\frac{\varepsilon}{\Gamma_\infty a_0}(1+KM_\infty)^2\mathrm{H}_n^{(2)}\left(\Gamma_\infty(a_0+\delta_L)\right) - \mathrm{H}_n^{(2)\prime}\left(\Gamma_\infty(a_0+\delta_L)\right)\right]}\frac{\mathrm{H}_n^{(2)}\left(\Gamma_\infty(a_0+\delta_L)\right)}{G}\right] \quad (3.203)$$
$$\times\, \mathrm{e}^{-\mathrm{i}k_z\bar{z}}\,\mathrm{d}k_z\,\mathrm{e}^{-\mathrm{i}n\bar{\phi}}\,\mathrm{e}^{\mathrm{i}\omega_0 t}.$$

This can be written in compact form as

$$p'_{t_{in}}(a_0,\bar{\phi},\bar{z},t) = \frac{\xi_{lq}P_{lq}}{4}(-1)^l\mathrm{e}^{-\mathrm{i}l\beta}\sum_{n=-\infty}^{\infty}(-1)^n\mathrm{e}^{\mathrm{i}n\beta}I_n^{(lbl)}(a_0,\bar{z})\mathrm{e}^{-\mathrm{i}n\bar{\phi}}\,\mathrm{e}^{\mathrm{i}\omega_0 t}, \quad (3.204)$$

where

$$I_n^{(lbl)}(a_0,\bar{z}) = \int_{-\infty}^{\infty}(k_0+k_zM_\infty)\,\Psi_{lq}\,\mathrm{H}_{l-n}^{(2)}\left(\Gamma_\infty b\right)S_n(k_z,\omega_0)\mathrm{e}^{-\mathrm{i}k_z\bar{z}}\,\mathrm{d}k_z, \quad (3.205)$$

and

$$S_n(k_z,\omega_0) = \left[\mathrm{J}_n\left(\Gamma_\infty(a_0+\delta_L)\right)\frac{1}{G}\right.$$
$$\left. + \frac{\left[\mathrm{J}'_n\left(\Gamma_\infty(a_0+\delta_L)\right) - \frac{R}{G}\frac{\varepsilon}{\Gamma_\infty a_0}(1+KM_\infty)^2\mathrm{J}_n\left(\Gamma_\infty(a_0+\delta_L)\right)\right]}{\left[\frac{R}{G}\frac{\varepsilon}{\Gamma_\infty a_0}(1+KM_\infty)^2\mathrm{H}_n^{(2)}\left(\Gamma_\infty(a_0+\delta_L)\right) - \mathrm{H}_n^{(2)\prime}\left(\Gamma_\infty(a_0+\delta_L)\right)\right]}\frac{\mathrm{H}_n^{(2)}\left(\Gamma_\infty(a_0+\delta_L)\right)}{G}\right]. \quad (3.206)$$

The inverse Fourier z-transform integral in eq. (3.205) with the superscript (lbl) denoting *linear boundary layer* cannot be solved analytically, which means that a numerical integration routine is required to evaluate it. Equations (3.204) and (3.205) are the essential results of this section. It is important to note that the integrand contains certain singularity points along the k_z-axis, but all the singularities are integrable. Once again it is worth noting that eqs. (3.37), (3.101) and (3.204) are exactly the same apart from the integral, which contains the terms that differentiate each case from each other.

3.3.4.1 Critical Layer

Finally, it is important to note that the expressions derived here contain the logarithm term $\ln\left(\frac{s^2+g}{g}\right)$. This poses a potential issue, because the argument of the logarithm can become negative, in which case the logarithm would become imaginary.

The region where this happens coincides with the region where there is the critical layer. For the linear boundary layer the critical layer lies in the region $-k_0/M_w < k_z < -k_0/M_\infty$ as shown in Fig. (3.7). The critical layer is the point at which $k_0 + k_zM(\bar{r}_c) = 0$. At this point the Pridmore-Brown equation is no longer valid and thus cannot be used to describe the pressure field. Previous researchers (Hanson and Magliozzi (1985), McAninch (1983), Tam and Morris (1980), Brambley et al. (2012) Gaffney and McAlpine (2017), Lu (1990), Campos et al. (1999))

utilised a power series solution around the singularity in order to bridge it, namely a Frobenius solution.

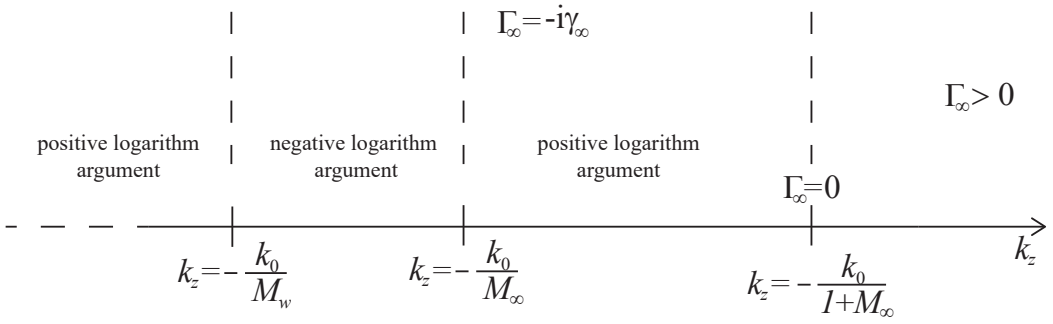

FIGURE 3.7: Critical layer along the k_z-axis.

However, according to Gaffney (2016) and Brambley et al. (2012) the critical layer region contributes very little to the integrand in eq.(3.205). That led to the conclusion that the inclusion of the critical layer region in the integration can be omitted without significant loss in the accuracy. Although the solution with the critical layer is in the scope of future investigation, the work presented here does not include it. In order to ensure that, the lower limit of the integral in eq.(3.205) is truncated before the critical layer region.

3.3.4.2 Special Case

As explained during the derivation process presented in section 3.3, the only requirement for the validity of the linear velocity profile method is that the boundary layer is sufficiently small compared to the fuselage radius. That requirement stems from the fact that a power series is utilised which involves ε which is the non-dimensional boundary-layer thickness. Therefore, as will be seen in later chapters, for the method to be practically valid one must ensure that the boundary layer is sufficiently thin.

It is important to note that this restriction applies only to the thickness of the boundary layer and not the velocity profile involved. That effectively means that the methodology and derivation process outlined in section 3.3 can be applied to any arbitrary velocity profile, always provided that the thickness is sufficiently small. In fact, this is pointed out by Eversman and Beckemeyer (1972) who suggested that any arbitrary velocity profile can be used, including a quarter-sine or 1/7th power-law profile. Indeed, the exact same methodology presented in section 3.3 can be applied to any arbitrary velocity profile, with the differences between the profiles expressed in the Mach distribution function $\varphi(\zeta)$ in eq.(3.138). The difference in function $\varphi(\zeta)$ will yield different results in the integrals of eqs. (3.171) and (3.173). However, up to that point of the analysis, the equations obtained will be the same regardless of the velocity profile used. Apart from the quarter-sine or 1/7th power-law profile

that could be used as suggested by Eversman and Beckemeyer (1972), any arbitrary profile is applicable, such as a polynomial profile (Pohlhausen solution) or a manufactured profile based on measurements. The difference in the analysis lies solely on the manipulation of the function $\varphi(\zeta)$, which depending on the profile adds to the complexity of the problem.

However, there is one special case of velocity profile that might present problems during the derivation of its analytical solution. Regardless of the velocity profile, the critical layer region will lie at the position shown in Fig. (3.7). Generally this position is in the region where the integrand becomes insignificant and can be omitted as explained in Gaffney (2016). However, in the case when there is separation in the flow, the Mach number distribution inside the detached boundary layer may involve negative values. An example of flow separation inside the boundary layer is shown in Fig. (3.8).

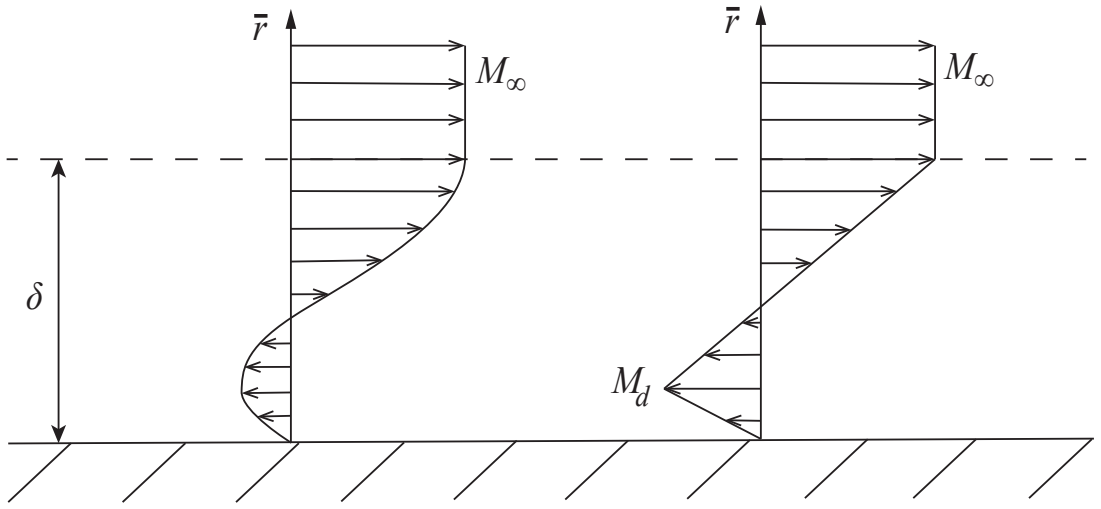

FIGURE 3.8: Flow separation inside the boundary layer. **[left]** Arbitrary profile, **[right]** simplified linear profile.

Let us consider the simplified linear case shown in Fig. (3.8). With the presence of the M_d value which is negative, the critical layer region shown in Fig. (3.7), which in normal cases would span from $-k_0/M_w$ to $-k_0/M_\infty$ (both of these values are in the negative k_z region far away from the region that contributes the most in the integration), now will occupy the region $-k_0/M_\infty < k_z < -k_0/M_d$ where $-k_0/M_d > 0$. This will inevitably shift the critical layer region to occupy a large part of the integration domain that contributes the most in the integration. The problem is shown in Fig. (3.9). In this case, it is no longer valid to omit the contribution of the critical layer to the integration and therefore it must be taken into account. The analysis that includes the critical layer is not in the scope of this thesis. Therefore, the analytical methods presented in this work should not be used to model the refraction effect of a boundary layer that undergoes flow separation.

3.3.5 Total Far-Field

In order to derive the far-field pressure expression when there is a linear boundary layer present, the same procedure is followed as in the step-function boundary layer case in section

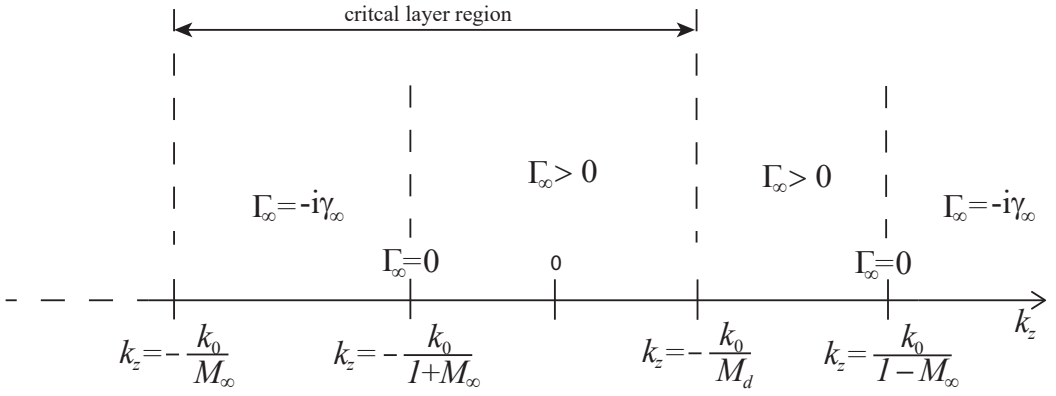

FIGURE 3.9: Critical layer along the k_z-axis when flow separation is present.

3.2.6. As in section 3.2.6, the correct expression for the incident field is required as given in eq.(3.24)

$$\overline{p'_{i\infty_n}}(\bar{r},k_z) = \pi^2 \xi_{lq} P_{lq}\, \mathrm{e}^{-\mathrm{i}(l-n)\beta}\,(k_0 + k_z M_\infty)\,\Psi_{lq}\,\mathrm{J}_{n-l}\,(\Gamma_\infty b)\,\mathrm{H}_n^{(2)}\,(\Gamma_\infty \bar{r}) \quad \text{for} \quad \bar{r} > b + a. \tag{3.207}$$

The Fourier-transformed scattered field outside the boundary layer (which is the scattered field that radiates towards the far-field) is given in eq.(3.194). Thus the total pressure in the far-field will be, as already mentioned in previous sections, the sum of the incident and the scattered field. Thus, the total Fourier transformed far-field pressure is

$$\overline{p'_{t_{nff}}}(\bar{r},k_z) = \overline{p'_{i\infty_n}}(\bar{r},k_z) + \overline{p'_{s\infty_n}}(\bar{r},k_z), \tag{3.208}$$

which, by substituting eqs. (3.24) and (3.194), leads to

$$\overline{p'_{t_{nff}}}(\bar{r},k_z) = F_n(k_z,\omega_0)\Bigg[\mathrm{J}_{n-l}\,(\Gamma_\infty b) + \mathrm{H}_{n-l}^{(2)}\,(\Gamma_\infty b)\frac{\left[\mathrm{J}'_n\,(\Gamma_\infty(a_0+\delta_L)) - \frac{R}{G}\frac{\varepsilon}{\Gamma_\infty a_0}(1+KM_\infty)^2\mathrm{J}_n\,(\Gamma_\infty(a_0+\delta_L))\right]}{\left[\frac{R}{G}\frac{\varepsilon}{\Gamma_\infty a_0}(1+KM_\infty)^2\mathrm{H}_n^{(2)}\,(\Gamma_\infty(a_0+\delta_L)) - \mathrm{H}_n^{(2)\prime}\,(\Gamma_\infty(a_0+\delta_L))\right]}\Bigg]\mathrm{H}_n^{(2)}\,(\Gamma_\infty \bar{r}), \tag{3.209}$$

where, as before,

$$F_n(k_z,\omega_0) = \pi^2 \xi_{lq} P_{lq}\,(k_0 + k_z M_\infty)\,\Psi_{lq}\,\mathrm{e}^{-\mathrm{i}(l-n)\beta}. \tag{3.210}$$

Following the same procedure as in the near-field case, an inverse Fourier z-transform must be performed in order to obtain the total field in real space, i.e.

$$p'_{t_{ff}}(\bar{r},\bar{\phi},\bar{z},t) \;=\; \frac{1}{(2\pi)^2}\sum_{n=-\infty}^{\infty}\int_{-\infty}^{\infty}\overline{p'_{t_{nff}}}(\bar{r},k_z)\,\mathrm{e}^{-\mathrm{i}k_z\bar{z}}\,\mathrm{d}k_z\,\mathrm{e}^{-\mathrm{i}n\bar{\phi}}\,\mathrm{e}^{\mathrm{i}\omega_0 t}. \tag{3.211}$$

As in the uniform flow case and the step-function boundary layer case, the integral

$$I_n \;=\; \frac{1}{2\pi}\int_{-\infty}^{\infty} \overline{p'_{t_{nff}}}\,(\bar{r},k_z)\,\mathrm{e}^{-\mathrm{i}k_z\bar{z}}\,\mathrm{d}k_z. \tag{3.212}$$

is in the appropriate form to be evaluated by the method of stationary phase as presented in appendix D. In fact the procedure is exactly the same, the only difference being the bracketed term in eq.(D.7) of appendix D is replaced with the bracketed term in eq.(3.209). The rest of the procedure is unchanged and presented in appendix F.

As in the step-function boundary layer case, in this section only the key results are shown:

$$p'_{t_{ff}}\,(\bar{R},\bar{\theta},\bar{\phi},t) = \frac{\mathrm{i}\tilde{\zeta}_{lq}P_{lq}k_0}{2\bar{R}}\frac{S(\bar{\theta})}{\Theta}\Psi_{lq}(\Delta_\infty)\mathrm{e}^{-\mathrm{i}k_0\bar{R}S(\bar{\theta})}\mathrm{e}^{\mathrm{i}\omega_0 t}\sum_{n=-\infty}^{\infty}\mathfrak{L}_n(\bar{\theta})\mathrm{e}^{-\mathrm{i}(l-n)\beta}\mathrm{e}^{\frac{1}{2}n\pi\mathrm{i}}\mathrm{e}^{-\mathrm{i}n\bar{\phi}}, \tag{3.213}$$

where

$$\mathfrak{L}_n(\bar{\theta}) = \left[\mathrm{J}_{n-l}\,(\Delta_\infty b)+\mathrm{H}^{(2)}_{n-l}\,(\Delta_\infty b)\frac{\left[\mathrm{J}'_n\,(\Delta_\infty(a_0+\delta_L))-\frac{R(\bar{\theta})}{G(\bar{\theta})}\frac{\varepsilon(\Theta^{1/2}+M_\infty C(\bar{\theta}))^2}{k_0a_0\sin\bar{\theta}\Theta^{1/2}}\mathrm{J}_n\,(\Delta_\infty(a_0+\delta_L))\right]}{\left[\frac{R(\bar{\theta})}{G(\bar{\theta})}\frac{\varepsilon(\Theta^{1/2}+M_\infty C(\bar{\theta}))^2}{k_0a_0\sin\bar{\theta}\Theta^{1/2}}\mathrm{H}^{(2)}_n\,(\Delta_\infty(a_0+\delta_L))-\mathrm{H}^{(2)\prime}_n\,(\Delta_\infty(a_0+\delta_L))\right]}\right], \tag{3.214}$$

with

$$\begin{aligned} G(\bar{\theta}) =& \Bigg\{1+\varepsilon^2\Bigg[\left(n^2+\nu\frac{C^2(\bar{\theta})}{\Theta}\right)\left[\frac{C(\bar{\theta})(2M_\infty+M_w)+3\Theta^{1/2}}{6\left(\Theta^{1/2}+M_wC(\bar{\theta})\right)}\right] \\ &-\frac{\nu}{\Theta}\left[\frac{C^2(\bar{\theta})(M_\infty-M_w)^2}{4}+\left(\Theta^{1/2}+M_wC(\bar{\theta})\right)\left(C(\bar{\theta})(\frac{2}{3}M_\infty-\frac{1}{6}M_w)+\frac{1}{2}\Theta^{1/2}\right)\right]\Bigg]\Bigg\}, \end{aligned} \tag{3.215}$$

and

$$\begin{aligned} R(\bar{\theta}) =& \Bigg\{\frac{\nu C^2(\bar{\theta})+n^2\Theta}{\left(\Theta^{1/2}+M_wC(\bar{\theta})\right)\left(\Theta^{1/2}+M_\infty C(\bar{\theta})\right)}-\nu \\ &-\varepsilon\Bigg[\frac{n^2\Theta}{C^2(\bar{\theta})(M_\infty-M_w)}\Bigg[C(\bar{\theta})\left(\frac{C(\bar{\theta})(M_\infty-2M_w)-\Theta^{1/2}}{\left(\Theta^{1/2}+M_wC(\bar{\theta})\right)\left(\Theta^{1/2}+M_\infty C(\bar{\theta})\right)}\right) \\ &+\frac{1}{(M_\infty-M_w)}\ln\left(\frac{\Theta^{1/2}+M_\infty C(\bar{\theta})}{\Theta^{1/2}+M_wC(\bar{\theta})}\right)\Bigg] \\ &+\frac{\nu}{(M_\infty-M_w)}\Bigg[\frac{C(\bar{\theta})}{\left(\Theta^{1/2}+M_wC(\bar{\theta})\right)}-\frac{(M_\infty-M_w)}{2} \\ &-\frac{1}{(M_\infty-M_w)}\ln\left(\frac{\Theta^{1/2}+M_\infty C(\bar{\theta})}{\Theta^{1/2}+M_wC(\bar{\theta})}\right)\Bigg]\Bigg]\Bigg\}. \end{aligned} \tag{3.216}$$

Also, $\Delta_\infty \;=\; \frac{k_0\sin\bar{\theta}}{(1-M_\infty^2\sin^2\bar{\theta})^{1/2}}$, $\Theta=(1-M_\infty^2\sin^2\bar{\theta})$, $S(\bar{\theta})=\frac{\left(\Theta^{1/2}+M_\infty\cos\bar{\theta}\right)}{\sigma_\infty^2}$,
$C(\bar{\theta})=\frac{\left(\cos\bar{\theta}+M_\infty\Theta^{1/2}\right)}{\sigma_\infty^2}$ and $\sigma_\infty^2=1-M_\infty^2$.

Equation (3.213) is the essential conclusion of this section. It describes the acoustic pressure in the far-field around the fuselage using spherical polar coordinates centered on the cylindrical

fuselage, while taking into account the linear boundary layer on the surface of the fuselage.

3.3.6 Far-Field Validation

As in the case of the step-function boundary layer, the validation process involves reducing the linear velocity profile to a uniform flow. Assuming that the analytical methods used in the previous section are valid, when the boundary layer vanishes, the derived solution described in eq.(3.213) must reduce to the uniform flow far-field solution given by eq.(3.67). For the derived solution to be analytically valid the following needs to be true: eq.(3.213) converges to eq.(3.67) when $\delta_L \to 0$ or $\varepsilon \to 0$.

When $\varepsilon \to 0$,

$$R(\bar{\theta}) = \frac{\nu C^2(\bar{\theta}) + n^2\Theta}{\left(\Theta^{1/2} + M_w C(\bar{\theta})\right)\left(\Theta^{1/2} + M_\infty C(\bar{\theta})\right)} - \nu, \tag{3.217}$$

and $G(\bar{\theta}) = 1$ making their ratio finite. Also the term in the bracket $\mathfrak{L}_n(\bar{\theta})$,

$$\frac{\varepsilon(\Theta^{1/2} + M_\infty C(\bar{\theta}))^2}{k_0 a_0 \sin\bar{\theta}\Theta^{1/2}} \to 0, \tag{3.218}$$

which means that the bracket $\mathfrak{L}_n(\bar{\theta})$ from eq.(3.214) will reduce to

$$\mathfrak{L}_n(\bar{\theta}) = \left[\mathrm{J}_{n-l}\left(\Delta_\infty b\right) - \frac{\mathrm{J}_n'\left(\Delta_\infty a_0\right)}{\mathrm{H}_n^{(2)\prime}\left(\Delta_\infty a_0\right)}\mathrm{H}_{n-l}^{(2)}\left(\Delta_\infty b\right)\right], \tag{3.219}$$

which is identical to its uniform flow counterpart in eq.(3.67). No other terms in eq.(3.213) are dependent on ε or δ_L, so the expression reduces to

$$\begin{aligned} p'_{t_{ff}}(\bar{R},\bar{\theta},\bar{\phi},t) =& \frac{\mathrm{i}\xi_{lq}P_{lq}k_0}{2\bar{R}}\frac{S(\bar{\theta})}{\Theta}\Psi_{lq}(\Delta_\infty)\mathrm{e}^{-\mathrm{i}k_0\bar{R}S(\bar{\theta})}\mathrm{e}^{\mathrm{i}\omega_0 t} \\ &\times \sum_{n=-\infty}^{\infty}\left[\mathrm{J}_{n-l}\left(\Delta_\infty b\right) - \frac{\mathrm{J}_n'\left(\Delta_\infty a_0\right)}{\mathrm{H}_n^{(2)\prime}\left(\Delta_\infty a_0\right)}\mathrm{H}_{n-l}^{(2)}\left(\Delta_\infty b\right)\right]\mathrm{e}^{-\mathrm{i}(l-n)\beta}\mathrm{e}^{\frac{1}{2}n\pi\mathrm{i}}\mathrm{e}^{-\mathrm{i}n\bar{\phi}}, \end{aligned} \tag{3.220}$$

which is exactly the same as the uniform flow expression from eq.(3.67) apart from the difference in notation as explained in section 3.2.7.

3.3.7 Section Summary

The aim of this section was to derive some key expressions and equations that will be used to produce pressure calculations when there is a linear boundary layer velocity profile with a slip at the wall present on the surface of the fuselage. Specifically, the first of these expressions describe the pressure on the fuselage surface in eqs. (3.204) and (3.205). The far-field solution for the same problem is also derived and presented in this section. Equation (3.213) gives the pressure in the far-field of the fuselage when there is a linear boundary layer on it. The main advantage of using such a simple profile is the fact that an analytical solution for the Pridmore-Brown equation is rendered possible. Thus, the necessity of using high-fidelity numerical methods disappears.

As stated before, the linear boundary layer profile may not seem realistic enough in order to produce results that closely match those of a more representative profile, such as a 1/7th power-law profile. However, as will be seen later on by manipulating the thickness and the slip at the wall one can create a linear boundary layer that can closely match the same effects as any other more complex boundary layer profile. Furthermore, it is once again noted that the linear boundary layer theory is subject to the restriction of thickness. In order for the theory to be valid a sufficiently thin boundary layer is required. The validity bounds of the proposed theory will be investigated in later chapters of this thesis. The results in this section represent a novel work of an analytical solution of fan noise refraction by a linear boundary layer that has not been presented before to the best of the author's knowledge.

Chapter 4

Code Development

The expressions derived in the previous chapter need to be coded efficiently in order to demonstrate the effectiveness of using these analytical methods. Therefore, the next challenge is the development of a code that efficiently calculates the pressure either on the surface of the fuselage, i.e. using eqs. (3.37)-(3.38), (3.101)-(3.102), (3.204)-(3.205), or in the far-field, i.e. using eq.(3.67), (3.121), (3.213). These equations involve Fourier series, which means a convergence study must be carried out. Furthermore, an integration routine must be developed that will compute efficiently the inverse Fourier integrals $I_n^{(sbl)}$ in eq.(3.102) or $I_n^{(lbl)}$ in eq.(3.205), since these integrals cannot be solved analytically. Finally, due to the presence of singular and transitional points in the k_z domain, special care must be taken when handling both eq.(3.102) and eq.(3.205). The aim of this chapter is not only to describe the methods used to overcome these numerical difficulties, but also to provide validation results that demonstrate the effectiveness of the code.

4.1 Integration Routine

As explained before, calculating the pressure on the fuselage surface using eqs.(3.101) and (3.204) requires solving the integral from eqs.(3.102) and (3.205). This integral cannot be solved analytically so one must resort to numerical methods. This particular integral also presents problems since the integrand involves singular and transitional points along the k_z-axis. These points are shown in Fig.(3.4).

By studying Fig.(3.4), it becomes clear that compartmentalisation is required in order to perform the integration correctly. That is because there are regions where the "radial wavenumbers" become imaginary (regions **I** and **VII**) or regions where one of them is imaginary but the other one remains real (regions **II**, **V**, **VI** and **VII**). This means that the expression of the integrand requires different manipulation for different regions. In order to tackle this problem the integration domain is split into the regions **I** to **VII** and the final value of the integral is found by summing the values of the integrals from each different region.

An additional difficulty encountered in this integration problem are the possible singular points that occur along the k_z-axis. Specifically, the points where either Γ_0 or Γ_∞ become zero

are possible singularity points where the numerical routine might struggle to produce a value. Tables 4.1 and 4.2 show some of the possible combinations which might cause the integrand to return a "Not-A-Number" when being evaluated. In order to investigate these cases, the quantity Δ is introduced which is the part of the integrand in eq.(3.102) that may require to be evaluated asymptotically in cases when the numerator/denominator tend to zero and/or infinity.

$$\Delta(\Gamma_0,\Gamma_\infty)=\frac{\Psi_{lq}\,\mathrm{H}^{(2)}_{l-n}\left(\Gamma_\infty b\right)}{\pi^2\Gamma_0\,a_0(a_0+d)\left(k_0+k_zM_\infty\right)^2 D_n\left(k_z,\omega_0\right)\mathrm{H}^{(2)}_n\left(\Gamma_\infty(a_0+d)\right)\mathrm{J}'_n\left(\Gamma_0a_0\right)}. \tag{4.1}$$

For the sake of brevity, the value of Δ will be presented for two possible singular points along the k_z-axis:
i) At $k_z=-\frac{k_0}{1+M_0}$, where $\Gamma_0\to 0$ and $\Gamma_\infty=-\mathrm{i}\gamma_\infty$, where
$\gamma_\infty=\frac{k_0}{1+M_0}\sqrt{(M_\infty-M_0)(2+M_0-M_\infty)}$ which is finite. This point is the transition point from region **I** to region **II**.
ii) At $k_z=-\frac{k_0}{1+M_\infty}$, where $\Gamma_\infty\to 0$ and $\Gamma_0=\frac{k_0}{1+M_\infty}\sqrt{(M_\infty-M_0)(2+M_\infty-M_0)}$ which is real and finite. This point is the transition point from region **II** to region **III**.
The other transition points are remarkably similar to the two cases presented here.

Indices l and n	$\lim_{\Gamma_0\to 0}\ \Delta(\Gamma_0,-\mathrm{i}\gamma_\infty)$
$l=n=0$	$-\frac{a}{\gamma_\infty^2}\mathrm{i}^{2n-1}\frac{\mathrm{K}_0\left(\gamma_\infty b\right)\mathrm{I}_1\left(\gamma_\infty a\right)}{2\pi(a_0+d)\,\mathrm{K}'_0\left(\gamma_\infty(a_0+d)\right)}$
$n>l>0$	$\frac{\gamma_\infty a\mathrm{J}_l\left(\kappa_{lq}a\right)}{\kappa_{lq}^2+\gamma_\infty^2}\mathrm{i}^{2n-1}\frac{\mathrm{I}'_l\left(\gamma_\infty a\right)\mathrm{K}_{n-l}\left(\gamma_\infty b\right)}{\pi a_0^n(a_0+d)\,\mathrm{K}_n\left(\gamma_\infty(a_0+d)\right)c_1}$
$n=l>0$	$\frac{\gamma_\infty a\mathrm{J}_n\left(\kappa_{lq}a\right)}{\kappa_{lq}^2+\gamma_\infty^2}\mathrm{i}^{2n-1}\frac{\mathrm{I}'_n\left(\gamma_\infty a\right)\mathrm{K}_0\left(\gamma_\infty b\right)}{\pi a_0^n(a_0+d)\,\mathrm{K}_n\left(\gamma_\infty(a_0+d)\right)c_2}$
$l>0, n=-p, p>l$	$\frac{-\gamma_\infty a\mathrm{J}_l\left(\kappa_{lq}a\right)}{\kappa_{lq}^2+\gamma_\infty^2}\frac{(-1)^{1-p}}{\mathrm{i}}\frac{\mathrm{I}'_l\left(\gamma_\infty a\right)\mathrm{K}_{l+p}\left(\gamma_\infty b\right)}{\pi a_0^p(a_0+d)\,\mathrm{K}_p\left(\gamma_\infty(a_0+d)\right)c_3}$

TABLE 4.1: Evaluation of the limit of $\Delta(\Gamma_0,-\mathrm{i}\gamma_\infty)$, at $k_z=-\frac{k_0}{1+M_0}$.

Indices l and n	$\lim_{\Gamma_\infty\to 0}\ \Delta(\Gamma_0,\Gamma_\infty)$
$l=n=0$	$-\frac{1}{2}a^2\frac{1}{\pi^2\Gamma_0a_0(a_0+d)\,\mathrm{J}'_0\left(\Gamma_0a_0\right)c_4}\frac{\ln(\Gamma_\infty b)}{\ln(\Gamma_\infty(a_0+d))}$
$n>l>0$	$\frac{\mathrm{J}_l\left(\kappa_{lq}a\right)}{\kappa_{lq}^2}(-1)^{n-l}\frac{(n-l-1)!}{(l-1)!\,(n-1)!}\frac{(\frac{1}{2}\Gamma_\infty)^{2l}b^{l-n}a^l}{\pi^2\Gamma_0a_0(a_0+d)^{-n+1}\,\mathrm{J}'_n\left(\Gamma_0a_0\right)c_5}$
$n=l>0$	$\frac{-2\mathrm{J}_l\left(\kappa_{lq}a\right)}{\kappa_{lq}^2}\frac{a^n}{((n-1)!)^2}\frac{1}{\pi^2\Gamma_0a_0(a_0+d)^{-n+1}\,\mathrm{J}'_n\left(\Gamma_0a_0\right)c_6}(\frac{1}{2}\Gamma_\infty)^{2n}\ln(\Gamma_\infty b)$
$l>0, n=-p, p>l$	$\frac{a^l\mathrm{J}_l\left(\kappa_{lq}a\right)}{\kappa_{lq}^2}\frac{(-1)^p(l+p-1)!}{(l-1)!\,(p-1)!}\frac{b^{-l-p}}{\pi^2\Gamma_0a_0(a_0+d)^{-p+1}\,\mathrm{J}'_p\left(\Gamma_0a_0\right)c_7}$

TABLE 4.2: Evaluation of the limit of $\Delta(\Gamma_0,\Gamma_\infty)$, at $k_z=-\frac{k_0}{1+M_\infty}$.

The quantities c_1 through c_7 that appear on the tables are constant and are dependent only on geometric and flow characteristics. The evaluation of these limits is performed using small argument approximations for the Hankel and Bessel functions.
When $\Gamma_0\to 0$ the integrand is finite, but when $\Gamma_\infty\to 0$ the limit of the integrand involves logarithms which may cause problems during the numerical integration, despite the fact that in all the cases where logarithms are involved the limit can be proven to be finite. To avoid

possible infinite values being produced, the midpoint rule of integration is chosen. The midpoint rule, unlike trapezoid or Simpson's rules, integrates the integrand without taking into account the edges of the domain. Thus, by splitting the domain as shown in Fig.(3.4) and using the midpoint rule, the transition points and the "numerical singularity" points, where zero over zero limiting behaviour occurs, will be excluded from the integration. It must also be noted that the points where Ψ_{lq} becomes infinite also cause problems during the numerical integration, that is why the compartmentalisation of the domain also takes that into account.

4.2 Small Argument Approximation for the Step-Function Boundary Layer Far-Field

The numerical difficulties encountered in the case of the step-function boundary layer fuselage surface pressure are also present in the far-field case. Specifically, eq.(3.121) presents a singular point when $\Delta_0 \to 0$. As will be shown, this singularity can be bridged since the limit of the expression as $\Delta_0 \to 0$ approaches a finite value which can be used instead of the general expression given in eq.(3.121).

Unlike in the fuselage surface pressure case where both the "radial wavenumbers" would alternate between real and imaginary values as shown in eqs.(3.77) and (3.78), as well as in Fig.(3.4), in the far-field case only the value of Δ_0 will alternate between real and imaginary values. That is because in order to solve the integral using the method of stationery phase, the regions **I**, **II** and **VII** are omitted as explained in appendix D. Notice that this does not happen in the linear boundary layer case because there is no "internal" radial wavenumber, there is only Γ_∞ or Δ_∞. However for the step-function boundary layer case, region **VI** remains, which means that $\Gamma_0 = -\mathrm{i}\gamma_0$ or $\Delta_0 = -\mathrm{i}\delta_0$ in that region. Immediately, it follows from eq.(3.124) that,

$$\delta_0 = \frac{k_0}{(1 - M_\infty^2 \sin^2\bar{\theta})^{1/2}} \sqrt{C\,(\bar{\theta})[C\,(\bar{\theta})\sigma_0^2 - 2M_0(1 - M_\infty^2 \sin^2\bar{\theta})^{1/2}] - (1 - M_\infty^2 \sin^2\bar{\theta})}. \quad (4.2)$$

It is easy to calculate the polar angle $\bar{\theta_0}$ in which the radicand of eq.(4.2) (or eq.(3.124)) becomes zero. At angles smaller than $\bar{\theta_0}$, Δ_0 is imaginary and is replaced by $-\mathrm{i}\delta_0$. The transitioning behaviour of Δ_0 is shown in Fig. (4.1).
Around that point, the expression of eq.(3.121) produces extreme values that cannot be computed. It is the terms involving Δ_0 that are the issue here. The only term dependent on Δ_0 in eq.(3.121) is the ratio $\frac{Y_n\,(\Delta_0)}{D_n\,(\Delta_\infty,\Delta_0)}$. This ratio is proven to have a finite limit dependent on $\bar{\theta}$ which can be used around the point where the ratio cannot be computed using its regular expression. In order to evaluate the limit of the ratio small argument approximations for Bessel and Hankel functions are used, found in Rienstra and Hirschberg (2004). Starting with the limit of the bracket term from eq.(3.117),

$$\begin{aligned}
&\lim_{\Delta_0\to 0} Y_n\,(\Delta_0) = \\
&\lim_{\Delta_0\to 0}\left[\frac{\mathrm{i}}{\pi}(n-1)!\,(\frac{1}{2}\Delta_0(a_0+\delta_{SF}))^{-n} - \frac{(\frac{1}{2}\Delta_0(a_0+\delta_{SF}))^n}{n!}\frac{-\frac{\mathrm{i}}{2\pi}n!\,(\frac{1}{2}\Delta_0 a_0)^{-n-1}}{\frac{(\frac{1}{2}\Delta_0 a_0)^{n-1}}{2(n-1)!}}\right] = \\
&\lim_{\Delta_0\to 0}\frac{\mathrm{i}}{\pi}(n-1)!\,(\frac{1}{2}\Delta_0)^{-n}\left[(a_0+\delta_{SF})^{-n} + (a_0+\delta_{SF})^n a_0^{-2n}\right].
\end{aligned} \quad (4.3)$$

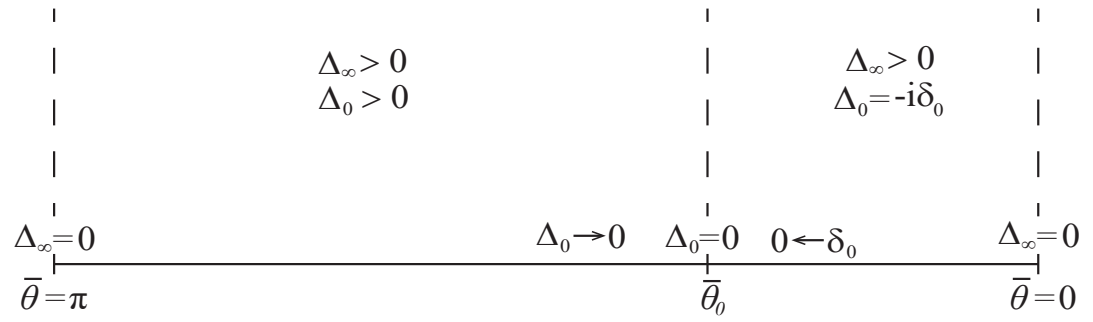

FIGURE 4.1: Transition of Δ_0 value along the $\bar{\theta}$-axis.

Accordingly, the limit of $D_n(\Delta_\infty, \Delta_0)$ will be from eq.(3.123),

$$
\begin{aligned}
&\lim_{\Delta_0 \to 0} D_n(\Delta_\infty, \Delta_0) = \\
&\lim_{\Delta_0 \to 0} \left[-\frac{\mathrm{i}}{2\pi} n! \left(\frac{1}{2}\Delta_0 (a_0 + \delta_{SF})\right)^{-n-1} - \frac{\left(\frac{1}{2}\Delta_0 (a_0 + \delta_{SF})\right)^{n-1}}{2(n-1)!} \frac{-\frac{\mathrm{i}}{2\pi} n! \left(\frac{1}{2}\Delta_0 a_0\right)^{-n-1}}{\frac{\left(\frac{1}{2}\Delta_0 a_0\right)^{n-1}}{2(n-1)!}} \right] \\
&\times \frac{\Delta_0}{k_0^2 \left(1 + \frac{C(\bar{\theta}) M_0}{(1 - M_\infty^2 \sin^2 \bar{\theta})^{1/2}}\right)^2} \\
&- \left[\frac{\mathrm{i}}{\pi} (n-1)! \left(\frac{1}{2}\Delta_0 (a_0 + \delta_{SF})\right)^{-n} - \frac{\left(\frac{1}{2}\Delta_0 (a_0 + \delta_{SF})\right)^{n}}{n!} \frac{-\frac{\mathrm{i}}{2\pi} n! \left(\frac{1}{2}\Delta_0 a_0\right)^{-n-1}}{\frac{\left(\frac{1}{2}\Delta_0 a_0\right)^{n-1}}{2(n-1)!}} \right] \\
&\times \frac{\sin \bar{\theta} (1 - M_\infty^2 \sin^2 \bar{\theta})^{1/2}}{k_0 S^2(\bar{\theta})} \frac{\mathrm{H}_n^{(2)\prime}(\Delta_\infty (a_0 + \delta_{SF}))}{\mathrm{H}_n^{(2)}(\Delta_\infty (a_0 + \delta_{SF}))},
\end{aligned}
\tag{4.4}
$$

which finally becomes

$$\lim_{\Delta_0\to 0} D_n\left(\Delta_\infty, \Delta_0\right) =$$
$$\lim_{\Delta_0\to 0} \frac{\mathrm{i}}{\pi}(n-1)!\left(\frac{1}{2}\Delta_0\right)^{-n}\Bigg[\left[(a_0+\delta_{SF})^{n-1}(a_0)^{-2n}-(a_0+\delta_{SF})^{-n-1}\right]\frac{n}{k_0^2\left(1+\frac{C\left(\bar{\theta}\right)M_0}{(1-M_\infty^2\sin^2\bar{\theta})^{1/2}}\right)^2}$$
$$-\left[(a_0+\delta_{SF})^{-n}+(a_0+\delta_{SF})^{n}a_0^{-2n}\right]\frac{\sin\bar{\theta}(1-M_\infty^2\sin^2\bar{\theta})^{1/2}}{k_0\,S^2\left(\bar{\theta}\right)}\,\frac{\mathrm{H}_n^{(2)\prime}\left(\Delta_\infty(a_0+\delta_{SF})\right)}{\mathrm{H}_n^{(2)}\left(\Delta_\infty(a_0+\delta_{SF})\right)}\Bigg]. \tag{4.5}$$

By combining eqs. (4.3) and (4.5), the limit of the ratio can be found

$$\lim_{\Delta_0\to 0}\frac{Y_n\left(\Delta_0\right)}{D_n\left(\Delta_\infty,\Delta_0\right)} =$$
$$\lim_{\Delta_0\to 0}\frac{\mathrm{i}}{\pi}(n-1)!\left(\frac{1}{2}\Delta_0\right)^{-n}\left[(a_0+\delta_{SF})^{-n}+(a_0+\delta_{SF})^{n}a_0^{-2n}\right]/\Bigg[\frac{\mathrm{i}}{\pi}(n-1)!\left(\frac{1}{2}\Delta_0\right)^{-n}$$
$$\times\Bigg[\left[(a_0+\delta_{SF})^{n-1}(a_0)^{-2n}-(a_0+\delta_{SF})^{-n-1}\right]\frac{n}{k_0^2\left(1+\frac{C\left(\bar{\theta}\right)M_0}{(1-M_\infty^2\sin^2\bar{\theta})^{1/2}}\right)^2} \tag{4.6}$$
$$-\left[(a_0+\delta_{SF})^{-n}+(a_0+\delta_{SF})^{n}a_0^{-2n}\right]\frac{\sin\bar{\theta}(1-M_\infty^2\sin^2\bar{\theta})^{1/2}}{k_0\,S^2\left(\bar{\theta}\right)}\,\frac{\mathrm{H}_n^{(2)\prime}\left(\Delta_\infty(a_0+\delta_{SF})\right)}{\mathrm{H}_n^{(2)}\left(\Delta_\infty(a_0+\delta_{SF})\right)}\Bigg]\Bigg],$$

which becomes

$$\lim_{\Delta_0\to 0}\frac{Y_n\left(\Delta_0\right)}{D_n\left(\Delta_\infty,\Delta_0\right)} =$$
$$\left[(a_0+\delta_{SF})^{-n}+(a_0+\delta_{SF})^{n}a_0^{-2n}\right]/\Bigg[\left[(a_0+\delta_{SF})^{n-1}(a_0)^{-2n}-(a_0+\delta_{SF})^{-n-1}\right]\frac{n}{k_0^2\left(1+\frac{C\left(\bar{\theta}\right)M_0}{(1-M_\infty^2\sin^2\bar{\theta})^{1/2}}\right)^2}$$
$$-\left[(a_0+\delta_{SF})^{-n}+(a_0+\delta_{SF})^{n}a_0^{-2n}\right]\frac{\sin\bar{\theta}(1-M_\infty^2\sin^2\bar{\theta})^{1/2}}{k_0\,S^2\left(\bar{\theta}\right)}\,\frac{\mathrm{H}_n^{(2)\prime}\left(\Delta_\infty(a_0+\delta_{SF})\right)}{\mathrm{H}_n^{(2)}\left(\Delta_\infty(a_0+\delta_{SF})\right)}\Bigg], \tag{4.7}$$

which is finite and dependent only on $\bar{\theta}$, since Δ_∞ is also dependent only on $\bar{\theta}$. The evaluation of the limit from the imaginary side, $\delta_0 \to 0$, yields exactly the same result as in eq.(4.7). Therefore, when the code does not produce a valid value for the ratio around $\bar{\theta_0}$, eq.(4.7) can be used instead.

4.3 Code Validation

4.3.1 Convergence

As it has been previously mentioned, the expressions for both the near and the far-field are in terms of a Fourier series. The presence of the series means that the convergence must be investigated both for the uniform flow case and the two boundary layer cases. A relative error

is introduced that determines the contribution of every harmonic in the series.

$$\epsilon = \sqrt{\frac{\frac{1}{M}\sum^{M}|p'_{N'} - p'_N|^2}{\frac{1}{M}\sum^{M}|p'_N|^2}}, \tag{4.8}$$

where, $p'_{N'}$ is the pressure calculated at the $(N+1)$th harmonic and p'_N is the pressure calculated at the Nth harmonic, and M is the number of grid points. When this error becomes sufficiently small, the series is considered to have converged. It is important to note that in the convergence graphs shown below, the x-axis represents N as in number of harmonics and not number of terms. This means that a series with N harmonics will include terms from $-N$ to N, i.e. $2N+1$ terms, or in other words the sums in eqs. (3.37), (3.67), (3.101), (3.121), (3.204) and (3.213) have limits $\sum_{n=-N}^{N}$.

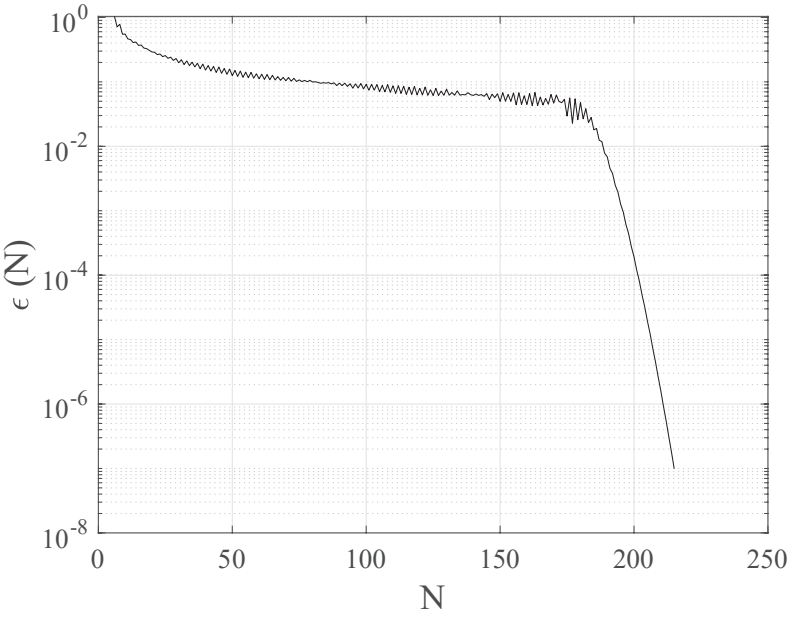

FIGURE 4.2: Relative error in logarithmic scale vs. number of harmonics in the series for far-field polar directivity with fixed $\bar{\phi} = 3\pi/2$ (eq.(3.213)) at a frequency of $k_0 a = 20$ and Mach number 0.75.

As can be seen from Fig.(4.2), convergence is achieved including about 210 harmonics. Note that in the relative error graphs the y-axis refers to the value of the error as shown in eq.(4.8) and not the percentage. In order to obtain the percentage relative error, one can simply multiply the vertical axis by 100. By inspecting eq.(3.67), convergence can actually be proven analytically, by taking the limit as $n \to \infty$ of the bracket term in eq.(3.67). The bracket term consists of a Bessel function term $\mathrm{J}_{n-l}(\Delta_z b)$ and the ratio term $\frac{\mathrm{J}'_n(\Delta_z a_0)}{\mathrm{H}_n^{(2)\prime}(\Delta_z a_0)}$. In order to evaluate the limits of these terms as $n \to \infty$, large order asymptotic expansions for Bessel and Hankel functions are used as presented in Rienstra and Hirschberg (2004). More specifically, these

expansions are:

$$\begin{aligned} \mathrm{J}_n(x) &\simeq \frac{1}{\sqrt{2\pi n}}\left(\frac{ex}{2n}\right)^n \Rightarrow \mathrm{J}'_n(x) \simeq \sqrt{\frac{n}{2\pi}}\left(\frac{e}{2n}\right)^n x^{n-1}, \\ \mathrm{Y}_n(x) &\simeq -\sqrt{\frac{2}{\pi n}}\left(\frac{ex}{2n}\right)^{-n} \Rightarrow \mathrm{Y}'_n(x) \simeq \sqrt{\frac{2n}{\pi}}\left(\frac{e}{2n}\right)^{-n} x^{-n-1}, \end{aligned} \tag{4.9}$$

where prime denotes differentiation with respect to the function's argument. Firstly, the Bessel function term:

$$\lim_{n\to\infty} \mathrm{J}_n(\Delta_z b) = \lim_{n\to\infty} \frac{1}{\sqrt{2\pi n}}\left(\frac{e\Delta_z b}{2n}\right)^n = 0, \tag{4.10}$$

because $\lim_{n\to\infty}\left(\frac{e\Delta_z b}{2n}\right)^n = \lim_{n\to\infty}\exp\left(n\ln\left(\frac{e\Delta_z b}{2n}\right)\right) = 0.$

On the other hand the ratio term is:

$$\frac{\mathrm{J}'_n(\Delta_z a_0)}{\mathrm{H}^{(2)\prime}_n(\Delta_z a_0)} = \frac{\mathrm{J}'_n(\Delta_z a_0)}{\mathrm{J}'_n(\Delta_z a_0) - \mathrm{i}\mathrm{Y}'_n(\Delta_z a_0)} \simeq \frac{\sqrt{\frac{n}{2\pi}}\left(\frac{e}{2n}\right)^n (\Delta_z a_0)^{n-1}}{\sqrt{\frac{n}{2\pi}}\left(\frac{e}{2n}\right)^n (\Delta_z a_0)^{n-1} - \mathrm{i}\sqrt{\frac{2n}{\pi}}\left(\frac{e}{2n}\right)^{-n}(\Delta_z a_0)^{-n-1}}, \tag{4.11}$$

which becomes

$$\frac{\mathrm{J}'_n(\Delta_z a_0)}{\mathrm{H}^{(2)\prime}_n(\Delta_z a_0)} \simeq \frac{1}{1 - 2\mathrm{i}\left(\frac{2n}{e\Delta_z a_0}\right)^{2n}}. \tag{4.12}$$

By multiplying with the complex conjugate, eq.(4.12) becomes

$$\frac{\mathrm{J}'_n(\Delta_z a_0)}{\mathrm{H}^{(2)\prime}_n(\Delta_z a_0)} = \frac{1}{1 + 4\left(\frac{2n}{e\Delta_z a_0}\right)^{4n}} + \mathrm{i}\frac{2\left(\frac{2n}{e\Delta_z a_0}\right)^{2n}}{1 + 4\left(\frac{2n}{e\Delta_z a_0}\right)^{4n}}. \tag{4.13}$$

Equation (4.13) is a complex number with a real and an imaginary part. The real part can be easily shown to approach zero for large n. In the imaginary part, both the numerator and the denominator tend to infinity as $n \to \infty$. This is dealt with using L' Hopital's rule:

$$\lim_{n\to\infty} \frac{2\left(\frac{2n}{e\Delta_z a_0}\right)^{2n}}{1 + 4\left(\frac{2n}{e\Delta_z a_0}\right)^{4n}} = \lim_{n\to\infty} \frac{4\left(\frac{2n}{e\Delta_z a_0}\right)^{2n}\left(\ln\left(\frac{2n}{e\Delta_z a_0}\right) + 1\right)}{16\left(\frac{2n}{e\Delta_z a_0}\right)^{4n}\left(\ln\left(\frac{2n}{e\Delta_z a_0}\right) + 1\right)} \Rightarrow \lim_{n\to\infty} \frac{1}{4\left(\frac{2n}{e\Delta_z a_0}\right)^{2n}} = 0. \tag{4.14}$$

It is evident that both terms converge to zero at high harmonics. This is also demonstrated in the following graphs. Figures (4.3) and (4.4) confirm what is analytically proven above. Both the Bessel function term and the ratio term converge to zero at the higher harmonics. Note that in Figures (4.3) and (4.4), n represents not only the order as it appears in the derived expression, but also the harmonics required for convergence. It is clear that the dominant term is the Bessel function term as it requires a larger value of n to converge, and thus determines the convergence of the whole series. Furthermore, it is evident that the higher the frequency the more harmonics it takes for the expression to converge, which is expected since it can be analytically proven that the higher the argument of the Bessel function the larger n is required to approach zero. Note that the Mach number has a similar effect on the argument of the Bessel Function and therefore it is reasonable to expect that it will have a similar effect as the frequency.

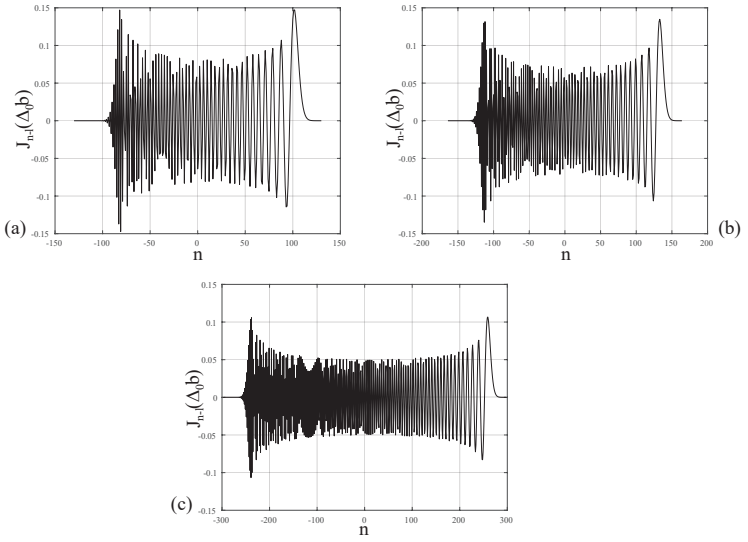

FIGURE 4.3: Bessel function term vs. order in the series for uniform flow with fixed $\bar{\theta}$ and non-dimensional frequencies, **[(a)]** $k_0 a = 12$, **[(b)]** $k_0 a = 16$, **[(c)]** $k_0 a = 32$.

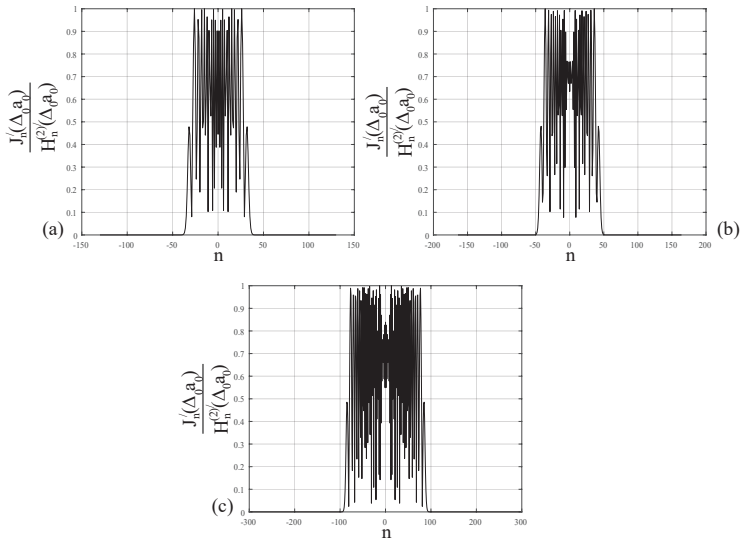

FIGURE 4.4: Absolute value of the derivatives term vs. order in the series for uniform flow with fixed $\bar{\theta}$ and non-dimensional frequencies, **[(a)]** $k_0 a = 12$, **[(b)]** $k_0 a = 16$, **[(c)]** $k_0 a = 32$.

Similar behaviour is exhibited for the step-function and linear boundary layer case. In fact, this is expected since by comparing eqs. (3.67), (3.121) and (3.213) one observes that the Bessel function term remains the same in both equations. Having the same dominant term means that the expressions will demonstrate similar behaviour in their convergence. By examining Fig.(4.5), one can observe that the error is once again oscillatory (and very similar for the two boundary layer cases) until it reaches convergence rapidly due to the Bessel function term having reached its final value. Moreover, the frequency effect is once again demonstrated since higher frequency leads to more harmonics required for convergence.

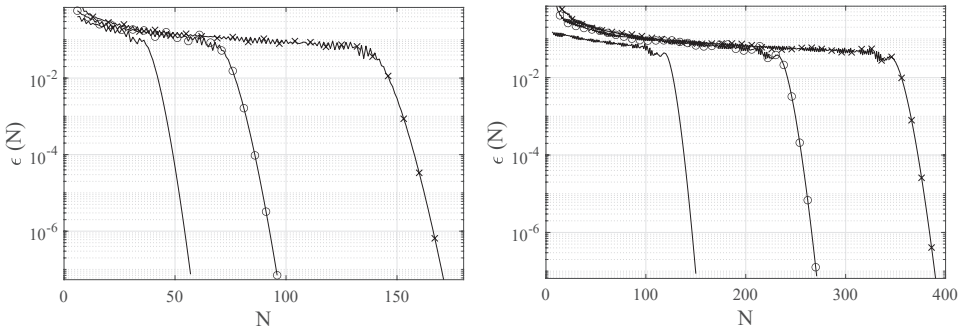

FIGURE 4.5: Relative error in logarithmic scale vs. number of harmonics in the series for the linear boundary layer far-field polar directivity pressure (eq.(3.213)) [left], and the step-function boundary layer far-field polar directivity pressure (eq.(3.121)) [right]. Results are presented for three different frequencies, $k_0a = 5$ [no marker], $k_0a = 10$ [◯], $k_0a = 20$ [×] for the linear boundary layer case, and $k_0a = 16$ [no marker], $k_0a = 32$ [◯], $k_0a = 48$ [×] for the step-function boundary layer case. The other parameters are $(l, q) = (10, 1)$, $M_\infty = 0.5$ and $\delta = 0.01a_0$.

The same behaviour is observed in the case of the near-field surface pressure. Here, the convergence of the step-function and the linear boundary layer case is shown for three frequencies. Once again, the higher the frequency the more harmonics it takes for the expressions (in this case eqs.(3.101) and (3.204)) to converge. The results presented in Fig.(4.6) are produced by setting a rectangular grid of points along the $\bar{z}$ and $\bar{\phi}$ axes. This grid represents a part of the fuselage surface as will be shown later. Note that the fuselage surface expressions exhibit no oscillations in their convergence graphs. That is attributed to the main difference between the far-field and the fuselage surface pressure expressions, which is the numerical integration routine. The numerical integration tends to smooth out any instabilities.

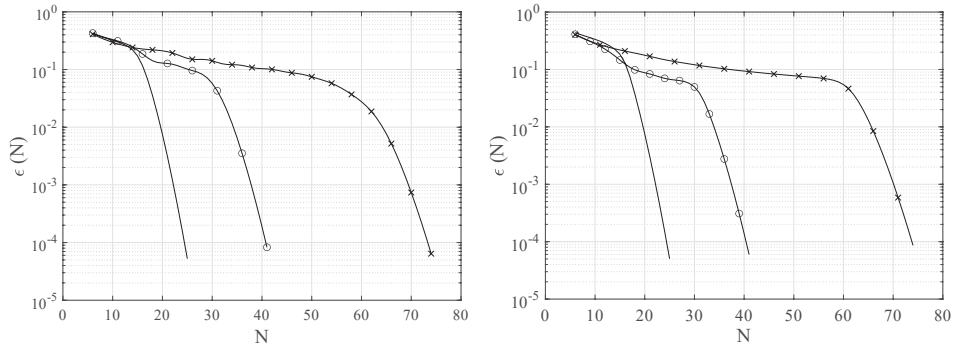

FIGURE 4.6: Relative error in logarithmic scale vs. number of harmonics in the series for the linear boundary layer fuselage surface pressure (eq.(3.204)) [left], and the step-function boundary layer fuselage surface pressure (eq.(3.101)) [right]. Results are presented for three different frequencies, $k_0a = 5$ [no marker], $k_0a = 10$ [◯], $k_0a = 20$ [×] for both cases. The other parameters are $(l, q) = (10, 1)$, $M_\infty = 0.5$ and $\delta = 0.01a_0$.

4.3.2 Further Validation

Another form of code benchmarking would be to compare the results with the results of another existing code. However, since the inclusion of the linear and step-function boundary layer is new work, an existing in-house code that is available is the one that calculates the

pressure on the surface of the cylindrical fuselage without the presence of a boundary layer written by McAlpine et al. (2015). This is eq.(3.37) which is similar to eqs. (3.101) and (3.204) with the fundamental difference being the inverse Fourier integral. Several comparisons were conducted and are presented below. These include different modes and frequencies. The following graphs show the Sound Pressure Level (SPL) on the fuselage surface from $\bar{z} = -a_0$ to $\bar{z} = 5a_0$, with the source plane at $\bar{z} = 0$ and its azimuthal position at $\beta = 0^o$. The SPL is measured in dB and is defined as:

$$\text{SPL} = 20 \log \frac{|p'|}{p_{ref}\sqrt{2}}. \tag{4.15}$$

Furthermore, since the cylinder plots can be misleading since they inevitably hide certain regions and make it more difficult interpreting the colour scales with a large dB range, more attention is given to the unfurled absolute difference plots. These plots show the absolute difference between the SPL of the code developed in this work and the existing code developed previously, $|\text{SPL}_{\text{new}} - \text{SPL}_{\text{old}}|$. These plots are unfurled cylinder plots meaning that they represent the same area as the cylinder plot.
Firstly, Fig.(4.7) shows an illustrative plot of the results of the two codes. They are remarkably similar apart from an instability apparent in the shadow zone (around $\bar{\phi} = 180^o$) using the old code, which is attributed to the integration routine. The code developed here appears to correct this instability. The shadow zone is expected there since this area is not in direct line of sight of the source which is located on the other side of the cylinder, $\bar{\phi} = 0^o$. The absolute difference plot for the same case that follows in Fig.(4.8) makes it clear that the only substantial difference in the SPL occurs in certain localised areas of the shadow zone, which renders it irrelevant since the shadow zone generally exhibits levels almost 100 dB lower than the illuminated side which is of interest. Therefore, the differences in the shadow zone are expected since those areas exhibit the extreme minima of the SPL spectrum.

Figure (4.9) shows the same features. The difference is close to zero for the whole cylinder except in some localised areas in the shadow zone or in areas that exhibit very low levels, such as the further upstream area in Fig, (4.9[right]). This upstream area represents a null zone for that particular mode, which means that it will exhibit levels much lower than other areas, effectively rendering it a shadow zone. Furthermore, one can observe a frequency effect, meaning the higher the frequency the higher the discrepancies tend to be. Once again, this is expected since at higher frequency, certain fluctuations are introduced that have to do with the presence of shorter wavelengths. Also, numerically, higher frequencies tend to introduce more complex patterns in the integrands in eqs. (3.37), (3.101) and (3.204) leading to more discrepancies in the integration routines of the two codes. Apart from some minor discrepancies, these figures confirm the validity of the code generated in this work since it can be safely concluded that the two codes produce the same results.

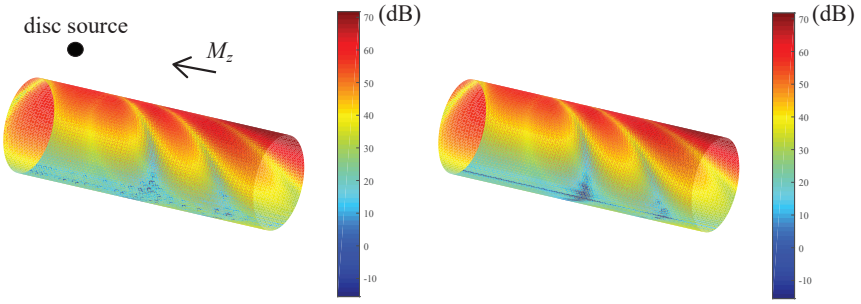

FIGURE 4.7: SPL on the fuselage surface for uniform flow (eq.(3.37)) for mode $(l, q) = (5, 1)$ and frequency $k_0 a = 16$ generated with **[left]** old code and **[right]** new code developed in this work.

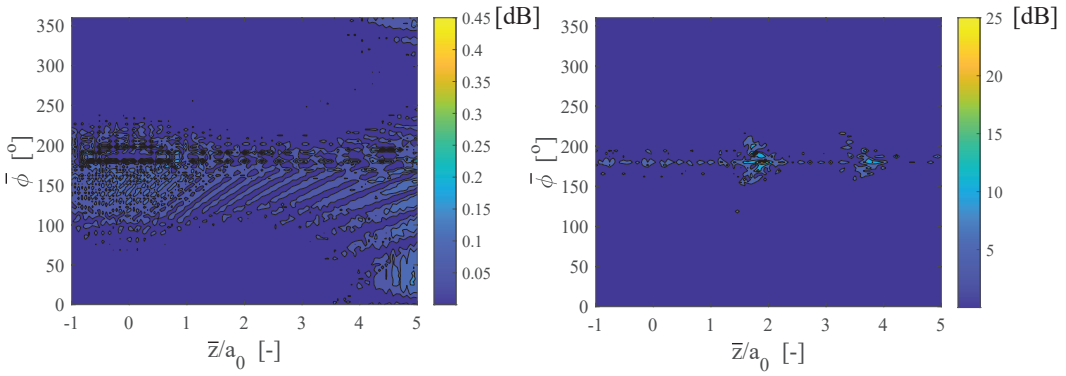

FIGURE 4.8: Absolute difference of the SPL on the fuselage surface for uniform flow (eq.(3.37)) for mode $(l, q) = (5, 1)$, $M_\infty = 0.5$ and frequencies **[left]** $k_0 a = 8$ and **[right]** $k_0 a = 16$. Note the different scales on each plot.

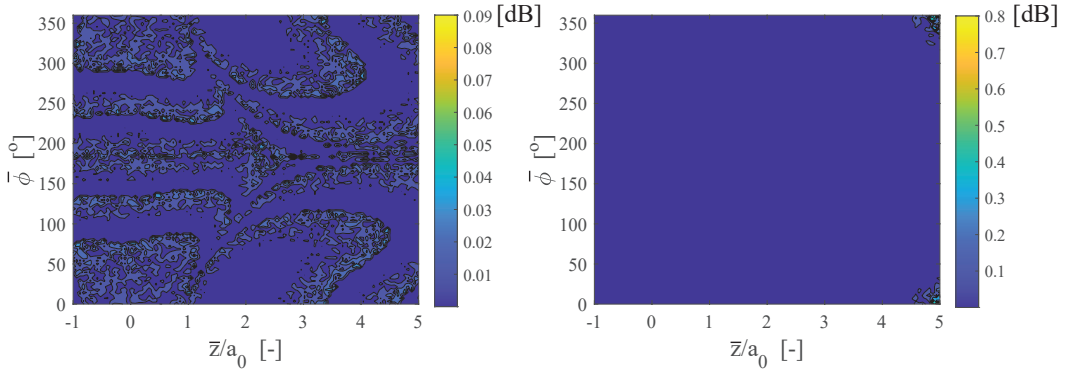

FIGURE 4.9: Absolute difference of the SPL on the fuselage surface for uniform flow (eq.(3.37)) for mode $(l, q) = (10, 1)$ and frequency $k_0 a = 16$ **[left]**, and mode $(l, q) = (20, 1)$ and frequency $k_0 a = 24$ **[right]**. Note the different scales on each plot.

With the code for the uniform flow expressions validated, the next step is to validate the codes for the linear boundary layer and step-function boundary layer. At this point, the way to achieve this is by reducing the boundary layer expressions to the uniform flow ones by setting $M_0 \to M_\infty$ in the case of the step-function boundary layer, or $M_w \to M_\infty$ in the case of the linear boundary layer. Bear in mind that comparisons with other existing codes that include a boundary layer have been conducted and will be presented in later chapters. It has already been analytically proven that the boundary layer expressions reduce to the equivalent expressions for uniform flow when the two Mach numbers are equal. This must also be true for the numerical code developed in this work. By equating the two Mach numbers, the coded boundary layer expressions (eqs. (3.101), (3.121), (3.204) and (3.213)) should yield the same results as the coded uniform flow expressions (eqs. (3.37) and (3.67)).

Once again, the predicted SPL will be used to compare the results both for the near-field and the far-field. The far-field results will be presented in the form of a polar directivity plot, a grid of varying polar angle $\bar{\theta}$ for a fixed azimuthal angle $\bar{\phi}$. For the near-field surface pressure the absolute difference of the two SPLs is presented to show the convergence of the boundary layer code to the uniform flow code. This plot will refer to the same fuselage area as in the previous contour plots. Figure (4.10) confirms that the coded boundary layer expressions successfully reduce to the uniform flow results. The difference exhibited in the figures is so small to be virtually non-existent in the case of the step-function boundary layer case. On the other hand, the linear boundary layer case presents some discrepancies in the shadow zone. This is mainly because it is not possible to set M_w exactly equal to M_∞ in the code since that will create numerical singularities. Instead, the value of M_w is set very close to the value of M_∞. This small numerical discrepancy leads to some small differences in the results. However, the differences are very small and only in the shadow zone where discrepancies are always bound to appear. Figure (4.11) exhibits almost no discrepancy at all with the two results almost coinciding with each other. This is indicative of the simplicity of the far-field expression that lacks a numerical integration routine and therefore is less likely to produce instabilities.

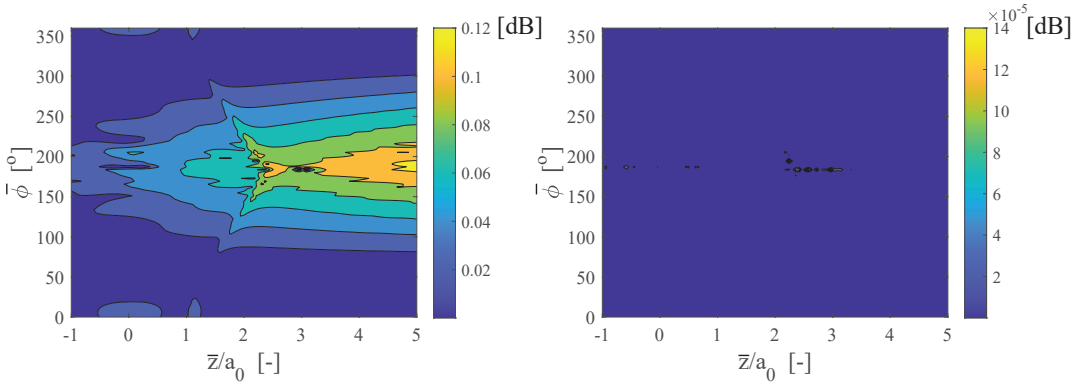

FIGURE 4.10: [left] Absolute difference of SPL generated from eq.(3.204) with $M_w \simeq M_\infty$ and SPL generated from eq.(3.37). [right] Absolute difference of SPL generated from eq.(3.101) with $M_0 = M_\infty$ and SPL generated from eq.(3.37). The other parameters are $M_\infty = 0.5$, $(l, q) = (10, 1)$ and $k_0 a = 16$. Note the different scales on each plot.

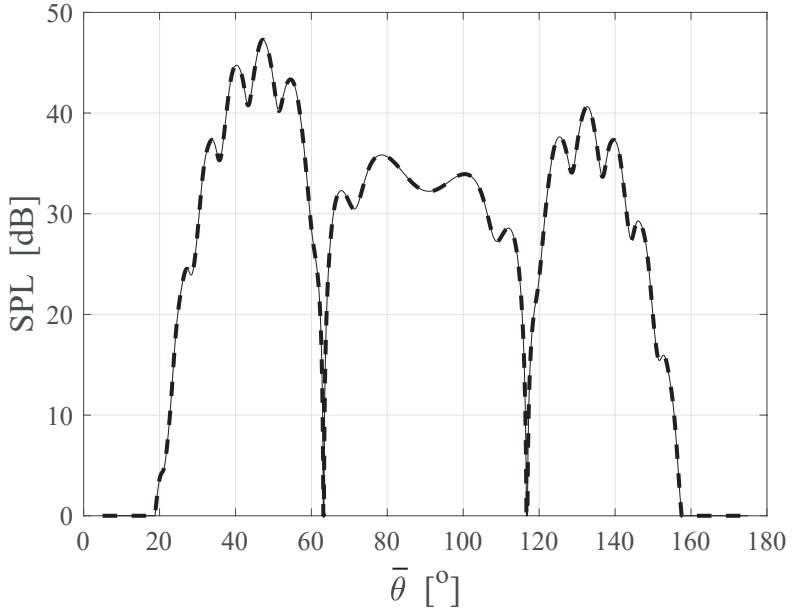

FIGURE 4.11: Far-field polar directivity plot for uniform flow using eq.(3.67) [solid line] and linear boundary layer using eq.(3.213) where $M_w \simeq M_\infty$ [dashed line]. The other parameters are $M_\infty = 0.5$, $(l, q) = (10, 1)$ and $k_0 a = 16$.

Chapter 5

Validation

Having successfully coded the derived expressions, the next step of the analysis is to validate them. Therefore, the present chapter includes results that demonstrate the validity of the key equations derived in chapter 3. Special focus is given to the ability of the novel theoretical approach to quantify the refraction effect due to the presence of a boundary layer on the surface of the fuselage. The installed field in uniform flow has already been investigated and validated in McAlpine et al. (2015), therefore it is not in the scope of the work presented here to demonstrate or validate results in the absence of a boundary layer on the fuselage. Instead, the differences between predictions for the installed field with and without a boundary layer are investigated, since they highlight the regions where the refraction effect due to the boundary layer causes shielding. The metrics that are used are chosen because of their ability to highlight those regions.

The two novel theoretical approaches presented in chapter 3 aim to provide a quicker alternative to the use of high-fidelity numerical methods. However, they are subject to some restrictions as seen in chapter 3. Therefore, the validation process aims to accomplish three goals:

(i) Prove that the theoretical methods produce results that capture the refraction and shielding effect due to the presence of the boundary layer.

(ii) Prove that the theoretical methods using simplified velocity profiles can approximate the same effects as more complex and real-life profiles such as the 1/7th power-law profile representative of a turbulent boundary layer profile.

(iii) Investigate the validity bounds of the theoretical methods in terms of the boundary-layer thickness.

Through a series of examples, the theoretical methods are compared with already existing results that have been generated using numerical methods. The numerical results are either taken from the PhD thesis or papers by Gaffney (Gaffney and McAlpine (2017), Gaffney and McAlpine (2018), Gaffney (2016)) or are recreated using the code developed by Gaffney and McAlpine (2017), which involved the use of high-fidelity numerical methods, namely Runge-Kutta routines, to accurately predict the boundary-layer effects of realistic profiles such

as the quarter-sine or the 1/7th power-law. Thus, the two theoretical methods are tested both for their ability to capture the boundary-layer effects but also for their ability to accurately approximate the effects of representative complex profiles such as the 1/7th power-law profile.

5.1 Metrics

Since the validation process aims to prove the theoretical methods' ability to quantify the shielding effect due to the presence of boundary layer, appropriate metrics are used in order to highlight the effect and the location on the fuselage that it is most prominent. There are two metrics used to quantify the shielding on the fuselage surface: the difference Δ_{bl} and the shielding coefficient upstream S_+.

The difference Δ_{bl} is defined as before

$$\Delta_{bl} = \mathrm{SPL}_{bl} - \mathrm{SPL}, \tag{5.1}$$

where SPL_{bl} is the sound pressure level calculated with a boundary layer in the modeling, while SPL is the sound pressure level calculated with uniform flow. A value of Δ_{bl} close to zero means little to no shielding since the predicted SPLs are similar with or without the boundary layer. A more negative value of Δ_{bl} means that the predicted SPL with a boundary layer is much lower than the SPL with uniform flow, indicating that less sound energy finds its way to the fuselage surface leading to more shielding.

The shielding coefficient upstream is defined as

$$S_+ = \frac{\sum^{\mathrm{M}} \overline{p^2}_{bl}}{\sum^{\mathrm{M}} \overline{p^2}} \tag{5.2}$$

where M is the number of grid points, $\overline{p^2}_{bl}$ is the mean square pressure with a boundary layer, and $\overline{p^2}$ is the mean square pressure without a boundary layer. The shielding coefficient gives an estimate of the amount of sound energy that reaches the surface of the fuselage. A shielding coefficient value close to zero means that very little energy reaches the surface and most of it is refracted away. A shielding coefficient value closer to unity means that most of the energy reaches the surface indicating little to no shielding.

Apart from these two metrics, predictions of the SPL also will be shown on the fuselage surface. Figure (5.1) shows the locations on the fuselage surface where the metrics/results are calculated. The grid extends from slightly downstream of the plane of the source ($\bar{z}/a_0 = -1$), since the source is located at $\bar{z}/a_0 = 0$, up to $\bar{z}/a_0 = 5$ upstream. More focus is given on the upstream region since the theoretical model developed in this work assumes that there is no nacelle around the fan, and, therefore, ignores diffraction around the nacelle's lip. Therefore, results very close to the plane of the source ($\bar{z}/a_0 = 0$), or downstream of it (negative values of $\bar{z}$), should not be considered realistic.

The shielding coefficient upstream S_+ is a cumulative metric that includes every grid point upstream, both axial and azimuthal. The same is the case when presenting results for the SPL contours that are displayed for the whole range of grid points all over the fuselage surface

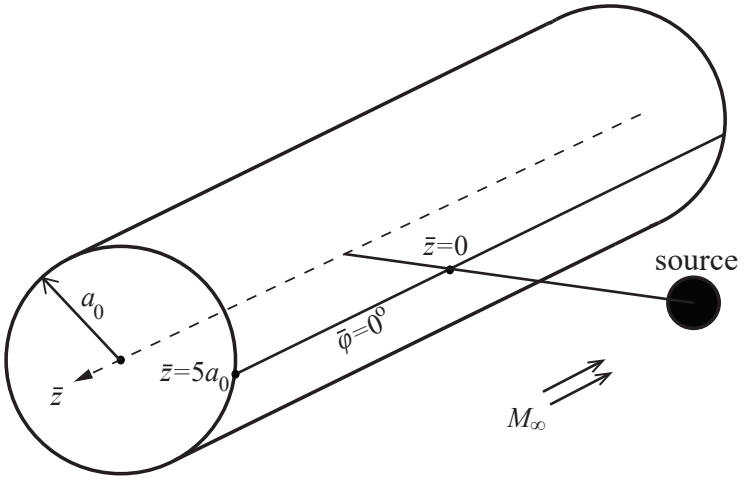

FIGURE 5.1: Schematic of the locations where the sound pressure is calculated.

section shown in Fig. (5.1). Moreover, the difference Δ_{bl}, is chosen to be displayed on the line of azimuthal angle zero, $\bar{\phi} = 0^o$, which is the azimuthal position of the source as well. The difference Δ_{bl} on $\bar{\phi} = 0^o$, gives an insight into the refraction and shielding mechanisms due to the presence of the boundary layer. Additionally, this location represents a region of high interest since it is directly adjacent to the source which means that the highest pressure values will occur there, in contrast to the shadow zone (the region which is not in direct line of sight of the source) which is at around $\bar{\phi} = 180^o$.

5.2 Validation Model

Since the primary aim of this chapter is the validation of the theoretical methods through comparison of their predictions with predictions produced by numerical schemes, a proper configuration must be determined in order for the theoretical results to be comparable with the numerical ones. The only other model that uses a fan noise source such as the one used in this work is the previous work by Gaffney (Gaffney and McAlpine (2017), Gaffney and McAlpine (2018), Gaffney (2016)). According to Gaffney, the dimensions of the following model approximately resemble the dimensions of a twin-engine aircraft for medium haul flights. The dimensions are shown in table 5.1, with all the lengths normalised with the fuselage radius which will be chosen as unity, $a_0 = 1$. All the following examples in this chapter use these dimensions.

Parameter	Value
a/a_0	0.5
b/a_0	3
β	0^o
$\bar{z}/a_0$	[-1,5]

TABLE 5.1: Dimensions of validation model as used in Gaffney (2016).

5.3 Velocity Profile Matching

As already mentioned, the aim of this work is to prove that a simplified boundary layer velocity profile can successfully approximate a more complex profile. It is apparent that an arbitrary linear velocity profile or step-function velocity profile will not produce results that closely match those of a more complex profile such as the 1/7th power-law or a quarter-sine profile. Physically speaking, it is clear that an equivalent linear velocity profile with no slip at the wall with the same thickness as a 1/7th power-law boundary layer profile will not match the power-law profile. It is therefore necessary that the equivalent simplified profiles that are used in this work are prescribed in such a way that they at least physically resemble the original profile that they are supposed to approximate. This is done by manipulating the thickness of the equivalent profiles, δ_L for the linear or δ_{SF} for the step-function profile, and the slip at the wall M_w for the linear profile, or the internal Mach number M_0 for the step-function velocity profile.

Some researchers (Hanson (1984) and Mariano (1971)) have suggested approaches that could be used to create equivalent simplified profiles to match more complex ones. Hanson (1984) suggested using the displacement thickness of the original profile as the thickness of an equivalent step-function profile. Mariano (1971) suggested using an equivalent linear profile with a thickness half that of the original 1/7th power-law profile and no slip at the wall. However, such methods are largely empirical, and are applicable for numerical methods as explained by Mariano (1971), who used the half-thickness rule when utilising a finite-difference scheme. In this work a more robust and physically based approach is chosen in order to create equivalent simplified profiles. More specifically, the concept of the matching methods presented here is to create equivalent profiles that match the same physical properties as the original more complex and realistic profile.

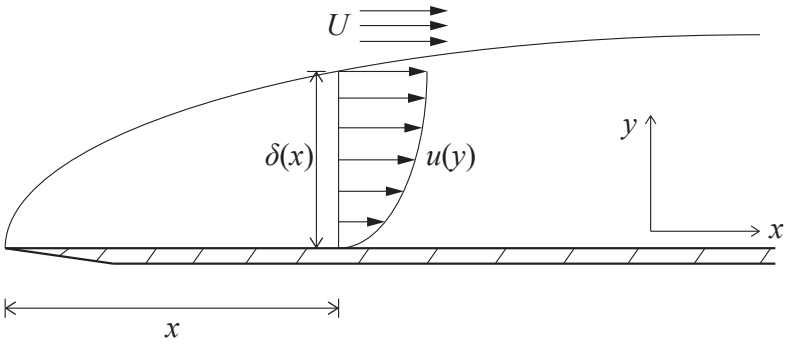

FIGURE 5.2: Boundary layer growth over a flat plate.

The quantities or properties that physically define a boundary layer and are chosen to be investigated here are the displacement thickness, δ^*, momentum thickness ϑ and the shape factor H. The displacement thickness represents the mass flowrate that is lost due to the presence of friction in the flow (which consequently forms the boundary layer):

$$\delta^* = \int_{y=0}^{\delta} (1 - \frac{u}{U}) \mathrm{d}y. \tag{5.3}$$

The momentum thickness represents the momentum flowrate that is lost due to the presence of friction in the flow:

$$\vartheta = \int_{y=0}^{\delta} \frac{u}{U}\left(1 - \frac{u}{U}\right)\mathrm{d}y. \tag{5.4}$$

The shape factor is their ratio, $H = \frac{\delta^*}{\vartheta}$ which provides a more complete overview of the physical properties of the boundary layer.

For any velocity profile, these integrals can be solved to produce expressions that relate the boundary-layer thickness of the profile with the displacement and momentum thickness of the profile. Also, in the case of the linear or step-function velocity profiles, the slip at the wall and the internal Mach number also appear in the expressions. Thus, by equating two physical properties of the original velocity profile with the same physical properties of the equivalent profile (linear or step-function) one can obtain appropriate values for the rest of the necessary characteristics in order to create the equivalent profile, namely the actual thickness and the slip at the wall (in the linear profile case) or the actual thickness and the internal Mach number (in the case of the step-function velocity profile).

Three matching methods have been investigated and their results are presented later on.

(i) *Equal shape factor method*: The equivalent profile is assumed to have the same ratio of displacement and momentum thicknesses as the original profile (or in practice match both the displacement and momentum thicknesses to equate the shape factor). This yields appropriate values for the actual thickness of the equivalent profile (δ_L or δ_{SF}) and its slip on the wall M_w (for the linear profile case) or its internal Mach number M_0 (for the step-function profile case).

(ii) *Equal actual and displacement thickness method*: The equivalent profile is assumed to have the same actual and displacement thickness as the original profile. This yields an appropriate value for the equivalent profile's slip on the wall M_w (for the linear profile case) or its internal Mach number M_0 (for the step-function profile case).

(iii) *Equal actual and momentum thickness method*: The equivalent profile is assumed to have the same actual and momentum thickness as the original profile. This yields an appropriate value for the equivalent profile's slip on the wall M_w (for the linear profile case) or its internal Mach number M_0 (for the step-function profile case).

For instance, consider the example of creating an equivalent linear profile to match a 1/7th power-law profile using the method of equal shape factor. There are two unknowns in the problem, δ_L and M_w. By assuming an equal shape factor (or equal displacement and momentum thicknesses) and a known power-law boundary-layer thickness δ_{PL}, there are two equations that can be used to solve for the two unknown variables. The two equations are $\delta_L^* = \delta_{PL}^*$ and $\vartheta_L = \vartheta_{PL}$ where the PL subscript denotes a 1/7th power-law property. From eqs. (5.3) and (5.4), one can obtain, $\delta_L^* = \frac{1}{2}\left(1 - \frac{M_w}{M_\infty}\right)\delta_L$, $\vartheta_L = \frac{1}{6}\left(1 - \frac{M_w}{M_\infty}\right)\left(1 + 2\frac{M_w}{M_\infty}\right)\delta_L$, $\delta_{PL}^* = \frac{1}{8}\delta_{PL}$ and $\vartheta_{PL} = \frac{7}{72}\delta_{PL}$. Therefore, one can solve for δ_L and M_w to obtain $M_w = \frac{2}{3}M_\infty$ and $\delta_L = \frac{3}{4}\delta_{PL}$.

The same procedure is carried out for each of the other two methods and for any profile. Figure (5.3) shows the resulting equivalent linear profiles that match the 1/7th power-law profile with each approach. In contrast to Mariano's empirical method, the other physically-based methods are a better visual approximation to the profile. As shown in

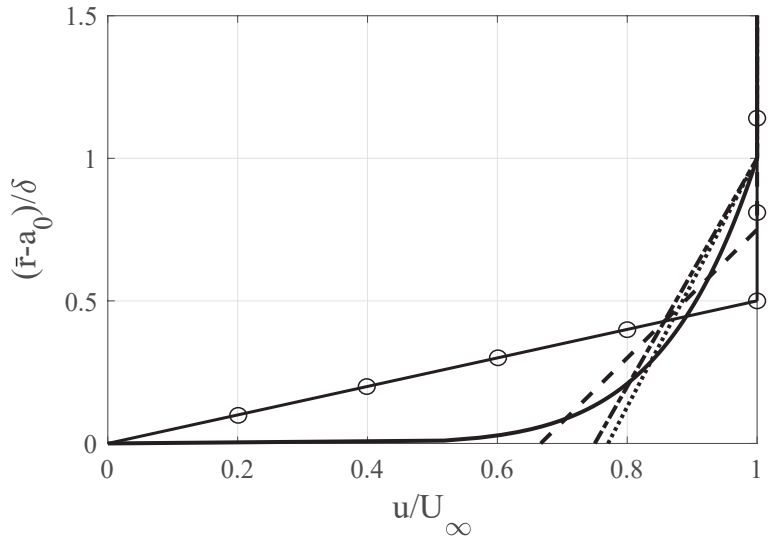

FIGURE 5.3: 1/7th power-law profile [solid line] and the equivalent linear velocity profiles that match it. Equal shape factor method [dashed line], equal actual and displacement thickness method [dash-dotted line], equal actual and momentum thickness method [dotted line], empirical method by Mariano (1971) [solid line-(◯)].

Fig. (5.3), the power-law profile exhibits a sublinear region which is characterised by very high Mach number very close to the surface. That is reflected in the matching equivalent linear profiles by the fact that they exhibit very high Mach number at the wall. On the other hand, Mariano's matching does not succeed in resembling the original power-law, since the resulting linear profile is much thinner and in combination with zero Mach at the wall, it leads to a profile with a very steep gradient that is uncharacteristic of the original power-law profile. The gradients of the other matching linear profiles are far more successful in approximating the gradient of the original power-law profile.

An investigation has been carried out to determine which of these matching approaches proves to be optimal in approximating the original profile. An example is given here in Fig. (5.4) for a 1/7th power-law profile. This result can also be found in the published papers by Rouvas and McAlpine (2022a) and Rouvas and McAlpine (2022b). It is observed that Mariano's matching method is not applicable in this kind of theoretical analysis. Even though the prediction does capture the modal pattern for that frequency, it is clear that it grossly overpredicts shielding (more negative values of Δ_{bl}). On the other hand, the physically-based methods are much more accurate both in depicting the modal pattern of the shielding and the amplitude. It is quite clear that Mariano's empirical rule is not suitable to apply in this work, whereas the physically-based methods produce far more realistic predictions comparable with numerical results for a power-law profile.

By examining how the three physically-based approaches differ from each other, one can see that the most accurate prediction is that of the equal shape factor equivalent linear profile. Its accuracy is retained for the whole range of calculations, with a slight underprediction of shielding compared to the numerical result. By comparing Figs. (5.3) and (5.4) some useful

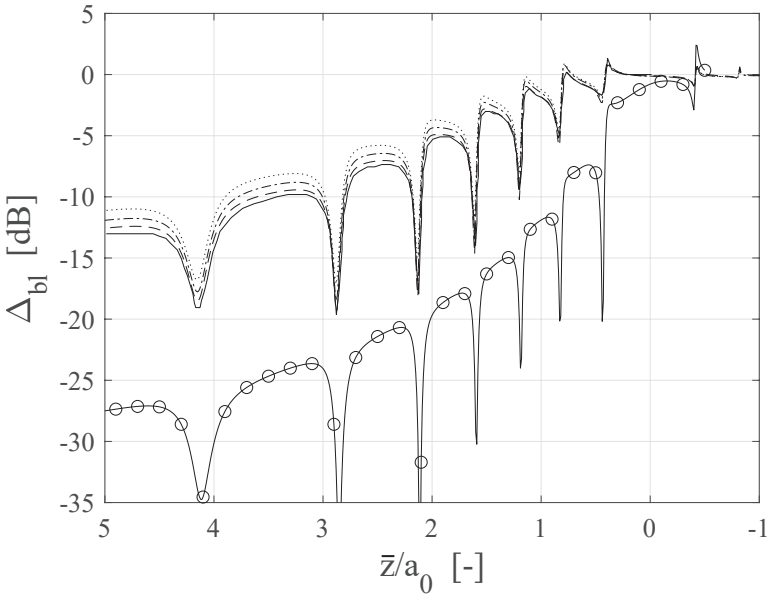

FIGURE 5.4: Δ_{bl} at $\bar{\phi} = 0^o$. Numerical prediction using 1/7th power-law profile recreated from Gaffney (2016) [solid line]. Theoretical predictions using equivalent linear profiles to match the power-law profile with equal shape factor method [dashed line], equal actual and displacement thickness method [dash-dotted line], equal actual and momentum thickness method [dotted line] and empirical method by Mariano (1971) [solid line-(◯)]. The other parameters are: $k_0 a = 20$, $M_\infty = 0.75$, $\delta = 0.01 a_0$ and $(l, q) = (4, 1)$.

conclusions can be drawn. Although the equal actual and displacement thickness method and the equal actual and momentum thickness method produce equivalent profiles that are thicker than the profile produced by the equal shape factor method, they predict less shielding. This is somewhat unexpected and counter-intuitive. It is reasonable to expect that thicker layers would produce more shielding since sound waves are more exposed to the refraction properties of the layer. Yet, this is not the case here, where thicker layers appear to produce less shielding. The reason that the equal shape factor method profile produces more shielding even though it is thinner is because of its steeper gradient compared to the other two profiles. This effect can also be observed by examining the two equivalent profiles produced by the actual and displacement thickness method and the actual and momentum thickness method. They both have the same thickness but the equal actual and displacement method profile has a slightly steeper gradient, which leads to a prediction of slightly more shielding.

The equal shape factor equivalent profile proves to be the most representative way to simplify a more complex profile. Its thickness and gradient are arranged in such a way that they successfully approximate the same effect as a more complex profile. This is not unexpected considering that of all the three equivalent profiles produced by each of the matching approaches, the equal shape factor profile most closely physically resembles the original profile. It displaces the same mass and momentum flowrate as the original profile, while the other two equivalent profiles only match one of the physical properties of the original profile they are based on. This effect makes the equal shape factor the optimal approach for matching a complex velocity profile. Therefore the results that follow in this thesis use equivalent

simplified profiles (linear or step-function) that have equal shape factor with the actual profile they are approximating.

5.4 Boundary Layer Effect

This section is dedicated to the validation of the ability of the theoretical methods to successfully quantify the boundary layer effect. This section's main scope is comparison with existing numerical results. As in Fig. (5.4), the theoretical predictions of shielding will be compared with numerical predictions conducted by Gaffney (2016). Gaffney used a numerical Runge-Kutta scheme to solve the problem of sound propagation through a shear layer. The fan noise source he used was very similar to the one used in this work except that he also included diffraction around the lip of the fan duct by using a Wiener-Hopf solution for a mode exiting a circular duct (Gaffney and McAlpine (2018), Gaffney (2016)). According to his findings, the only substantial differences between the two sources (disc source used here versus the Wiener-Hopf source used in Gaffney and McAlpine (2018)) are manifested for polar angles close to or over 90^o. In axial coordinates, that means the differences will be at $\bar{z}$ very close to the source and downstream of the source (negative $\bar{z}$).

The theoretical predictions are compared with the numerical results for a wide variety of different examples. Different frequency, azimuthal order, free stream Mach number, velocity profile and boundary-layer thickness examples are included in the comparisons. Thus, not only the comparisons that demonstrate the validation of the theoretical methods are presented, but also the important trends are identified along with the effects the source and flow characteristics have on the shielding. The numerical predictions are either taken directly from the results in Gaffney (Gaffney and McAlpine (2017), Gaffney and McAlpine (2018), Gaffney (2016)), or results are recreated using the code developed by Gaffney.

For the majority of the results, the equivalent linear profile is primarily used for the predictions, but several examples of the equivalent step-function profile prediction are also shown. Towards the end of the chapter, a more comprehensive investigation into the differences between the two theoretical methods is presented.

Firstly, the effects of the source characteristics on the shielding are investigated. After that, the effects of the flow characteristics on the shielding are investigated. However, the boundary-layer thickness effect, despite being a flow characteristic, is investigated separately due to its importance on the shielding and its influence on the accuracy of the equivalent linear profile theoretical method. Since the shielding effect is of utmost importance here, the shielding metrics Δ_{bl} and S_+ are used to quantify it. Moreover, the SPL contours are shown on the surface of the fuselage which also gives valuable insight into the shielding problem. Note that when the SPL is shown it is normalised by taking the maximum value of the SPL to equal 0 dB.

5.4.1 Source Characteristics

In this section the effect of the source characteristics on the shielding is investigated. The source characteristics, frequency and azimuthal order of the mode, are varied whereas the rest of the variables of the problem remain unchanged. The aim is to identify trends and the sensitivity of shielding on varying the source characteristics. Comparisons with numerical results are presented. The numerical results have been generated using a quarter-sine profile

$$M = M_\infty \sin\left(\frac{\pi}{2\delta}\bar{r}\right), \tag{5.5}$$

thus the theoretical predictions will use equivalent profiles that match that quarter-sine profile. The results will be presented for two boundary-layer thicknesses, thin ($\delta = 0.01a_0$) and thick ($\delta = 0.1a_0$), and for uniform flow ($\delta = 0$).

5.4.1.1 Frequency

Frequency is one of the key source characteristics, and in all the examples its non-dimensional form is used, i.e. the Helmholtz number k_0a. The calculations conducted are for k_0a=[5, 10 and 20], which represents a fairly wide range of frequencies. As will be seen in later chapters, $k_0a = 5$ is a very low blade passing frequency during flight whereas $k_0a = 20$ represents a relatively high blade passing frequency often occurring during the climbing phase of flight when the engine operates at high rpm. All other parameters are kept constant: flight Mach number $M_\infty = 0.75$ and incident mode $(l, q) = (4, 1)$. This incident mode is chosen because it is well cut-on and also it could represent a rotor-stator interaction mode.

Figures (5.5) and (5.6) show predictions of the SPL contours on the fuselage surface. The difference in the frequency is clearly visible when observing the uniform flow results (i.e. $\delta = 0$). The lower frequency produces a much smoother and simpler pressure pattern than the higher frequency that is characterised by a more complex lobed pattern, which is typical of high frequency. Another expected difference between low and high frequency is the location of the maximum SPL or the location of the principal lobe incident on the fuselage. That difference is expected and common in fan noise directivity and propagation since higher frequency leads to higher cut-off ratio. In turn, higher cut-off ratio means that the propagation angle of the principal lobe will be closer to being parallel to the duct's centerline. Therefore, it will be incident on the fuselage further upstream as seen in Figs. (5.5[top]) and (5.6[top]) where the maximum SPL is further upstream in the higher frequency case.

The drastic effect of the boundary layer is clearly visible even for the thin boundary-layer case. For both frequency cases the presence of a boundary layer causes the maximum SPL location to move closer to the plane of the source indicating more refraction upstream. Sound refraction upstream is more pronounced because the further upstream the sound propagates the shallower the angle that it is incident on the boundary layer. That means that the sound will enter the boundary layer at a more oblique fashion making it more susceptible to refraction. Another way of looking at this phenomenon is that the shallower the angle of incidence on the boundary layer the greater the distance inside the layer sound has to travel in order to reach the fuselage, rendering the boundary layer effectively thicker. That increase in

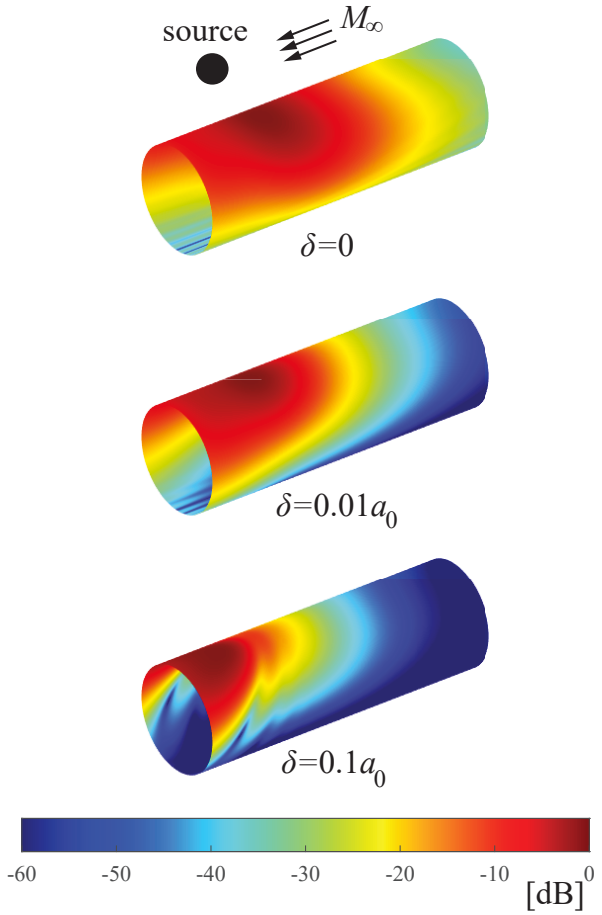

FIGURE 5.5: Total SPL on the surface of the fuselage for uniform flow and two boundary-layer thickness cases with the quarter-sine profile. The other parameters are: $k_0 a = 5$, $M_\infty = 0.75$ and $(l, q) = (4, 1)$.

the effective thickness upstream leads to more refraction and therefore shielding upstream. On the other hand, closer to the plane of the source, sound is incident on the boundary layer at a much steeper angle (almost perpendicular) leading to minimal refraction. At that location only the significantly weaker effect of refraction at the azimuthal direction takes place since convection effects become irrelevant.

The thickness effect is also very clear when comparing the two thickness cases for each of the frequency cases. The thicker boundary-layer produces drastically more shielding than the thinner boundary-layer case. Once again, that is because sound travels a greater distance inside a thicker boundary layer than it does inside a thinner one. That makes it more susceptible to refraction. Even for the thin boundary-layer case, the shadow zone is extended compared to the uniform flow case. With the presence of a boundary layer that refracts sound to the extent that the sound does not reach the surface, it is expected that less sound will diffract around the cylindrical surface to reach the shadow zone. Furthermore, away from $\bar{\phi} = 0^o$, sound will be incident on the boundary layer at shallower angles meaning more refraction as explained before. That will inevitably enlarge the shadow zone. Some minor instabilities in the pattern are observed at high frequency and with a thick boundary-layer, which are expected because the theoretical method is less valid as the boundary-layer thickness is increased. That is exacerbated by the fact that higher frequency means shorter

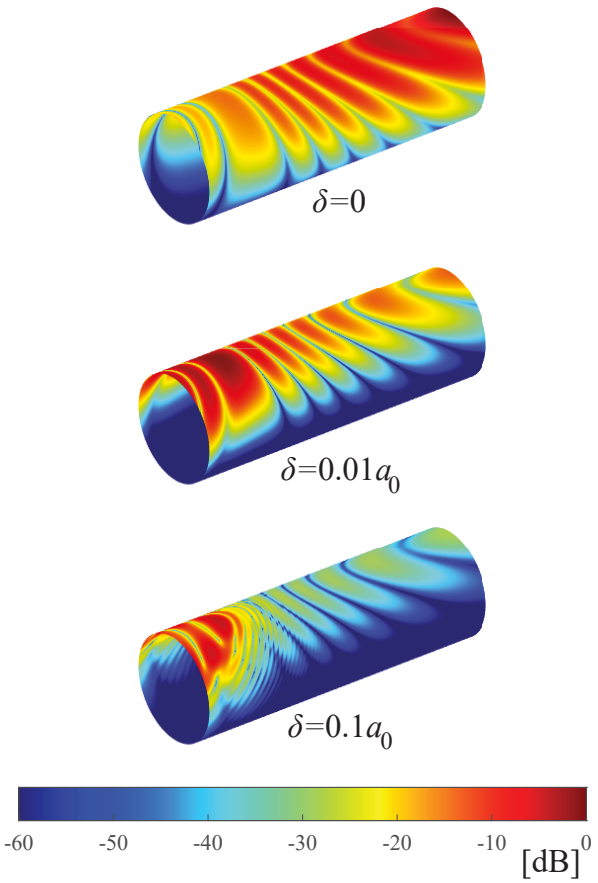

FIGURE 5.6: Total SPL on the surface of the fuselage for uniform flow and two boundary-layer thickness cases with the quarter-sine profile. The other parameters are: $k_0 a = 20$, $M_\infty = 0.75$ and $(l, q) = (4, 1)$.

wavelengths compared to the boundary-layer thickness resulting in effectively a larger thickness.

Figures (5.5) and (5.6) give a good insight into how the presence of the boundary layer affects the resulting pressure pattern on the fuselage surface. However, they are illustrative results. Therefore, the following figures include comparisons with existing numerical results in order to verify and validate the theoretical method to predict the realistic effect of the boundary layer. Figure (5.7) shows the difference Δ_{bl} which is the main shielding metric. The effect the thickness has on the shielding stands out clearly. The thicker boundary-layer case produces up to three times more shielding than the thin boundary-layer case.

Moreover, the effect the frequency has on the shielding cannot be ignored. Lower frequency generally produces less shielding. This is expected due to the effective thickness phenomenon explained before. Lower frequency sound has larger wavelengths, while higher frequency sound has shorter wavelengths. When the wavelengths are significantly shorter compared to the boundary-layer thickness, the refraction effect is more pronounced because effectively the sound travels a greater distance inside the boundary layer. Therefore, the higher the frequency the thicker the effective boundary layer leading to more refraction and shielding. This frequency effect is found to be quite substantial by observing the thick boundary-layer case

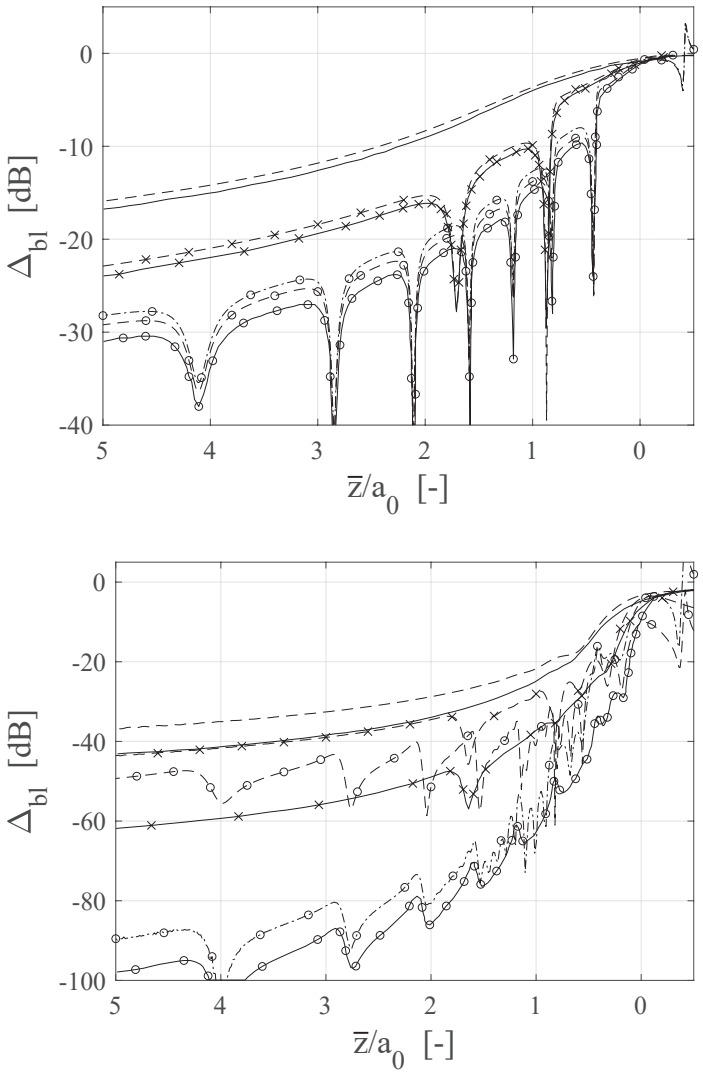

FIGURE 5.7: Δ_{bl} at $\bar{\phi} = 0^o$ for $\delta = 0.01a_0$ [top] and $\delta = 0.1a_0$ [bottom]. Numerical predictions using a quarter-sine profile recreated from Gaffney (2016) [solid lines]. Theoretical predictions using an equivalent linear profile to match the quarter-sine profile [dashed lines]. Theoretical predictions using an equivalent step-function profile to match the quarter-sine profile [dash-dotted line]. Results for frequencies $k_0a = 5$ [no marker], $k_0a = 10$ [$\times$] and $k_0a = 20$ [$\bigcirc$]. The other parameters are: $M_\infty = 0.75$ and $(l, q) = (4, 1)$.

where the high frequency upstream shielding reaches up to 90 dB, effectively reaching the same levels as the shadow zone region. It is safe to conclude that the shielding is highly sensitive to changes in the frequency.

It is also important to note, that the upstream effect on the shielding is also very significant. As seen before in Figs. (5.5) and (5.6), the further upstream the sound travels the more likely it is to be refracted away. This is reflected on the difference Δ_{bl} as well, where it is observed that the shielding is steadily increased with increasing $\bar{z}$. Once again, an alternative way of explaining this upstream effect is the effective thickness of the boundary layer. The further upstream the sound travels the shallower the angle that it is incident on the layer. By entering the layer at a more oblique fashion, the sound has to travel a greater distance inside the layer

(effectively making the boundary layer thicker) and that makes it more susceptible to refraction. By observing the higher frequency predictions one can notice that for further upstream $\bar{z}$, the shielding seems to stabilise at a constant value. That is because at these upstream regions, total reflection is starting to occur. No matter how much further upstream the sound travels, it is incident on the layer at such a shallow angle that it never reaches the fuselage surface stabilising the quantifiable shielding.

Having identified the trends present, next the comparisons between the theoretical and numerical predictions are examined. For the thin boundary-layer case, the two predictions are remarkably close to each other across the range of frequencies. Nevertheless, their discrepancy is smaller for the lower frequency. That is explained through the frequency-wavelength effect, since higher frequency means effectively a thicker layer which leads to a deterioration in the accuracy of the equivalent linear profile approach as seen in chapter 3. This deterioration in accuracy due to increased boundary-layer thickness is clearly visible in Fig. (5.7[bottom]), where for the thick boundary-layer case only the low frequency predictions agree with each other. For the higher frequencies the equivalent linear profile prediction struggles to capture the same level of shielding as the numerical prediction. Especially for the $k_0 a = 20$ case (the effectively thickest boundary-layer case), the underprediction of the equivalent linear profile approach is close to 40 dB. It is safe to conclude that the equivalent linear profile approach is not valid for very thick boundary layers as the theory in chapter 3 is based on an asymptotic expansion for a thin boundary-layer.

On the other hand, the illustrative prediction of the equivalent step-function profile displays an unexpected result. Although for the thin boundary-layer case the predictions of the two equivalent simplified profile approaches are very close to each other with the equivalent linear profile prediction being a little better at approximating the numerical prediction, for the thick boundary-layer case the equivalent step-function profile approach seems to retain similar accuracy as in the thin boundary-layer case, and it is significantly better at approximating the numerical prediction than the equivalent linear profile approach. This ability of the equivalent step-function profile approach to retain its accuracy stems from the fact that during its derivation there is no constraint or limitation imposed on the boundary-layer thickness as opposed to the equivalent linear profile approach which is based on the boundary layer being sufficiently small. Nevertheless, for the thicker boundary-layer case the discrepancy between the equivalent step-function profile prediction and the numerical prediction slightly larger. That is expected since the thinner the boundary layer, the easier it is for it to be asymptotically similar to a simplified profile. A more robust comparison between the two theoretical approaches will be conducted later on towards the end of this chapter.

Lastly, the frequency effect on the shielding is demonstrated in terms of the shielding coefficient upstream S_+ in Fig. (5.8). For the thick boundary-layer case the vast majority of the incident energy is refracted away with only less than 1% of it reaching the fuselage surface. Only for very low frequencies, when the effective thickness is somewhat smaller, is the shielding coefficient above 1%. For the thin boundary-layer case, the same slight underprediction in shielding as before is shown here. This slight discrepancy between the theoretical and numerical prediction is also apparent for the thick boundary-layer case. However, this discrepancy is not as large as it was in the Δ_{bl} at $\bar{\phi} = 0^{\text{o}}$ results. On the contrary the two predictions almost coincide with each other. This is because the shielding coefficient

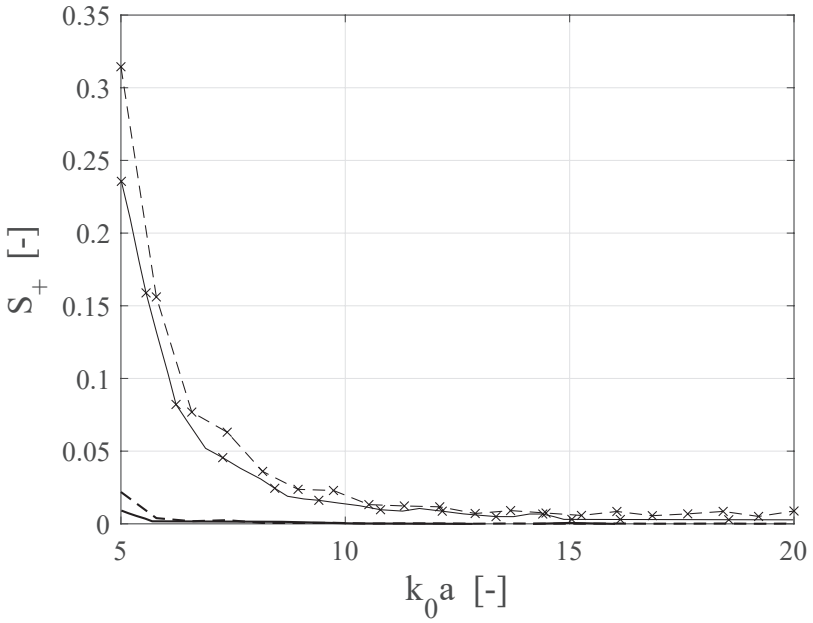

FIGURE 5.8: Shielding coefficient upstream S_+ vs. Helmholtz number. Numerical predictions using a quarter-sine profile recreated from Gaffney (2016) [solid lines]. Theoretical predictions using an equivalent linear profile to match the quarter-sine profile [dashed lines]. Results for $\delta = 0.01a_0$ [$\times$] and $\delta = 0.1a_0$ [no marker]. The other parameters are: $M_\infty = 0.75$ and $(l, q) = (4, 1)$.

S_+ is a cumulative metric taking into consideration the whole surface of the cylinder. Therefore, the vast amounts of shielding in the shadow zones or close to the shadow zone dominate the final value of the coefficient, making the discrepancies in Fig. (5.7[bottom]) which shows the shielding on the near side of the cylinder, irrelevant. The severe sensitivity of shielding on the frequency is exhibited here until about $k_0a = 10$. For higher frequencies this sensitivity disappears because total reflection occurs at most of the cylinder area, leading to a stabilisation of the shielding coefficient.

5.4.1.2 Azimuthal order

In this section, the effect of varying azimuthal order l is investigated. The numerical results that are used for comparison use a quarter-sine profile, thus the equivalent profiles will match that profile. The Mach number is constant at $M_\infty = 0.75$ and the frequency at $k_0a = 20$. The azimuthal order varies to the value of 24 where the mode is barely cut-on. This allows an investigation in a wide range of cut-off ratios.

Figure (5.9) shows the difference Δ_{bl} for the thin boundary-layer case. For the more well cut-on mode (16,1) the pattern exhibits fewer lobes and nulls than that of mode (4,1) shown in Fig. (5.7), which is expected for a mode of lower cut-off ratio. Even simpler is the lobed pattern of the just cut-on mode (24,1) for the same reason. By comparing the predictions of the two modes one can surmise that the mode's azimuthal order does not affect shielding. The shielding levels for both modes follow the same general pattern with the same amplitude

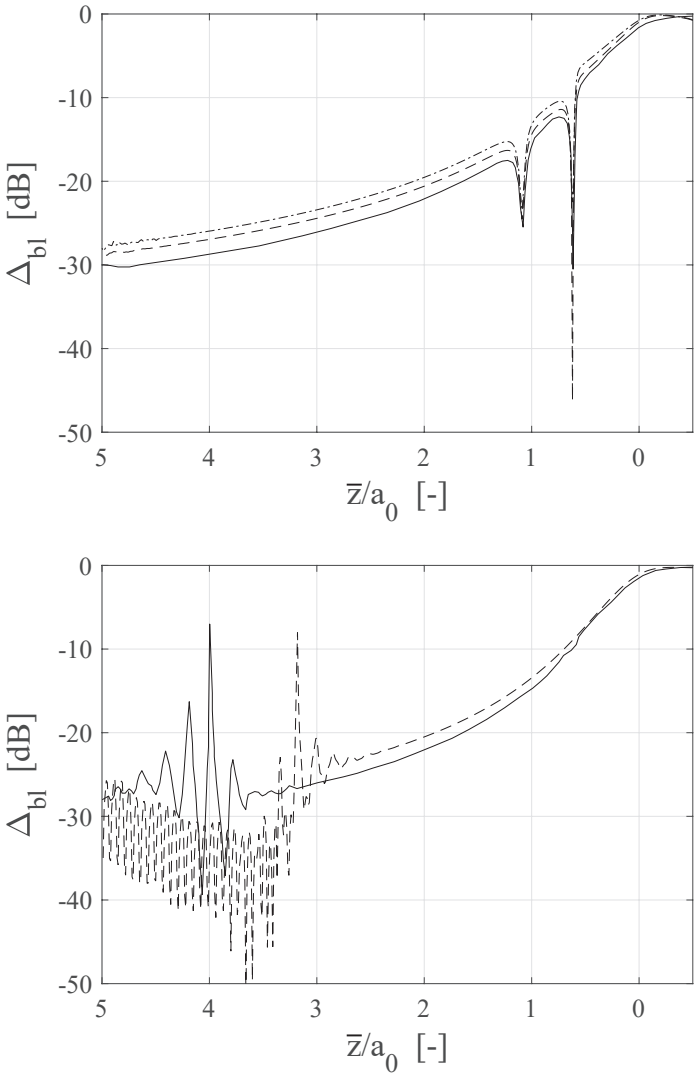

FIGURE 5.9: Δ_{bl} at $\bar{\phi} = 0^o$ for $(l,q) = (16,1)$ [top] and $(l,q) = (24,1)$ [bottom]. Numerical predictions using a quarter-sine profile recreated from Gaffney (2016) [solid lines]. Theoretical predictions using an equivalent linear profile to match the quarter-sine profile [dashed lines]. Theoretical predictions using an equivalent step-function profile to match the quarter-sine profile [dash-dotted line]. The other parameters are: $M_\infty = 0.75$, $k_0 a = 20$ and $\delta = 0.01 a_0$.

more or less at -25 dB at $\bar{z}/a_0 = 3$ and -20 dB at $\bar{z}/a_0 = 1.5$. Further upstream than $\bar{z}/a_0 = 3$ the predictions for the just cut-on mode (24,1) exhibit major instabilities in the shielding pattern. These instabilities are attributed to numerical noise. The just cut-on mode (24,1) propagates in a single principal lobe travelling at an almost perpendicular angle from the fan duct. This makes the principal lobe incident on the fuselage very close to the plane of the source. Further upstream the sound field is comprised of a null zone, which typically exhibits pressure levels close to 100 dB lower than the lobe areas. Therefore the difference Δ_{bl} at this region will involve differences between very small values that reach the numerical noise floor making the pattern very unstable.

The agreement between the theoretical predictions and the numerical prediction continues to

be very good. Moreover, their discrepancy does not appear to be affected by the azimuthal order. The only substantial difference between the two predictions is in the upstream region of the (24,1) mode case. However, this region, as explained before, is effectively a shadow zone characterised by very small values that reach the numerical noise floor. Therefore, the discrepancies there stem from the differences in the two prediction methods and the way they handle very small values. The equivalent step-function approach exhibits lower accuracy than the equivalent linear approach for this thin boundary-layer thickness as in the previous case of the more cut-on mode (4,1). It is safe to conclude that the predictions agree well with each other, and the accuracy of the theoretical predictions does not depend on the azimuthal order of the mode.

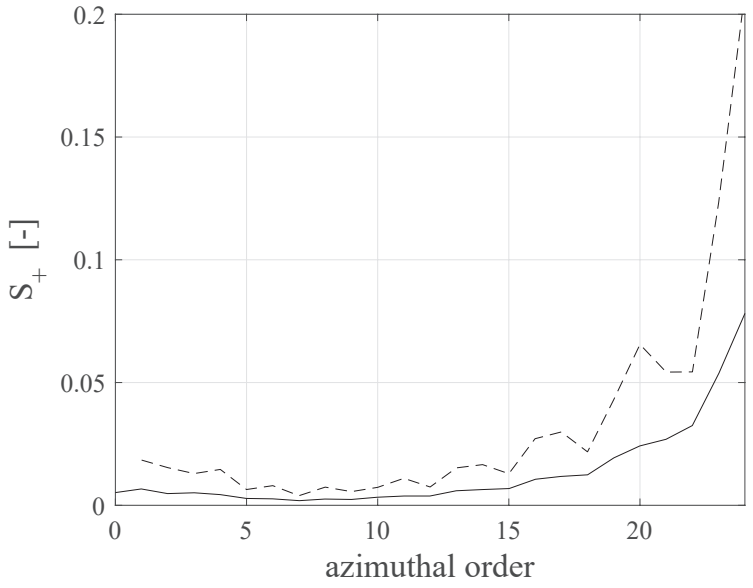

FIGURE 5.10: Shielding coefficient upstream S_+ vs. azimuthal order. Numerical prediction using a quarter-sine profile recreated from Gaffney (2016) [solid line]. Theoretical prediction using an equivalent linear profile to match the quarter-sine profile [dashed line]. The other parameters are: $M_\infty = 0.75$, $k_0 a = 20$ and $\delta = 0.01 a_0$.

On the other hand, by observing Fig. (5.10) one can notice a sudden decrease in overall shielding for less cut-on modes (higher azimuthal orders). As long as the modes are fairly well cut-on, there is minimal change in the shielding coefficient. As soon as the modes become closer to cut-off, the coefficient S_+ exhibits an increase, indicating a decrease in shielding that is dependent on the azimuthal order. This is attributed to the cut-off ratio of the modes. The lower the cut-off ratio (higher azimuthal order for the same frequency) the steeper the propagation angle of the mode. This means that the mode will be incident on the boundary layer at a steeper angle, and therefore it will be subject to less shielding. The cut-off ratio effect will be discussed in more depth in chapter 7.

This concludes the section dedicated to the source characteristics and how they affect the shielding. Frequency tends to affect shielding in a more drastic way than the azimuthal order, because shorter wavelengths lead to effectively thicker boundary layers. However, the azimuthal order in certain circumstances can lead to significant changes to the shielding. The boundary-layer thickness, effective or actual, proves to be the factor with the most influence

on the shielding results. A thorough investigation into the dependence of shielding on the boundary-layer thickness will be conducted later on. Another key finding is the apparent ability of the equivalent step-function profile approach to retain its accuracy regardless of the boundary-layer thickness. This finding will also be further investigated later on.

5.4.2 Flow Characteristics

In this section the effect of the flow characteristics on the shielding is investigated. The flow characteristics, flow velocity and boundary-layer velocity profile, will be varied, whereas the rest of the variables will remain unchanged. Note that another flow characteristic is the boundary-layer thickness, but since its effect has been proven already to be substantial, it is deemed necessary to be given its own section later on. As before, the aim is to identify trends and the sensitivity of shielding to changes in the flow characteristics, and provide comparisons with numerical results. The results will be presented for the two boundary-layer thicknesses, thin ($\delta = 0.01a_0$) and thick ($\delta = 0.1a_0$), a constant relatively high frequency $k_0a = 20$, which is characteristic of the climbing phase of flight as will be seen in later chapters and explained in the published paper by Rouvas and McAlpine (2022a). The mode will be kept constant at $(l, q) = (4, 1)$ which is well cut-on to avoid any cut-on/cut-off transition effects.

5.4.2.1 Flow Velocity

Flow velocity is one of the major characteristics of the flow and it has been suggested in chapter 4 that it has a similar effect as the frequency. The calculations that have been conducted involve three different free stream Mach numbers, M_∞ =[0.25, 0.5 and 0.75]. The velocity profile is the quarter-sine profile.

Figure (5.11) demonstrates the importance of the Mach number effect. The Mach number affects the shielding in a very similar way that the frequency does. A higher Mach number leads to more shielding in quite a drastic way too. Whereas a low Mach number produces little to no shielding, the more representative flight velocity $M_\infty = 0.75$ produces almost 30 times more shielding. This occurs because the convective effect of the flow effectively shortens the wavelengths upstream of the source. Therefore, a higher free-stream Mach number results in effectively shorter wavelengths, causing more shielding because of the effectively thicker boundary layer compared to the wavelengths.

The comparison with the numerical prediction reveals similar behavior as before. The thin boundary-layer case exhibits very small discrepancies across the range of the free-stream Mach numbers. It is important to note that for the lower Mach numbers the agreement is even better. That is expected because the lower Mach number means that the wavelengths are effectively longer compared to the boundary-layer thickness, effectively leading to a thinner boundary layer increasing the accuracy of the equivalent linear profile approach. An interesting side effect of that is observed in the thick boundary-layer case in Fig. (5.11[bottom]) where the discrepancies between the numerical and the theoretical predictions are more pronounced. Nonetheless, for the low Mach number case, $M_\infty = 0.25$, the discrepancies are uncharacteristic of such a thick boundary-layer case. The discrepancies are not as large as

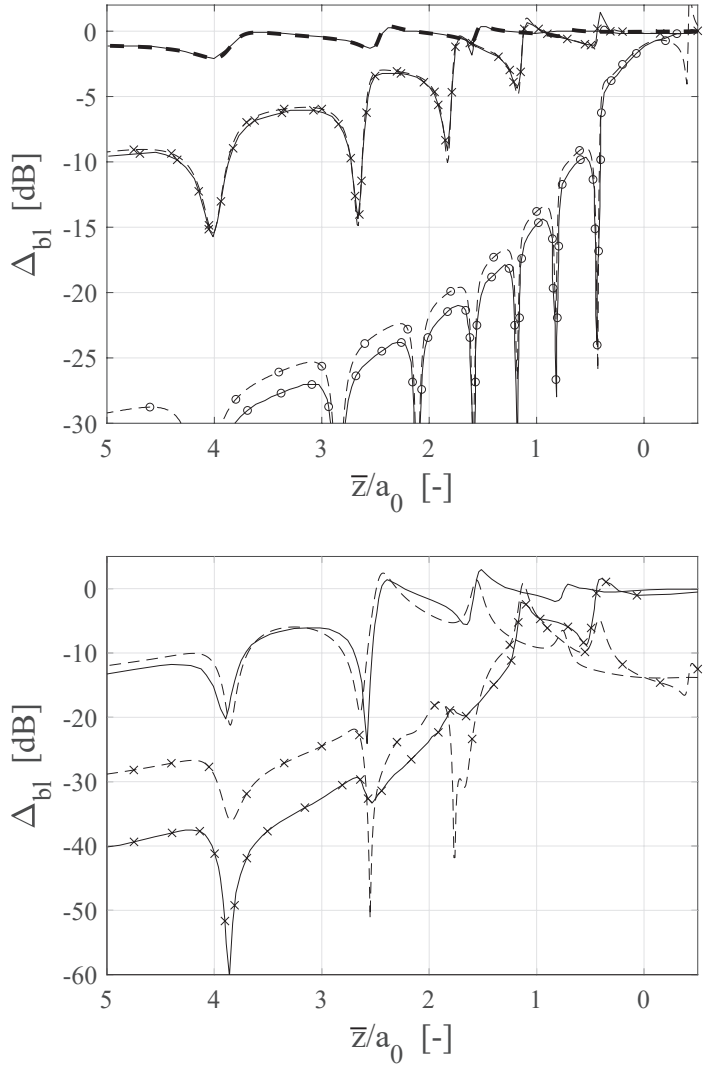

FIGURE 5.11: Δ_{bl} at $\bar{\phi} = 0^o$ for $\delta = 0.01a_0$ [top] and $\delta = 0.1a_0$ [bottom]. Numerical predictions using a quarter-sine profile recreated from Gaffney (2016) [solid lines]. Theoretical predictions using an equivalent linear profile to match the quarter-sine profile [dashed lines]. Results for flow Mach numbers $M_\infty = 0.25$ [no marker], $M_\infty = 0.5$ [$\times$] and $M_\infty = 0.75$ [$\bigcirc$]. The other parameters are: $k_0 a = 20$ and $(l, q) = (4, 1)$.

expected because the thickness effect is mediated by the Mach number effect. Namely, the low Mach number means that the wavelengths are effectively relatively large compared to the boundary-layer thickness. That results in an effectively thinner boundary-layer, thus improving the accuracy of the equivalent linear profile approach.

The shielding coefficient results in Fig. (5.12) reveal once again very good agreement between the numerical and theoretical predictions even for the thicker boundary-layer case. However, the theoretical approach seems to be problematic for very low free-stream Mach numbers with a thick boundary-layer. Normally, the behavior of the S_+ should be as it is depicted in the thin boundary-layer case, namely approaching the value of unity as the flow (and the boundary layer with it) disappears. The theoretical approach involves expressions (eqs. (3.174)-(3.175),

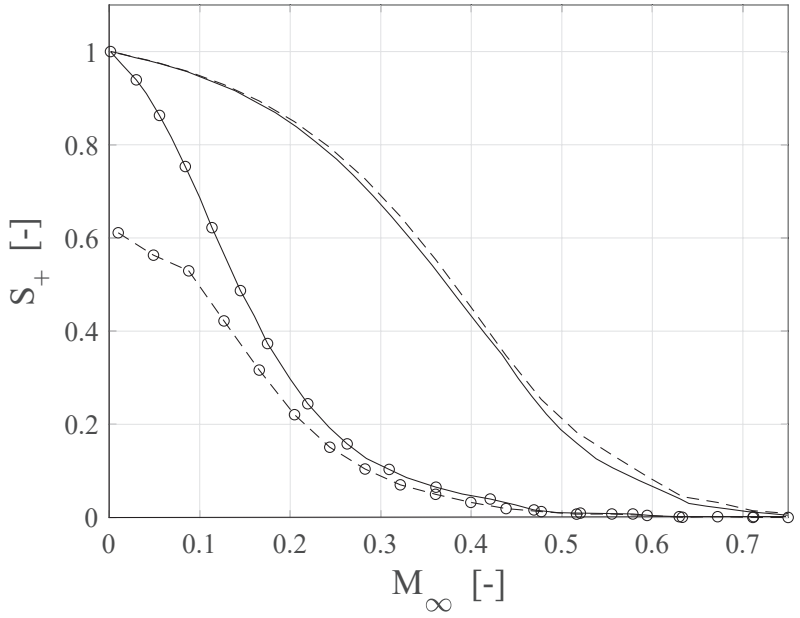

FIGURE 5.12: Shielding coefficient upstream S_+ vs. varying flow Mach number. Numerical predictions using a quarter-sine profile recreated from Gaffney (2016) [solid lines]. Theoretical predictions using an equivalent linear profile to match the quarter-sine profile [dashed lines]. Results for $\delta = 0.01a_0$ [no marker] and $\delta = 0.1a_0$ [◯]. The other parameters are: $k_0 a = 20$ and $(l, q) = (4, 1)$.

(3.191)-(3.192), (3.206)) with terms that become singular when $M_\infty = M_w$. When $M_\infty \to 0$, it follows that $M_w \to 0$. Therefore, with dual limits tending to zero this is very difficult to handle numerically. In the thin boundary-layer case these singular terms are multiplied with a relatively small value of ε (see eqs. (3.191), (3.192) and (3.206)), mediating their effect in the final value of the expression. On the other hand, when the boundary layer is thicker, these singular terms are multiplied by a larger value of ε causing their contribution to dominate the final value of the expression. Thus, the thick boundary-layer case is incorrect for very small Mach numbers.

5.4.2.2 Profiles

In this section, the effect of different boundary-layer velocity profiles is investigated. So far, the quarter-sine profile was being used to produce numerical results, and the theoretical results used profiles that matched that quarter-sine profile. In this section, numerical results generated using an original linear and a 1/7th power-law profile are compared with theoretical results that are generated using equivalent profiles that match those original profiles. The other parameters will be kept constant, $k_0 a = 20$, $M_\infty = 0.75$ and $(l, q) = (4, 1)$.

The theoretical results for a linear profile compare very well against the numerical results only for the thin boundary-layer case in Fig. (5.13). The thick boundary-layer case exhibits very poor agreement between the numerical and the theoretical results. This is consistent with the findings so far that the thicker the boundary layer the worse the accuracy of the equivalent

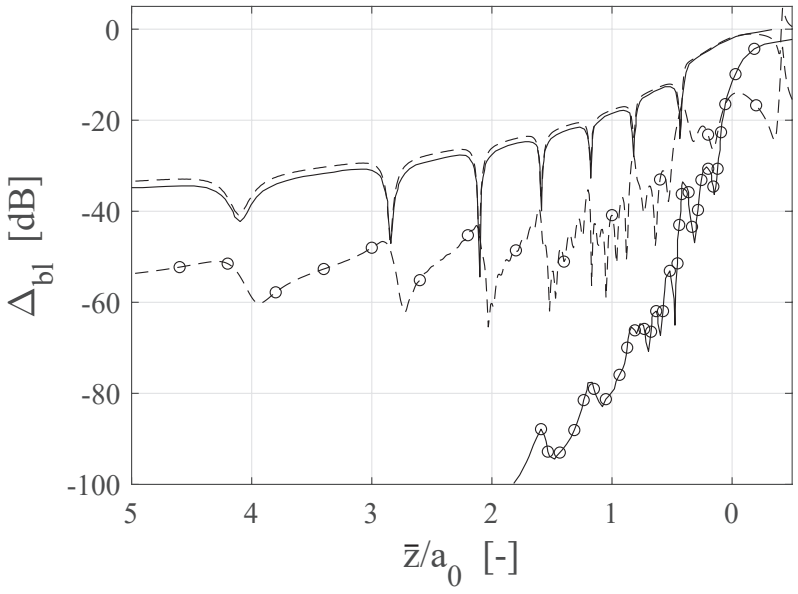

FIGURE 5.13: Δ_{bl} at $\bar{\phi} = 0^o$ for $\delta = 0.01a_0$ [no marker] and $\delta = 0.1a_0$ [◯]. Numerical predictions using a linear profile recreated from Gaffney (2016) [solid lines]. Theoretical predictions using the same linear profile [dashed lines]. The other parameters are: $M_\infty = 0.75$, $k_0 a = 20$ and $(l, q) = (4, 1)$.

linear profile approach. On the other hand, for the power-law results in Fig. (5.14) the predictions are more accurate even for the thick boundary-layer case. For the thin power-law boundary-layer case the two theoretical predictions (equivalent linear and step-function profile approach) are very close to each other and the numerical prediction. For the thick boundary-layer case, the equivalent step-function approach is noticeably closer to the numerical prediction. This finding is once again consistent with previous findings that the equivalent step-function profile approach retains its accuracy regardless of the thickness.

Nonetheless, the equivalent linear profile approach generally behaves better at thicker layers in the case of the power-law profile. This can be seen by comparing Fig. (5.14[bottom]) (which involves matching the power-law profile) against Figs. (5.7[bottom]) and (5.13) (which involve the same examples but for matching a quarter-sine and a linear profile respectively). It can be seen that the discrepancy between the theoretical prediction and the numerical prediction is much smaller in the power-law case (Fig. (5.14[bottom])) than in the other profiles (Figs. (5.7[bottom]) and (5.13)) for the same axial locations. This increased accuracy stems from the fact that the power-law profile generally produces less shielding than the other two. The numerical prediction for the power-law profile shielding is close to -60 dB, whereas for the other two profiles it is -100 dB or more. More shielding implicitly suggests an effectively thicker layer which, as has been seen, has an adverse effect on the accuracy of the equivalent linear profile approach.

Another more quantifiable way of explaining this is by examining the thicknesses of the equivalent linear profiles that attempt to match the more complex profiles. The three original profiles in Figs. (5.7), (5.13) and (5.14) have equal thicknesses, $\delta_{QS} = \delta_{L,original} = \delta_{PL} = 0.1a_0$, respectively. The equivalent linear profile to match these profiles will have thicknesses,

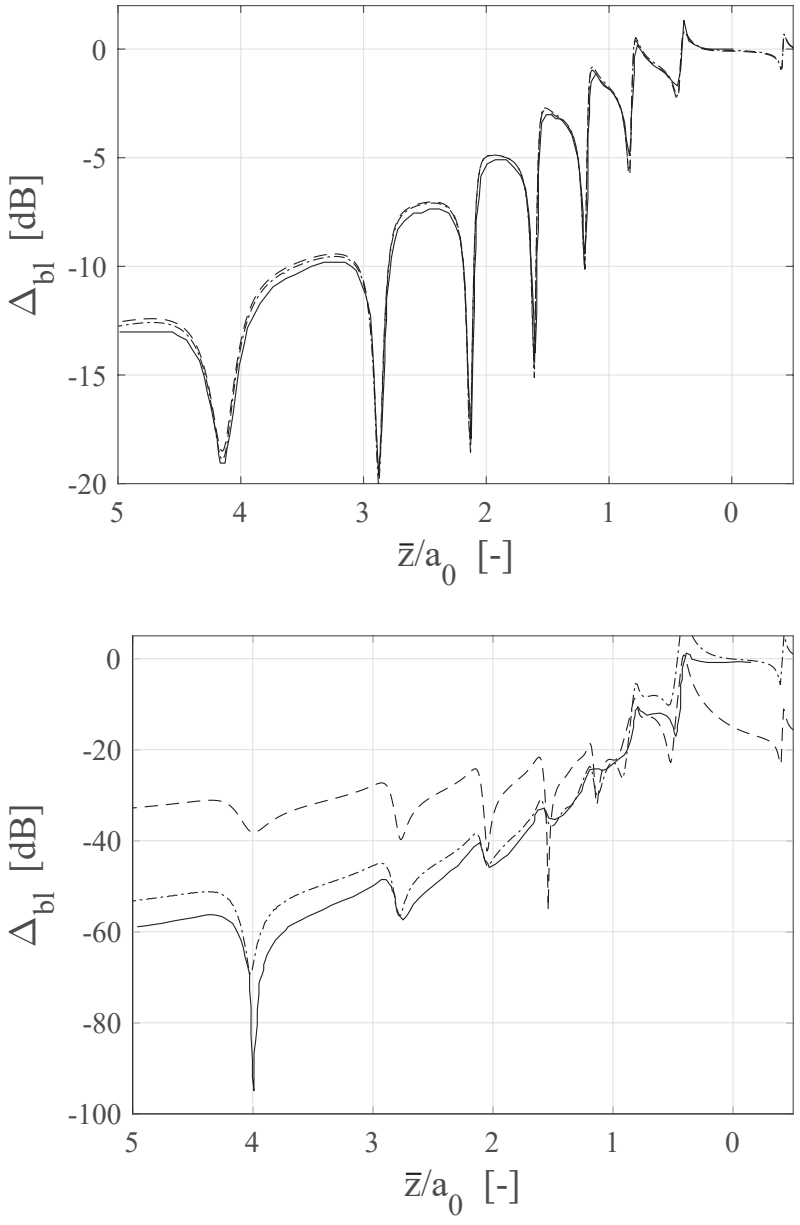

FIGURE 5.14: Δ_{bl} at $\bar{\phi} = 0^o$ for $\delta = 0.01a_0$ [top] and $\delta = 0.1a_0$ [bottom]. Numerical predictions using a 1/7th power-law profile recreated from Gaffney (2016) [solid lines]. Theoretical predictions using an equivalent linear profile to match the power-law profile [dashed lines]. Theoretical predictions using an equivalent step-function profile to match the power-law profile [dash-dotted line]. The other parameters are: $M_\infty = 0.75$, $k_0 a = 20$ and $(l, q) = (4, 1)$.

$\delta_L = 0.7768\delta_{QS}$, $\delta_L = \delta_{L,original}$ and $\delta_L = 0.75\delta_{PL}$. The equivalent linear profile that matches the power-law is the thinnest and therefore has the best accuracy. On the other hand, the equivalent linear profile that matches the original linear profile has the largest thickness and therefore the worst accuracy as is reflected in the prediction in Fig. (5.13).

This concludes this section on the flow characteristics and how they affect shielding. The Mach number proves to be a very influential parameter with similar trend and behavior as the

frequency. The boundary-layer profile also affects shielding, with the 1/7th power-law profile producing less because of its shallower gradient and shape. The key finding here is the fact that the equivalent linear profile approach is very capable of approximating the shielding produced by a 1/7th power-law profile, which is the representative of a turbulent boundary-layer on a fuselage during flight. Furthermore, the equivalent step-function profile approach proves to be even better at approximating the same effect even at large thicknesses. More attention to that fact will be given in the next section. The next section is dedicated to the effect of the boundary-layer thickness on the shielding. Although the boundary-layer thickness is a flow characteristic, it is decided that because of its drastic effect on the shielding and on the accuracy of the theoretical methods, there should be a whole section dedicated to its influence.

5.4.3 Thickness Effect

In this section the effect of boundary-layer thickness on the shielding is investigated. Although its effect has already been demonstrated in previous results, it is important to iterate how drastic it is. Furthermore, a major goal of this section is to more thoroughly investigate the difference between the two theoretical methods (equivalent linear and equivalent step-function profile), and demonstrate how the boundary-layer thickness affects their accuracy in replicating the numerical predictions.

Apart from the boundary-layer thickness, all the other parameters are kept constant, $k_0 a = 20$, $M_\infty = 0.75$ and $(l, q) = (4, 1)$. Since the 1/7th power-law profile is of major practical interest, the results focus mainly on this profile. However, initially some results for the quarter-sine profile are presented that facilitate comparison with previous numerical results.

Figures (5.15) and (5.16) present quarter-sine profile results. Firstly, the drastic effect of the presence of the boundary layer is noted. Even a very thin boundary layer ($\delta = 0.0025 a_0$) can still produce up to almost 20 dB shielding. By ignoring the lobed pattern, it can be observed that for the smaller boundary-layer thicknesses (Fig. (5.15)), the increase in shielding is almost linear with increasing $\bar{z}$. But for the thicker boundary-layers (Fig. (5.16)), the shielding takes place abruptly at small $\bar{z}$ and after that the rate of shielding stabilises. As explained before, this is attributed to the phenomenon of total reflection upstream. For large enough boundary-layer thicknesses, there will be a certain axial point beyond which the sound waves will be incident on the layer at such a shallow angle that they will be reflected off it without reaching the wall.

Figures (5.15) and (5.16) show the deterioration of the equivalent linear profile approach's accuracy. On the other hand, the equivalent step-function profile approach shows its ability to retain good agreement with the numerical results even for larger boundary-layer thicknesses. Starting from the small boundary-layer thickness results in Fig. (5.15), for very thin boundary layers the equivalent linear profile prediction is closer to the numerical prediction than the equivalent step-function profile. However, as the boundary-layer thickness becomes larger one can see that the equivalent step-function profile prediction is now closer to the numerical one, while the equivalent linear profile approach starts to underpredict shielding. Eventually, at large boundary-layer thicknesses (Fig. (5.16)), the equivalent linear profile approach underpredicts shielding by almost 35 dB. On the other hand, the equivalent step-function

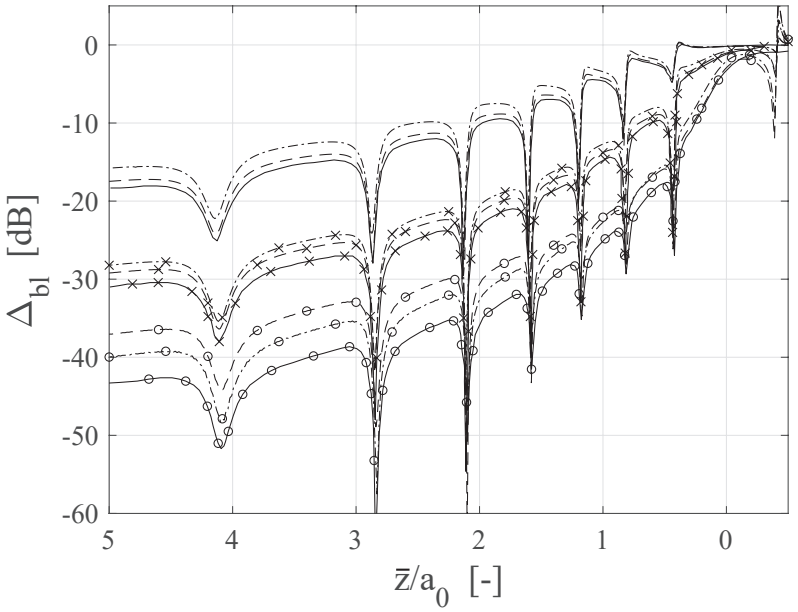

FIGURE 5.15: Δ_{bl} at $\bar{\phi} = 0^o$ for $\delta = 0.0025a_0$ [no marker], $\delta = 0.01a_0$ [$\times$] and $\delta = 0.025a_0$ [$\bigcirc$]. Numerical predictions using a quarter-sine profile recreated from Gaffney (2016) [solid lines]. Theoretical predictions using an equivalent linear profile to match the quarter-sine profile [dashed lines]. Theoretical predictions using an equivalent step-function profile to match the quarter-sine profile [dash-dotted line]. The other parameters are: $M_\infty = 0.75$, $k_0 a = 20$ and $(l, q) = (4, 1)$.

profile prediction, despite never actually being able to capture the numerical value, is remarkably close to it.

Turning now attention to the more representative 1/7th power-law profile and the results that refer to its shielding in Fig. (5.17), the same consistent findings are manifested once again. With growing boundary-layer thickness the shielding upstream is increased. Note that Fig. (5.17) shows the difference Δ_{bl} at an axial point far upstream, exacerbating any discrepancies between the numerical and theoretical predictions. The comparison between the predictions reveals the already shown deterioration of the accuracy of the equivalent linear profile approach. Moreover, as before the equivalent step-function profile approach retains about the same level of accuracy throughout this range of boundary-layer thickness. This is a surprising finding that indicates that for thicker boundary layers it may not be necessary to solve the Pridmore-Brown equation. The much simpler step-function analysis, based on only solving the convected Helmholtz equation, appears to approximate the realistic shielding effect of a power-law profile, typical of the boundary-layer velocity profile on a fuselage during flight.

In order to better understand this finding, and to gain a more inclusive perspective on the problem, some contour maps are presented in Figs. (5.18) through (5.23). In these contour maps the SPL contours on the fuselage surface is presented. The cylinders are unfurled in order to uncover any obscure areas. The profile in question is the 1/7th power-law profile. For all the contour maps the difference between the theoretical and the numerical predictions that stands out is at the plane of the source and further downstream. The discrepancy there can be ignored because it stems from the fact that the numerical model that generated these contour

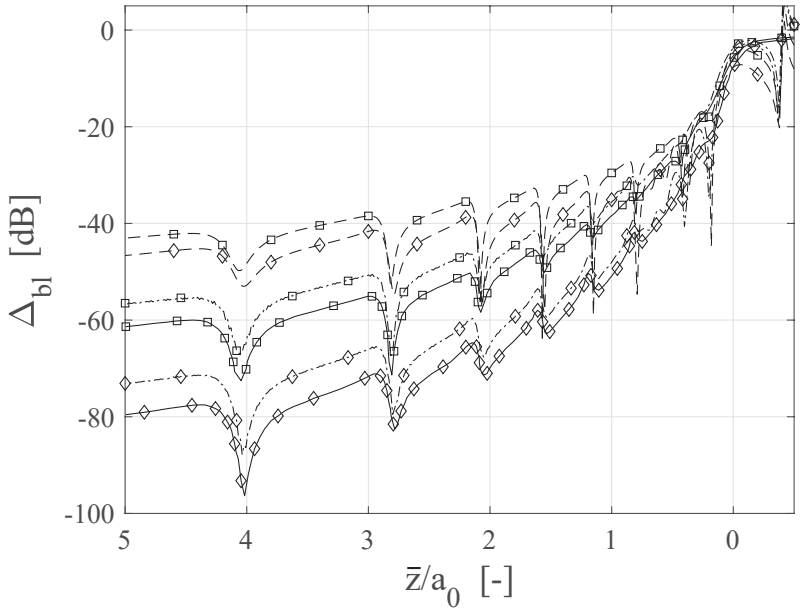

FIGURE 5.16: Δ_{bl} at $\bar{\phi} = 0^o$ for $\delta = 0.05a_0$ [box] and $\delta = 0.075a_0$ [diamond]. Numerical predictions using a quarter-sine profile recreated from Gaffney (2016) [solid lines]. Theoretical predictions using an equivalent linear profile to match the quarter-sine profile [dashed lines]. Theoretical predictions using an equivalent step-function profile to match the quarter-sine profile [dash-dotted line]. The other parameters are: $M_\infty = 0.75$, $k_0 a = 20$ and $(l, q) = (4, 1)$.

maps includes diffraction around the lip of the fan duct (Gaffney and McAlpine (2018) and Gaffney (2016)). Therefore, results close to the plane of the source and downstream of it will exhibit discrepancies with the numerical results. Apart from that region, upstream the discrepancies between the three predictions are minuscule for the thin boundary-layer cases, up to $\delta = 0.03a_0$. For thicker boundary-layer cases, it is apparent that the equivalent linear profile approach underpredicts the shielding upstream, with more noticeable differences in the color maps. On the other hand, the equivalent step-function profile prediction is remarkably close to the numerical prediction for the whole range of boundary-layer thicknesses. Even for the extremely thick boundary-layer case of $\delta = 0.1a_0$ the contour maps are very similar to each other, apart from some instabilities close to the plane of the source.

This concludes this section on the boundary-layer thickness effect, and how it affects the shielding and the accuracy of the two theoretical methods. A major finding is that the equivalent step-function profile approach can be used to approximate the effects of a complex profile even for very thick boundary layers. For thinner and more realistic boundary-layer thicknesses both theoretical methods could be used to approximate the effects of a complex profile. This finding is highly significant because it implies that it may not be necessary to solve the Pridmore-Brown equation in order to generate realistic results for sound refraction by a boundary layer.

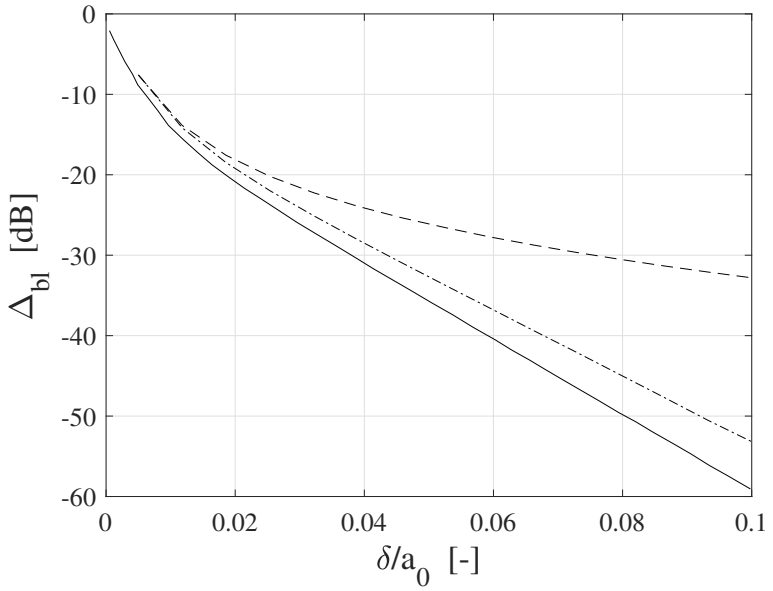

FIGURE 5.17: Δ_{bl} at $\bar{\phi} = 0^o$ and $\bar{z} = 5a_0$ for varying boundary-layer thickness. Numerical predictions using a 1/7th power-law profile recreated from Gaffney and McAlpine (2017) [solid lines]. Theoretical predictions using an equivalent linear profile to match the power-law profile [dashed lines]. Theoretical predictions using an equivalent step-function profile to match the power-law profile [dash-dotted line]. The other parameters are: $M_\infty = 0.75$, $k_0 a = 20$ and $(l, q) = (4, 1)$.

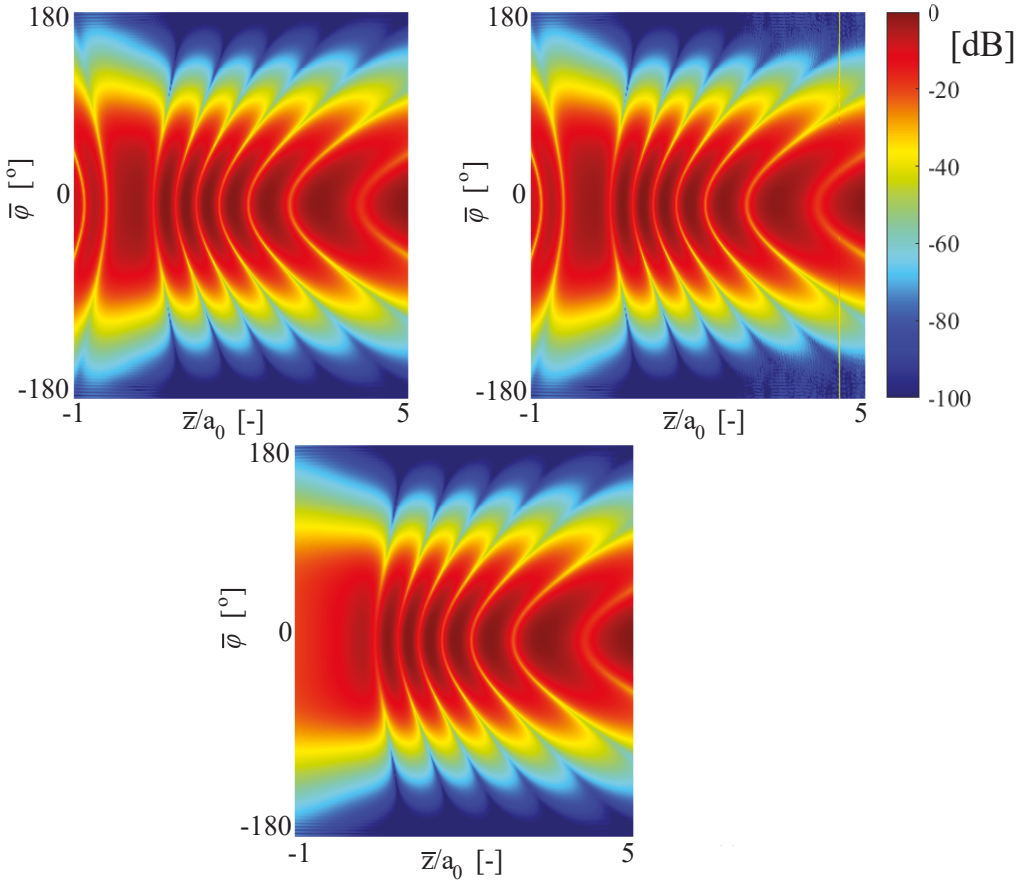

FIGURE 5.18: Total SPL on the surface of the fuselage for boundary-layer thickness $\delta = 0.01a_0$. Numerical prediction using a 1/7th power-law profile recreated from Gaffney (2016) [bottom]. Theoretical prediction using an equivalent linear profile to match the power-law profile [top left]. Theoretical prediction using an equivalent step-function profile to match the power-law profile [top right]. The other parameters are: $M_\infty = 0.75$, $k_0 a = 20$ and $(l, q) = (4, 1)$.

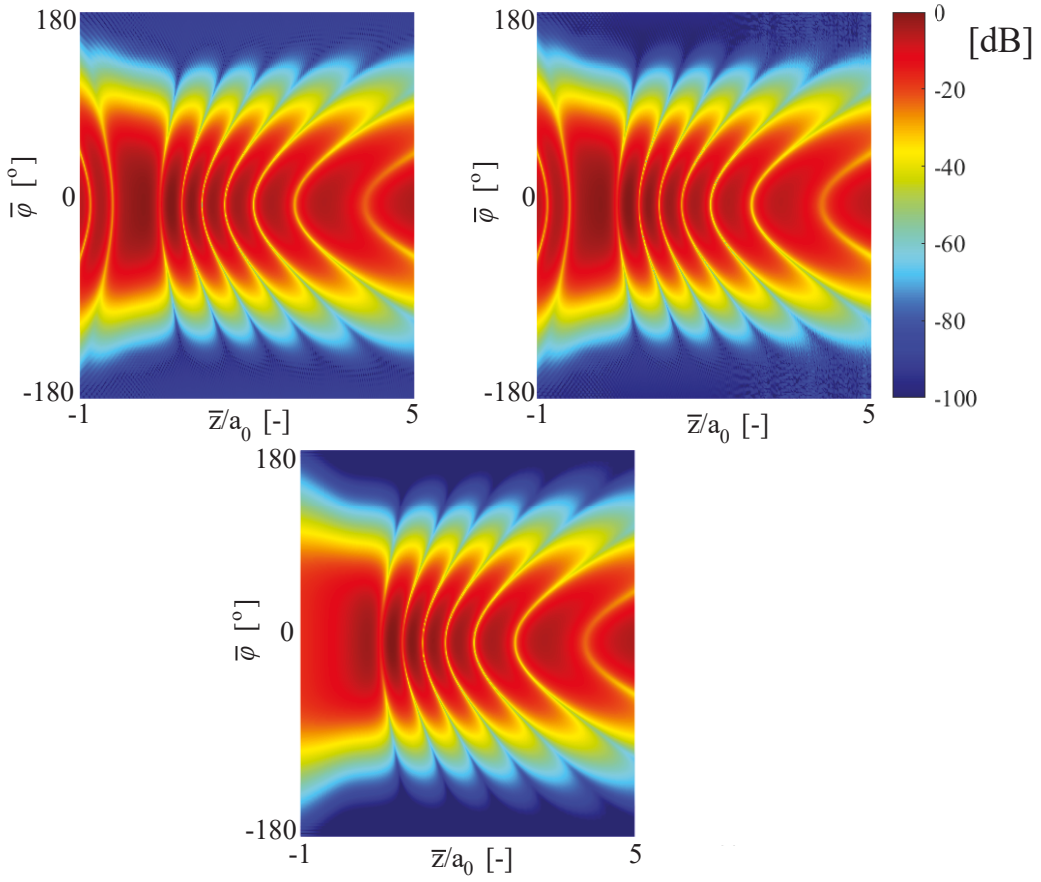

FIGURE 5.19: Total SPL on the surface of the fuselage for boundary-layer thickness $\delta = 0.02a_0$. Numerical prediction using a 1/7th power-law profile recreated from Gaffney (2016) [bottom]. Theoretical prediction using an equivalent linear profile to match the power-law profile [top left]. Theoretical prediction using an equivalent step-function profile to match the power-law profile [top right]. The other parameters are: $M_\infty = 0.75$, $k_0 a = 20$ and $(l, q) = (4, 1)$.

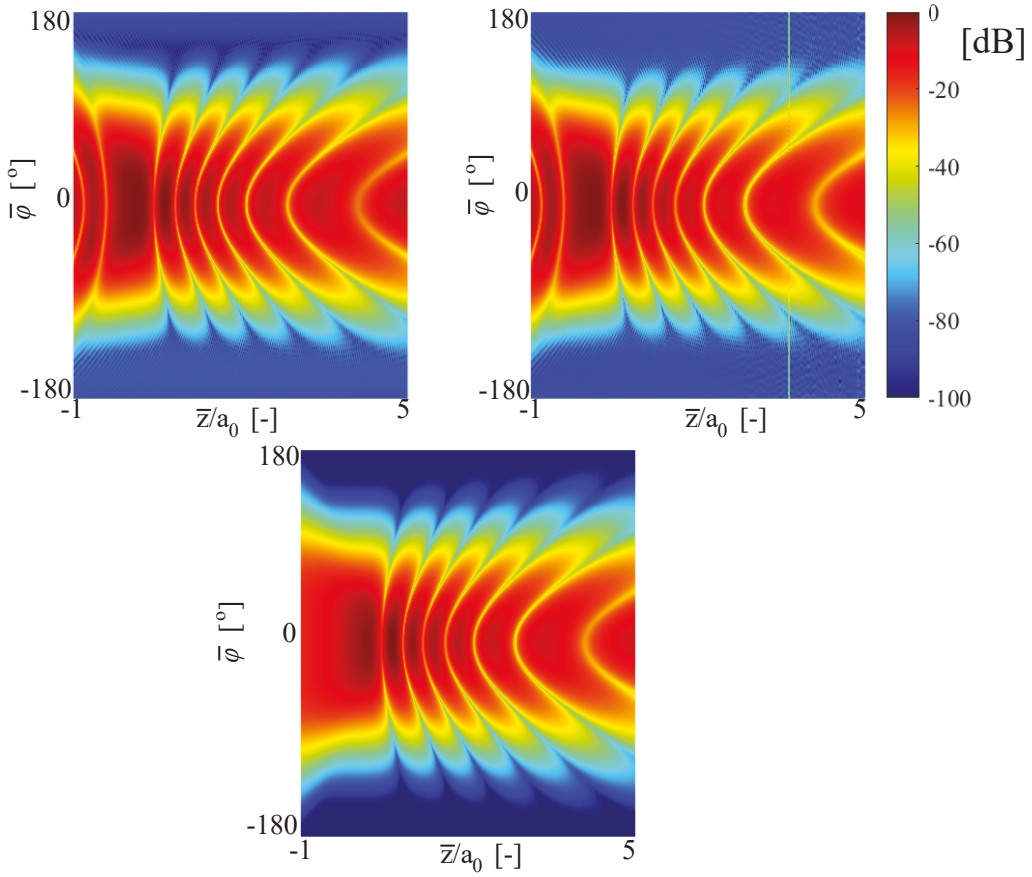

FIGURE 5.20: Total SPL on the surface of the fuselage for boundary-layer thickness $\delta = 0.03a_0$. Numerical prediction using a 1/7th power-law profile recreated from Gaffney (2016) [bottom]. Theoretical prediction using an equivalent linear profile to match the power-law profile [top left]. Theoretical prediction using an equivalent step-function profile to match the power-law profile [top right]. The other parameters are: $M_\infty = 0.75$, $k_0 a = 20$ and $(l, q) = (4, 1)$.

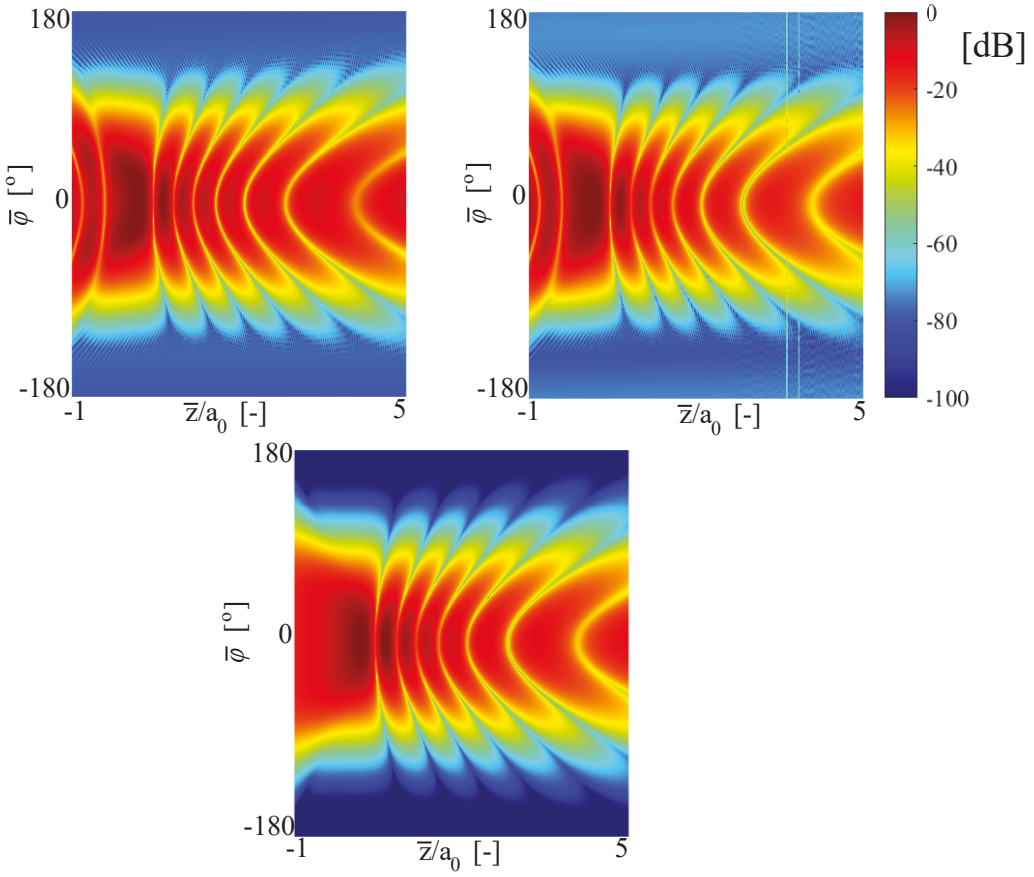

FIGURE 5.21: Total SPL on the surface of the fuselage for boundary-layer thickness $\delta = 0.04a_0$. Numerical prediction using a 1/7th power-law profile recreated from Gaffney (2016) [bottom]. Theoretical prediction using an equivalent linear profile to match the power-law profile [top left]. Theoretical prediction using an equivalent step-function profile to match the power-law profile [top right]. The other parameters are: $M_\infty = 0.75$, $k_0 a = 20$ and $(l, q) = (4, 1)$.

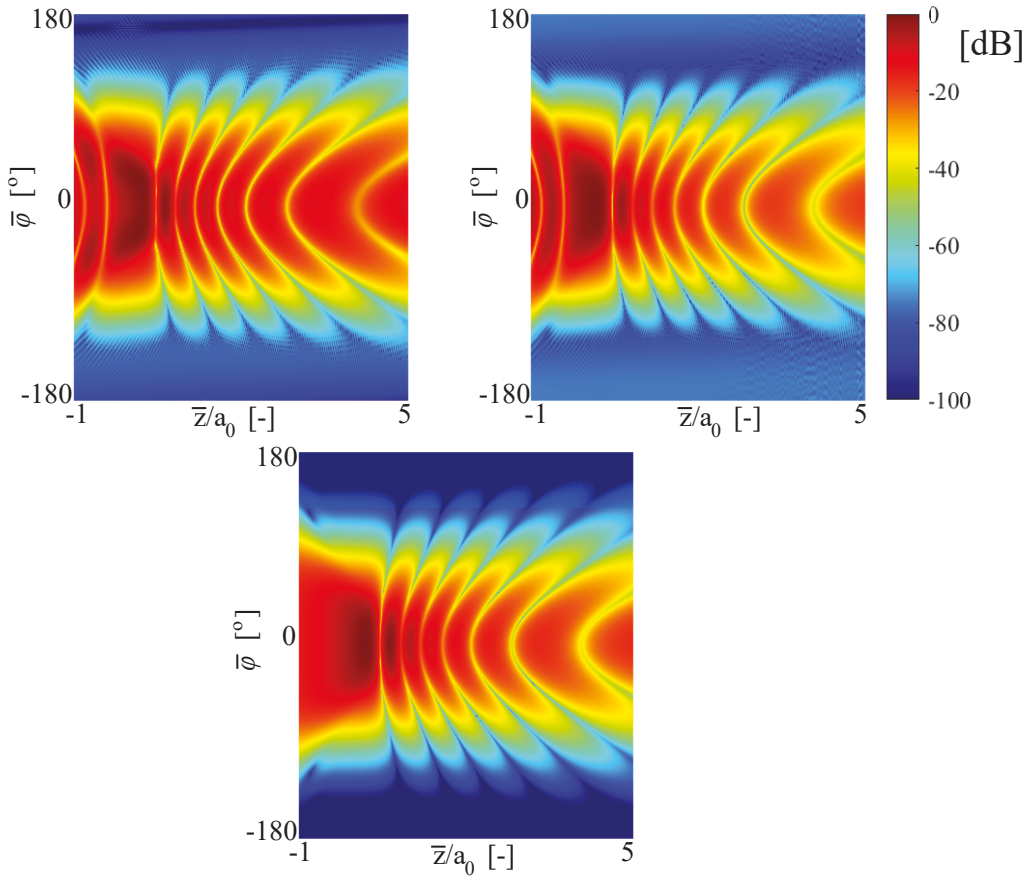

FIGURE 5.22: Total SPL on the surface of the fuselage for boundary-layer thickness $\delta = 0.05a_0$. Numerical prediction using a 1/7th power-law profile recreated from Gaffney (2016) [bottom]. Theoretical prediction using an equivalent linear profile to match the power-law profile [top left]. Theoretical prediction using an equivalent step-function profile to match the power-law profile [top right]. The other parameters are: $M_\infty = 0.75$, $k_0 a = 20$ and $(l, q) = (4, 1)$.

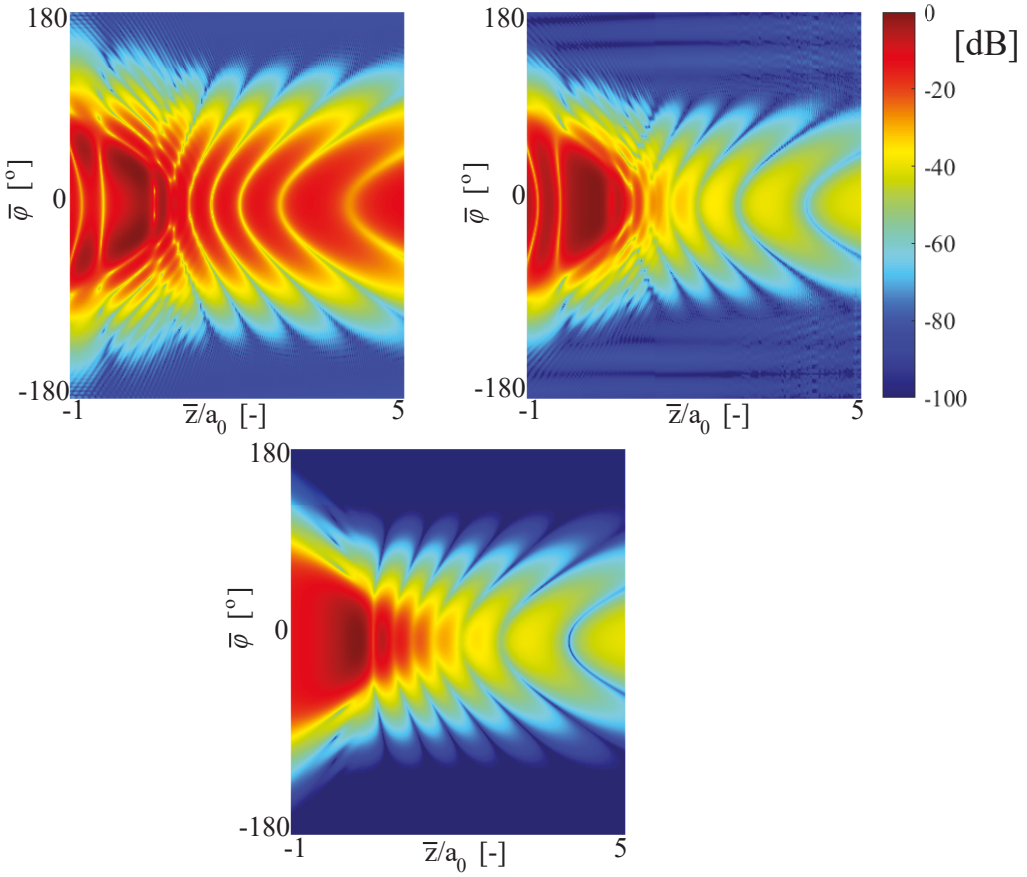

FIGURE 5.23: Total SPL on the surface of the fuselage for boundary-layer thickness $\delta = 0.1a_0$. Numerical prediction using a 1/7th power-law profile recreated from Gaffney (2016) [bottom]. Theoretical prediction using an equivalent linear profile to match the power-law profile [top left]. Theoretical prediction using an equivalent step-function profile to match the power-law profile [top right]. The other parameters are: $M_\infty = 0.75$, $k_0 a = 20$ and $(l, q) = (4, 1)$.

Chapter 6

Parametric Study

Having established that both the linear and the step-function equivalent velocity profile can approximate the refraction effects of other boundary layer profiles, the next step is a further investigation into the shielding and refraction effect of the boundary layer in a more realistic or representative configuration. For that reason, a parametric study has been carried out to demonstrate the refraction effect of the fuselage boundary layer for a range of different parameters and flight conditions with a multimodal source. The reason for conducting this study is to provide insight into the installation and shielding effects of an exemplar aircraft in flight, and also to demonstrate the capability of the theoretical method to provide quick and accurate trends for realistic situations.

The model to be used for this study will approximate the dimensions and configuration of a typical wide-body aircraft such as the Airbus A330 or Airbus A350 or the Boeing 787. This configuration is chosen since it is typically equipped with an ultra high by-pass ratio turbofan engine such as the Trent 7000 or XWB. Engines in the future are projected to become even larger with even higher by-pass ratios, such as the Rolls-Royce UltraFan (plc.), and that is why the study will involve typical ultra high by-pass ratio engine dimensions and characteristics. Another important parameter that will be examined is the modal output of the engine. In a realistic flight situation, the acoustic energy of the engine is seldom distributed uniformly among the modes. It is more likely, depending on the stage of flight, that a dominant rotor-locked mode will occur which will dominate the acoustic pressure pattern. Therefore, an important parameter will be the cut-off ratio of the rotor-locked mode since it also gives an indication on the direction of propagation of the principal radiation lobe.

The flow and source characteristics are chosen to simulate an aircraft climbing up to cruise, giving a wide range of values. An important parameter to be discussed is the flight Mach number. Its values are selected to reflect a typical flight path culminating in a typical maximum value during the cruising stage of flight. As will be shown, the flight Mach number is a highly influential acoustic parameter. The same can be said about the frequency of the acoustic output of the engine. The values of the BPF are chosen to realistically reflect the rpm of the engine in the various stages of flight with higher rpm leading to higher frequencies. Lastly, the parameter of the boundary-layer thickness is chosen to represent typical values

along the fuselage during flight. Realistically, it is expected that a turbulent boundary layer will develop on the fuselage, therefore a 1/7th power-law profile is applicable here.

6.1 Construction of the Model

The dimensions of a typical wide-body aircraft are used for the parametric study model. The key dimensions are shown in table (6.1) and Fig. (6.1). The fan duct radius is typically around half of the fuselage radius. The fan source will be placed next to the fuselage at 0^o azimuthal angle, i.e. $\beta = 0^o$.

Parameter	Value
a/a_0	0.5
b/a_0	3.5
β	0^o
$\bar{z}_{ps}/a_0$	0
$\bar{z}_{ec}/a_0$	4
$\bar{\theta}_{ff}$	[5^o,175^o]
$\bar{\phi}_{ff}$	$3\frac{\pi}{2}$

TABLE 6.1: Dimensions of parametric study model.

The parameters $\bar{z}_{ps}$ and $\bar{z}_{ec}$, are respectively the position of the plane of the source (the plane of the fan inlet), and the position of the end of the nose cone. These parameters represent the axial range of the calculations for the fuselage surface pressure results. This range of $\bar{z}$ represents the entire section of the fuselage upstream of the source that can be approximated by a cylinder with constant radius. Beyond $\bar{z}_{ec}$, the nose cone structure cannot be modeled by the current theoretical formulation. The parameters $\bar{\theta}_{ff}$ and $\bar{\phi}_{ff}$ refer to the grid for the far-field calculations. The expressions in sections 3.1.4.1, 3.2.6 and 3.3.5 can give the far-field pressure at any point of a sphere with radius $\bar{R}$ centered on the fuselage, $(\bar{\theta}, \bar{\phi})$. Nonetheless, in the following sections, far-field results will be calculated for the hemisphere underneath the fight path, $\bar{\phi}_{ff} = 3\frac{\pi}{2}$, since this directivity pattern will propagate towards the ground. Note that the polar angle $\bar{\theta}$ should not approach extreme values of 0^o or 180^o as these introduce numerical singularities when calculating the pressure.

As mentioned before, the study will include a range of operating conditions. This means that the flight Mach number and altitude will vary, consequently changing the boundary layer thickness on the fuselage. Furthermore, the theoretical approach used assumes a constant boundary-layer thickness. Nonetheless, for every operating condition there are three values of a constant boundary-layer thickness that can be defined, and used in order to give an accurate estimate of the amount of shielding or refraction produced. These three constant values represent the range of values of the growing boundary-layer thickness on the fuselage's surface that will be studied.

Therefore, the range of the $\bar{z}$-grid points, from $\bar{z}_{ps}$ to $\bar{z}_{ec}$, dictate the values used for the boundary-layer thickness δ. The thinnest boundary layer that occurs in the range $[\bar{z}_{ec}, \bar{z}_{ps}]$ is at the end of nose cone. The boundary layer continues growing until it reaches its maximum

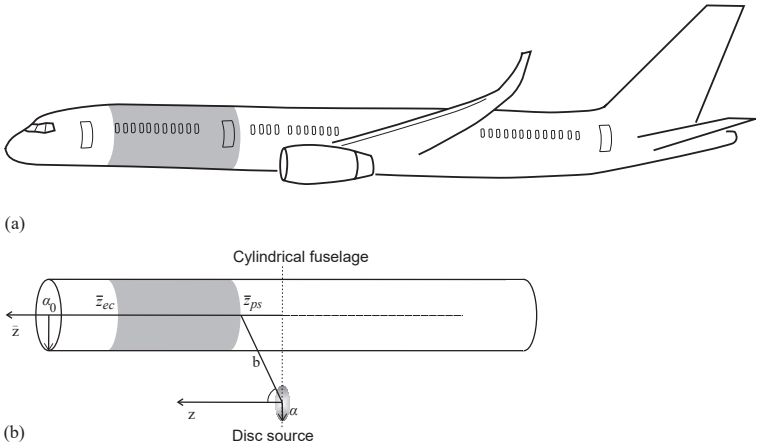

FIGURE 6.1: Model configuration and dimensions.

thickness value which occurs at the plane of the source because this is the $\bar{z}$ point which is furthest downstream from the aircraft nose. The thinnest boundary layer that occurs at the end of the nose cone is the first value to be investigated in the study, and will be referred to from now on as the *thin* boundary layer. The thickest boundary layer that occurs at the plane of the source is the second value to be investigated in the study, and will be referred to from now on as the *thick* boundary layer. Finally, an average value for the thickness between those two is obtained, referred to from now on as the *average* boundary layer. Note that the average boundary-layer thickness is calculated by integrating the boundary-layer thickness over the axial range, which gives a more realistic average than a simple arithmetic mean of the thin and thick layers. Using these three constant thickness values, an estimate can be extrapolated that can fairly accurately predict the effect of a growing boundary layer.

It is important at this point to clarify some assumptions concerning the boundary-layer growth. First of all, in the present study it is assumed that the boundary layer that develops on the fuselage is turbulent and follows a 1/7th power law velocity profile. Therefore, both the equivalent linear and equivalent step-function profiles will be matched to the 1/7th power-law profile. This profile is chosen as it is the most commonly used way to represent an actual turbulent boundary-layer profile.

Secondly, the boundary-layer thickness growth along the cylindrical fuselage is assumed to be the same as the growth over a flat plate. This is a valid assumption considering that the boundary-layer thickness will not exceed the value of 10 % of the fuselage radius, rendering the curvature of the geometry less important. By assuming flat plate theory the values for the thickness of the thin boundary layer (at the end of nose cone) and the thick boundary layer (at the plane of the source) can be found using the relationship $\delta(x) = 0.37x/\mathrm{Re}_x^{1/5}$, where x is the distance taken from the nose of the model aircraft and $\mathrm{Re}_x^{1/5}$ is the Reynolds number at point x as shown in Fig. (6.2). The distance x will be the distance of the end of the nose cone from the

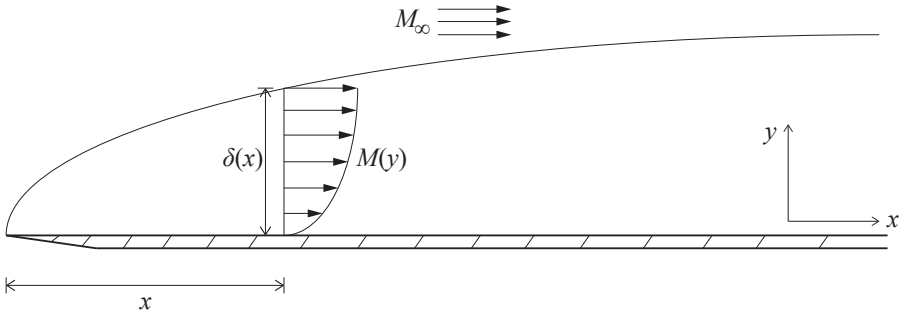

FIGURE 6.2: Boundary layer thickness growth over a flat plate.

nose for the thin boundary layer, while for the thick boundary layer it will be the distance of the plane of the source from the nose.

6.2 Operating Conditions

The operating conditions of the model flight path presented here are dictated by the cut-off ratio of the dominant rotor-locked mode $\zeta_{(20,1)}$, flight altitude and flight Mach number. In this model, the number of fan blades is taken to be $B = 20$ which is a typical value for a high by-pass ratio engine used on a wide-body aircraft. Therefore, assuming there are no instabilities in the inlet flow, the dominant rotor-locked cut-on mode will be $(l, q) = (20, 1)$ although a possibility of the second radial order mode, $(l, q) = (20, 2)$ being cut-on will be investigated later on too. The presence of a rotor-locked mode is very much expected at some point in flight and is bound to affect significantly the installed acoustic field (Schwaller et al. (1997), Schwaller et al. (2006), Achunche et al. (2009)). As seen in table (6.2) the rotor-locked mode $(20, 1)$ will be cut-off in the first two operating conditions (just cut-off in the second operating condition). Then, at operating condition 3 it will be just cut-on, and will continue to be more cut-on until the last condition 6. This range of cut-off ratio will provide an insight into the directivity of the installed field since it includes cut-off, cut-on and transitioning conditions.

As shown in Fig. (6.3) the six operating conditions simulate the later climbing stage and cruising stage of the flight path. The flight Mach number and flight altitude values are chosen in order to represent these stages. The aircraft will accelerate during the climb until it stabilises at the cruising altitude, which is typically around 9000 m (or sometimes higher) at a typical Mach number of 0.75. Furthermore, since the theoretical approach presented in this work does not include a diffuser in front of the fan, which is typically the case, the range of flight Mach number is chosen so that the diffuser normally would accelerate or decelerate the fan inlet flow very little. Diffusers usually regulate the fan inlet Mach number to about 0.6-0.7.

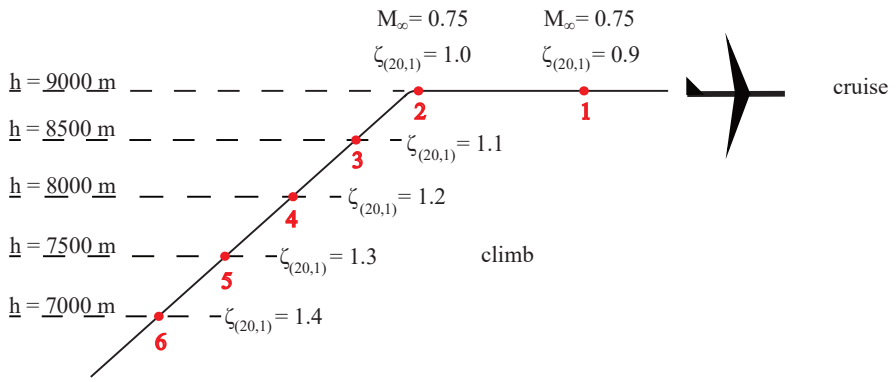

FIGURE 6.3: Operating conditions examined in the parametric study.

Operating Conditions	1	2	3	4	5	6
$\zeta_{(20,1)}$	0.9	1.0	1.1	1.2	1.3	1.4
Altitude (m)	9000	9000	8500	8000	7500	7000
M_∞	0.75	0.75	0.7	0.7	0.65	0.65
$k_0 a$ (BPF)	13.22	14.69	17.45	19.04	21.95	23.64
Fan rpm (%)	49.3	54.8	65.5	72.0	83.6	90.6
δ/a_0 at plane of source	0.0619	0.0619	0.0621	0.0614	0.0616	0.061
δ/a_0 at end of nose cone	0.0326	0.0326	0.0327	0.0324	0.0325	0.0322

TABLE 6.2: Operating conditions examined in the parametric study.

By assuming that the frequency that corresponds to a specified cut-off ratio is the first blade passing frequency (BPF), the rpm of the fan can be found as seen in table (6.2). The engine rpm also reflects the flight stage of each operating condition, with high rpm in the climbing stage which gradually decreases until stabilisation in the cruising stage at about 50 %. Finally, with the operating conditions known the different boundary layer thickness values are calculated. With the fuselage radius being represented here by its typical value for a wide-body aircraft (that value is approximately $a_0 = 2.89$ m), the boundary-layer thickness at the plane of the source is around 0.18 m. The plane of the source in this representative model is roughly 20 m from the nose of the aircraft. The value of the boundary-layer thickness at that point is not unrealistic as shown by Dierke et al. (2013). Dierke et al. performed a CFD analysis on a model aircraft and computed the boundary-layer growth up to 20 m from the aircraft nose and concluded that the value of the boundary-layer thickness is between 0.1 to 0.2 m, making the value chosen here representative of a real-life situation.

6.3 Source Characteristics

As mentioned before it is in the scope of this parametric study to demonstrate the effectiveness of the theoretical method and its reduced computational speed compared against high-fidelity numerical methods. Multi-mode sources are used which for a numerical method to simulate all the modes would be very time-consuming. For each operating condition, every cut-on mode's contribution is calculated, and then the contributions are summed incoherently. However, the presence of a dominant rotor-locked mode means that an equal energy per mode assumption is not realistic (Schwaller et al. (1997), Schwaller et al. (2006), Achunche et al. (2009)). For that reason, a number of different sources are investigated that have different power distribution among the cut-on modes.

Five different multi-mode sources are used in the present study. They all have the same total power of unity, $W_t = 1$. Their differences lie in the distribution of the total power among the cut-on modes.

1. Equal energy source W_{ee}. The total power of unity is divided equally among the cut-on modes. Thus, each mode has the same modal sound power $W_{lq} = W_t/\text{number of modes}$.
2. Rotor-locked source W_{10}. The total power of unity is divided equally among the cut-on modes apart from the rotor-locked mode (20,1), which has 10 times larger modal sound power (or 10 dB higher in PWL terms).
3. Rotor-locked source W_{20}. The total power of unity is divided equally among the cut-on modes apart from the rotor-locked mode (20,1), which has 100 times larger modal sound power (or 20 dB higher in PWL terms).
4. Rotor-locked source W_{30}. The total power of unity is divided equally among the cut-on modes apart from the rotor-locked mode (20,1), which has 1000 times larger modal sound power (or 30 dB higher in PWL terms).
5. Rotor-locked source $W_{20,10}$. The total power of unity is divided equally among the cut-on modes apart from the first radial order rotor-locked mode (20,1), which has 100 times larger modal sound power (or 20 dB higher in PWL terms), and a second radial order rotor-locked mode (20,2) which has 10 times larger modal sound power (or 10 dB higher in PWL terms).

Having prescribed the modal sound power of the modes, each individual modal amplitude is obtained with the following expression given in McAlpine et al. (2015),

$$|P_{lq}|^2 = \frac{2\rho_0 c_0 W_{lq}}{\pi\left[a^2 - \left(\frac{l}{\kappa_{lq}}\right)^2\right] J_l^2(\kappa_{lq}a)\left[(1+M_0^2)\,\mathrm{Re}(\xi_{lq}) - M_0(1+|\xi_{lq}|^2)\right]}. \tag{6.1}$$

Thus the contribution of each mode is weighted by its modal amplitude before they are all summed incoherently to obtain the total contribution of the source. Since the modes are summed incoherently, only the square of the modal amplitude is required (given by eq.(6.1)), not the phases of the individual modes. According to previous research (Schwaller et al. (1997), Schwaller et al. (2006), Achunche et al. (2009)) the most realistic of these prescribed

sources is likely to be the W_{20} source, since in previously reported experimental measurements the dominant rotor-locked mode can exhibit an amplitude around 20 dB higher than the rest of the cut-on modes, as shown in Fig. (6.4).

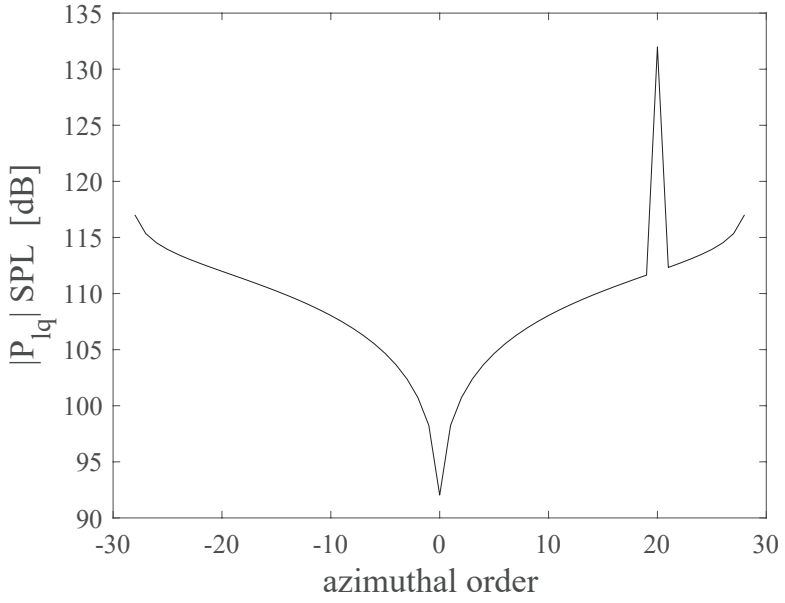

FIGURE 6.4: Modal amplitude in SPL form for operating condition 6 and source W_{20}. Only first radial order modes shown.

Nonetheless, the equal energy source, W_{ee}, is very useful in order to create a baseline. It is also not uncommon for the rotor-locked mode to exhibit a level up to 30 dB higher, thus the source W_{30} should give further insight into the distribution and propagation of sound power. It has also been reported that a second radial order rotor-locked mode could develop, hence the inclusion of source $W_{20,10}$. Note that the second radial order mode (20,2) is not cut-on until operating condition 5, therefore until condition 5, source $W_{20,10}$ is identical to source W_{20}. Furthermore, since the dominant rotor-locked mode is not cut-on for the first two operating conditions, every source is reduced to the W_{ee} source for operating conditions 1 and 2.

6.4 Source Power Distribution

In this section, the differences between the different types of sources are highlighted. The difference in power distribution leads to different pressure contour patterns on the fuselage surface. The results that follow show the SPL contour on the surface of the fuselage. The SPL is normalised so that the maximum value on the surface is at 0 dB (a convention that is used for all the figures showing pressure levels on the surface of the fuselage). Another metric being used in this section that highlights the distribution of power on the fuselage surface is the difference Δ_{source}, which is defined as

$$\Delta^{i}_{\text{source}} = \text{SPL}_i - \text{SPL}_{ee}, \tag{6.2}$$

where SPL_{ee} is the SPL calculated with the equal energy source W_{ee}, whilst i denotes either 10, 20, 30 or 20,10 representing values calculated for the sources W_{10}, W_{20}, W_{30} or $W_{20,10}$ respectively. This metric will pinpoint the difference between the power distributions of the rotor-locked sources and the baseline source W_{ee}, essentially demonstrating the location where the rotor-locked mode's principal radiation lobe is incident on the surface of the fuselage. For the majority of the results that follow in this section, the boundary-layer thickness is assumed to be average. The effect of different thicknesses will be investigated in later sections. Moreover, the results shown in the following sections are generated using an equivalent linear profile. The difference between linear and step-function results will be investigated in a later chapter.

Figure (6.5) gives the SPL on the surface of the fuselage for operating conditions 1, 3 and 6 with the equal energy source. The pressure pattern is fairly smooth with no distinctive regions for all operating conditions. That is expected with the W_{ee} source used is the equal energy source, which has no dominant mode, leading to all the modes' lobed patterns to smooth out each other. No particular pattern stands out because no particular mode stands out. They all have the same sound power attributed to them. For all the conditions the characteristic shadow zone is visible at the far side of the fuselage as expected. The difference between the three operating conditions' results is the location and spread of the maximum SPL area. Operating condition 1 exhibits a much more concentrated maximum SPL area close to the plane of the source. That is expected because further upstream of the source, sound waves meet the boundary layer at a shallower angle making them more susceptible to refraction. That is the case for all operating conditions. However the number of cut-on modes at operating condition 1 are only 111, in contrast to operating condition 6 whose number of cut-on modes are 258. That means that for higher operating conditions (going from 1 towards 6) more cut-on modes are added that are inevitably more spread out, since the already existing modes become even more cut-on. That leads to a more extensive and less localised affected area since the energy is more evenly spread out.

Figure (6.5) provides a good baseline result and also gives insight into the effect of ascending $\zeta_{(20,1)}$ (going from operating condition 1 towards 6). Figure (6.6) examines the effect of different sources. Results are for the same operating condition 3, when the dominant rotor-locked mode is just cut-on. When the mode is just cut-on, the mode angle is very steep and that is the reason why in all source cases the maximum SPL area is very close to the plane of the source. Furthermore, the more powerful the rotor-locked mode the more localised the area of maximum SPL. Source W_{10} exhibits small difference compared to the equal energy source. However, W_{20} starts to exhibit more shielding upstream making the maximum SPL area more distinctive. The same is true for the W_{30} source in a more extreme manner. This localisation of the affected area is expected, especially for operating condition 3. The rotor-locked mode is just cut-on which means its principal lobe propagates at a steeper angle, and so it meets the boundary layer at a steeper angle (close to perpendicular), minimising the effect of refraction and therefore shielding. The rest of the cut-on modes propagate at shallower angles further upstream, which means that sound waves travel a greater distance to meet the fuselage after transmitted into the boundary layer. That effectively means a thicker boundary layer or more shielding for these more cut-on modes that propagate further upstream. Therefore, energy tends to be refracted away upstream, whereas the rotor-locked

mode which carries the bulk of the sound power is not shielded so much because of its steeper propagation angle, leading to a concentration of energy close to the plane of the source.

After examining the transitioning effect of operating condition 3, Fig. (6.7) presents results for operating condition 5 when the rotor-locked mode is more cut-on. That is evident by comparing Figs. (6.6) and (6.7) where the maximum SPL has moved further upstream for all source types. That is expected since the bulk of sound power is carried by the dominant mode (20,1) which has become more cut-on and travels in a shallower angle, therefore incident on the fuselage further upstream. Note that at operating condition 5 the second radial order rotor-locked mode (20,2) is just cut-on. However, mode (20,2) is much less powerful than mode (20,1) (only 10 dB compared to 20 dB) meaning its effect is hardly visible downstream of (20,1) mode's principal lobe. That is not surprising, since W_{10} generally has a very weak effect as shown in Figs. (6.6.a-b) and (6.7.a-b), leading to the conclusion that a rotor-locked mode only 10 times more powerful does not affect significantly the total pressure field. It seems that the vast number of the rest of the cut-on modes carry enough energy to offset the effect of the rotor-locked mode. Even though at condition 5 the rotor-locked mode is more cut-on which means it is more susceptible to refraction and shielding, because it meets the boundary layer at a shallower angle, it still dominates the pressure pattern especially in the case of source W_{30}. For that source case, even the dominant mode's secondary lobe starts to stand out in the pattern downstream of the principal lobe. Even though the secondary lobe is less powerful than the principal lobe, it is subject to less shielding because it travels at a steeper angle towards the boundary layer.

The effect of ascending $\zeta_{(20,1)}$ (going from operating condition 1 towards 6) is demonstrated in Fig. (6.8). The difference $\Delta^{30}_{\text{source}}$ highlights the areas where the W_{30} source differs from the equal energy source. Figure (6.8) clearly shows how the rotor-locked mode becomes more and more cut-on, with its principal lobe propagating at shallower angles, and incident with the fuselage further and further upstream. There is always an excess of energy compared to source W_{ee} at the position of the principal lobe (positive values), but away from that position there is a deficit of energy compared to source W_{ee} (negative values) in order to compensate for the excess around the principal lobe, since all the sources have the same total sound power. Therefore, the rest of the cut-on modes of the W_{30} source, which are incident with the fuselage away from the position of the dominant mode's principal lobe, carry less energy than their W_{ee} counterparts. Note that as the rotor-locked mode becomes more cut-on, its secondary lobe begins to develop downstream and become more dominant.

Figure (6.9) demonstrates the weak effect source $W_{20,10}$ has on the results. Mode (20,2) is just cut-on at operating condition 5, and that is evident from the excess of energy very close to the plane of the source compared with the W_{20} source. However, that is a difference of 0.5 dB which becomes smaller for the rest of the domain, which is expected because the rest of the domain is unaffected by the newly cut-on mode (20,2) that travels at steep angles. It is safe to conclude that an excess of 10 dB sound power attributed to one mode is not enough to affect the pressure pattern formed by the superposition of all the remaining modes.

At this point this section is concluded with the key findings being the importance of the cut-off ratio $\zeta_{(20,1)}$, and the significance of the more powerful rotor-locked sources, W_{20} and W_{30}. The rotor-locked mode's cut-off ratio is key in estimating the area in which the maximum SPL

occurs. Moreover, this area becomes much more localised, and the acoustic energy is more concentrated there when a more powerful rotor-locked mode is present, compared to the rest of the cut-on modes.

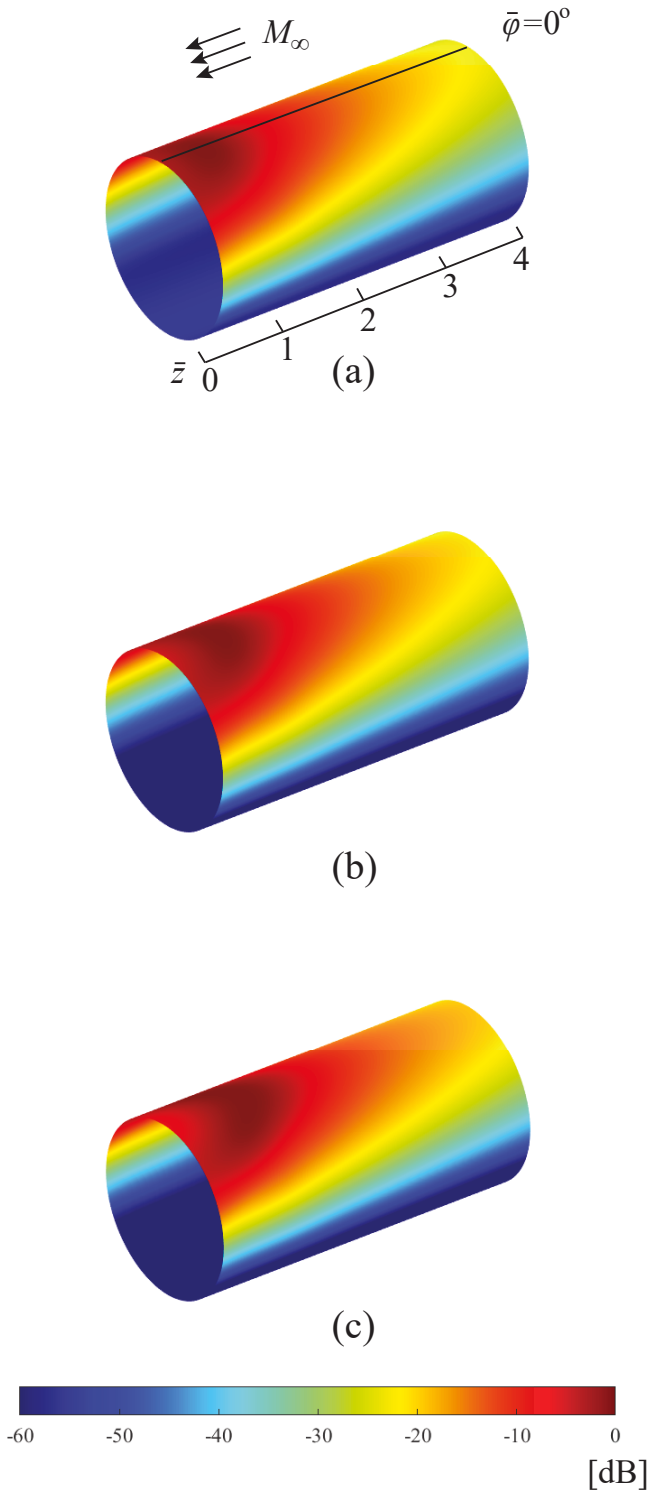

FIGURE 6.5: Total SPL on the surface of the fuselage for W_{ee} source. Results for operating conditions 1 [(a)], 3 [(b)] and 6 [(c)]. Average boundary-layer thickness is used for the calculations.

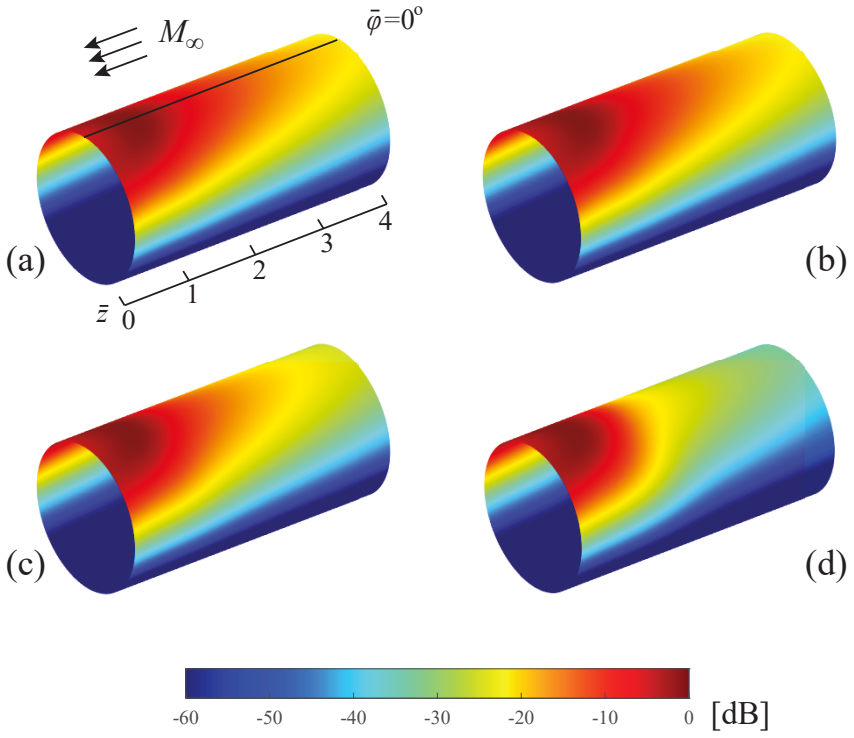

FIGURE 6.6: Total SPL on the surface of the fuselage for operating condition 3. Results for sources W_{ee} [(a)], W_{10} [(b)], W_{20} [(c)], W_{30} [(d)]. Average boundary-layer thickness is used for the calculations.

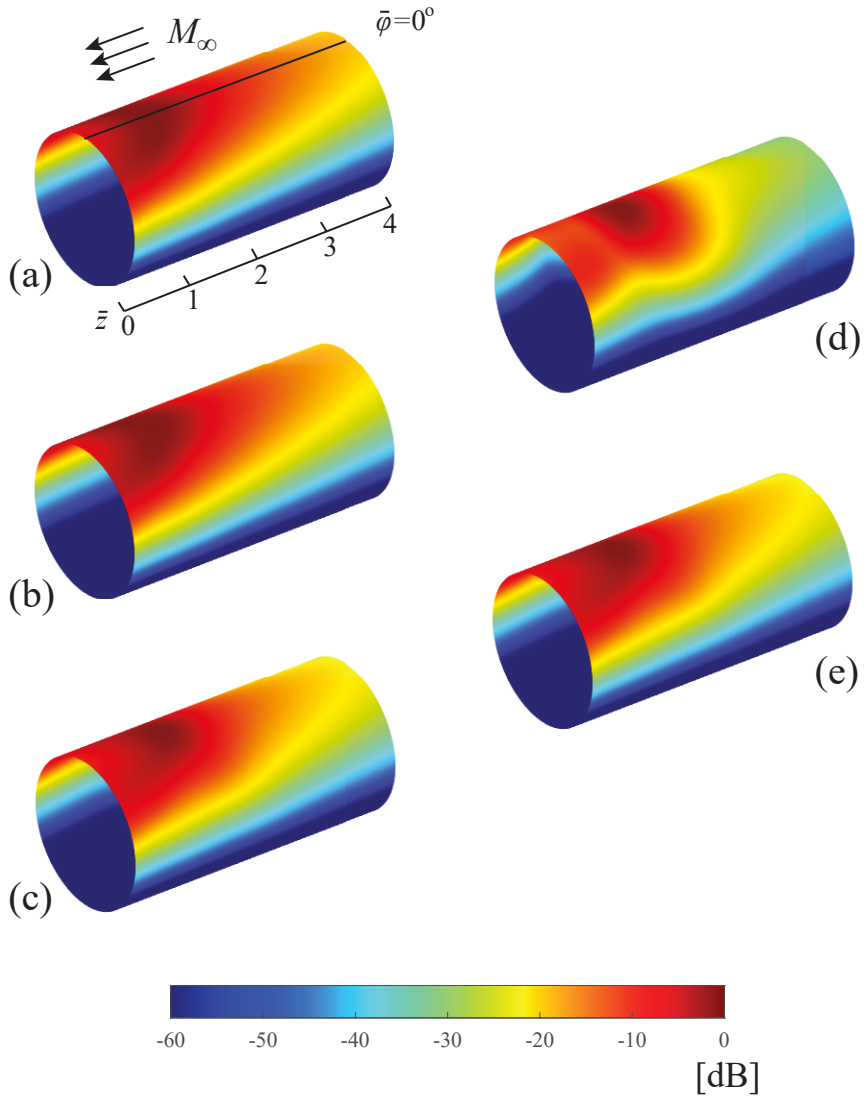

FIGURE 6.7: Total SPL on the surface of the fuselage for operating condition 5. Results for sources W_{ee} [(a)], W_{10} [(b)], W_{20} [(c)], W_{30} [(d)], $W_{20,10}$ [(e)]. Average boundary-layer thickness is used for the calculations.

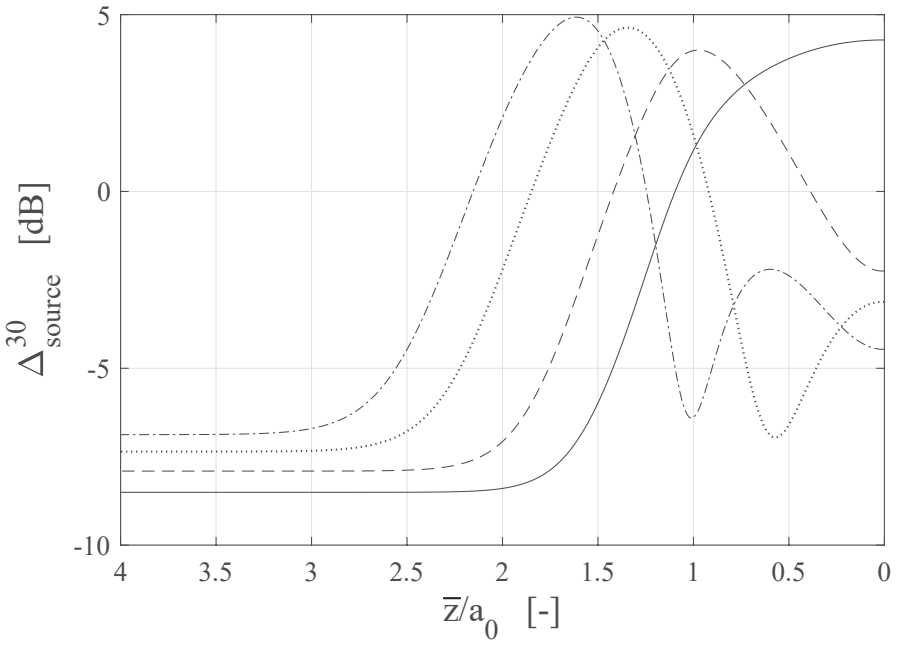

FIGURE 6.8: Δ^{30}_{source} on the fuselage surface at $\bar{\phi} = 0^o$. Results for operating conditions 3 [solid line], 4 [dashed line], 5 [dotted line] and 6 [dashed-dotted line]. Average boundary-layer thickness is used for the calculations.

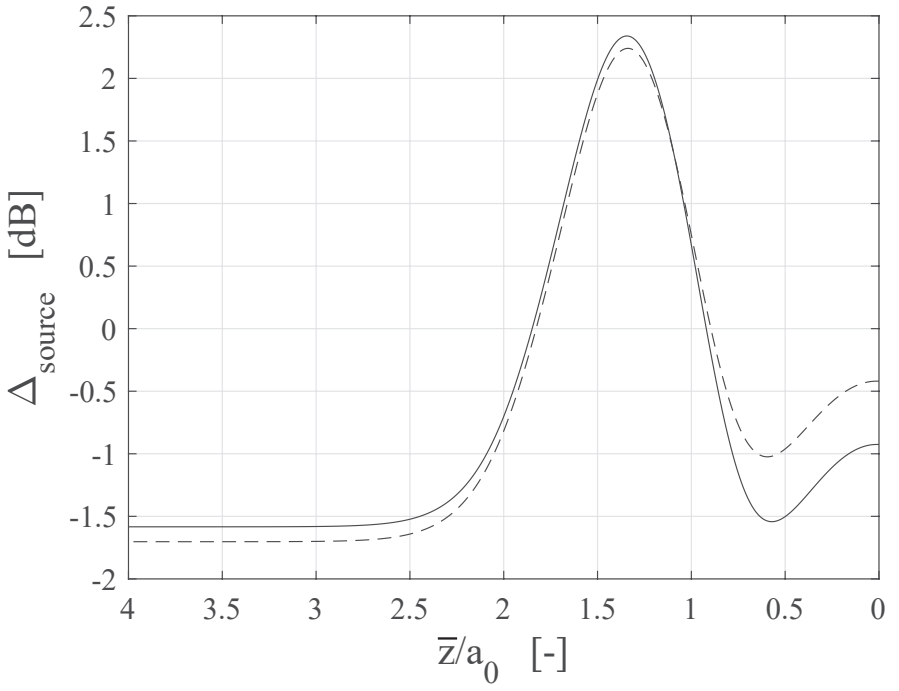

FIGURE 6.9: Δ_{source} on the fuselage surface at $\bar{\phi} = 0^o$ for operating condition 5. Results for W_{20} source [solid line] and $W_{20,10}$ source [dashed line]. Average boundary-layer thickness is used for the calculations.

6.5 Source Effect on Shielding

Having established the effect the different sources and operating conditions have on the SPL contour on the fuselage, the focus is now shifted onto the shielding. Specifically in this section, the effect the different sources and conditions have on shielding is examined. The two metrics used to quantify the shielding on the fuselage surface are, the difference Δ_{bl} and the shielding coefficient upstream S_+, as they have been defined in chapter 5.

The boundary-layer thickness effect on shielding will be investigated in the next section, therefore the results in this section are calculated using the average boundary-layer thickness. Also, the difference between the equivalent linear and equivalent step-function profile will be investigated in a later chapter, therefore the results in this section are generated using an equivalent linear profile.

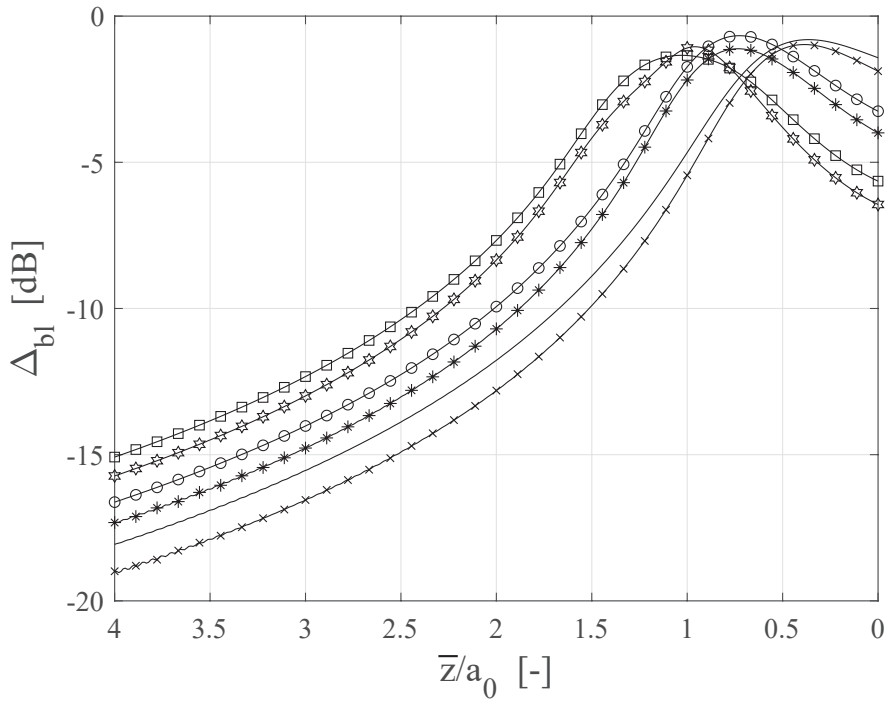

FIGURE 6.10: Δ_{bl} at $\bar{\phi} = 0^o$ for W_{20} source and all operating conditions. Operating condition 1 [no marker], operating condition 2 [$\times$], operating condition 3 [$\bigcirc$], operating condition 4 [$*$], operating condition 5 [box] and operating condition 6 [pentagram]. Average boundary-layer thickness is used for the calculations.

Figure (6.10) illustrates the effect of ascending operating conditions on shielding. By examining Fig. (6.10) and table (6.2) it is noticed that the operating conditions are paired off with the flight Mach number. Conditions 1 and 2 have the same Mach number, and the same is true for the pairs of conditions 3-4 and 5-6. That pairing is visible in Fig. (6.10) as well indicating a very strong relationship involving the Mach number. The trend is also expected from previous findings. It has been already established in previous chapters that Mach number has a similar effect to frequency. A higher Mach number leads to more shielding, whereas a lower Mach number leads to less shielding. That is because upstream the flow tends

to shorten the wavelength, and with a shorter effective wavelength compared to the boundary-layer thickness this means more refraction and shielding. That effect is reflected in Fig. (6.10) where the higher the conditions the less shielding is observed, because higher conditions (towards 6) have lower Mach number.

This dependency on Mach number seems to be stronger than the dependency on frequency. The effect of frequency can be observed in the pairs of conditions. Within each pair that has the same Mach number, the frequency is increased. That will lead to more shielding as established in previous chapters. In each pair the second condition exhibits more shielding than the first (condition 2 Δ_{bl} is below 1, 4 below 3, 6 below 5). This apparent pairing demonstrates that the Mach number effect is stronger than the frequency effect.

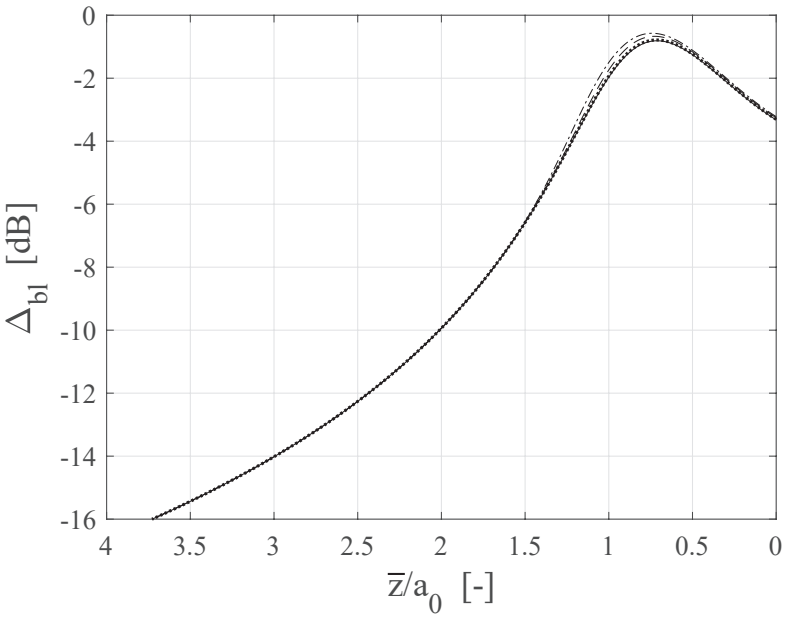

FIGURE 6.11: Δ_{bl} at $\bar{\phi} = 0^o$ for operating condition 3. Results for source W_{ee} [solid line], W_{10} [dotted line], W_{20} [dashed line], W_{30} [dash-dotted line]. Average boundary-layer thickness is used for the calculations.

Figures (6.11),(6.12), (6.13) and (6.14) show the effect of different source types on Δ_{bl} for operating conditions 3, 4, 5 and 6 respectively. By examining the figures one can notice that the presence of a dominant rotor-locked mode actually makes very little difference on the shielding. The prediction for the rotor-locked sources are remarkably close to the equal energy source. The only differences occur at the position of the dominant mode's principal lobe, where for condition 3 there is a slight decrease in shielding when the rotor-locked mode is present. In the other instances there is a slight increase in shielding with the presence of a rotor-locked mode.

This is possibly attributed to the fact that operating condition 3 represents a transitioning situation where the dominant mode is just cut-on, which means that it will propagate towards the boundary layer at a steeper angle which will make it less susceptible to shielding. When the rotor-locked mode is more cut-on in later conditions (Figs. (6.12), (6.13) and (6.14)), it is more readily refracted and therefore shielded, but its presence still only slightly affects the overall shielding pattern.

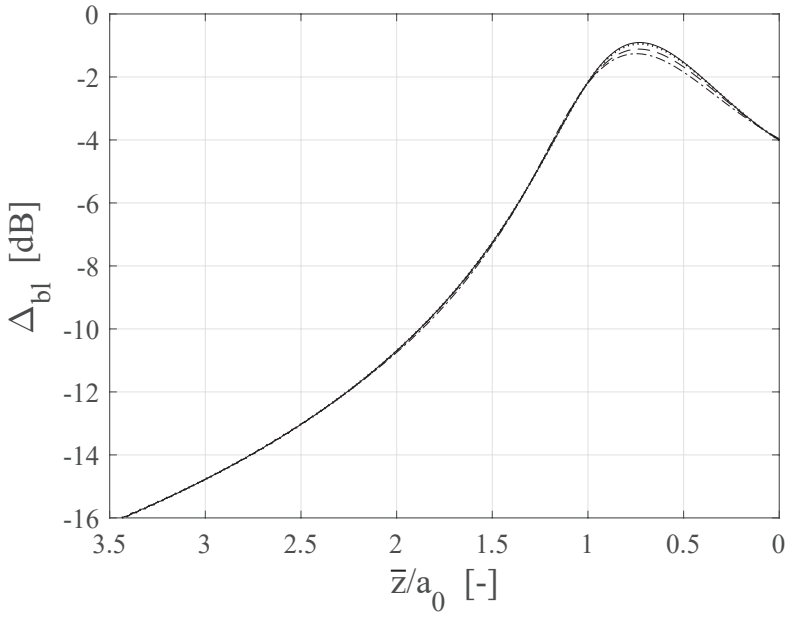

FIGURE 6.12: Δ_{bl} at $\bar{\phi} = 0^o$ for operating condition 4. Results for source W_{ee} [solid line], W_{10} [dotted line], W_{20} [dashed line], W_{30} [dash-dotted line]. Average boundary-layer thickness is used for the calculations.

The only impactful differences in the shielding of different rotor-locked sources occurs with W_{30} when the rotor-locked mode is much more powerful than the rest of the cut-on modes. At later conditions (5 and 6) the rotor-locked mode's secondary lobe starts to become cut-on as discussed in the previous section. Since the secondary lobe is very close to cut-off, at these conditions it travels towards the boundary layer at a much steeper angle than the rest of the cut-on modes, thus it is less shielded by the boundary layer, and consequently dominating the shielding pattern. The same dominance is not observed for operating condition 3 and the principal lobe. A possible explanation, is that operating condition 3 introduces newly cut-on modes, the majority of which are very close to cut-off, having cut-off ratios even smaller than the rotor-locked mode. The presence of all those unshielded modes close to the principal lobe of the rotor-locked mode tends to keep the shielding pattern smooth. Operating conditions 5 or 6 do not introduce so many nearly cut-off modes, giving the opportunity to the dominant mode's secondary lobe to stand out.

Lastly in this section, the shielding coefficient is presented for all operating conditions. Although previous figures showed that the presence of a rotor-locked mode did not make a practical difference (in terms of dB) at the region adjacent to the source (at $\bar{\phi} = 0^o$), the shielding coefficient result in Fig. (6.15) highlights the significant amount of energy that makes its way to the surface of the fuselage when there is a dominant mode present. At operating condition 3 ($\zeta_{(20,1)} = 1.1$), when the dominant mode is just cut-on and propagates at a steep angle, the energy delivered on the surface is larger with the presence of the more powerful rotor-locked mode. For the W_{20} source, roughly 8 % more of the total power finds its way to the surface than in the W_{ee} case for operating condition 3. For the W_{30} source that number is 20 %.

The decrease in shielding at condition 3 is reflected in Fig. (6.11) where there is a slight decrease in shielding. However, Fig. (6.11) only shows results at $\bar{\phi} = 0^o$. It seems that this

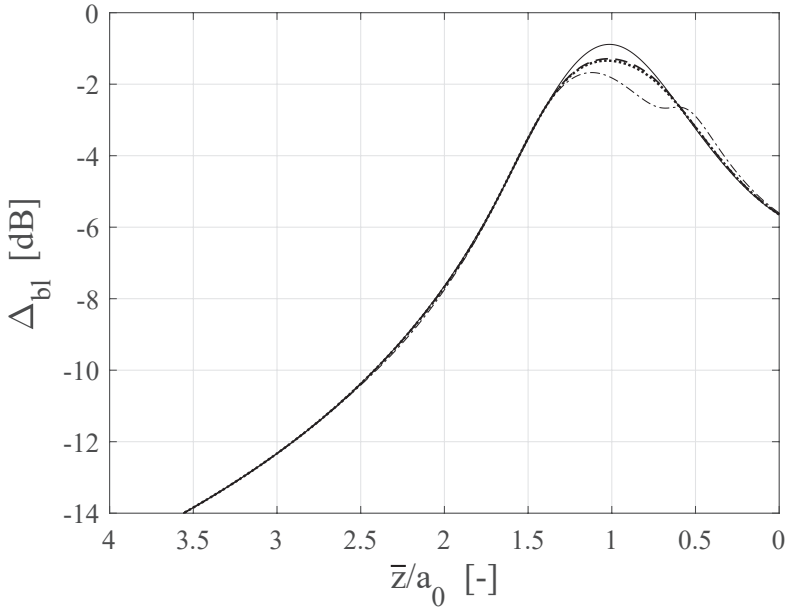

FIGURE 6.13: Δ_{bl} at $\bar{\phi} = 0^o$ for operating condition 5. Results for source W_{ee} [solid line], W_{20} [dotted line], $W_{20,10}$ [dashed line], W_{30} [dash-dotted line]. Average boundary-layer thickness is used for the calculations.

decrease in shielding is accumulated when one considers the whole grid on the surface of the cylindrical fuselage. The weakness of the W_{10} and $W_{20,10}$ sources is once more pointed out, as the W_{10} source results almost coincide with the W_{ee} source results, and the $W_{20,10}$ results almost coincide with the W_{20} results for the conditions 5-6 where their difference lies. Note that as expected, all sources reduce to the equal energy source for the first two conditions because the rotor-locked mode is cut-off.

It is also noted that there is a trend of decreasing shielding for higher $\zeta_{(20,1)}$. As was the case with condition 3 where the addition of newly cut-on modes that were still close to cut-off led to an overall decrease in shielding, the same seems to be happening for higher conditions. In every new condition the newly added modes contain a lot of modes that are increasingly close to cut-off, leading to a decrease in shielding due to their steep propagating angle. Note that this is not the case for the W_{30} source because at higher conditions the dominant mode, which carries a significant percentage of the overall power, becomes more cut-on and thus more shielded. This means that for higher conditions for W_{30}, most of the energy is refracted away being carried by the dominant mode.

This result concludes this section with the key findings being that the more powerful the dominant mode, the more energy reaches the fuselage surface. However, although true physically, practically in terms of dB the shielding (Δ_{bl}) is only slightly affected by the presence of a rotor-locked mode.

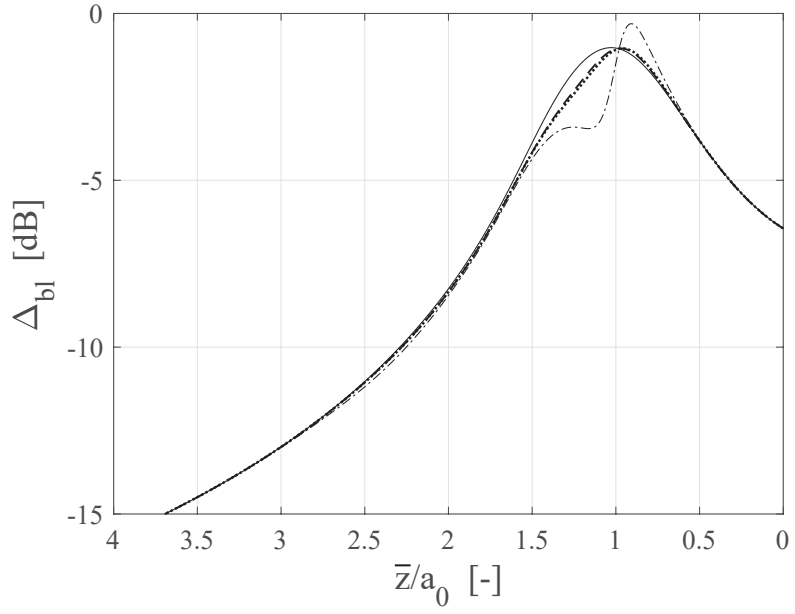

FIGURE 6.14: Δ_{bl} at $\bar{\phi} = 0^o$ for operating condition 6. Results for source W_{ee} [solid line], W_{20} [dotted line], $W_{20,10}$ [dashed line], W_{30} [dash-dotted line]. Average boundary layer thickness is used for the calculations.

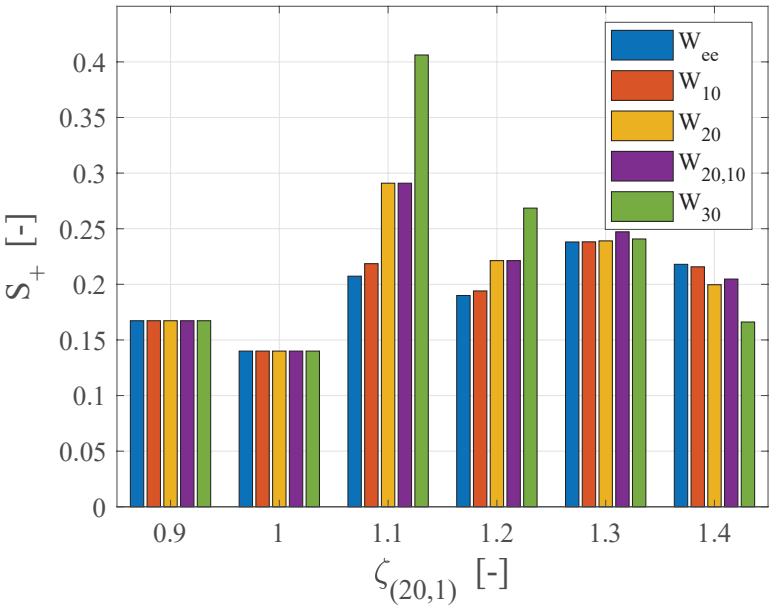

FIGURE 6.15: Shielding coefficient upstream S_+ for all operating conditions. Results for source W_{ee} [blue], W_{10} [red], W_{20} [yellow], $W_{20,10}$ [magenda], W_{30} [green]. Average boundary-layer thickness is used for the calculations.

6.6 Thickness Effect on Shielding

In this section, the effect of boundary-layer thickness on shielding is investigated. The source will be kept constant as W_{20} and an equivalent linear profile is used. The difference between equivalent linear and equivalent step-function will be investigated in the next chapter. The focus is on operating conditions 3 and 6, since respectively they represent a transitioning case and a well cut-on case, giving a comprehensive outlook of the problem.

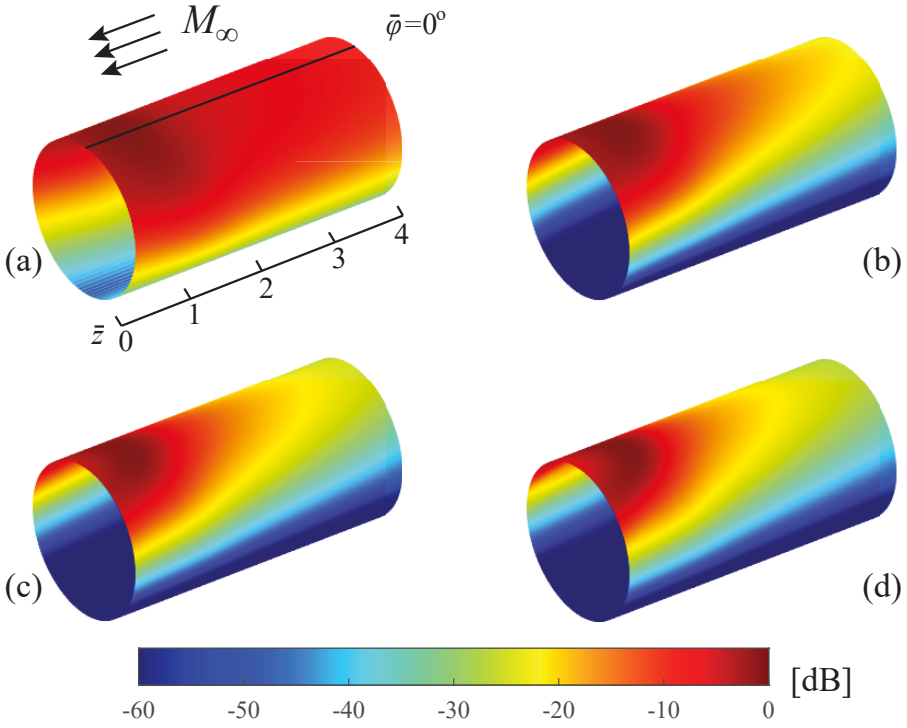

FIGURE 6.16: Total SPL on the surface of the fuselage for operating condition 3 and W_{20} source. Results for uniform flow [(a)], thin boundary layer [(b)], average boundary layer [(c)], thick boundary layer [(d)].

Figures (6.16) and (6.17) show the SPL on the fuselage surface for operating conditions 3 and 6 respectively. One can immediately notice the drastic shielding effect the presence of the boundary layer has when compared with the uniform flow results. In both conditions the shielding is very pronounced upstream concentrating the maximum SPL near the source plane. That is expected since the further upstream sound waves propagate the shallower the incident angle on the boundary layer increasing susceptibility to refraction. Furthermore, the shallower the angle the greater the distance the sound wave needs to travel inside the boundary layer effectively rendering the boundary layer effectively thicker leading to more refraction and shielding.

It is worth noting the importance of the dominant mode's secondary lobe in operating condition 6. When the rotor-locked mode is well cut-on in the uniform flow result, it is clear that the maximum SPL occurs at the position of the principal lobe, while downstream the secondary lobe's position also exhibits a high intensity area, although not as intense as the principal lobe. However, with the addition of the boundary layer, the principal lobe is shielded

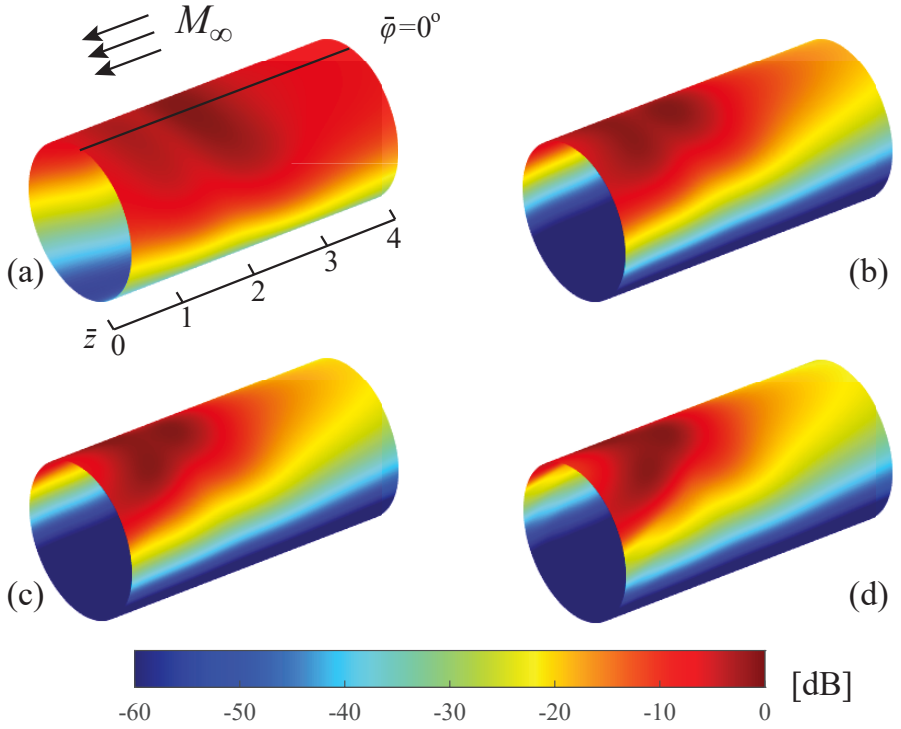

FIGURE 6.17: Total SPL on the surface of the fuselage for operating condition 6 and W_{20} source. Results for uniform flow [(a)], thin boundary layer [(b)], average boundary layer [(c)], thick boundary layer [(d)].

much more than the secondary lobe because it is further upstream. As a result, for the thick or even average boundary layer the maximum SPL area is dominated by the secondary lobe.

Figures (6.18), (6.19) and (6.20) show the Δ_{bl} at the near side of the cylinder for the three thickness cases in order to quantify the shielding. Generally, close to the plane of the source the predictions for the three boundary-layer thicknesses are similar to each other because in this area sound waves travel towards the boundary layer at a very steep angle thus minimising the refraction effect rendering the thickness of the layer irrelevant. It should follow that difference results at or very close to the plane of the source converge to zero. However, since analysis in this work does not include diffraction around the fan duct lip, results very close to the plane of the source should not be considered realistic. Further upstream, the effect of thickness on shielding is drastic, and, as expected, the thicker the boundary layer the more shielding is produced.

Finally, the thickness effect is demonstrated in Fig. (6.21) where almost consistently for the range of operating conditions the difference in the shielding coefficient between thin and thick case is over 15 %. This indicates that the thick boundary layer shields or refracts away 15 % more of the total energy compared to the thin boundary layer case. The results shown in this section confirm the strong dependence of shielding on boundary-layer thickness.

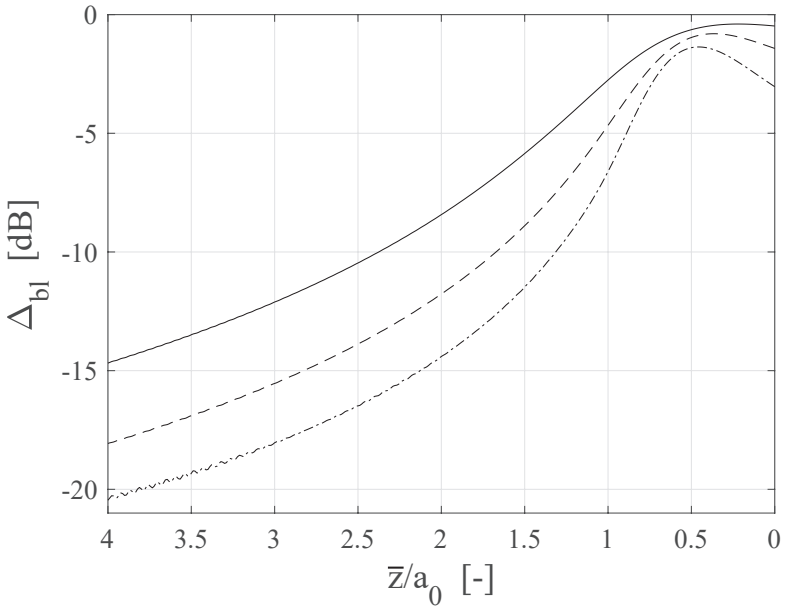

FIGURE 6.18: Δ_{bl} at $\bar{\phi} = 0^o$ for operating condition 1 and W_{20} source. Results for thin boundary layer [solid line], average boundary layer [dashed line] and thick boundary layer [dash-dotted line].

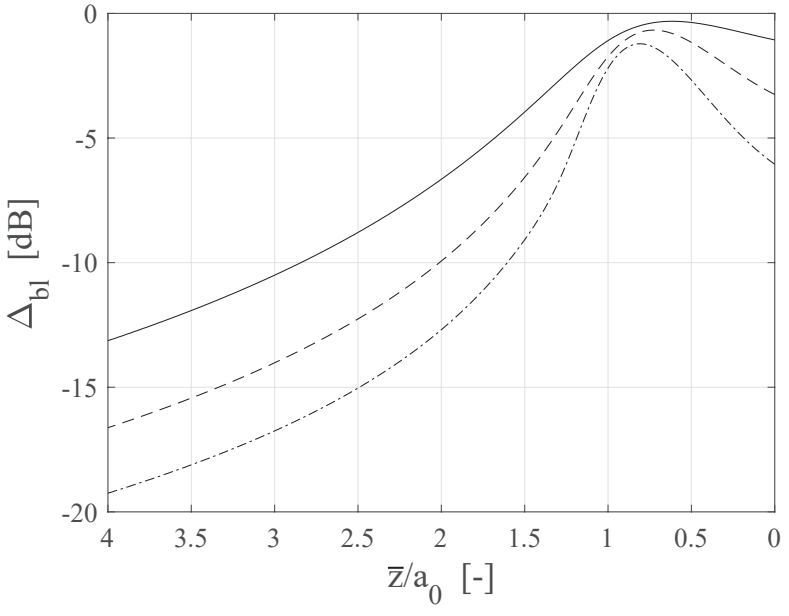

FIGURE 6.19: Δ_{bl} at $\bar{\phi} = 0^o$ for operating condition 3 and W_{20} source. Results for thin boundary layer [solid line], average boundary layer [dashed line] and thick boundary layer [dash-dotted line].

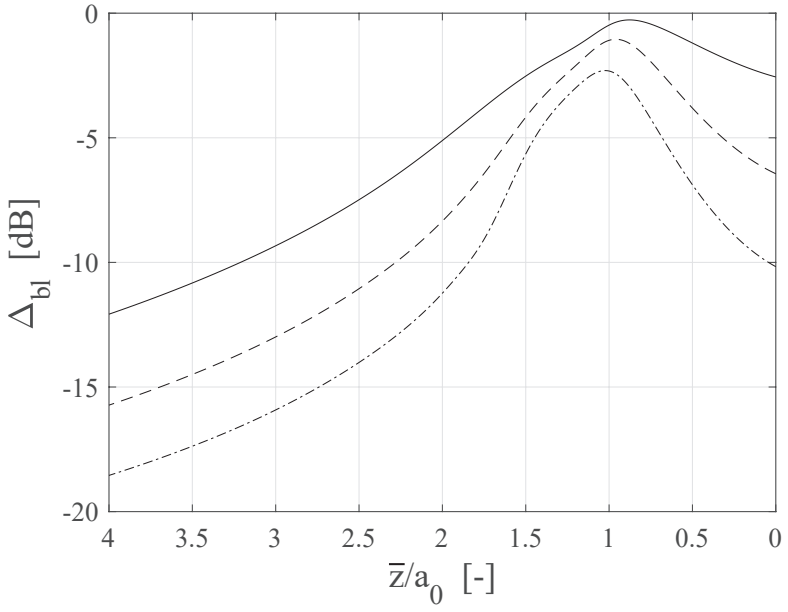

FIGURE 6.20: Δ_{bl} at $\bar{\phi} = 0^o$ for operating condition 6 and W_{20} source. Results for thin boundary layer [solid line], average boundary layer [dashed line] and thick boundary layer [dash-dotted line].

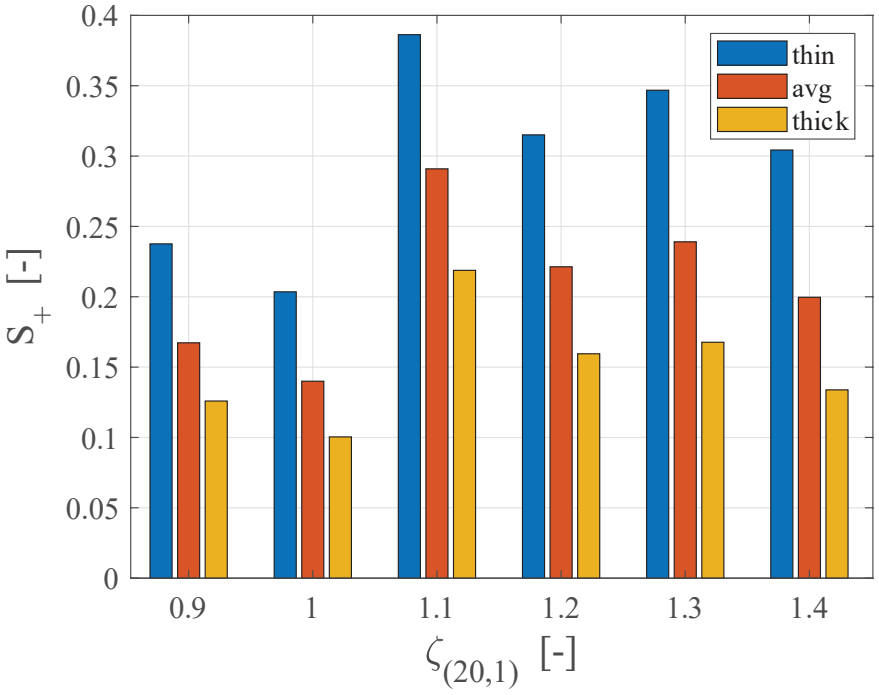

FIGURE 6.21: Shielding coefficient upstream S_+ for all operating conditions and W_{20} source. Results for thin boundary layer [blue], average boundary layer [red], thick boundary layer [yellow].

6.7 Far-Field

This section is dedicated to far-field results. These results aim to give a perspective on how the far-field directivity can be influenced by the presence of a boundary layer on the fuselage. As mentioned at the start of the chapter, results will be presented in the form of polar directivity. This format is chosen because it has been established that the presence of a boundary layer causes effects felt longitudinally because they are in essence convection effects and so the direction of the flow is crucial. Therefore azimuthal directivity plots, albeit they can as easily be generated, would not provide any useful insights. The polar directivity plots that follow correspond to a hemisphere underneath the flight path. Therefore, the calculations were conducted at $\bar{\phi}_{ff} = 3\frac{\pi}{2}$ which corresponds to that region. Since the present work does not include diffraction around the lip of the fan duct or the physical presence of any kind of nacelle, results downstream are not to be considered realistic. For that reason, the polar directivity plots that follow only show results for the upstream region, namely $0 < \bar{\theta} < 90^{o}$. All polar directivity plots are generated at $\bar{R}$ equal to a hundred wavelengths away from the fuselage to ensure the validity of the derived expressions used since they involve large argument approximations.

This section follows the same structure as the results sections for the fuselage pressure, namely the source effect on polar directivity will be shown first (keeping the boundary-layer thickness constant at its average value), and then the boundary-layer thickness effect. All the results are generated using an equivalent linear profile. In the next chapter, some results are presented that have been generated using an equivalent step-function profile and are compared against the corresponding results generated with an equivalent linear profile. The first three figures demonstrate the effect of increasing operating conditions or $\zeta_{(20,1)}$.

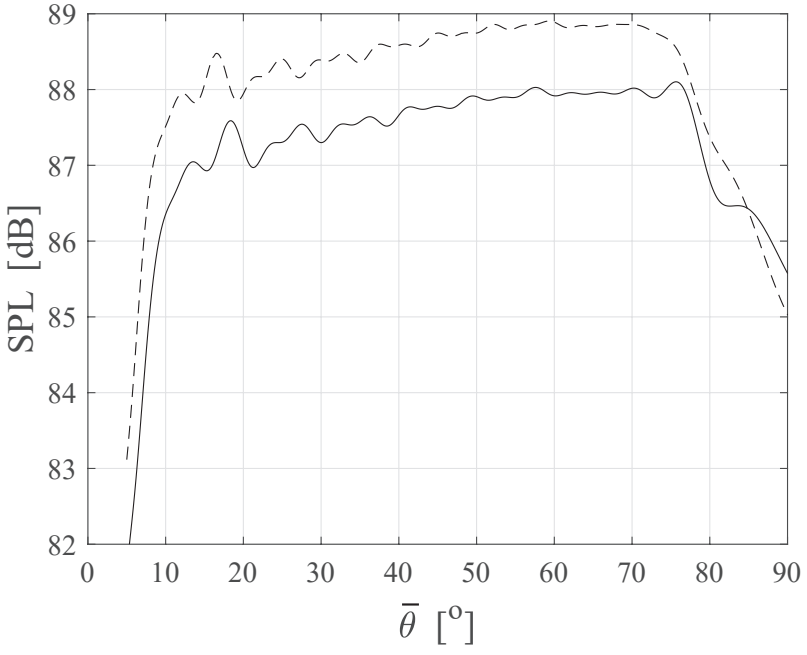

FIGURE 6.22: Polar directivity upstream for W_{20} source and average boundary-layer thickness. Results for operating condition 1 [solid line] and 2 [dashed line].

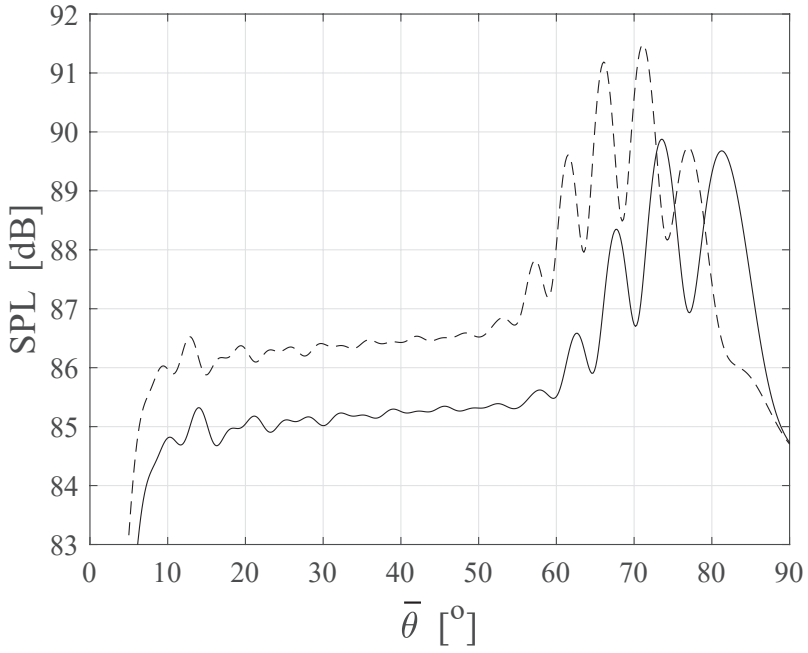

FIGURE 6.23: Polar directivity upstream for W_{20} source and average boundary-layer thickness. Results for operating condition 3 [solid line] and 4 [dashed line].

Figures (6.22), (6.23) and (6.24) show the directivity for each operating condition and source W_{20}. Similar to the fuselage pressure results, the pattern for the first two operating conditions is fairly smooth because there is no dominant mode cut-on yet, and thus all modes' contributions are the same. However, the presence of a rotor-locked mode in higher conditions is clearly visible in the directivity plots in Figs. (6.23) and (6.24). The principal lobe of the rotor-locked mode is distinctive as it exhibits a difference from the rest of the multi-mode pattern up to 5 dB. Furthermore, the cut-off ratio effect can be observed very clearly as it did in the surface pressure results. The more cut-on the dominant mode is the shallower its propagation angle. Therefore, at condition 3 when the rotor-locked mode is barely cut-on, the directivity plot exhibits a distinctive lobe very close to 90°. With each next condition as the rotor-locked becomes more cut-on, this distinctive lobe moves upstream, or more correctly its propagation angle approaches zero. Eventually, for condition 6 the lobe has moved to around 55° polar angle. For all these figures a pattern of alternating maxima and minima develops which is characteristic of reflection and interference, which is expected with the cylinder being adjacent to the source. Sound waves will propagate from the source and reflect off the fuselage surface, or refract away from the surface, eventually arriving in the far-field.

6.7.1 Source Effect on Polar Directivity

This section deals with the source effect on polar directivity. All calculations were conducted using the average boundary-layer thickness and an equivalent linear profile. As in the surface pressure results, the focus is on the operating conditions 3 and 6 as they represent a transitioning and a well cut-on case respectively.

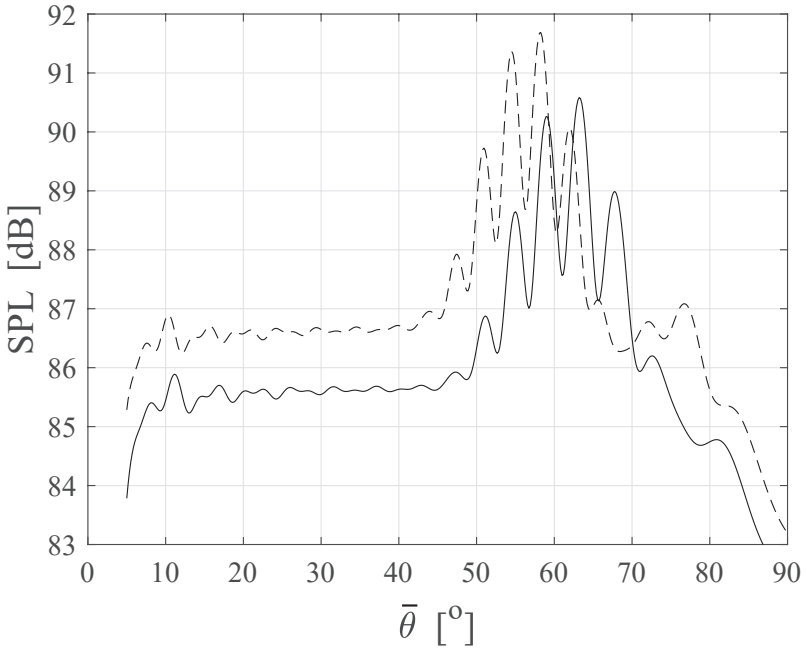

FIGURE 6.24: Polar directivity upstream for W_{20} source and average boundary-layer thickness. Results for operating condition 5 [solid line] and 6 [dashed line].

Figures (6.25) and (6.26) illustrate the power distribution differences between the sources. Once again, as in the surface pressure results, the weakness of the W_{10} and $W_{20,10}$ sources is demonstrated with the first one producing minor differences compared to the equal energy source, namely a small increase of level at the position of the rotor-locked mode's principal lobe. On the other hand, source $W_{20,10}$ produces a directivity almost identical to that of the W_{20} source. Only at the position of the principal lobe of the second radial order rotor-locked mode (20,2) a small increase of level appears which is expected. The second radial order mode (20,2) is less cut-on than the first order (20,1) which means it propagates at an angle closer to 90°. This is observed in Fig. (6.26), where this increase of level is closer to 90° than the distinctive lobe at 55° for which the first radial order rotor-locked mode (20,1) is responsible for.

As shown in the surface pressure results, this increase of level at certain regions will inevitably lead to a deficit (i.e. lower level) at the remaining regions in order for all the sources to have an equal power output. This is demonstrated in Figs. (6.25) and (6.26) where the more powerful sources W_{20} and W_{30} exhibit an increase of level at the position of the rotor-locked mode's principal lobe, but away from that angle they exhibit lower levels than that of the equal energy source. Finally, for source W_{30} the secondary lobe of the rotor-locked mode has become clearly visible in operating condition 6 (Fig. (6.26)). Obviously, the secondary lobe propagates at an angle closer to 90° compared to the principal lobe, and it does not have the same intensity as the principal lobe, but it dominates the region around it nonetheless.

This concludes this section with the key finding the importance of the presence of the rotor-locked mode. Similar to the conclusion reached in the surface pressure results, the rotor-locked mode dominates the far-field directivity pattern as it concentrates the power.

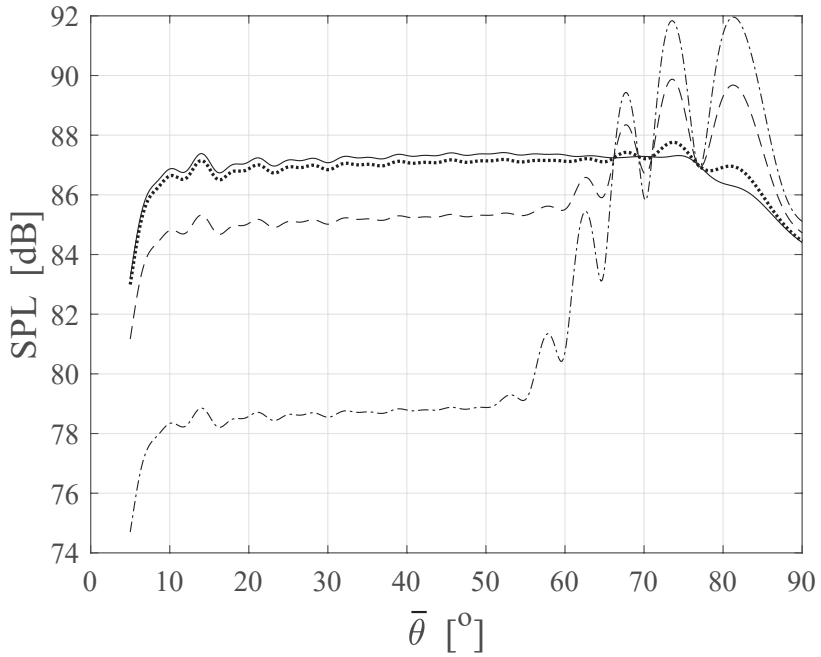

FIGURE 6.25: Polar directivity upstream for operating condition 3. Average boundary-layer thickness is used for the calculations. Results for source W_{ee} [solid line], W_{10} [dotted line], W_{20} [dashed line], W_{30} [dash-dotted line].

6.7.2 Thickness Effect on Polar Directivity

In this section the effect of the boundary-layer thickness on the polar directivity is investigated. An equivalent linear profile is used to generate the results since the difference between the two theoretical approaches' far-field directivity prediction will be investigated in the next chapter.

Figures (6.27) and (6.28) show very similar behaviour. For both operating conditions the presence of the boundary layer creates a phase shift in the directivity compared to the directivity of the uniform flow. This phase shift, although still visible, is largely irrelevant at polar angles away from the dominant mode's propagation angle. However, around the rotor-locked mode's angle this phase shift becomes substantial. Furthermore, this phase shift is observed between the directivities generated using different boundary-layer thicknesses, illustrating the importance of the boundary layer effects in the far-field. When a rotor-locked mode is involved in the engine's acoustic output the boundary layer should be considered in evaluating the far-field polar directivity. Note that the amplitude is unaffected by the thickness of the boundary layer, since it is the distance from the source that controls the level in the far-field (geometric spreading).

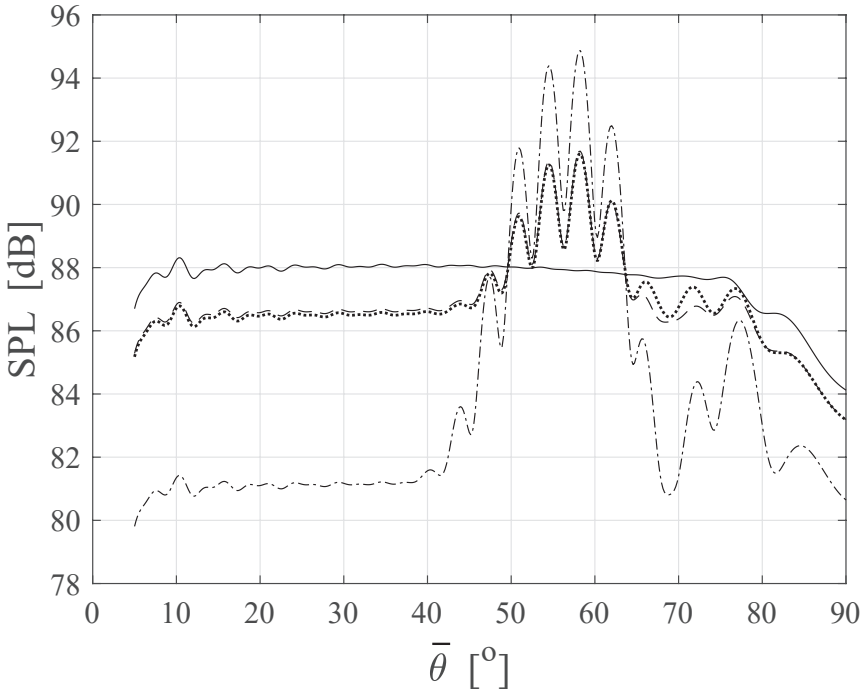

FIGURE 6.26: Polar directivity upstream for operating condition 6. Average boundary-layer thickness is used for the calculations. Results for source W_{ee} [solid line], $W_{20,10}$ [dotted line], W_{20} [dashed line], W_{30} [dash-dotted line].

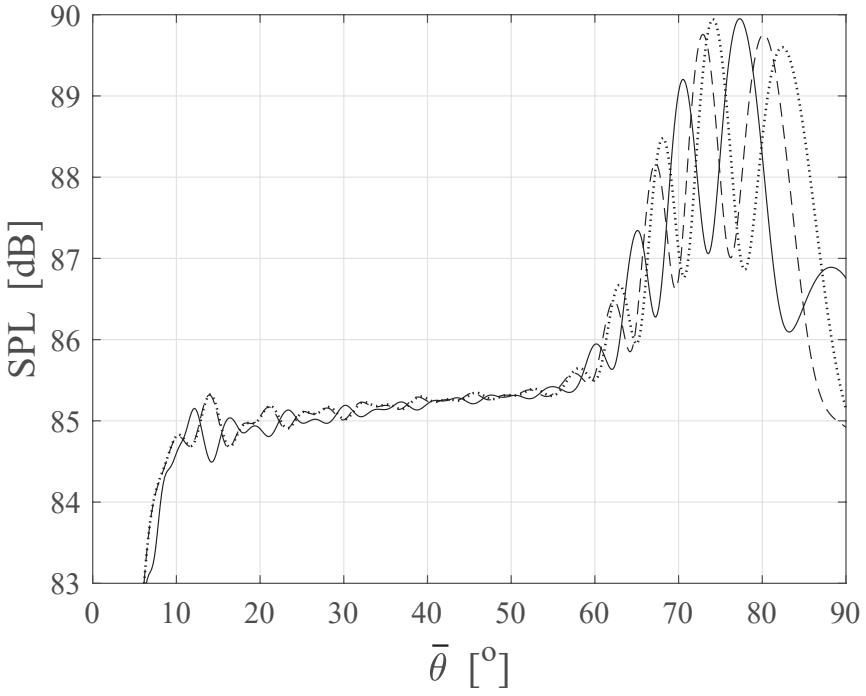

FIGURE 6.27: Polar directivity upstream for operating condition 3 and source W_{20}. Results for uniform flow [solid line], thin boundary layer [dashed line] and thick boundary layer [dotted line].

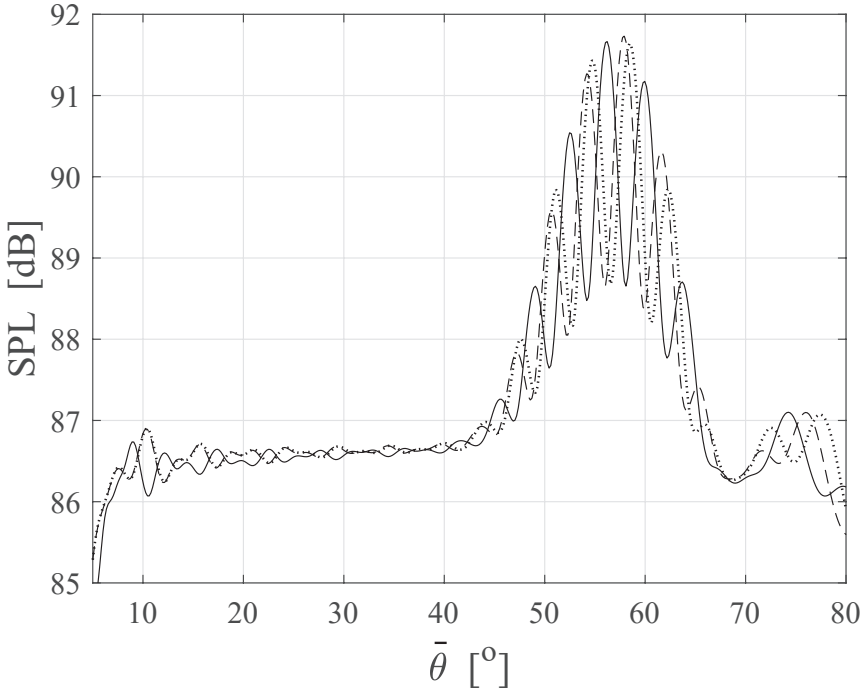

FIGURE 6.28: Polar directivity upstream for operating condition 6 and source W_{20}. Results for uniform flow [solid line], thin boundary layer [dashed line] and thick boundary layer [dotted line].

Chapter 7

Discussion of the Results

In this chapter, attention is focused on a selection of key results that are either important or somewhat counter-intuitive in the author's opinion. The previous chapter presented the results of the parametric study covering a variety of effects, namely source power distribution, the effect the source has on shielding, the effect the boundary-layer thickness has on shielding, and also the differences in the predictions of the two theoretical approaches. The results revealed the importance of the Mach number and its relevance to the shielding. The results also illustrated that the shielding tends not to be influenced by the type of source, at least not in practical terms (on a dB scale), as presented in Rouvas and McAlpine (2022a) which is based on the present work. As was expected the significant effect of the boundary-layer thickness was demonstrated. However, there are certain physical effects that have not been discussed yet in depth, and have already shown their impact in the results presented in the previous chapter. Furthermore, since the capability of the equivalent step-function profile approach to simulate a representative 1/7th power-law profile has already been shown in chapter 5, it is in the scope of this chapter to present comparisons between the two theoretical approaches. Therefore, the parametric study has been conducted using an equivalent step-function profile as well.

The importance and impact of the modes' distribution and cut-off ratios has already been implied in the previous chapter. In this chapter, a more in depth discussion is presented in order to illustrate the cut-off ratio effect on the overall pressure on the fuselage surface. Moreover, although for most configurations the shielding is largely unaffected by the presence of a dominant rotor-locked mode (Rouvas and McAlpine (2022a)), there are instances where the combination of source power and cut-off ratio may lead to the secondary lobe to be dominant in the shielding and overall pressure pattern. The effect of the dominant mode on the total SPL contour pattern on the fuselage surface has been demonstrated in the previous chapter, and here a more comprehensive look into the physical mechanisms of the effect is given. Furthermore, in this chapter an azimuthal effect created by the source's directivity is examined. Finally, comparisons between the two theoretical approaches (equivalent linear profile vs. step-function profile) are presented. The previous chapter only presented results generated with an equivalent linear profile.

7.1 Effect of Cut-off Ratio

This section examines the effect the cut-off ratio of the modes has on shielding. The cut-off ratio as a parameter can provide a lot of insight into the physical problem since it is directly related to the group velocity angle of the mode. This angle is defined as

$$\psi_z = \cos^{-1}\left[\frac{S\sqrt{1-M_z^2}}{\sqrt{1-M_z^2\,S^2}}\right], \tag{7.1}$$

where $S = \sqrt{1-\frac{1}{\zeta^2_{(l,q)}}}$ and the mode's cut-off ratio

$$\zeta_{(l,q)} = \frac{k_0}{\kappa_{lq}\sqrt{1-M_z^2}}, \tag{7.2}$$

as given in Rice et al. (1979). Therefore, as explained before, the closer to cut-off a mode is (as $\zeta_{(l,q)}$ approaches unity), the propagation angle approaches 90^o relative to the duct axis, meaning the waves propagate towards the fuselage surface at a steeper or more perpendicular angle. The cut-off ratio can therefore be used as an indicator for the distribution of the modes in terms of their incident angles on the fuselage surface. Furthermore, the cut-off ratio is an expression that combines both the most important flow characteristic, Mach number M_z, and the most important acoustic characteristic, frequency k_0. This dependence on both M_z and k_0 makes it useful when attempting to estimate a trend.

As shown in the previous chapter in Fig. (6.10), the dependency of shielding on the Mach number is shown to be very strong. Also, the frequency dependence is observed as explained in the previous chapter by examining the pairs of conditions. It is clear that for higher conditions there is a tendency for less shielding dictated by the fact that higher conditions have lower Mach number. Since flow has a shortening effect on the wavelengths upstream, the higher the Mach number the shorter the effective wavelengths compared to the boundary-layer thickness, which consequently leads to more shielding. Therefore, for higher conditions that are characterised by lower Mach number the shielding is reduced. The frequency, albeit having a far wider range of values across the operating conditions (k_0a ranges from 13 to 23 whereas Mach number only ranges from 0.75 to 0.65), appears to have a weaker effect than the Mach number, which leads to the counter-intuitive effect of higher frequency causing less refraction and therefore less shielding. Figure (6.10) is not the only instance where this happens. The same pairing and trend across the operating conditions is observed in Fig. (6.15). By observing the W_{ee} source shielding coefficient in Fig. (6.15) one can notice the same pairing between every two conditions, and a general upward trend in the shielding coefficient indicating less and less shielding.

In order to better understand the mechanisms that lead to this upward trend in the shielding coefficient, the contributions of the modes present in each of the operating conditions are split into two subsets. For each condition there is a subset of modes that are already cut-on from the previous operating condition. The rest of the cut-on modes represent the subset of modes that are newly added and were cut-off in the previous condition. The shielding coefficient of the W_{ee} source shown in Fig. (6.15) is presented here again, but with the modes' subsets contributions split.

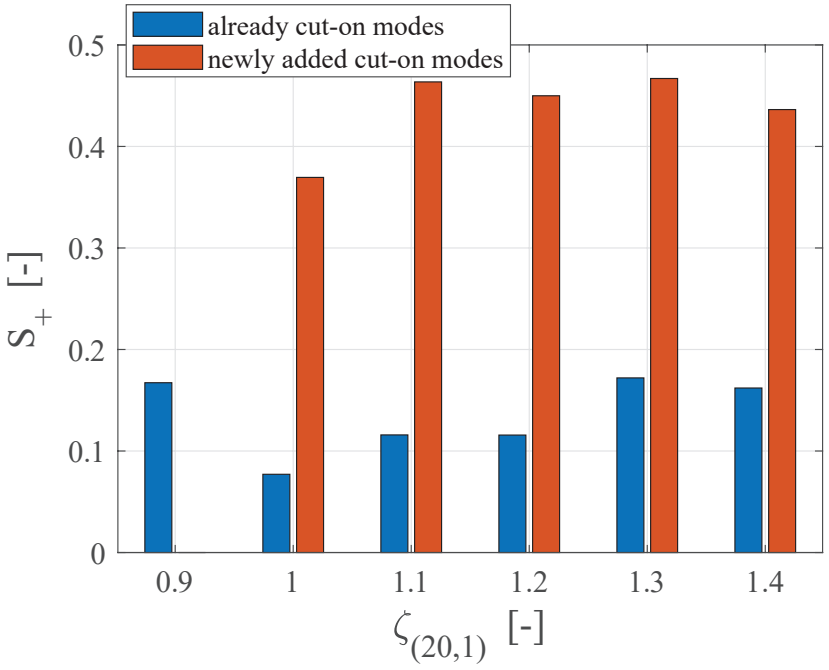

FIGURE 7.1: Shielding coefficient upstream S_+ for all operating conditions and W_{ee} source. Contribution of already cut-on modes [blue], contribution of newly added cut-on modes [red]. Average boundary-layer thickness is used for the calculations.

In Fig. (7.1) it is observed that there is substantial difference in shielding between the two subsets of modes. The newly added modes are much closer to cut-off than the already cut-on modes, which means that they propagate to the boundary layer at a steeper angle leading to substantially less refraction and shielding. However, the already cut-on modes are a larger set of modes than the newly added subset, which means that rarely the newly added modes dominate the overall pressure pattern. This happens in operating conditions 2 and 3 where the already cut-on modes are a relatively smaller subset compared to the newly added ones. In higher conditions, it becomes clear that the already cut-on mode subset dictates the trend by comparing Figs. (7.1) and (6.15). This is also demonstrated in table (7.1) where it is shown that for each condition only about 20 to 30 newly cut-on modes are added for each change in condition in comparison to the already existing modes that are over 150 for the higher conditions.

Another crucial information in table (7.1) is the average cut-off ratio of the two subsets of modes, which is found by simply taking the average of the cut-off ratios of the modes in each subset. The average cut-off ratio may not be a vigorous metric but it is useful here to identify the trends in the shielding. For both mode subsets the average cut-off ratio tends to decrease with ascending operating condition. This implies that for higher conditions there will be a general tendency for less shielding, since the modes that are added tend to make the overall average of the group less cut-on. That consequently means that sound tends to propagate towards the boundary layer at a steeper angle making it less susceptible to refraction and shielding. This finding implies that the modal output of the fan could be used as a means for

Operating Conditions	1	2	3	4	5	6
$\zeta_{(20,1)}$	0.9	1.0	1.1	1.2	1.3	1.4
Number of cut-on modes	111	133	164	193	225	258
Average ζ of already cut-on modes subset	1.9806	2.2007	2.2106	2.1702	2.1657	2.1583
Average ζ of newly added modes subset	—	1.0545	1.0486	1.0386	1.0354	1.0351

TABLE 7.1: Mode subsets average cut-off ratios.

identifying trends in the shielding, since generally decreasing cut-off ratio effectively means decreasing shielding.

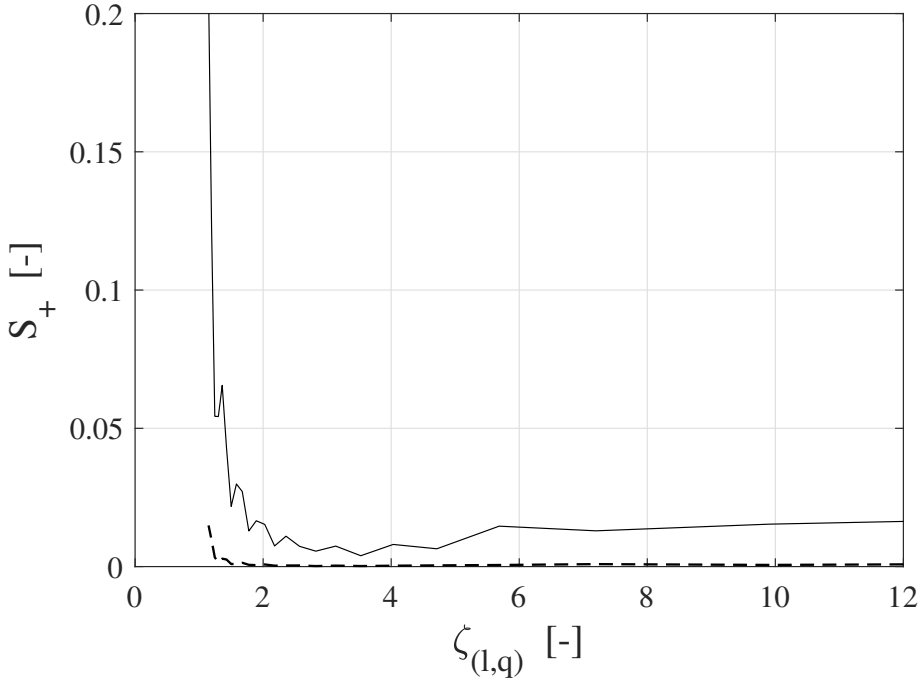

FIGURE 7.2: Shielding coefficient upstream S_+ for frequency $k_0 a = 20$. Prediction for $\delta = 0.01 a_0$ [solid line] and $\delta = 0.1 a_0$ [dashed line]. Equivalent linear profile is used for the calculations.

By examining the values in table (7.1) one can immediately realise that although the cut-off ratio is decreasing, it does so in very small increments. Despite these small increments, their impact cannot be ignored in the overall shielding. Figure (6.15) for the equal energy source shows an increase of 8 % more power reaching the fuselage surface at higher conditions. This decrease in shielding is also demonstrated in Fig. (6.10) where the Δ_{bl} exhibits a difference of up to 4 dB between the first and higher conditions. This very sensitive relationship between the cut-off ratio and the shielding coefficient is demonstrated in Figs. (7.2) and (7.3). These figures are reproduced from chapter 5, namely Figs. (5.10) and (5.8). In this chapter, these figures are presented again, but with their horizontal axis expressed as cut-off ratio. In the case of Fig. (7.2), Fig. (5.10) has been modified so that the azimuthal order values on the horizontal

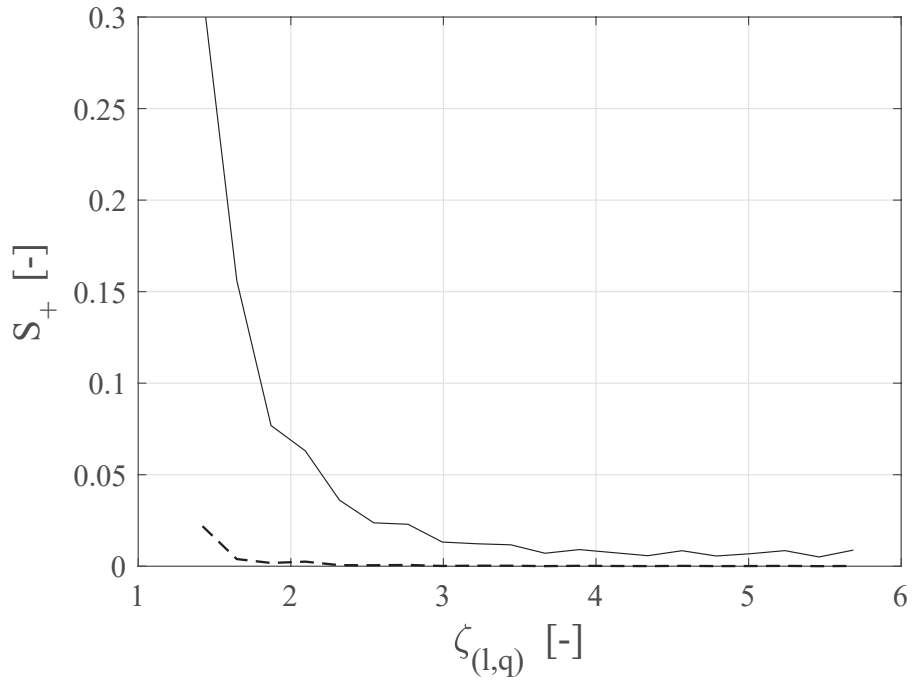

FIGURE 7.3: Shielding coefficient upstream S_+ for mode $(l, q) = (4, 1)$. Prediction for $\delta = 0.01a_0$ [solid line] and $\delta = 0.1a_0$ [dashed line]. Equivalent linear profile is used for the calculations.

axis are now expressed as cut-off ratio values. The same for the case of Fig. (7.3), where Fig. (5.8) has been modified so that the frequency values on the horizontal axis are expressed as cut-off ratio values.

By examining Figs. (7.2) and (7.3) one can observe that for low cut-off ratios (lower than 2.5), the shielding coefficient exhibits an extremely steep increase for decreasing cut-off ratio. On the other hand, for higher cut-off ratios the shielding coefficient is remarkably stable, and does not seem to be affected at all by increasing cut-off ratio. It is therefore expected that at lower cut-off ratios, a further decrease in cut-off ratio can lead to a disproportionate increase in shielding coefficient (or decrease in shielding). Table (7.1) exhibits average cut-off ratio values well inside this lower cut-off ratio region. It is therefore fair to expect a somewhat disproportionate decrease in shielding for higher conditions that exhibit slightly decreased average cut-off ratios.

Figures (7.2) and (7.3) effectively demonstrate the total reflection phenomenon. The higher the cut-off ratio (the more cut-on a mode is) the shallower the angle the sound is incident on the boundary layer. At some point, the sound rays will propagate at an angle shallow enough that they will be refracted away by the boundary layer totally without reaching the surface, what is called total reflection. That is the reason why both Figs. (7.2) and (7.3) exhibit a plateau region for higher cut-off ratios. Effectively, it is seen that above cut-off ratio of about 4, total reflection is achieved meaning that further increases in the cut-off ratio will not make any difference since no more sound will reach the surface of the cylinder.

Another explanation for the importance of the cut-off ratio and the mode propagation angle can be provided by using Snell's law. Although in acoustics Snell's law is only applied to

plane waves, it still represents a fundamental analogy that describes acoustic refraction due to a shear layer in the flow. Figure (7.4) depicts plane waves incident on a boundary layer that is characterised by no flow in the region of width δ adjacent to the surface. The plane waves emanate from the source at an incident angle θ_i, the same way the principal lobe of a mode emanates from the fan duct at angle ψ_z from the duct's centreline as shown in eq.(7.1). Then the plane wavefronts are incident on the layer's edge and are transmitted through the layer at a new propagation angle θ_t. There is also a reflected wave however it is omitted from this analogy. Snell's law for plane waves that originate from a uniform flow region with Mach number M_∞ transmitted through a layer with no flow velocity is given by Glegg and Devenport (2017), eq.(10.2.7), page 236:

$$\cos\theta_t = \frac{\cos\theta_i}{1 - M_\infty \cos\theta_i} \tag{7.3}$$

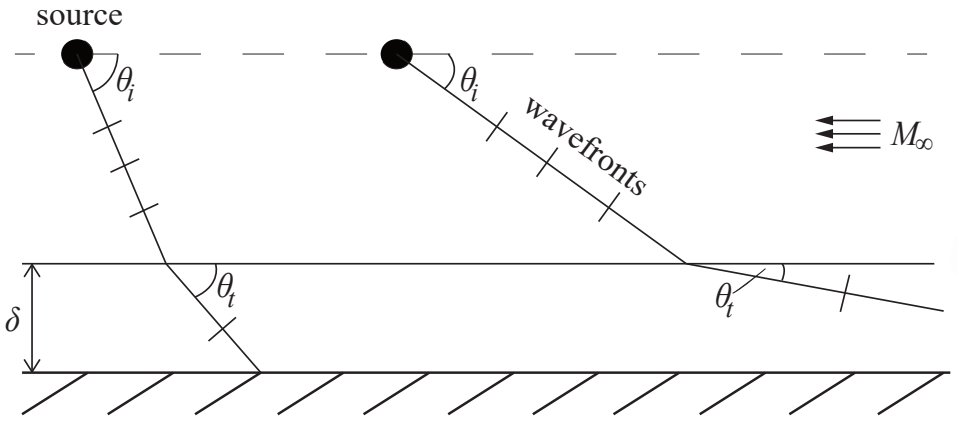

FIGURE 7.4: Interaction of a plane wave with a shear layer.

Equation (7.3) provides an excellent analogy for the problem investigated here. When the incident angle θ_i is very large (close to 90°), in other words the waves travel almost perpendicular to the centerline which translates to very small cut-off ratio, then from eq.(7.3) it follows that $\cos\theta_t \simeq \cos\theta_i$ or $\theta_t \simeq \theta_i$. That effectively means that for propagation angles close to 90° the waves will hardly be refracted. They will continue to travel in the same direction which means that shielding is minimal. This is observed in the results multiple times in chapters 5 and 6, as well as in Figs. (7.2) and (7.3) where for small cut-off ratios (or propagation angles close to 90°) there is a sharp decrease in shielding.

On the other hand, for smaller incident or propagation angles θ_i, it follows from eq.(7.3) that $\cos\theta_t > \cos\theta_i$ or $\theta_t < \theta_i$. It also follows that as the incident angle θ_i becomes smaller, the angle θ_t becomes smaller at a higher rate. That effectively means the shallower the angle of incidence on the layer the more refraction and therefore shielding is produced. This upstream effect has been observed and discussed in chapters 5 and 6. Furthermore, from eq.(7.3) one can notice that there will be a value of angle θ_i for which the value of angle θ_t is zero. From that point and for θ_i values smaller than that, no waves propagate into the layer or reach the fuselage surface

leading to a stabilisation of shielding at its maximum value. This is observed in Figs. (7.2) and (7.3) where for large cut-off ratios, or in other words for small incident angles, the shielding coefficient reaches its minimum value and stabilises to a fixed value.

7.1.1 Universal Parameter

At this point in the work, it has been shown that the cut-off ratio, either in its average form ζ or its singular mode form $\zeta_{(l,q)}$, is a good indicator of the acoustic behaviour of the configuration. As explained in section 7.1, the cut-off ratio as a controlling non-dimensional number has the advantage of combining the source characteristics (frequency k_0, mode order l and duct radius a) as well as the important flow characteristic, M_∞, see eq. (7.2). As a result, it gives a comprehensive insight into the physical mechanisms involved in the problem. However, as shown in chapter 6, there is another flow characteristic or parameter not present in the cut-off ratio expression in eq. (7.2). That parameter is the boundary-layer thickness, δ or ε in its non-dimensional form.

Therefore, it would be beneficial to introduce a universal non-dimensional parameter that will include all the source and flow characteristics, namely mode order l and intake duct radius a, flight Mach number M_∞, frequency k_0 and the non-dimensional boundary-layer thickness ε, which involves the physical δ thickness normalised with the fuselage radius a_0 which is another useful physical parameter. One such universal parameter that combines every physical property involved in the problem can be defined as

$$\xi = \zeta\,\varepsilon, \tag{7.4}$$

where ζ is the cut-off ratio in its average form or its singular mode form $\zeta_{(l,q)}$, referring to the average cut-off ratio of all the modes or the cut-off ratio of just one mode (l,q) respectively. In essence, parameter ξ is a metric that indicates shielding. Contrary to the shielding coefficient S_+, smaller values of ξ will indicate less shielding, while larger values will indicate more shielding.

Let us consider the following examples. By assuming a constant non-dimensional boundary-layer thickness ε, one can manipulate ξ by manipulating accordingly the cut-off ratio ζ. Smaller values of ζ, which correspond to smaller values of ξ, will lead to less shielding because the modes will propagate towards the boundary layer at a steeper angle and therefore will be subject to less refraction as explained in section 7.1 and Fig. (7.4). On the other hand, for a constant boundary-layer thickness ε, larger values of ζ, which correspond to larger values of ξ, will lead to more shielding because the modes will propagate towards the boundary layer in a shallower angle.

Now consider a constant cut-off ratio ζ. One can manipulate the ξ by manipulating accordingly the boundary-layer thickness ε. As seen in chapters 5 and 6, smaller ε will lead to less shielding, while larger values will inevitably lead to more shielding since the boundary-layer thickness becomes significantly larger than the wavelength. Therefore, it is evident that the universal parameter ξ can be used to give an estimate of the amount of shielding that is expected for any given configuration, which includes frequency, flight Mach number, mode order, intake duct radius, fuselage radius and boundary-layer thickness.

7.2 Dominance of Rotor-Locked Secondary Lobe

In the previous chapter the effect of the presence of a dominant rotor-locked mode was investigated. It was concluded that the presence of a rotor-locked mode did not make a considerable difference in the shielding (see Figs. (6.11) through (6.14)) although it did make a substantial impact on the overall pressure pattern on the fuselage surface, as seen in Figs. (6.6) and (6.7). Furthermore, it has been demonstrated that the more powerful the dominant mode compared to the rest of cut-on modes, the more substantial its influence on the overall pressure pattern. The source W_{30} case also revealed an emerging dominance of the secondary lobe of the rotor-locked mode in certain conditions.

According to previous research (Schwaller et al. (1997), Schwaller et al. (2006), Achunche et al. (2009)), the blade passing frequency rotor-locked mode is routinely up to 20 dB higher than the rest of the cut-on modes, thus the W_{20} source is representative of this scenario. However, experimental measurements (Schwaller et al. (1997), Schwaller et al. (2006), Achunche et al. (2009)) reveal plenty of deviation around this 20 dB value. It is therefore useful to evaluate the impact of the more powerful source W_{30}, as it can give more insight into the physical problem. It has been observed in the previous chapter that for certain configurations and powerful rotor-locked sources, the shielding pattern can be altered, albeit not dramatically. The more substantial impact is observed in the overall SPL pattern on the fuselage surface. This section aims to highlight the influence of the rotor-locked mode, and especially its secondary lobe, on the shielding and overall pressure pattern.

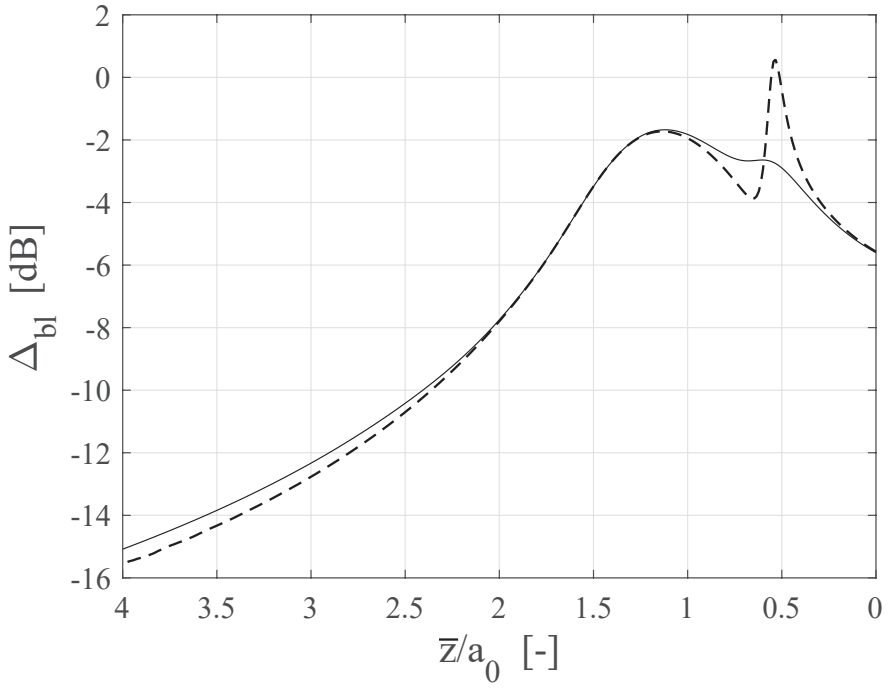

FIGURE 7.5: Δ_{bl} at $\bar{\phi} = 0^o$ for operating condition 5. Results for source W_{30} [solid line] and the single rotor-locked mode only [dashed line]. Average boundary layer-thickness is used for the calculations.

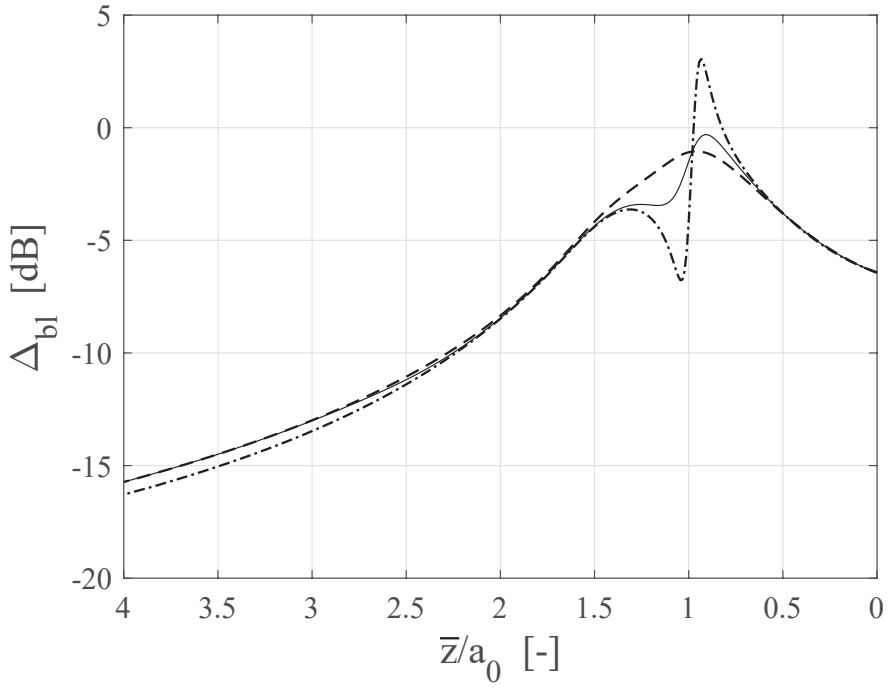

FIGURE 7.6: Δ_{bl} at $\bar{\phi} = 0^o$ for operating condition 6. Results for source W_{30} [solid line], source W_{20} [dashed line] and the single rotor-locked mode only [dash-dotted line]. Average boundary-layer thickness is used for the calculations.

Figure (7.5) shows the difference Δ_{bl} for operating condition 5. Both the contribution of the rotor-locked mode only is shown, as well as the total contribution of all the cut-on modes including the rotor-locked mode at 30 dB higher. At this operating condition, the secondary lobe is just cut-on, as evidenced that it is located very close to the plane of the source. The principal lobe is located further upstream at around $\bar{z}/a_0 = 1.25$. By examining the rotor-locked mode plot, one can see that the principal lobe, which is further upstream, is subject to more shielding, while the secondary lobe naturally is subject to less shielding as it is located less upstream. However, the secondary lobe is barely developed, as it is just cut-on, which means that although it is less shielded it does not yet surpass the contribution of the more shielded principal lobe. Therefore, when the rest of the cut-on modes' contributions are added, the effect of the dominant secondary lobe is greatly diminished or rather offset by the rest of the contributions. Despite that fact, the W_{30} shielding pattern still exhibits a small decrease at the location of the rotor-locked secondary lobe, demonstrating the importance of a powerful enough rotor-locked mode.

The impact of the rotor-locked secondary lobe is more pronounced in Fig. (7.6) where the difference Δ_{bl} for operating condition 6 is depicted. In this instance the secondary lobe is much better developed which means that the difference in SPL between the principal and the secondary lobe is smaller. That being said, the principal lobe is still subject to more shielding than the secondary lobe, leading to the secondary lobe's contribution to surpass the principal lobe's contribution. This difference in shielding is apparent not only in the rotor-locked mode, but also in the W_{30} case, where differences up to 3 dB between the locations of the lobes is observed. Moreover, the shielding pattern of the W_{30} case is dominated by the shielding

pattern of the rotor-locked mode, highlighting the influence of the dominant mode. Even for the W_{20} case, the lowest shielding location is dictated by the lowest shielding location of the rotor-locked mode, which is at the location of the secondary lobe. Therefore, it is clear that there can be configurations where the rotor-locked secondary lobe will be more relevant than the principal lobe, at least in terms of shielding.

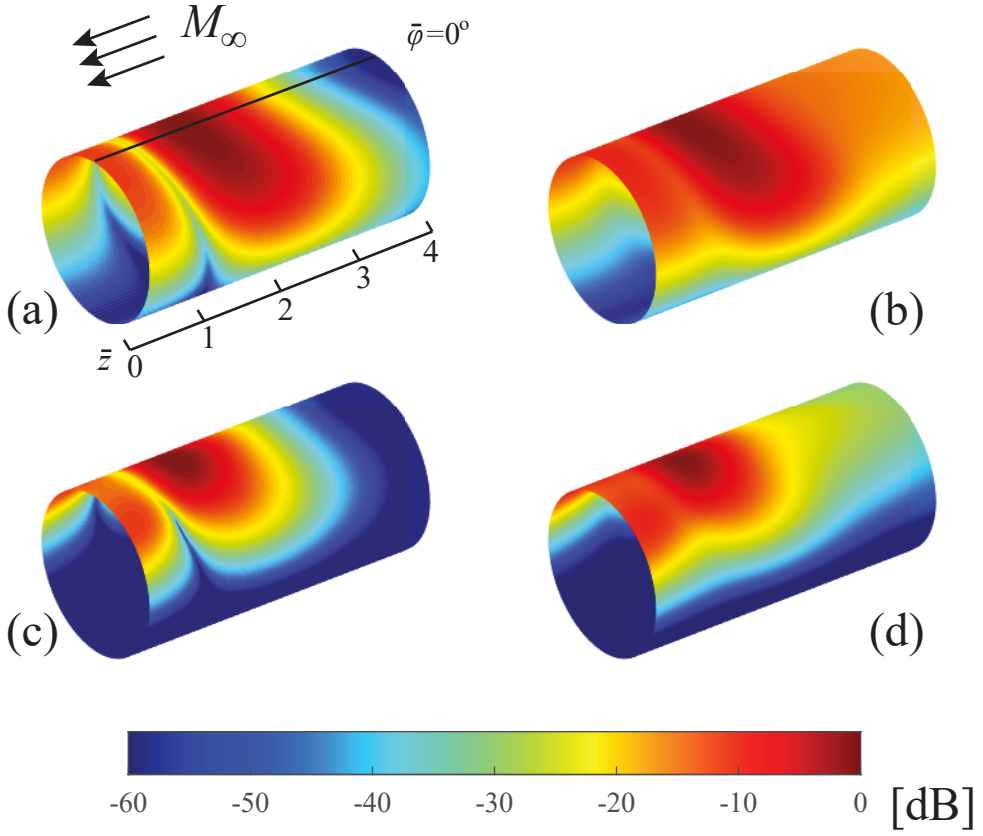

FIGURE 7.7: SPL on the surface of the fuselage for operating condition 5. Results for the single rotor-locked mode with uniform flow [(a)], single rotor-locked mode with average boundary-layer thickness [(c)], source W_{30} with uniform flow [(b)], source W_{30} with average boundary-layer thickness [(d)].

However, as illustrated in the previous chapter, it is important to also consider the overall pressure pattern on the fuselage surface, and not only the shielding. Cylinder plots for operating condition 5 in Fig. (7.7) show the weakness of the secondary lobe at this condition. The area it affects is smaller and less intense than the principal lobe's area which tends to dominate both the uniform flow and the average boundary-layer pressure contour pattern. This is expected because at this point, the secondary lobe is just cut-on, and therefore underdeveloped compared to the principal lobe, as shown in Fig. (7.7(a)). Comparing the four cylinder plots together, one can realise the importance of the presence of a rotor-locked mode. The contour pattern that forms for the single rotor-locked mode heavily influences the resulting total pattern, when all the other cut-on modes are added. The major difference between the plots with the single rotor-locked mode, and the W_{30} plots, is the smoothing out of the null zones present in the rotor-locked mode plots. That is expected and consistent with

multi-mode analysis since the rest of the modes, having a wide range of propagation angles, will "fill in" the null zones, leading to a smoother pattern.

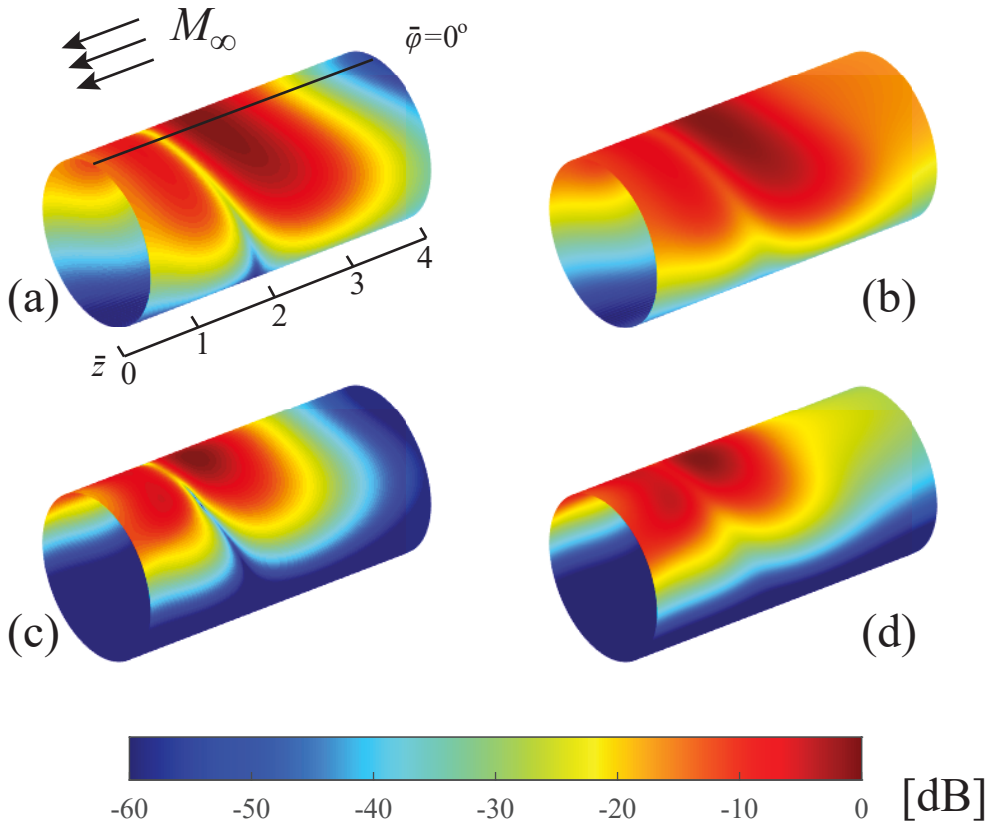

FIGURE 7.8: SPL on the surface of the fuselage for operating condition 6. Results for the single rotor-locked mode with uniform flow [(a)], single rotor-locked mode alone with average boundary-layer thickness [(c)], source W_{30} with uniform flow [(b)], source W_{30} with average boundary-layer thickness [(d)].

The same conclusion can be drawn by observing the operating condition 6 cylinder plots in Fig. (7.8). However, in this case the presence of the secondary lobe cannot be ignored. Comparing Figs. (7.7(a)) and (7.8(a)), one can notice that the secondary lobe in condition 6 occupies a much larger area and is more intense. Naturally, with no boundary layer to refract upstream sound, the principal lobe dominates the pattern for both the single rotor-locked mode and the W_{30} source cases. However, with the inclusion of the boundary layer, the further upstream principal lobe area is shielded much more than the secondary lobe area. This results in a secondary lobe area that extends to the same size as the principal lobe area, and has pressure levels very similar to the principal lobe area. Therefore, the contribution of the secondary lobe should not be ignored when designing the acoustic lagging of the fuselage.

7.3 Linear vs. Step-Function Approach Comparison

In this section, the two theoretical approaches are compared to each other. Theoretical predictions generated using an equivalent linear profile are compared against predictions

generated using an equivalent step-function velocity profile. All the parametric study results presented in the previous chapter using an equivalent linear profile are reproduced using an equivalent step-function profile and are compared against each other. In this section, some key findings and comparisons are presented. The section follows the same structure as the sections in chapter 6, i.e. firstly, an investigation will be presented to determine the differences the two approaches have on the source-power effects, and, secondly, an investigation on their differences on the boundary-layer thickness effects.

7.3.1 Source Effect

In the results that follow, the thickness used in the calculations is the average boundary-layer thickness. Effect of varying thickness will be examined later. Varying source types and operating conditions are examined here in order to determine the differences between the equivalent linear profile approach and the equivalent step-function profile approach.

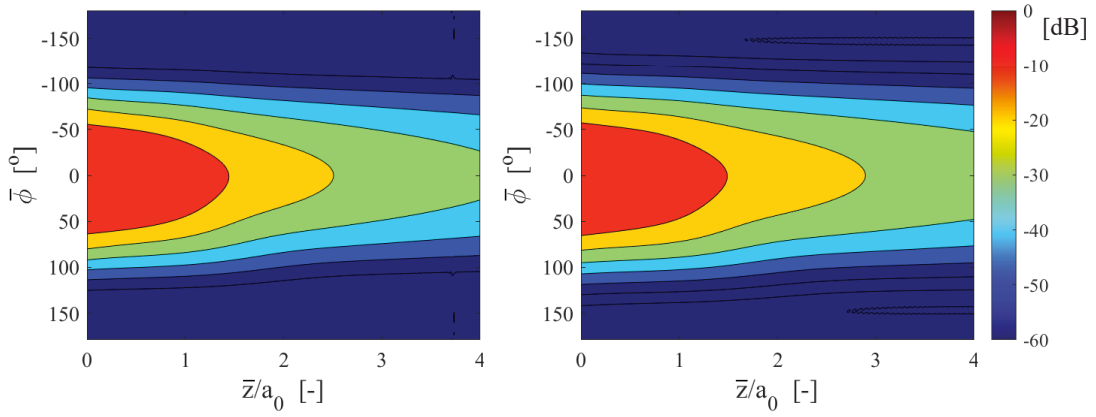

FIGURE 7.9: SPL on the surface of the fuselage for W_{20} source and operating condition 3. Results for equivalent step-function profile [left], equivalent linear profile [right]. Average boundary-layer thickness is used for the calculations.

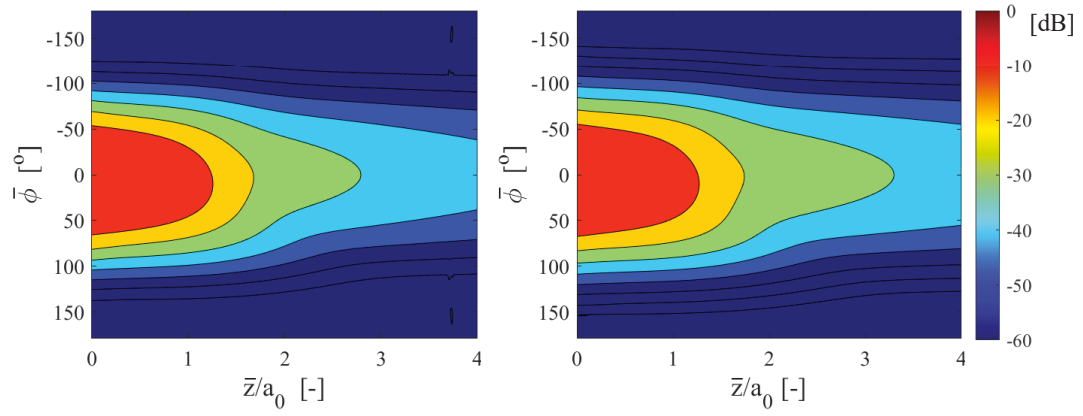

FIGURE 7.10: SPL on the surface of the fuselage for W_{30} source and operating condition 3. Results for equivalent step-function profile [left], equivalent linear profile [right]. Average boundary-layer thickness is used for the calculations.

Figures (7.9) and (7.10) show contour maps of the SPL on the surface of the cylinder for condition 3 and sources W_{20} and W_{30}. The two theoretical predictions agree well with each other, especially close to the plane of the source. Further upstream, the equivalent step-function profile results seem to predict slightly more shielding than the equivalent linear profile results. Bearing in mind that the average boundary layer is about 4.5 % of the fuselage radius, a reasonable underprediction in shielding from the equivalent linear profile approach is to be expected for this thickness of boundary layer (see Fig. (5.17)).

Furthermore, it is expected that the difference between the two approaches will be more noticeable further upstream, as exhibited in Figs. (7.9) and (7.10). As explained before, the further upstream the sound waves propagate the larger the distance they travel inside the boundary layer resulting in an effectively thicker layer. A thicker layer means deterioration in the accuracy of the equivalent linear profile approach as discussed in previous chapters. This deterioration in accuracy creates the discrepancy between the two approaches' predictions (see Fig. (5.17)) that can be seen more noticeably when $\bar{z}/a_0 > 2$. Closer to the plane of the source, the sound waves enter the boundary layer at steeper angles, and therefore travel a smaller distance inside it, resulting in effectively a thinner layer, which means better accuracy for the equivalent linear approach, and consequently better agreement between the two theoretical predictions.

Moreover, by examining Figs. (7.9) and (7.10) it is quite clear that the agreement of the two approaches does not depend on the power of the dominant mode. For both source types the comparison between the two approaches follows the same behaviour. That is rather expected, as it has already been proven in previous chapters that the validity and accuracy of the equivalent linear profile prediction depends heavily on the boundary-layer thickness.

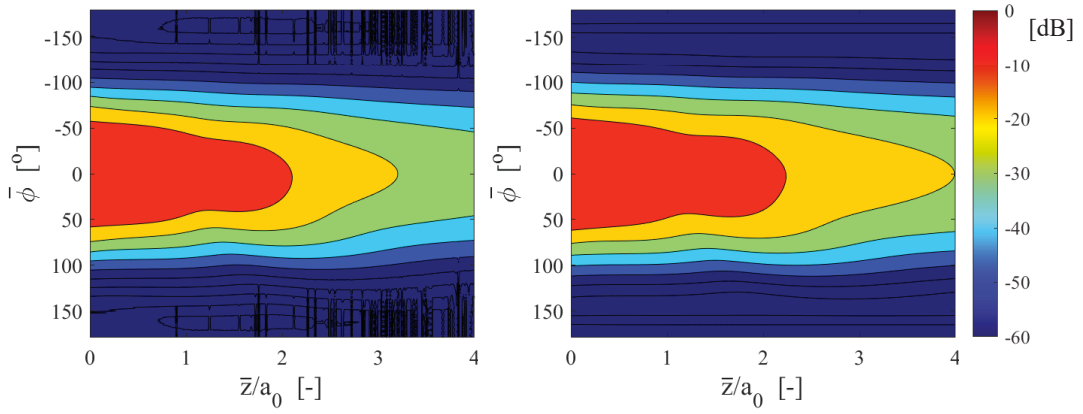

FIGURE 7.11: SPL on the surface of the fuselage for W_{20} source and operating condition 6. Results for equivalent step-function profile [left], equivalent linear profile [right]. Average boundary-layer thickness is used for the calculations.

Similar behaviour is observed for the results in operating condition 6 in Figs. (7.11) and (7.12). However, there is a visible discrepancy between the predictions using the source W_{30} at the plane of the source. As mentioned earlier, predictions very close to the plane of the source should not be considered realistic as the present work does not include diffraction around the lip of the nacelle. A possible explanation for the discrepancy there is an inability of the

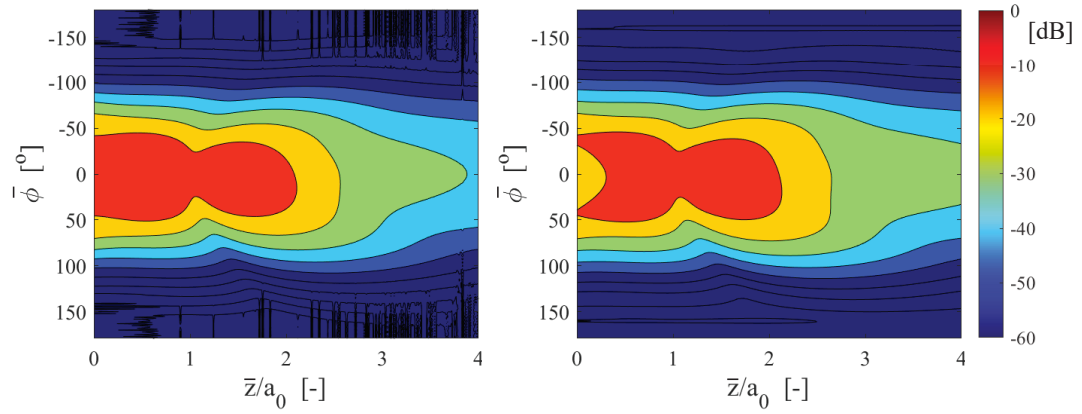

FIGURE 7.12: SPL on the surface of the fuselage for W_{30} source and operating condition 6. Results for equivalent step-function profile [left], equivalent linear profile [right]. Average boundary-layer thickness is used for the calculations.

theoretical methods developed to model the phenomenon of refraction in the azimuthal direction which becomes relevant only in the region very close to the plane of the source.

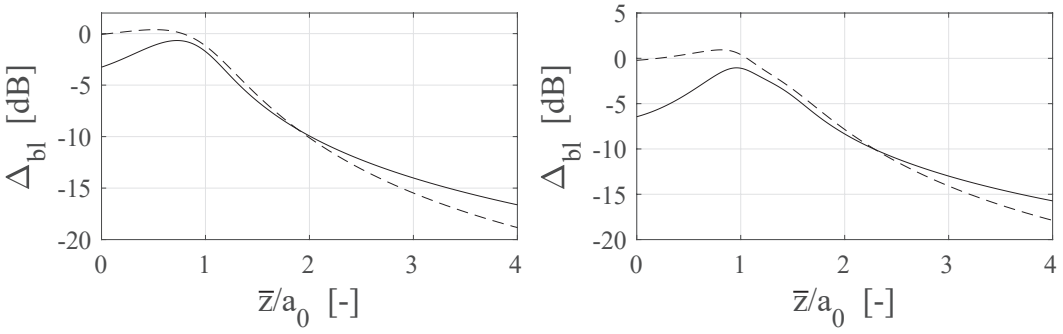

FIGURE 7.13: Δ_{bl} at $\bar{\phi} = 0^o$ for operating condition 3 [left] and 6 [right]. W_{20} source and average boundary-layer thickness used. Results using an equivalent linear profile [solid lines] and an equivalent step-function profile [dashed lines].

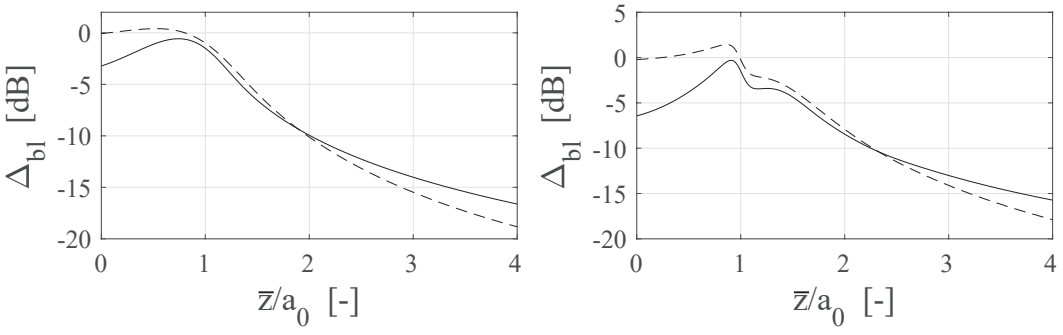

FIGURE 7.14: Δ_{bl} at $\bar{\phi} = 0^o$ for operating condition 3 [left] and 6 [right]. W_{30} source and average boundary-layer thickness used. Results using an equivalent linear profile [solid lines] and an equivalent step-function profile [dashed lines].

Figures (7.13) and (7.14) provide some more quantifiable information on the differences between the shielding predictions of the two approaches. Ignoring the region of inaccuracy very close to the plane of the source, in the rest of the domain the two approaches compare

very well against each other, considering that the average boundary-layer thickness used is thick enough to produce inaccuracies in the equivalent linear profile method (see Fig. (5.17)). Apart from further upstream ($\bar{z}/a_0 > 3$), where the discrepancy is bound to be larger as explained before due to the larger effective thickness, the discrepancy is smaller than 1 dB.

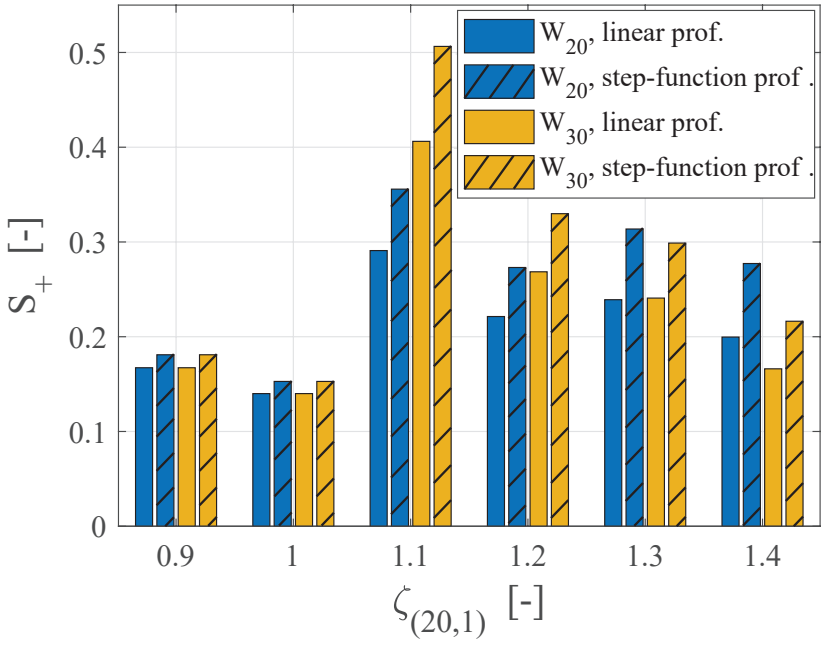

FIGURE 7.15: Shielding coefficient upstream S_+ for all operating conditions, average boundary-layer thickness and sources W_{20} [blue], W_{30} [yellow]. Results using an equivalent linear profile [no hash pattern] and an equivalent step-function profile [hash pattern].

Finally, the shielding coefficient distribution shown in Fig. (7.15) for the two types of sources provides an interesting perspective regarding the distribution of modes on each operating condition. The first two conditions are characterised by a smaller selection of modes that are quite uniformly distributed mainly along the middle section of the cylinder and less so at the extremes of the domain. As seen from Figs. (7.13) and (7.14), the two approaches exhibit the smallest discrepancy at the middle section of the cylinder, while the largest discrepancies are observed at the extremities. Therefore, the shielding coefficients for the two approaches agree very well against each other for the first two conditions.

However, as explained before, with increasing $\zeta_{(20,1)}$ more and more modes are added mainly close to cut-off. This means that they will be incident on the cylinder closer to the plane of the source as they will propagate at steeper mode angles. As observed from Figs. (7.13) and (7.14), closer to the plane of the source the step-function profile approach tends to underpredict shielding, and that is exactly reflected in Fig. (7.15) for the higher conditions. That is especially the case for condition 3, when the dominant mode is just cut-on, which means that the step-function profile method will predict that the bulk of the total energy will find its way to the fuselage surface more readily.

That concludes this section of the comparison between the predictions of the two theoretical approaches focused on varying conditions and sources. The key finding here is that the two

approaches agree reasonably well with each other, especially in the middle section of the cylindrical fuselage, say $1 < \bar{z}/a_0 < 3$. Furthermore, the discrepancy in the predictions of the two approaches does not seem to be affected by different sources or conditions in a practical way (on a dB scale). Nonetheless, the cumulative effect demonstrated by the more physical metric S_+ seems to slightly exaggerate the discrepancy.

7.3.2 Thickness Effect

In the results that follow, the effect of the boundary-layer thickness on the discrepancy of the predictions of the two theoretical approaches is investigated.

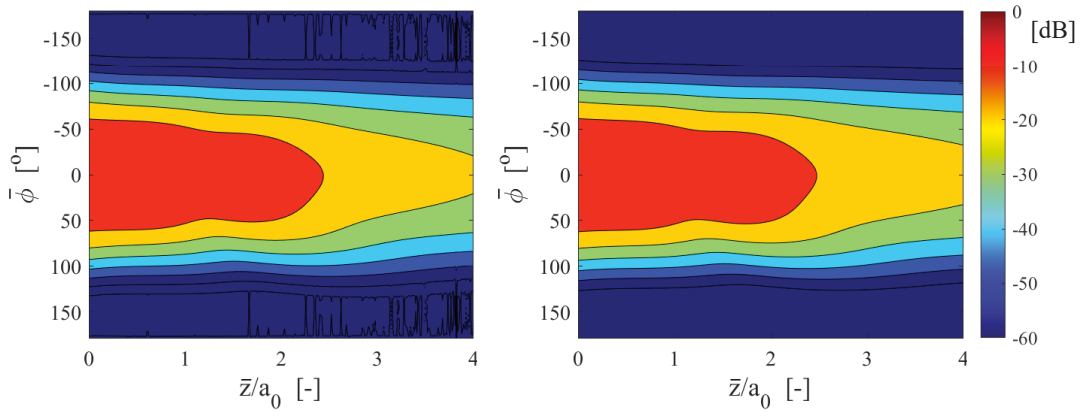

FIGURE 7.16: SPL on the surface of the fuselage for W_{20} source and operating condition 6. Thin boundary layer is used for the calculations. Results for equivalent step-function profile [left], equivalent linear profile [right].

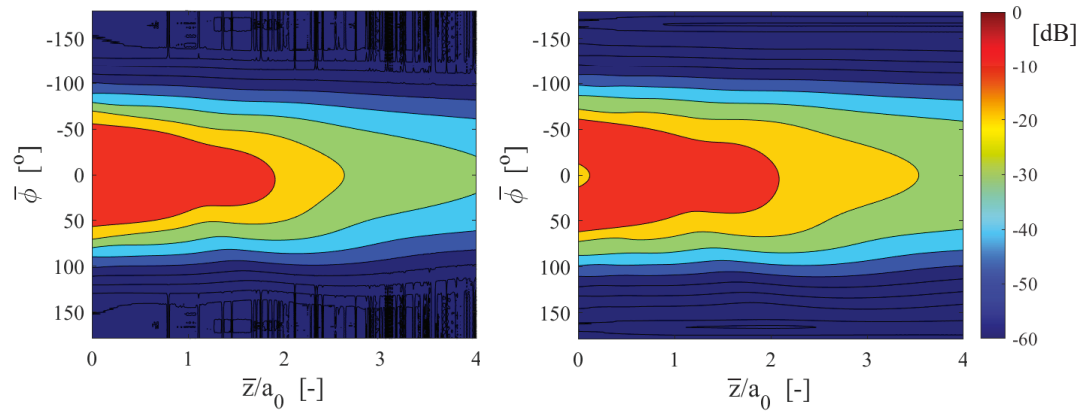

FIGURE 7.17: SPL on the surface of the fuselage for W_{20} source and operating condition 6. Thick boundary layer is used for the calculations. Results for equivalent step-function profile [left], equivalent linear profile [right].

The contour maps in Figs. (7.16) and (7.17) once again illustrate the fact that the equivalent linear profile approach loses accuracy with increasing boundary-layer thickness. Its tendency to underpredict shielding upstream is seen clearly in the thick boundary-layer case presented in Fig. (7.17). On the other hand, for the thin-boundary layer case the agreement between the two approaches' predictions is remarkably good, which is to be expected.

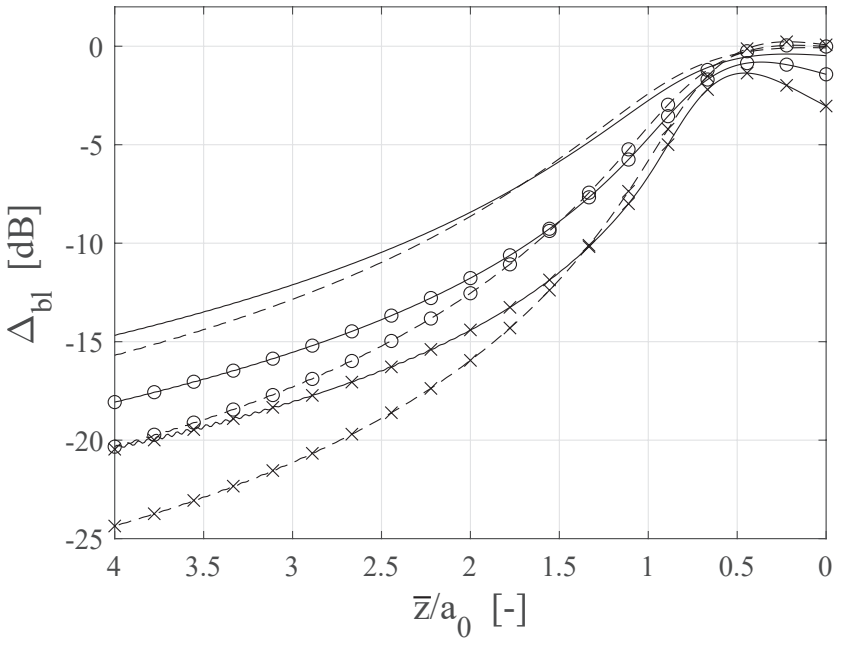

FIGURE 7.18: Δ_{bl} at $\bar{\phi} = 0^o$ for operating condition 1 and W_{20} source for the three boundary-layer thicknesses. Results using an equivalent linear profile [solid lines] and an equivalent step-function profile [dashed lines]. Results are presented for thin boundary layer [no marker], average boundary layer [◯] and thick boundary layer [×].

The Δ_{bl} plots in Figs. (7.18), (7.19) and (7.20) demonstrate the same trend, showing increasing discrepancy with increasing boundary-layer thickness (see Fig. (5.17)) in all operating conditions. Ignoring the region very close to the plane of the source, say $\bar{z}/a_0 < 0.5$, the thin boundary-layer case exhibits remarkable agreement between the two approaches even for regions further upstream, with the difference being less than 1 dB for all operating conditions. As for the average boundary-layer case, the agreement is very good (up to 1 dB) in the middle section of the cylindrical fuselage, up to $\bar{z}/a_0 < 3$ for operating condition 6 and a little further downstream for lower conditions. Furthermore, apart from further upstream, even the thick boundary-layer case presents regions where the two predictions are very close to each other. Of course these regions are fairly close to the plane of the source, say $\bar{z}/a_0 < 2$, as for upstream regions the effective thickness will be larger, and the discrepancy between the predictions is larger as seen in Figs. (7.18), (7.19) and (7.20).

That layout is advantageous when one tries to estimate the shielding produced by a growing boundary layer rather than a constant thickness layer. As observed in Figs. (7.18), (7.19) and (7.20), for all conditions the thin boundary-layer gives good agreement for the entire domain even at the most upstream region, where the boundary layer will be thinner during flight. The average boundary-layer also gives good agreement in the middle section of the cylinder, where this thickness is most representative during flight, whereas the thick boundary-layer tends to exhibit good agreement between the two predictions further downstream towards the plane of the source, again where the boundary layer will be thicker during flight.

Finally, Fig. (7.21) once again exhibits the loss of accuracy of the equivalent linear profile approach with increasing boundary-layer thickness. The thin boundary-layer case exhibits

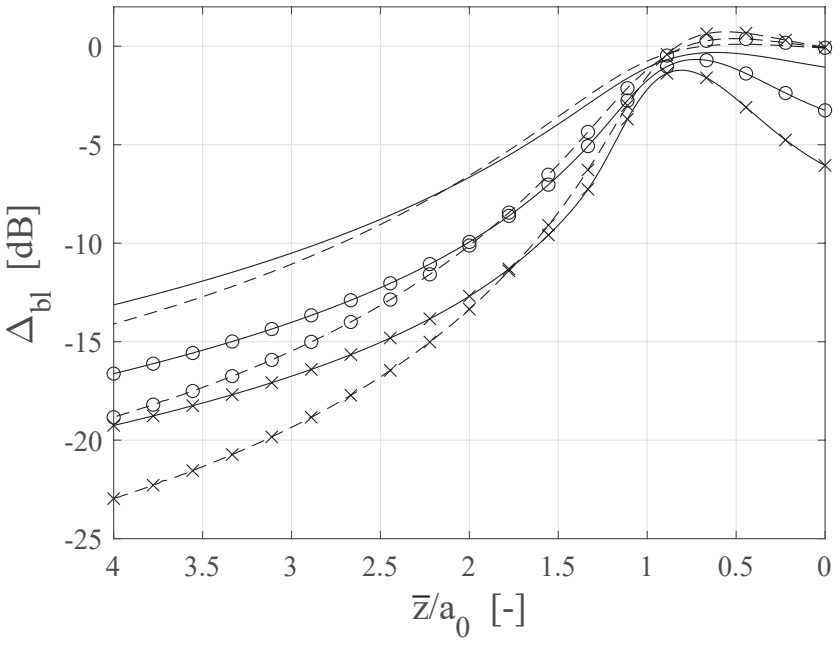

FIGURE 7.19: Δ_{bl} at $\bar{\phi} = 0^o$ for operating condition 3 and W_{20} source for the three boundary-layer thicknesses. Results using an equivalent linear profile [solid lines] and an equivalent step-function profile [dashed lines]. Results are presented for thin boundary layer [no marker], average boundary layer [◯] and thick boundary layer [×].

shielding coefficient predictions that are remarkably close to each other. On the other hand, the thick boundary-layer case exhibits a discrepancy five times larger across the range of operating conditions.

This concludes this section on the comparison between the two theoretical approaches. The key result here is that with a larger boundary-layer thickness, it will inevitably cause a loss of accuracy for the equivalent linear profile approach, which leads to a discrepancy between the predictions of the two approaches as the step-function profile approach tends to retain the same accuracy regardless the boundary-layer thickness (see Fig. (5.17)). Nonetheless, for the entire section of the fuselage that has been considered the two approaches agree well with each other.

7.3.3 Differences in the Far-field

This section contains results generated once again using both theoretical approaches. However, in this section, their differences are examined on the far-field and not on the fuselage surface. The polar directivity prediction using an equivalent linear profile is compared to the polar directivity prediction using a step-function profile. The thick boundary layer is used in the calculations to exaggerate any differences between the two approaches, since the thicker boundary layer causes a drop in the accuracy of the equivalent linear profile method.

By observing Figs. (7.22) and (7.23) it can immediately be seen that the two predictions almost coincide with each other for both conditions. The discrepancy between them is so small that it

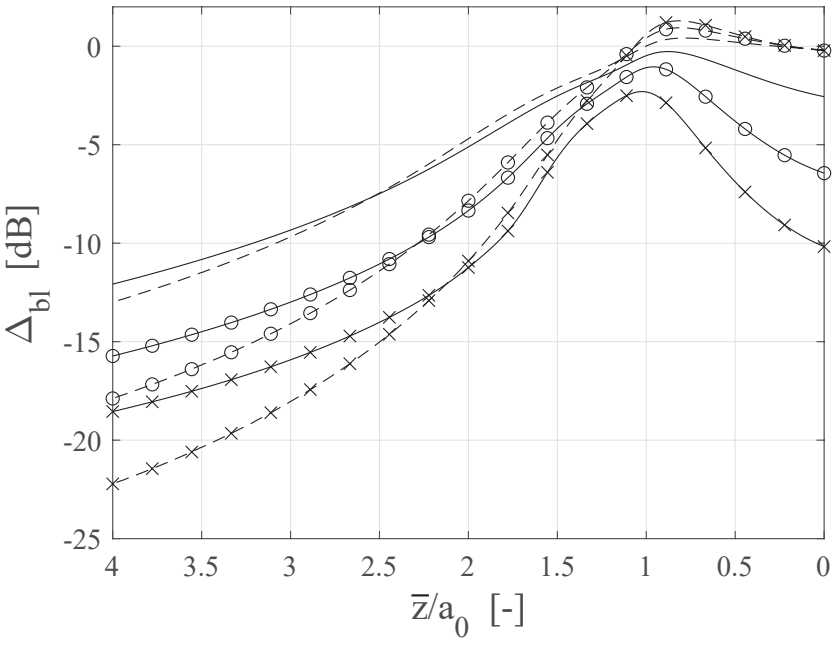

FIGURE 7.20: Δ_{bl} at $\bar{\phi} = 0^o$ for operating condition 6 and W_{20} source for the three boundary-layer thicknesses. Results using an equivalent linear profile [solid lines] and an equivalent step-function profile [dashed lines]. Results are presented for thin boundary layer [no marker], average boundary layer [◯] and thick boundary layer [×].

can be practically ignored. Bear in mind that this is for a thick boundary layer which has been proven to lead to significant differences between the two approaches' predictions, at least for the surface pressure results. It is safe to conclude that in the far-field, the profile used to model the boundary layer does not matter, which is expected as such nuances are bound to be less relevant in the far-field. This conclusion has also been reached by Belyaev (2012). However, it is important to remember that the boundary-layer thickness does play an important role in the far-field, since it is very influential in the shaping of the directivity pattern around the polar angle of the rotor-locked mode, as shown in the previous chapter.

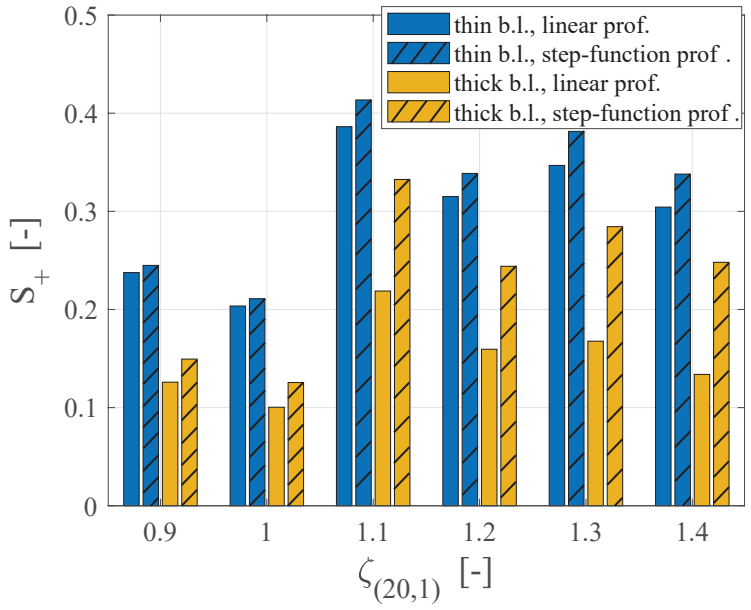

FIGURE 7.21: Shielding coefficient upstream S_+ for all operating conditions and source W_{20} for thin boundary layer [blue] and thick boundary layer [yellow]. Results using an equivalent linear profile [no hash pattern] and an equivalent step-function profile [hash pattern].

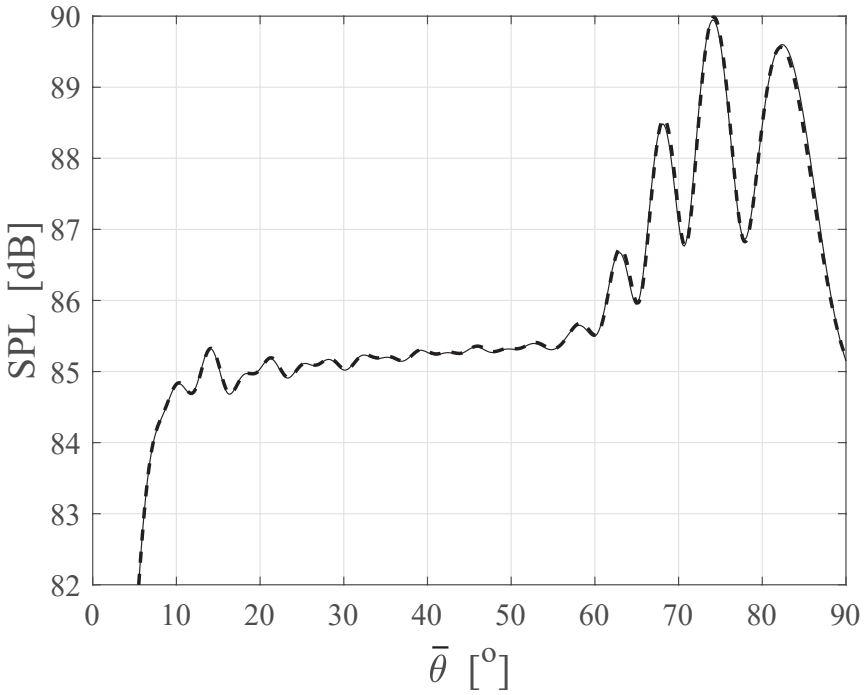

FIGURE 7.22: Polar directivity upstream for operating condition 3 and source W_{20}. The thick boundary layer is used for the calculations. Results using an equivalent linear profile [solid line] and an equivalent step-function profile [dashed line].

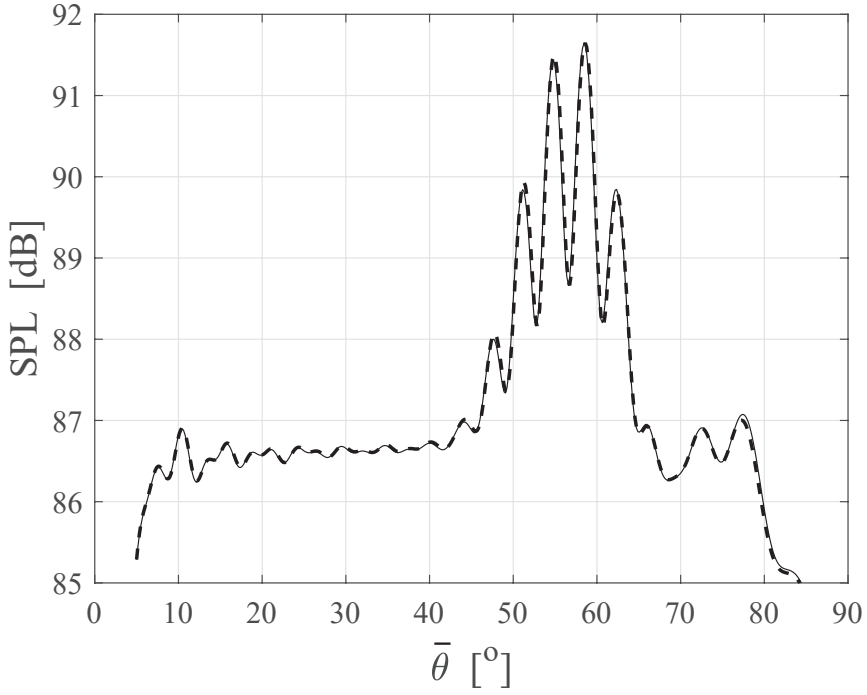

FIGURE 7.23: Polar directivity upstream for operating condition 6 and source W_{20}. The thick boundary layer is used for the calculations. Results using an equivalent linear profile [solid line] and an equivalent step-function profile [dashed line].

7.4 Source Orientation

This section aims to provide some insight into the source orientation. The results presented in this and the previous chapter mainly concerned the shielding. As such, the metrics were usually Δ_{bl} and S_+ which highlight the difference in level owing to the presence of the boundary layer. On the other hand, the difference Δ_{source} is a metric that highlights the differences between the sources, since it is the difference between the SPL of the rotor-locked source minus the equal energy source. By doing so, any boundary-layer effects are normalised since both sources are subject to the same boundary-layer effects. This allows certain purely azimuthal or orientation effects to come to light that would normally pass unnoticed. Δ_{source} plots have already been shown in the previous chapter (see Figs. (6.8) and (6.9)). Those plots only showed the difference at $\bar{\phi} = 0^{\text{o}}$. As has already been established in the last two chapters, it is always beneficial to examine the effects on the entirety of the fuselage surface to make sure whether there are any cumulative or azimuthal effects. This is the scope of this section, and thus the figures that follow show the difference Δ_{source} all over the fuselage surface.

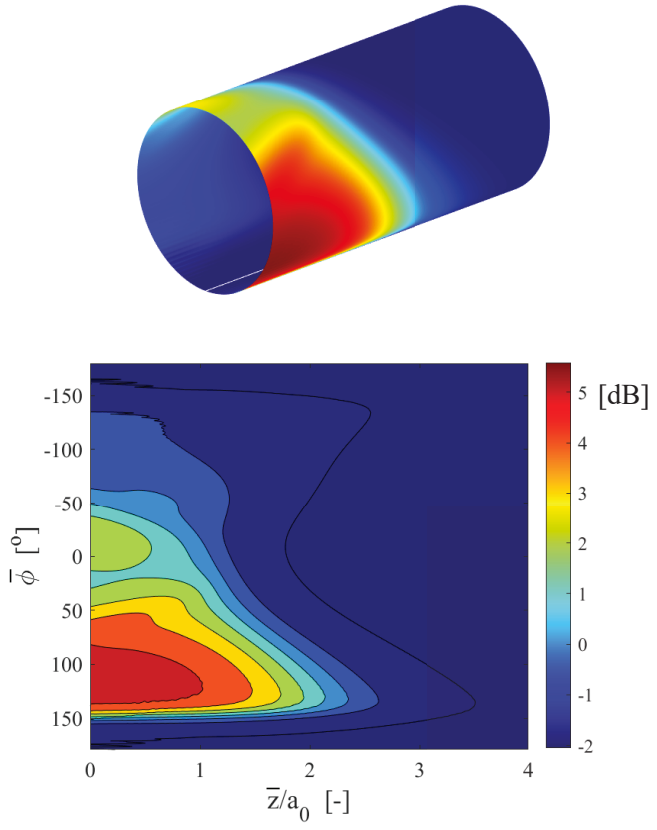

FIGURE 7.24: $\Delta^{20}_{\text{source}}$ on the fuselage surface for operating condition 3. Cylinder plot **[top]**, same plot unfurled **[bottom]**. Average boundary-layer thickness is used for the calculations.

Figures (7.24) and (7.25) show the difference $\Delta^{20}_{\text{source}}$ plotted all over the fuselage surface, not only on $\bar{\phi} = 0^{\text{o}}$. The difference between operating condition 3 and 6 is clearly visible with condition 6 exhibiting excess of power further upstream than condition 3 since the dominant

mode is more cut-on at that condition. Once again, the secondary lobe is visible behind the principal lobe in condition 6. A more interesting result in these plots is the fact that the maximum SPL is to the side of the cylinder, and not at $\bar{\phi} = 0^o$ directly adjacent to the source. Specifically the maximum $\Delta^{20}_{\text{source}}$ is in the region around $\bar{\phi} = 90^o$ to 125^o. This implies that the dominant rotor-locked mode affects the pressure levels on the cylinder in a lopsided fashion. This is a purely azimuthal or rather a source orientation effect, and it is attributed to the fact that the source is a simulation of a spinning mode. Sure enough, by repeating the results, but with the dominant rotor-locked mode equal to (-20,1) instead of (20,1), the plots are the same but flipped around the $\bar{\phi} = 0^o$ axis.

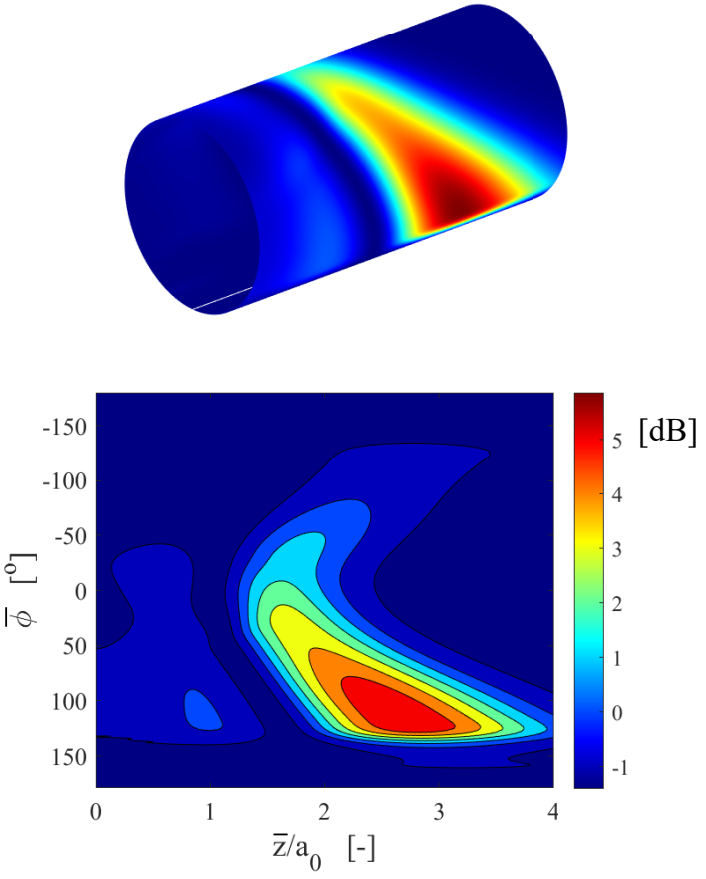

FIGURE 7.25: $\Delta^{20}_{\text{source}}$ on the fuselage surface for operating condition 6. Cylinder plot **[top]**, same plot unfurled **[bottom]**. Average boundary-layer thickness is used for the calculations.

This effect can be explained by revisiting the way the spinning modes propagate. As explained in McAlpine et al. (2015), a propagating spinning mode has an azimuthal and an axial component. That means that wavefronts propagate both in the azimuthal and the axial direction. Therefore, the sound wavefronts travel in a corkscrew-like manner as they exit the fan duct. They both propagate forwards along the positive direction of the z-axis and rotate around the z-axis at the same time. According to the convention used in the present work and in McAlpine et al. (2015), the spinning modes rotate counterclockwise. That means that the wavefronts tend to rotate towards the right side of the fuselage (positive $\bar{\phi}$) while on the left side of the fuselage (negative $\bar{\phi}$) the wavefronts "spin" away from the cylinder. This

asymmetry is demonstrated in Fig. (7.26). Note that in the figure, only the azimuthal direction of propagation is sketched. Consider an observer located on the right side of the fuselage, around $\bar{\phi} = 90^o$. This observer will see the wavefronts coming towards them. On the other hand, if an observer is located on the opposite side of the cylinder, left side, at around $\bar{\phi} = -90^o$, they will see wavefronts travelling away from them. This effect explains why the dominant mode's energy is not symmetric about $\bar{\phi} = 0^o$.

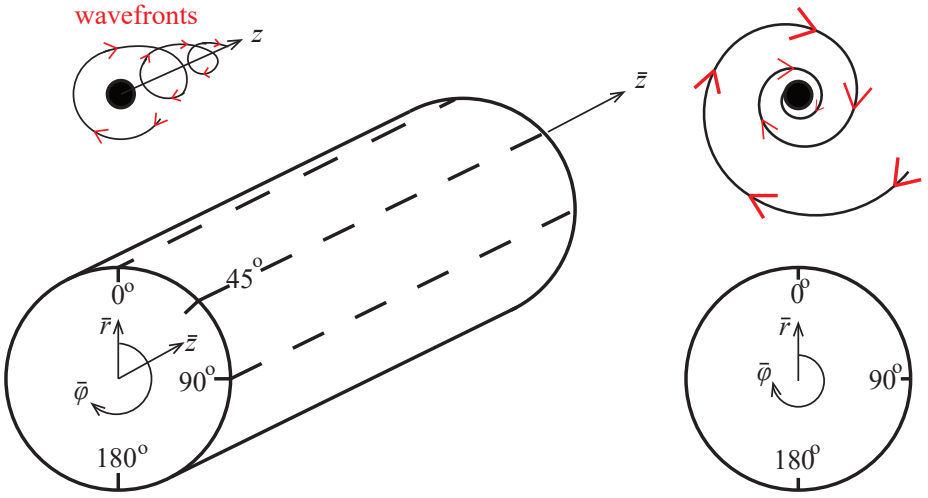

FIGURE 7.26: Schematic showing the orientation and general direction of the wavefronts. Side view [left] and front view [right].

It is important to note that this asymmetry is not only present in these difference Δ_{source} contour maps. By reexamining the contour maps in Figs. (7.11), (7.12), (7.16) and (7.17), one can now discern certain asymmetries in the SPL contour pattern. More specifically, on the right side of the cylinder (positive $\bar{\phi}$) the lobes and nulls are better defined than on the left side. The dominant mode there stands out more easily, namely its pattern is dominating the overall pattern in a more robust way there. That is a sign that on this location, the dominant mode is at the highest level compared to the rest of the cut-on modes. On the left side its level is slightly closer to the rest of the cut-on modes therefore the pattern tends to be smoother. This effect is even more pronounced in Fig. (7.12) where it is becoming clear that the right side of the lobe is more extended than the left indicating an excess of power. This effect adds nuance to the problem, and introduces new challenges in the fuselage lagging manufacturing process, since different areas will require different acoustic insulation, depending on the rotation direction of the fan.

Chapter 8

Conclusions and Future Work

8.1 Conclusions

The main goal of this thesis was the development of theoretical methods that can rapidly predict the fuselage acoustic installation effects of aero-engine fan tones. This goal was achieved by including the most representative theoretical model for a fan tone noise source and attempting to solve the problem of sound propagation through a shear layer analytically.

In chapter 3 analytic solutions were derived for the acoustic near-field and far-field as a result of a fan tone noise source being installed adjacent to the fuselage which has a boundary layer of constant thickness running down the length of it. The analytic solutions assume simpler boundary-layer velocity profiles, step-function and linear, and model the refraction caused by the velocity gradient using Fourier methods coupled with an asymptotic power series solution.

As shown in chapter 5, the theoretical model despite using simplified boundary-layer profiles, proved to be able to predict the same pressure field as that predicted by numerical methods for a representative 1/7th power-law profile. An appropriate method of matching the equivalent simpler profiles to the more complex ones is investigated. These analytic solutions provide alternatives to high-fidelity numerical methods since there is no need to solve numerically the Pridmore-Brown equation, and in the case of the step-function profile there is no need to solve the Pridmore-Brown equation altogether. The theoretical approaches were able to capture the amplitude and phase of the shielding quite accurately especially for thinner boundary-layers. Even for very thick boundary-layers, the step-function correctly captures the shielding trend and can be used as a quick prediction method.

The speed of these theoretical methods facilitates the execution of a multi-mode parametric study presented in chapter 6, which uses realistic flight parameters to model the shielding and refraction in various flight stages. The parametric study revealed trends that are very useful and should be taken into account during the fuselage lagging manufacturing process, but also during the evaluation of community noise in the far-field. The engine noise source directivity and modal output plays a vital role in the near- and far-field pressure pattern. Frequency and flight Mach number also play a major role in the shielding and refraction caused by the

boundary layer. However, both in the near- and far-field the boundary-layer thickness is the most influential factor as far as refraction is concerned.

The discussion in chapter 7 drew attention to a factor that can be used to predict trends in the shielding on the fuselage surface. The cut-off ratio, and consequently the mode propagation angle, plays a vital role in the amount of acoustic energy that reaches the fuselage. Both theoretical approaches agree well with each other for the range of parameters examined and since this range represents realistic situations, the linear profile's loss of accuracy is mediated.

The work in this thesis aims to provide a theoretical prediction method that can be used as a faster alternative to more traditional high-fidelity numerical methods. The analytical solution to the Pridmore-Brown equation eliminates the need to use Runge-Kutta routines which tend to have high computational cost especially for thicker boundary-layers. The theoretical approaches developed here not only eliminate this need for high-fidelity numerical methods, but also prove that it is not even necessary to solve the Pridmore-Brown equation to produce useful predictions. It is the view of the author that such theoretical tools should be used to quickly identify accurate trends in a multi-parameter problem. These theoretical tools provide quick preliminary estimates that are crucial in any analysis since they identify the areas where more accuracy, in the form of a high-fidelity numerical result, is needed. Thus, costly studies that are unnecessary are avoided.

The main original contribution to knowledge in this thesis is:

- The development of a theoretical method that can predict the installation effects of a realistic fan engine noise source that is mounted adjacent to a cylindrical fuselage which has a representative boundary-layer velocity profile running down its length based on an analytical formulation. The model can predict the acoustic pressure both in the near-field, more specifically the SPL on the surface of the fuselage which is used to determine the amount of acoustic lagging to be installed, and in the far-field, more specifically the sound directivity that will propagate to the ground which is essential in determining the noise the community experiences.

The objectives that have been accomplished in this thesis have already been mentioned in chapter 1. Here the major findings are listed:

- The optimal method for approximating a more complex profile using simpler profiles has been investigated.
  - Matching the physical properties of the profiles leads to the best results.
- The two theoretical approaches have been compared to each other in terms of their accuracy.
  - The linear profile gives accurate results for thinner boundary-layers, about 3 %-4 % of the fuselage radius.
  - For thicker boundary-layers, the step-function profile is more accurate while its accuracy does not deteriorate with increasing boundary-layer thickness.

- The refraction and shielding effect has been quantified in the near-field (fuselage surface):
  - Smaller wavelengths are more susceptible to refract sound away from the fuselage surface upstream of the source.
  - Increasing frequency or increasing Mach number will increase shielding with Mach number having a more drastic effect.
- The refraction effect has been quantified in the far-field and proven to cause phase shifts that should not be ignored, while the shape of the boundary-layer profile is not influential at all in the far-field.
- Multi-modal study reveals the significance of the cut-off ratio and the mode propagation angle.
  - Close to cut-off, the principal lobe is less shielded because it will be incident on the boundary layer at a more perpendicular angle.
  - Higher cut-off ratios cause the principal lobe to be refracted away in such an extent that the secondary lobe starts to become dominant.
- The power distribution of the modal output of the engine does not affect shielding in a practical way, however it is very influential on the pressure pattern on the fuselage surface and in the far-field.
- Cruising conditions are characterised by more shielding due to higher Mach numbers and cut-off ratios.
- The spinning nature of the fan tones leads to a slightly asymmetric SPL contour on the fuselage surface.

The derivation and validation of the linear profile theory is published in Rouvas and McAlpine (2021). The investigation on the optimal matching method between the simple and more complex profiles is published in Rouvas and McAlpine (2022b) and Rouvas and McAlpine (2022a). Furthermore, in Rouvas and McAlpine (2022a) part of the parametric study is also presented. Another paper is planned to present the findings of the multi-mode parametric study in full and interpret the results physically.

8.2 Future Work

The work presented in this thesis could be extended in the future. Some recommendations are presented by the author that might augment our knowledge on the subject.

Analytic solution for 1/7th power-law profile or quarter-sine. The asymptotic method used to solve the Pridmore-Brown equation for a linear boundary layer is in theory applicable to more complex profiles. The same solution applied to more complex profiles may lead to increased accuracy for a given boundary-layer thickness. The challenge that manifests here is the complexity of the solution. Implementing the same power series expansion for a more

complex profile may lead to integrals that cannot be solved analytically which would defeat the purpose of the work.

Inclusion of Critical Layer. Previous work on the significance of the critical layer in the Pridmore-Brown equation has revealed that the critical layer is not that important in the accuracy of the solution, at least in the parameter range of interest here. That is the main reason that it is not included in this thesis. However, the derivation of the solution including this critical layer has been conducted by the author but not yet coded and validated. Although the critical layer is unlikely to have a drastic effect on the near- or far-field SPL predictions, it is worth investigating to gain insight into the mathematical problem.

Haystacking. The phenomenon of haystacking or broadening of the fan tones due to the turbulence inside the boundary layer has been investigated numerically (see chapter 2). Of course, it is highly unlikely that an analytical model can be developed that will accurately predict the sound-turbulence interaction inside the boundary layer. However, once again asymptotic methods could be used to simplify the problem and provide solutions that are valid subject to restrictions.

Growing Boundary Layer. This thesis assumes a constant boundary-layer thickness, which is not realistic since the boundary layer grows axially. The problem of the growing boundary-layer is a particularly difficult one since it restricts the use of Fourier methods. Nevertheless, progress may be possible for a slowly growing boundary layer. For example, Rienstra's work on slowly varying ducts (Rienstra (1998), Rienstra (2003)) does not include a boundary layer but it does provide solutions for the mean flow and acoustic field that vary in the axial direction.

Appendix A

Incident Field Derivation

As outlined by McAlpine and Kingan (2012), the governing equation that describes the incident field due to the presence of a rotating monopole source q in uniform flow is the inhomogeneous convected wave equation,

$$\left(\nabla^2 - \frac{1}{c_0^2}\frac{\mathrm{D}^2}{\mathrm{D}t^2}\right)p' = -\rho_0\frac{\mathrm{D}q}{\mathrm{D}t}, \tag{A.1}$$

which written in full in cylindrical polar coordinates is,

$$\frac{\partial^2 p_i'}{\partial r^2} + \frac{1}{r}\frac{\partial p_i'}{\partial r} + \frac{1}{r^2}\frac{\partial^2 p_i'}{\partial \phi^2} + \frac{\partial^2 p_i'}{\partial z^2} - \frac{1}{c_0^2}\left(\frac{\partial}{\partial t} - U\frac{\partial}{\partial z}\right)^2 p_i' = -\rho_0\left(\frac{\partial}{\partial t} - U\frac{\partial}{\partial z}\right)q. \tag{A.2}$$

A single-frequency, rotating, monopole point source is considered with volume velocity

$$q(r,\phi,z,t) = Q_0 \mathrm{e}^{\mathrm{i}\omega_0 t}\frac{\delta(r-a)}{r}\left(\sum_{n=-\infty}^{\infty}\delta(\phi - \Omega t - 2\pi n)\right)\delta(z), \tag{A.3}$$

The three-dimensional delta function is used to describe the rotating monopole's radial and axial position (taken to be the duct's exit plane) and its periodicity around the source's centreline (or the duct's centreline). The monopole rotates around the centreline with angular velocity Ω. By taking the Fourier transform of eq. (A.2) the resulting equation can be solved using the method of variation of parameters. The full details of the solution are omitted for the sake of brevity. These details can be found in Ref. McAlpine and Kingan (2012). The Fourier transform involves Fourier transforms in z and t and the Fourier series in ϕ as follows:

$$\overline{p_{im}'}\,(r,k_z,\omega) = \int_{-\infty}^{\infty}\int_{-\pi}^{\pi}\int_{-\infty}^{\infty} p_i'(r,\phi,z,t)\mathrm{e}^{\mathrm{i}(k_z z + m\phi - \omega t)}\mathrm{d}z\mathrm{d}\phi\mathrm{d}t, \tag{A.4}$$

$$\Rightarrow p_i'(r,\phi,z,t) = \frac{1}{(2\pi)^3}\sum_{m=-\infty}^{\infty}\left(\int_{-\infty}^{\infty}\int_{-\infty}^{\infty}\overline{p_{im}'}\,(r,k_z,\omega)\mathrm{e}^{-\mathrm{i}(k_z z - \omega t)}\mathrm{d}k_z\mathrm{d}\omega\right)\mathrm{e}^{-\mathrm{i}m\phi}. \tag{A.5}$$

This transforms the derivatives as follows:

$$\frac{\partial}{\partial z} \to -\mathrm{i}k_z, \quad \frac{\partial}{\partial \phi} \to -\mathrm{i}m \quad \text{and} \quad \frac{\partial}{\partial t} \to \mathrm{i}\omega. \tag{A.6}$$

The Fourier transformed eq. (A.2) is

$$\frac{\mathrm{d}^2\overline{p'_{im}}}{\mathrm{d}r^2}+\frac{1}{r}\frac{\mathrm{d}\overline{p'_{im}}}{\mathrm{d}r}+\left\{\Gamma_z^2-\frac{m^2}{r^2}\right\}\overline{p'_{im}}=\mathcal{Q}_m, \tag{A.7}$$

where

$$\mathcal{Q}_m=-\mathrm{i}Q_0\rho_0c_0(k+k_zM_z)\frac{2\Omega(-1)^{m+1}\sin\pi(\frac{\omega-\omega_0}{\Omega})}{m\Omega-[\omega-\omega_0]}\frac{\delta(r-a)}{r}\sum_{n=-\infty}^{\infty}\delta(\omega-[\omega_0+n\Omega]) \tag{A.8}$$

is the Fourier transformed right hand side of the equation with the radial wavenumber

$$\Gamma_z^2=(k+k_zM_z)^2-k_z^2. \tag{A.9}$$

The method of variation of parameters requires the solution to the homogeneous version of eq. (A.7) which is Bessel's differential equation. Since a radiation condition as $r\to\infty$ will be applied, it is more convenient to select $\mathrm{J}_m(\Gamma_z r)$ and $\mathrm{H}_m^{(2)}(\Gamma_z r)$ as the linearly independent solutions of Bessel's equation. Then, using the method of variation of parameters, the solution to eq. (A.7) is

$$\begin{aligned}\overline{p'_{im}}=&\mathrm{J}_m(\Gamma_z r)\Big(A_m(k_z,\omega)-\mathrm{i}\frac{\pi}{2}\int_0^r\mathcal{Q}_m(s)\mathrm{H}_m^{(2)}(\Gamma_z s)\,s\mathrm{d}s\Big)+\\&\mathrm{H}_m^{(2)}(\Gamma_z r)\Big(B_m(k_z,\omega)+\mathrm{i}\frac{\pi}{2}\int_0^r\mathcal{Q}_m(s)\mathrm{J}_m(\Gamma_z s)\,s\mathrm{d}s\Big).\end{aligned} \tag{A.10}$$

Owing to the term $\frac{\delta(r-a)}{r}$ in $\mathcal{Q}_m$ (A.8), the solution is split into two domains, $r<a$ and $r>a$. The constants in eq. (A.10) can be found by applying the finiteness and radiation conditions. The Hankel function is singular as $r\to 0$, therefore it immediately follows from eq. (A.10) that $B_m=0$. Furthermore, in order to have only outward propagating waves as $r\to\infty$, it can be shown that

$$A_m=\frac{\pi}{2}Q_0\rho_0c_0(k+k_zM_z)\frac{2\Omega(-1)^{m+1}\sin\pi(\frac{\omega-\omega_0}{\Omega})}{m\Omega-[\omega-\omega_0]}\sum_{n=-\infty}^{\infty}\delta(\omega-[\omega_0+n\Omega])\mathrm{H}_m^{(2)}(\Gamma a). \tag{A.11}$$

With A_m and B_m known, taking the inverse Fourier time-transform gives

$$\overline{p'_{im}}(r,k_z,t)=\frac{\pi}{2}Q_0\rho_0c_0(k_{0m}+k_zM_z)\mathrm{H}_m^{(2)}(\Gamma_{zm}r_>)\mathrm{J}_m(\Gamma_{zm}r_<)\mathrm{e}^{\mathrm{i}(\omega_0+m\Omega)t}, \tag{A.12}$$

where

$$r_>=\begin{cases}r, & r>a\\ a, & r<a\end{cases}; \tag{A.13}$$

$$r_<=\begin{cases}a, & r>a\\ r, & r<a\end{cases}, \tag{A.14}$$

and $k_{0m}=\frac{\omega_0+m\Omega}{c_0}$ and $\Gamma_{zm}^2=(k_{0m}+k_zM_z)^2-k_z^2$.

Appendix B

Disc Source Derivation

This section briefly outlines the method used by McAlpine et al. (2015). For more details see Ref. McAlpine et al. (2015). The final incident field p_i' is the resulting field after integrating a distribution of monopoles over the cross section of the duct's termination. As outlined in Ref. McAlpine et al. (2015) and shown in Fig. (B.1), consider an annular ring source with N monopoles distributed around a circle of radius η. Monopole s is located at $(r, \phi, z) = (\eta, s\Delta\psi, 0)$ where $\Delta\psi = 2\pi/N$ and $s = 0, 1, 2, \ldots, N-1$.

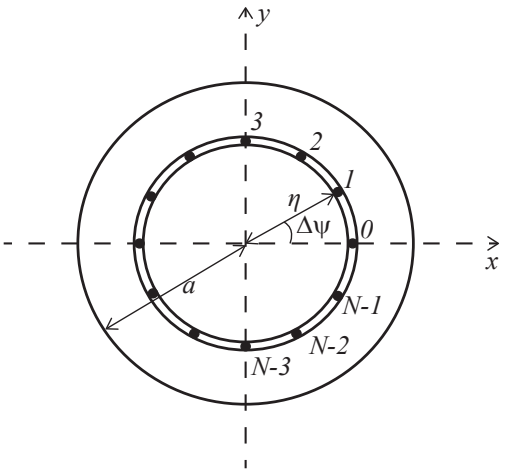

FIGURE B.1: Sketch of ring source. Taken from McAlpine et al. (2015).

Equation (A.12) is the Fourier-transformed pressure field of a rotating monopole source derived by McAlpine and Kingan (2012). Therefore, by setting $\Omega = 0$ in eq. (A.12), and performing an inverse Fourier z-transform, the field owing to stationary monopole source $s = 0$ is recovered

$$p_i'^{(0)}(r, \phi, z, t) = \frac{1}{(2\pi)^2} \sum_{m=-\infty}^{\infty} \left(\int_{-\infty}^{\infty} \overline{p_{im}'^{(0)}}(r, k_z, t) \mathrm{e}^{-\mathrm{i}k_z z} \mathrm{d}k_z \right) \mathrm{e}^{-\mathrm{i}m\phi}, \tag{B.1}$$

where from eq. (A.12)

$$\overline{p'^{(0)}_{im}}(r,k_z,t) = \frac{\pi}{2}Q^{(0)}\rho_0 c_0(k_0+k_zM_z)\mathrm{H}^{(2)}_m(\Gamma_z r_>)\mathrm{J}_m(\Gamma_z r_<)\mathrm{e}^{\mathrm{i}\omega_0 t}, \tag{B.2}$$

and the variables are now defined as

$$r_> = \begin{cases} r, & r > \eta \\ \eta, & r < \eta \end{cases}; \tag{B.3}$$

$$r_< = \begin{cases} \eta, & r > \eta \\ r, & r < \eta \end{cases}. \tag{B.4}$$

It is important to note the radial wavenumber's behaviour. With $\Omega = 0$, the wavenumber is defined as

$$\Gamma_z^2 = (k_0 + k_zM_z)^2 - k_z^2. \tag{B.5}$$

In order to ensure only outward propagating waves as $r \to \infty$, appropriate handling of Γ_z is required. In the range

$$\frac{-k_0}{1+M_z} < k_z < \frac{k_0}{1-M_z} \tag{B.6}$$

Γ_z is real and positive, whereas outside this range it will be imaginary $\Gamma_0 = -\mathrm{i}\gamma_z$ where $\gamma_z^2 = k_z^2 - (k_0 + k_zM_z)^2 > 0$.

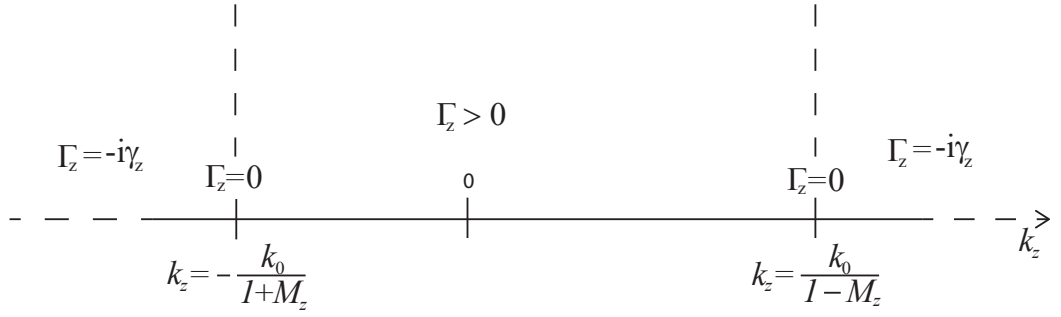

FIGURE B.2: Values of Γ_z along the k_z-axis. Taken from McAlpine et al. (2015).

As outlined in McAlpine et al. (2015), the new angular coordinate $\widetilde{\phi}$ is introduced such that monopole s is located at $\widetilde{\phi} = 0$. This means that

$$\widetilde{\phi} = \phi - s\Delta\psi. \tag{B.7}$$

For every point source s on the ring, eqs. (B.1) and (B.2) apply, i.e.

$$p'^{(s)}_i(r,\phi,z,t) = \frac{1}{(2\pi)^2}\sum_{m=-\infty}^{\infty}\left(\int_{-\infty}^{\infty}\overline{p'^{(s)}_{im}}(r,k_z,t)\mathrm{e}^{-\mathrm{i}k_z z}\mathrm{d}k_z\right)\mathrm{e}^{-\mathrm{i}m\widetilde{\phi}}, \tag{B.8}$$

or

$$p_i'^{(s)}(r,\phi,z,t) = \frac{Q^{(s)}\rho_0 c_0}{8\pi}\sum_{m=-\infty}^{\infty}\left(\int_{-\infty}^{\infty}(k_0+k_z M_z)\mathrm{H}_m^{(2)}\left(\Gamma_z r_>\right)\mathrm{J}_m\left(\Gamma_z r_<\right)\mathrm{e}^{-\mathrm{i}k_z z}\mathrm{d}k_z\right)\mathrm{e}^{-\mathrm{i}m(\phi-s\Delta\psi)}\mathrm{e}^{\mathrm{i}\omega_0 t}. \tag{B.9}$$

In McAlpine et al. (2015) each point source's strength $Q^{(s)}$ is calculated by using the axial particle velocity of the spinning mode (l,q) at position $(\eta, s\Delta\psi, 0)$,

$$Q^{(s)} = \frac{\xi_{lq}P_{lq}}{\rho_0 c_0}\mathrm{J}_l\left(\kappa_{lq}\eta\right)\mathrm{e}^{-\mathrm{i}ls\Delta\psi}\delta A, \tag{B.10}$$

where the elementary surface of the point source $\delta A = \eta\delta\eta\delta\psi$. The total incident field is

$$p_i'(r,\phi,z,t) = \sum_{s=0}^{N-1} p_i'^{(s)}(r,\phi,z,t), \tag{B.11}$$

which, by combining eqs. (B.1) and (B.10), and using the standard formula for a geometric progression, becomes

$$\begin{aligned} p_i'(r,\phi,z,t) =& N\frac{\xi_{lq}P_{lq}}{8\pi}\sum_{n=-\infty}^{\infty}\left(\int_{-\infty}^{\infty}(k_0+k_z M_z)\mathrm{H}_{l-nN}^{(2)}\left(\Gamma_z r_>\right)\mathrm{J}_{l-nN}\left(\Gamma_z r_<\right)\mathrm{J}_l\left(\kappa_{lq}\eta\right)\mathrm{e}^{-\mathrm{i}k_z z}\mathrm{d}k_z\right) \\ &\times \mathrm{e}^{\mathrm{i}nN\phi}\mathrm{e}^{-\mathrm{i}l\phi}\mathrm{e}^{\mathrm{i}\omega_0 t}\eta\delta\eta\delta\psi. \end{aligned} \tag{B.12}$$

The full details of the derivation of eq. (B.12) are in Ref. McAlpine et al. (2015).

The distributed source is formed by taking the limit as the number of sources in the ring $N \to \infty$. This also means that $N\delta\psi \to 2\pi$, and only the $n = 0$ term is required. By integrating from $\eta = 0$ to a, the pressure for field points outside the duct $r > a$ is recovered:

$$p_i'(r,\phi,z,t) = \frac{\xi_{lq}P_{lq}}{4}\int_{-\infty}^{\infty}(k_0+k_z M_z)\Psi_{lq}\mathrm{H}_l^{(2)}\left(\Gamma_z r\right)\mathrm{e}^{-\mathrm{i}k_z z}\mathrm{d}k_z\mathrm{e}^{-\mathrm{i}l\phi}\mathrm{e}^{\mathrm{i}\omega_0 t}, \tag{B.13}$$

where the function

$$\Psi_{lq} = \int_{\eta=0}^{a}\mathrm{J}_l\left(\Gamma_z\eta\right)\mathrm{J}_l\left(\kappa_{lq}\eta\right)\eta\mathrm{d}\eta, \tag{B.14}$$

can be evaluated exactly. For non-plane-wave excitation

$$\Psi_{lq} = \frac{\Gamma_z a}{\kappa_{lq}^2-\Gamma_z^2}\mathrm{J}_l(\kappa_{lq}a)\mathrm{J}_l'(\Gamma_z a), \quad \Gamma_z \neq \kappa_{lq}, \tag{B.15}$$

$$\Psi_{lq} = \frac{1}{2}\left(a^2 - \frac{l^2}{\kappa_{lq}^2}\right)\mathrm{J}_l^2(\kappa_{lq}a), \quad \Gamma_z = \kappa_{lq}. \tag{B.16}$$

Appendix C

Far-Field Validation

In order for the validity of the analytic solution (eq.(3.67)) to be verified, it must be compared to another known analytic solution. Currently there are no other analytic solutions that describe the far-field induced by a fan-disc source scattering by an adjacent cylinder. In order for the validity of the solution to be tested, the disc source is reduced to a single monopole source located at the centre of the former disc source. By doing so, an expression for a monopole source scattering by an adjacent cylinder is obtained. That expression can now be compared to the known benchmark stationary monopole solution by Bowman et al. (1969). This reference solution has no mean flow, so it is also required to set $M_z = 0$.

The disc source is reduced to a stationary monopole by setting
$l \to 0$, $q \to 1$, $M_z \to 0$, $a \to 0$, $\beta \to \phi_0$, $b \to r_0$. Consequently
$\sigma \to 1$, $S(\bar{\theta}) \to 1$, $\Delta_z \to k_0 \sin\bar{\theta}$, $\xi_{01} \to 1$. The new geometric parameters r_0 and ϕ_0 are shown in Fig.(C.1).

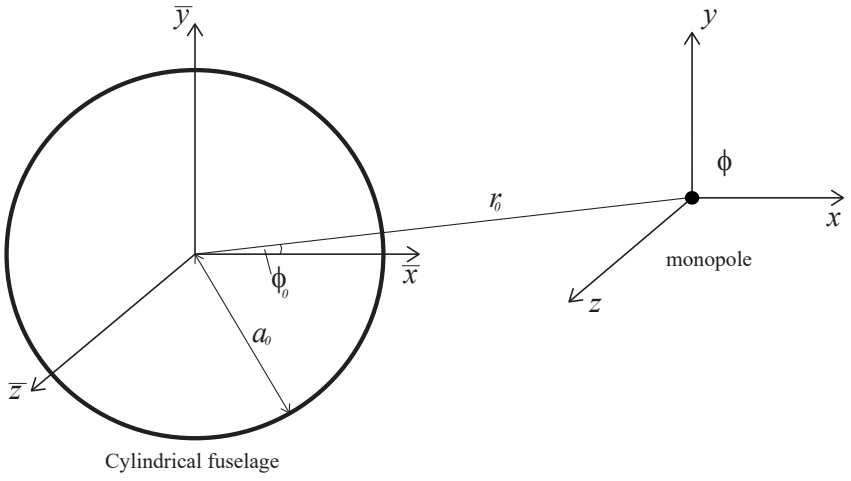

FIGURE C.1: Reduction of disc source to a monopole.

Also it is shown that $\Psi_{01} = \frac{1}{2}a^2$ and $\frac{P_{01}}{\rho_0 c_0}(\pi a^2) = Q_0$ or $P_{01} = \frac{Q_0 \rho_0 c_0}{\pi a^2}$. These relations are proven in McAlpine et al. (2015). So eq.(3.67) becomes

$$p_t'(\bar{R},\bar{\theta},\bar{\phi},t) = \frac{\mathrm{i}\tilde{\varsigma}_{01}P_{01}k_0}{2\bar{R}}\Psi_{01}\sum_{n=-\infty}^{\infty}\mathrm{e}^{\mathrm{i}n\phi_0}\,\mathrm{e}^{\frac{1}{2}n\pi\mathrm{i}}\,\mathrm{e}^{\mathrm{i}\omega_0 t}\,\mathrm{e}^{-\mathrm{i}k_0\bar{R}}\,\mathrm{e}^{-\mathrm{i}n\bar{\phi}}\times \left[\frac{\mathrm{J}_n(k_0\sin\bar{\theta}r_0)\mathrm{H}_n^{(2)\prime}(k_0\sin\bar{\theta}a_0)-\mathrm{H}_n^{(2)}(k_0\sin\bar{\theta}r_0)\,\mathrm{J}_n'(k_0\sin\bar{\theta}a_0)}{\mathrm{H}_n^{(2)\prime}(k_0\sin\bar{\theta}a_0)}\right], \tag{C.1}$$

or

$$p_t'(\bar{R},\bar{\theta},\bar{\phi},t) = \frac{\mathrm{i}Q_0\rho_0 c_0 k_0}{4\pi\bar{R}}\,\mathrm{e}^{-\mathrm{i}k_0\bar{R}}\,\mathrm{e}^{\mathrm{i}\omega_0 t}\sum_{n=-\infty}^{\infty}\mathrm{e}^{\frac{1}{2}n\pi\mathrm{i}}\,\mathrm{e}^{-\mathrm{i}n(\bar{\phi}-\phi_0)}\times \left[\mathrm{J}_n(k_0 r_0\sin\bar{\theta})-\frac{\mathrm{J}_n'(k_0 a_0\sin\bar{\theta})}{\mathrm{H}_n^{(2)\prime}(k_0 a_0\sin\bar{\theta})}\mathrm{H}_n^{(2)}(k_0 r_0\sin\bar{\theta})\right]. \tag{C.2}$$

By splitting the summation into two parts and replacing n with $-n$ in the first part, the following is obtained

$$p_t'(\bar{R},\bar{\theta},\bar{\phi},t) = \frac{\mathrm{i}Q_0\rho_0 c_0 k_0}{4\pi\bar{R}}\,\mathrm{e}^{-\mathrm{i}k_0\bar{R}}\,\mathrm{e}^{\mathrm{i}\omega_0 t}\Bigg(\sum_{n=0}^{\infty}\mathrm{e}^{\mathrm{i}n(\bar{\phi}-\phi_0)}\,\mathrm{e}^{-\frac{1}{2}n\pi\mathrm{i}}\times \left[\frac{(-1)^n\mathrm{J}_n(k_0 r_0\sin\bar{\theta})\,(-1)^n\mathrm{H}_n^{(2)\prime}(k_0 a_0\sin\bar{\theta})\;-\;(-1)^n\mathrm{H}_n^{(2)}(k_0 r_0\sin\bar{\theta})\,(-1)^n\mathrm{J}_n'(k_0 a_0\sin\bar{\theta})}{(-1)^n\mathrm{H}_n^{(2)\prime}(k_0 a_0\sin\bar{\theta})}\right]+ \sum_{n=1}^{\infty}\mathrm{e}^{-\mathrm{i}n(\bar{\phi}-\phi_0)}\,\mathrm{e}^{\frac{1}{2}n\pi\mathrm{i}}\left[\frac{\mathrm{J}_n(k_0 r_0\sin\bar{\theta})\,\mathrm{H}_n^{(2)\prime}(k_0 a_0\sin\bar{\theta})\;-\;\mathrm{H}_n^{(2)}(k_0 r_0\sin\bar{\theta})\,\mathrm{J}_n'(k_0 a_0\sin\bar{\theta})}{\mathrm{H}_n^{(2)\prime}(k_0 a_0\sin\bar{\theta})}\right]\Bigg). \tag{C.3}$$

Taking into consideration that $\mathrm{e}^{-\frac{1}{2}n\pi\mathrm{i}} = (-\mathrm{i})^n$ and $\mathrm{e}^{\frac{1}{2}n\pi\mathrm{i}} = \mathrm{i}^n$

$$p_t'(\bar{R},\bar{\theta},\bar{\phi},t) = \frac{\mathrm{i}Q_0\rho_0 c_0 k_0}{4\pi\bar{R}}\,\mathrm{e}^{-\mathrm{i}k_0\bar{R}}\,\mathrm{e}^{\mathrm{i}\omega_0 t}\Bigg(\sum_{n=0}^{\infty}(-\mathrm{i})^n\mathrm{e}^{\mathrm{i}n(\bar{\phi}-\phi_0)}(-1)^n\times \left[\frac{\mathrm{J}_n(k_0 r_0\sin\bar{\theta})\,\mathrm{H}_n^{(2)\prime}(k_0 a_0\sin\bar{\theta})\;-\;\mathrm{H}_n^{(2)}(k_0 r_0\sin\bar{\theta})\,\mathrm{J}_n'(k_0 a_0\sin\bar{\theta})}{\mathrm{H}_n^{(2)\prime}(k_0 a_0\sin\bar{\theta})}\right]+ \sum_{n=1}^{\infty}\mathrm{i}^n\,\mathrm{e}^{-\mathrm{i}n(\bar{\phi}-\phi_0)}\times \left[\frac{\mathrm{J}_n(k_0 r_0\sin\bar{\theta})\,\mathrm{H}_n^{(2)\prime}(k_0 a_0\sin\bar{\theta})\;-\;\mathrm{H}_n^{(2)}(k_0 r_0\sin\bar{\theta})\,\mathrm{J}_n'(k_0 a_0\sin\bar{\theta})}{\mathrm{H}_n^{(2)\prime}(k_0 a_0\sin\bar{\theta})}\right]\Bigg). \tag{C.4}$$

The following relations are used

$$\cos n(\bar{\phi}-\phi_0) = \frac{\mathrm{e}^{\mathrm{i}n(\bar{\phi}-\phi_0)}+\mathrm{e}^{-\mathrm{i}n(\bar{\phi}-\phi_0)}}{2} \Rightarrow \mathrm{e}^{\mathrm{i}n(\bar{\phi}-\phi_0)} = 2\cos n(\bar{\phi}-\phi_0)-\mathrm{e}^{-\mathrm{i}n(\bar{\phi}-\phi_0)}, \tag{C.5}$$

$$(-\mathrm{i})^n(-1)^n = \mathrm{i}^n, \tag{C.6}$$

to rewrite eq.(C.4)

$$
\begin{aligned}
p_t'\left(\bar{R},\bar{\theta},\bar{\phi},t\right) \;=\; & \frac{\mathrm{i}Q_0\rho_0c_0k_0}{4\pi\bar{R}}\,\mathrm{e}^{-\mathrm{i}k_0\bar{R}}\,\mathrm{e}^{\mathrm{i}\omega_0 t}\Bigg(\sum_{n=0}^{\infty}\left(-\mathrm{i}\right)^n\left(-1\right)^n 2\cos n(\bar{\phi}-\phi_0)\times \\
& \left[\frac{\mathrm{J}_n\left(k_0r_0\sin\bar{\theta}\right)\mathrm{H}_n^{(2)\prime}\left(k_0a_0\sin\bar{\theta}\right)\;-\;\mathrm{H}_n^{(2)}\left(k_0r_0\sin\bar{\theta}\right)\mathrm{J}_n'\left(k_0a_0\sin\bar{\theta}\right)}{\mathrm{H}_n^{(2)\prime}\left(k_0a_0\sin\bar{\theta}\right)}\right]- \\
& \sum_{n=0}^{\infty}\left(-\mathrm{i}\right)^n\left(-1\right)^n\mathrm{e}^{-\mathrm{i}n(\bar{\phi}-\phi_0)}\times \\
& \left[\frac{\mathrm{J}_n\left(k_0r_0\sin\bar{\theta}\right)\mathrm{H}_n^{(2)\prime}\left(k_0a_0\sin\bar{\theta}\right)\;-\;\mathrm{H}_n^{(2)}\left(k_0r_0\sin\bar{\theta}\right)\mathrm{J}_n'\left(k_0a_0\sin\bar{\theta}\right)}{\mathrm{H}_n^{(2)\prime}\left(k_0a_0\sin\bar{\theta}\right)}\right]+ \\
& \sum_{n=1}^{\infty}\left(-\mathrm{i}\right)^n\left(-1\right)^n\mathrm{e}^{-\mathrm{i}n(\bar{\phi}-\phi_0)}\times \\
& \left[\frac{\mathrm{J}_n\left(k_0r_0\sin\bar{\theta}\right)\mathrm{H}_n^{(2)\prime}\left(k_0a_0\sin\bar{\theta}\right)\;-\;\mathrm{H}_n^{(2)}\left(k_0r_0\sin\bar{\theta}\right)\mathrm{J}_n'\left(k_0a_0\sin\bar{\theta}\right)}{\mathrm{H}_n^{(2)\prime}\left(k_0a_0\sin\bar{\theta}\right)}\right]\Bigg),
\end{aligned}
\tag{C.7}
$$

or, since only the zeroth term will remain from the subtraction

$$
\begin{aligned}
p_t'\left(\bar{R},\bar{\theta},\bar{\phi},t\right) \;=\; & \frac{\mathrm{i}Q_0\rho_0c_0k_0}{4\pi\bar{R}}\,\mathrm{e}^{-\mathrm{i}k_0\bar{R}}\,\mathrm{e}^{\mathrm{i}\omega_0 t}\Bigg(\sum_{n=0}^{\infty}\left(-\mathrm{i}\right)^n\left(-1\right)^n 2\cos n(\bar{\phi}-\phi_0)\times \\
& \left[\frac{\mathrm{J}_n\left(k_0r_0\sin\bar{\theta}\right)\mathrm{H}_n^{(2)\prime}\left(k_0a_0\sin\bar{\theta}\right)\;-\;\mathrm{H}_n^{(2)}\left(k_0r_0\sin\bar{\theta}\right)\mathrm{J}_n'\left(k_0a_0\sin\bar{\theta}\right)}{\mathrm{H}_n^{(2)\prime}\left(k_0a_0\sin\bar{\theta}\right)}\right]- \\
& \left(-\mathrm{i}\right)^0\left(-1\right)^0\mathrm{e}^0\times \\
& \left[\frac{\mathrm{J}_0\left(k_0r_0\sin\bar{\theta}\right)\mathrm{H}_0^{(2)\prime}\left(k_0a_0\sin\bar{\theta}\right)\;-\;\mathrm{H}_0^{(2)}\left(k_0r_0\sin\bar{\theta}\right)\mathrm{J}_0'\left(k_0a_0\sin\bar{\theta}\right)}{\mathrm{H}_0^{(2)\prime}\left(k_0a_0\sin\bar{\theta}\right)}\right]\Bigg).
\end{aligned}
\tag{C.8}
$$

By taking out the zeroth term of the remaining summation and since $\cos 0 = \mathrm{e}^0 = 1$,

$$
\begin{aligned}
p_t'\left(\bar{R},\bar{\theta},\bar{\phi},t\right) \;=\; & \frac{\mathrm{i}Q_0\rho_0c_0k_0}{4\pi\bar{R}}\,\mathrm{e}^{-\mathrm{i}k_0\bar{R}}\,\mathrm{e}^{\mathrm{i}\omega_0 t}\Bigg(\sum_{n=1}^{\infty}\left(-\mathrm{i}\right)^n\left(-1\right)^n 2\cos n(\bar{\phi}-\phi_0)\times \\
& \left[\frac{\mathrm{J}_n\left(k_0r_0\sin\bar{\theta}\right)\mathrm{H}_n^{(2)\prime}\left(k_0a_0\sin\bar{\theta}\right)\;-\;\mathrm{H}_n^{(2)}\left(k_0r_0\sin\bar{\theta}\right)\mathrm{J}_n'\left(k_0a_0\sin\bar{\theta}\right)}{\mathrm{H}_n^{(2)\prime}\left(k_0a_0\sin\bar{\theta}\right)}\right]+ \\
& \left(-\mathrm{i}\right)^0\left(-1\right)^0\times \\
& \left[\frac{\mathrm{J}_0\left(k_0r_0\sin\bar{\theta}\right)\mathrm{H}_0^{(2)\prime}\left(k_0a_0\sin\bar{\theta}\right)\;-\;\mathrm{H}_0^{(2)}\left(k_0r_0\sin\bar{\theta}\right)\mathrm{J}_0'\left(k_0a_0\sin\bar{\theta}\right)}{\mathrm{H}_0^{(2)\prime}\left(k_0a_0\sin\bar{\theta}\right)}\right]\Bigg),
\end{aligned}
\tag{C.9}
$$

which can be rewritten

$$
\begin{aligned}
p_t'\left(\bar{R},\bar{\theta},\bar{\phi},t\right) \;=\; & \frac{\mathrm{i}Q_0\rho_0c_0k_0}{4\pi\bar{R}}\,\mathrm{e}^{-\mathrm{i}k_0\bar{R}}\,\mathrm{e}^{\mathrm{i}\omega_0 t}\Bigg(\sum_{n=1}^{\infty}\left(-\mathrm{i}\right)^n\left(-1\right)^n 2\cos n(\bar{\phi}-\phi_0)\times \\
& \left[\frac{\mathrm{J}_n\left(k_0r_0\sin\bar{\theta}\right)\mathrm{H}_n^{(2)\prime}\left(k_0a_0\sin\bar{\theta}\right)\;-\;\mathrm{H}_n^{(2)}\left(k_0r_0\sin\bar{\theta}\right)\mathrm{J}_n'\left(k_0a_0\sin\bar{\theta}\right)}{\mathrm{H}_n^{(2)\prime}\left(k_0a_0\sin\bar{\theta}\right)}\right]+ \\
& \left(-\mathrm{i}\right)^0\left(-1\right)^0\cos(0(\bar{\phi}-\phi_0))\times \\
& \left[\frac{\mathrm{J}_0\left(k_0r_0\sin\bar{\theta}\right)\mathrm{H}_0^{(2)\prime}\left(k_0a_0\sin\bar{\theta}\right)\;-\;\mathrm{H}_0^{(2)}\left(k_0r_0\sin\bar{\theta}\right)\mathrm{J}_0'\left(k_0a_0\sin\bar{\theta}\right)}{\mathrm{H}_0^{(2)\prime}\left(k_0a_0\sin\bar{\theta}\right)}\right]\Bigg),
\end{aligned}
\tag{C.10}
$$

since $\cos 0 = 1$. Notice that the last term is actually the zeroth term of the summation but with 1 instead of 2 in front of the cosine. Thus, by introducing the Neumann's symbol $\epsilon_n = 2$ for $n = 1, 2, 3, ...$ and $\epsilon_0 = 1$, the following is obtained

$$\begin{aligned} p'_t\left(\bar{R}, \bar{\theta}, \bar{\phi}, t\right) \; = \; & \frac{\mathrm{i}Q_0\rho_0 c_0 k_0}{4\pi\bar{R}}\, \mathrm{e}^{-\mathrm{i}k_0\bar{R}}\, \mathrm{e}^{\mathrm{i}\omega_0 t} \sum_{n=0}^{\infty} \epsilon_n\, (-\mathrm{i})^n\, (-1)^n\, \cos n(\bar{\phi} - \phi_0) \times \\ & \left[\mathrm{J}_n\left(k_0 r_0 \sin\bar{\theta}\right) - \frac{\mathrm{J}'_n\left(k_0 a_0 \sin\bar{\theta}\right)}{\mathrm{H}_n^{(2)\prime}\left(k_0 a_0 \sin\bar{\theta}\right)} \mathrm{H}_n^{(2)}\left(k_0 r_0 \sin\bar{\theta}\right) \right]. \end{aligned} \tag{C.11}$$

By manipulating algebraically even further

$$\begin{aligned} p'_t\left(\bar{R}, \bar{\theta}, \bar{\phi}, t\right) \; = \; & \frac{\mathrm{i}Q_0\rho_0 c_0 k_0}{4\pi\bar{R}}\, \mathrm{e}^{-\mathrm{i}k_0\bar{R}}\, \mathrm{e}^{\mathrm{i}\omega_0 t} \times \\ & \left[\sum_{n=0}^{\infty} \epsilon_n\, (-\mathrm{i})^n\, (-1)^n\, \cos n(\bar{\phi} - \phi_0)\, \mathrm{J}_n\left(k_0 r_0 \sin\bar{\theta}\right) - \right. \\ & \left. \sum_{n=0}^{\infty} \epsilon_n\, (-\mathrm{i})^n\, (-1)^n\, \cos n(\bar{\phi} - \phi_0)\, \frac{\mathrm{J}'_n\left(k_0 a_0 \sin\bar{\theta}\right)}{\mathrm{H}_n^{(2)\prime}\left(k_0 a_0 \sin\bar{\theta}\right)} \mathrm{H}_n^{(2)}\left(k_0 r_0 \sin\bar{\theta}\right) \right]. \end{aligned} \tag{C.12}$$

By breaking the zeroth term from the first summation and with $\epsilon_0 = 1, \cos 0 = 0, \epsilon_n = 2$ for $n = 1, 2, 3, ..., (-\mathrm{i})^n(-1)^n = \mathrm{i}^n$, eq.(C.12) becomes

$$\begin{aligned} p'_t\left(\bar{R}, \bar{\theta}, \bar{\phi}, t\right) \; = \; & \frac{\mathrm{i}Q_0\rho_0 c_0 k_0}{4\pi\bar{R}}\, \mathrm{e}^{-\mathrm{i}k_0\bar{R}}\, \mathrm{e}^{\mathrm{i}\omega_0 t} \left[\mathrm{J}_0\left(k_0 r_0 \sin\bar{\theta}\right) + \right. \\ & \sum_{n=1}^{\infty} 2\,\mathrm{i}^n\, \cos n(\bar{\phi} - \phi_0)\, \mathrm{J}_n\left(k_0 r_0 \sin\bar{\theta}\right) - \\ & \left. \sum_{n=0}^{\infty} \epsilon_n\, (-\mathrm{i})^n\, (-1)^n\, \cos n(\bar{\phi} - \phi_0)\, \frac{\mathrm{J}'_n\left(k_0 a_0 \sin\bar{\theta}\right)}{\mathrm{H}_n^{(2)\prime}\left(k_0 a_0 \sin\bar{\theta}\right)} \mathrm{H}_n^{(2)}\left(k_0 r_0 \sin\bar{\theta}\right) \right]. \end{aligned} \tag{C.13}$$

The relation WA 401(1) found in page 933 of Ref. Gradshteyn and Ryzhik (2007)

$$\exp(\mathrm{i}z\cos\phi) \; = \; \mathrm{J}_0\left(z\right) + 2\sum_{n=1}^{\infty} \mathrm{i}^n \cos n\phi\, \mathrm{J}_n\left(z\right) \tag{C.14}$$

is used to rewrite eq.(C.13)

$$\begin{aligned} p'_t\left(\bar{R}, \bar{\theta}, \bar{\phi}, t\right) \; = \; & \frac{\mathrm{i}Q_0\rho_0 c_0 k_0}{4\pi\bar{R}}\, \mathrm{e}^{-\mathrm{i}k_0\bar{R}}\, \mathrm{e}^{\mathrm{i}\omega_0 t} \left[\exp\{\mathrm{i}k_0 r_0 \sin\bar{\theta}\cos(\bar{\phi} - \phi_0)\} - \right. \\ & \left. \sum_{n=0}^{\infty} \epsilon_n\, (-\mathrm{i})^n\, (-1)^n\, \cos n(\bar{\phi} - \phi_0)\, \frac{\mathrm{J}'_n\left(k_0 a_0 \sin\bar{\theta}\right)}{\mathrm{H}_n^{(2)\prime}\left(k_0 a_0 \sin\bar{\theta}\right)} \mathrm{H}_n^{(2)}\left(k_0 r_0 \sin\bar{\theta}\right) \right]. \end{aligned} \tag{C.15}$$

The convention in Bowman et al. (1969) has reversed signs for the monopole source. The convention in this work is changed as well by setting $k_0 \to -k_0$ and $\omega_0 \to -\omega_0$. By doing so the current convention becomes the same as Bowman's (eq.(2.146) from Bowman et al. (1969)).

Eq.(C.15) becomes

$$p'_t(\bar{R},\bar{\theta},\bar{\phi},t) = -\frac{\mathrm{i}Q_0\rho_0 c_0 k_0}{4\pi\bar{R}}\,\mathrm{e}^{\mathrm{i}k_0\bar{R}}\,\mathrm{e}^{-\mathrm{i}\omega_0 t}\left[\exp\{-\mathrm{i}k_0 r_0\sin\bar{\theta}\cos(\bar{\phi}-\phi_0)\}-\right.$$
$$\left.\sum_{n=0}^{\infty}\epsilon_n\,(-\mathrm{i})^n\,(-1)^n\,\cos n(\bar{\phi}-\phi_0)\,\frac{\mathrm{J}'_n\,(-k_0a_0\sin\bar{\theta})}{\mathrm{H}_n^{(2)\prime}\,(-k_0a_0\sin\bar{\theta})}\mathrm{H}_n^{(2)}\,(-k_0r_0\sin\bar{\theta})\right]. \tag{C.16}$$

The negative arguments of the Bessel and Hankel functions can be converted by using the following relations found in Gradshteyn and Ryzhik (2007), page 927 , eqs. (1) and (9) and differentiate with respect to the positive argument

$$\begin{aligned}&\mathrm{J}_n(-x)=(-1)^n\,\mathrm{J}_n(x)\Rightarrow\frac{\mathrm{dJ}_n(-x)}{\mathrm{d}x}=(-1)^n\,\mathrm{J}'_n(x)\Rightarrow\\&-\mathrm{J}'_n(-x)=(-1)^n\,\mathrm{J}'_n(x)\Rightarrow\mathrm{J}'_n(-x)=-(-1)^n\,\mathrm{J}'_n(x),\end{aligned} \tag{C.17}$$

since prime denotes differentiation with respect to the function's argument. Same applies to the relation for the Hankel functions

$$\begin{aligned}&\mathrm{H}_n^{(2)}(-x)=-(-1)^n\,\mathrm{H}_n^{(1)}(x)\Rightarrow\frac{\mathrm{dH}_n^{(2)}(-x)}{\mathrm{d}x}=-(-1)^n\,\mathrm{H}_n^{(1)\prime}(x)\Rightarrow\\&-\mathrm{H}_n^{(2)\prime}(-x)=-(-1)^n\,\mathrm{H}_n^{(1)\prime}(x)\Rightarrow\mathrm{H}_n^{(2)\prime}(-x)=(-1)^n\,\mathrm{H}_n^{(1)\prime}(x).\end{aligned} \tag{C.18}$$

By applying eq.(C.17) and (C.18) into eq.(C.16) the following is obtained

$$p'_t(\bar{R},\bar{\theta},\bar{\phi},t) = -\frac{\mathrm{i}Q_0\rho_0 c_0 k_0}{4\pi\bar{R}}\,\mathrm{e}^{\mathrm{i}k_0\bar{R}}\,\mathrm{e}^{-\mathrm{i}\omega_0 t}\left[\exp\{-\mathrm{i}k_0 r_0\sin\bar{\theta}\cos(\bar{\phi}-\phi_0)\}-\right.$$
$$\sum_{n=0}^{\infty}\epsilon_n\,(-\mathrm{i})^n\,(-1)^n\,\cos n(\bar{\phi}-\phi_0)\,\frac{-(-1)^n\,\mathrm{J}'_n\,(k_0a_0\sin\bar{\theta})}{(-1)^n\,\mathrm{H}_n^{(1)\prime}\,(k_0a_0\sin\bar{\theta})}\times$$
$$\left.\left(-(-1)^n\,\mathrm{H}_n^{(1)}\,(k_0r_0\sin\bar{\theta})\right)\right]. \tag{C.19}$$

Finally, the following expression for a stationary monopole point source is obtained

$$p'_t(\bar{R},\bar{\theta},\bar{\phi},t) = -\frac{\mathrm{i}Q_0\rho_0 c_0 k_0}{4\pi\bar{R}}\,\mathrm{e}^{\mathrm{i}k_0\bar{R}}\,\mathrm{e}^{-\mathrm{i}\omega_0 t}\left[\exp\{-\mathrm{i}k_0 r_0\sin\bar{\theta}\cos(\bar{\phi}-\phi_0)\}-\right.$$
$$\left.\sum_{n=0}^{\infty}\epsilon_n\,(-\mathrm{i})^n\,\cos n(\bar{\phi}-\phi_0)\,\frac{\mathrm{J}'_n\,(k_0a_0\sin\bar{\theta})}{\mathrm{H}_n^{(1)\prime}\,(k_0a_0\sin\bar{\theta})}\mathrm{H}_n^{(1)}\,(k_0r_0\sin\bar{\theta})\right], \tag{C.20}$$

which is exactly the same as Bowman's expression (page 127, eq.(2.149) from Bowman et al. (1969)). Therefore we can conclude that the expression developed here is verified, since it is reduced successfully to a known benchmark solution.

Appendix D

Asymptotic Evaluation of the Integral using the Method of Stationary Phase for the Step-Function Boundary Layer Case

The integral in eq.(3.120) is in a suitable form to be solved using the method of stationary phase following the same procedure as in the case of uniform flow, which was presented in section 3.1.4.1. More specifically, the integral

$$I_n \;=\; \frac{1}{2\pi}\int_{-\infty}^{\infty} \overline{p'_{t_{nff}}}\,(\bar{r},k_z)\,\mathrm{e}^{-\mathrm{i}k_z\bar{z}}\,\mathrm{d}k_z. \tag{D.1}$$

is in the appropriate form to be evaluated by the method of stationary phase as presented in McAlpine and Kingan (2012). Define $I(x)$ such that

$$I(x) \;=\; \int_a^b f(t)\mathrm{e}^{\mathrm{i}x\phi(t)}\mathrm{d}t, \quad \text{as } x\to\infty. \tag{D.2}$$

Then, according to the method of stationery phase, if there is a single point $a \le c \le b$ such that $\phi'(c) = 0$, provided that $\phi''(c) \neq 0$, then

$$I(x) \;\sim\; f(c)\left(\frac{2\pi}{x|\phi''(c)|}\right)^{1/2}\; \mathrm{e}^{\mathrm{i}x\phi(c)\pm\mathrm{i}\pi/4}, \quad \text{as } x\to\infty. \tag{D.3}$$

As is usually the case for far-field analysis, spherical polar coordinates $(\bar{R},\bar{\theta},\bar{\phi})$ are utilized and the integral is solved in the limit as $\bar{R}\to\infty$. First substitute

$$\bar{r} \;=\; \bar{R}\sin\bar{\theta} \quad \text{and} \quad \bar{z} \;=\; \bar{R}\cos\bar{\theta}. \tag{D.4}$$

Then the dependence of the function $\overline{p'_{t\infty_n}}(\bar{r}, k_z)$ on $\bar{r}$ is via the Hankel function

$$\mathrm{H}_n^{(2)}(\Gamma_\infty \bar{r}) = \mathrm{H}_n^{(2)}(\Gamma_\infty \bar{R}\sin\bar{\theta}) \sim \sqrt{\frac{2}{\pi\Gamma_\infty \bar{R}\sin\bar{\theta}}}\, \mathrm{e}^{\frac{1}{2}n\pi\mathrm{i}}\, \mathrm{e}^{\frac{1}{4}\pi\mathrm{i}}\, \mathrm{e}^{-\mathrm{i}\Gamma_\infty \bar{R}\sin\bar{\theta}} \quad \text{as} \quad \bar{R}\to\infty. \tag{D.5}$$

Also, $\exp(-\mathrm{i}k_z\bar{z}) \to \exp(-\mathrm{i}k_z\bar{R}\cos\bar{\theta})$ so the integral in eq.(D.1) can be expressed in the form

$$I_n \sim \frac{1}{2\pi}\int_{-\infty}^{\infty} f_n(k_z, \bar{R}, \bar{\theta})\, \mathrm{e}^{-\mathrm{i}\bar{R}(\Gamma_\infty \sin\bar{\theta} + k_z\cos\bar{\theta})}\, \mathrm{d}k_z \quad \text{as} \quad \bar{R}\to\infty, \tag{D.6}$$

where

$$\begin{aligned} f_n(k_z, \bar{R}, \bar{\theta}) =& F_n(k_z, \omega_0)\Bigg[\mathrm{J}_{n-l}(\Gamma_\infty b) \\ &+ \Bigg[\frac{2\mathrm{i}\, Y_n(\Gamma_0)}{\pi(a_0+\delta_{SF})\,\mathrm{H}_n^{(2)}(\Gamma_\infty(a_0+\delta_{SF}))\left(k_0 + k_z M_\infty\right)^2 D_n(k_z,\omega_0)} \\ &- \mathrm{J}_n(\Gamma_\infty(a_0+\delta_{SF}))\Bigg]\frac{\mathrm{H}_{n-l}^{(2)}(\Gamma_\infty b)}{\mathrm{H}_n^{(2)}(\Gamma_\infty(a_0+\delta_{SF}))}\Bigg]\sqrt{\frac{2}{\pi\Gamma_\infty\bar{R}\sin\bar{\theta}}}\, \mathrm{e}^{\frac{1}{2}n\pi\mathrm{i}}\, \mathrm{e}^{\frac{1}{4}\pi\mathrm{i}}. \end{aligned} \tag{D.7}$$

Introduce the similarity variables following Chapman (2000)

$$(\bar{x}, \bar{y}, \bar{z}) = \left(\hat{R}\sin\hat{\theta}\cos\bar{\phi}, \hat{R}\sin\hat{\theta}\sin\bar{\phi}, \hat{R}\sigma_\infty\cos\hat{\theta}\right), \tag{D.8}$$

where

$$\sigma_\infty^2 = 1 - M_\infty^2, \tag{D.9}$$

$$\hat{R} = \frac{\bar{R}}{\sigma_\infty}(1 - M_\infty^2\sin^2\bar{\theta})^{1/2}, \tag{D.10}$$

$$\cos\hat{\theta} = \frac{\cos\bar{\theta}}{(1 - M_\infty^2\sin^2\bar{\theta})^{1/2}}, \tag{D.11}$$

$$\sin\hat{\theta} = \frac{\sigma_\infty\sin\bar{\theta}}{(1 - M_\infty^2\sin^2\bar{\theta})^{1/2}}, \tag{D.12}$$

And following Rienstra and Hirschberg (2004), introduce the variable τ

$$\tau = \sigma_\infty^2\frac{k_z}{k_0} - M_\infty, \tag{D.13}$$

which means that

$$\Gamma_\infty = \frac{k_0}{\sigma_\infty}(1-\tau^2)^{1/2}, \tag{D.14}$$

$$k_z = \frac{k_0}{\sigma_\infty^2}(\tau + M_\infty), \tag{D.15}$$

$$\mathrm{d}k_z = \frac{k_0}{\sigma_\infty^2}\mathrm{d}\tau. \tag{D.16}$$

Note that all those similarity variables are based on the free stream Mach number M_∞. However, in the case of the step-function boundary layer, unlike the case of the uniform flow, there is one more term that needs to be rewritten in terms of those free stream similarity variables. This term is Γ_0 which is the only one dependent on the Mach number inside the

boundary layer M_0. By introducing the following term for brevity purposes,

$$\sigma_0^2 \;=\; 1 - M_0^2, \tag{D.17}$$

Γ_0 can be rewritten in terms of the free stream similarity variables by using eq.(D.15),

$$\Gamma_0 = \frac{k_0}{\sigma_\infty}\sqrt{\sigma_\infty^2 + (\tau + M_\infty)\left[2M_0 - (\tau + M_\infty)\frac{\sigma_0^2}{\sigma_\infty^2}\right]}. \tag{D.18}$$

By introducing these similarity variables, the integral can be rewritten

$$I_n \;\sim\; \frac{1}{2\pi}\int_{-\infty}^{\infty} g_n\left(\tau, \hat{R}, \hat{\theta}\right) \mathrm{e}^{\mathrm{i}\hat{R}\hat{\phi}(\tau)}\,\mathrm{d}\tau \tag{D.19}$$

where

$$\begin{aligned} g_n\left(\tau, \hat{R}, \hat{\theta}\right) =& \frac{k_0}{\sigma_\infty^2} F_n\left(\tau, \omega_0\right)\Bigg[\mathrm{J}_{n-l}\left(\Gamma_\infty b\right) \\ &+ \Bigg[\frac{2\mathrm{i}\,Y_n\left(\Gamma_0\right)}{\pi(a_0+\delta_{SF})\,\mathrm{H}_n^{(2)}\left(\Gamma_\infty(a_0+\delta_{SF})\right)k_0^2\left(1+\frac{(\tau+M_\infty)M_\infty}{\sigma_\infty^2}\right)^2 D_n\left(\tau,\omega_0\right)} \\ &- \mathrm{J}_n\left(\Gamma_\infty(a_0+\delta_{SF})\right)\Bigg]\frac{\mathrm{H}_{n-l}^{(2)}\left(\Gamma_\infty b\right)}{\mathrm{H}_n^{(2)}\left(\Gamma_\infty(a_0+\delta_{SF})\right)}\Bigg]\sqrt{\frac{2}{\pi\frac{k_0}{\sigma_\infty}(1-\tau^2)^{1/2}\hat{R}\sin\hat{\theta}}}\,\mathrm{e}^{\frac{1}{2}n\pi\mathrm{i}}\,\mathrm{e}^{\frac{1}{4}\pi\mathrm{i}}, \end{aligned} \tag{D.20}$$

$$\hat{\phi}(\tau) = -\frac{k_0}{\sigma_\infty}(1-\tau^2)^{1/2}\sin\hat{\theta} - \frac{k_0}{\sigma_\infty}(\tau + M_\infty)\cos\hat{\theta}, \tag{D.21}$$

$$F_n\left(\tau, \omega_0\right) = \pi^2\xi_{lq}P_{lq}\,\mathrm{e}^{-\mathrm{i}(l-n)\beta}\,k_0\left(1+\frac{(\tau+M_\infty)M_\infty}{\sigma_\infty^2}\right)\Psi_{lq}(\Gamma_\infty), \tag{D.22}$$

and

$$\begin{aligned} D_n\left(\tau,\omega_0\right) =& \left[\mathrm{H}_n^{(2)\prime}\left(\Gamma_0(a_0+\delta_{SF})\right) - \mathrm{J}_n'\left(\Gamma_0(a_0+\delta_{SF})\right)\frac{\mathrm{H}_n^{(2)\prime}\left(\Gamma_0 a_0\right)}{\mathrm{J}_n'\left(\Gamma_0 a_0\right)}\right] \\ &\times \frac{\frac{k_0}{\sigma_\infty}\sqrt{\sigma_\infty^2 + (\tau+M_\infty)\left[2M_0 - (\tau+M_\infty)\frac{\sigma_0^2}{\sigma_\infty^2}\right]}}{\left(k_0 + \frac{k_0}{\sigma_\infty^2}(\tau+M_\infty)M_0\right)^2} \\ &- \left[\mathrm{H}_n^{(2)}\left(\Gamma_0(a_0+\delta_{SF})\right) - \mathrm{J}_n\left(\Gamma_0(a_0+\delta_{SF})\right)\frac{\mathrm{H}_n^{(2)\prime}\left(\Gamma_0 a_0\right)}{\mathrm{J}_n'\left(\Gamma_0 a_0\right)}\right] \\ &\times \frac{\frac{k_0}{\sigma_\infty}(1-\tau^2)^{1/2}}{\left(k_0 + \frac{k_0}{\sigma_\infty^2}(\tau+M_\infty)M_\infty\right)^2}\frac{\mathrm{H}_n^{(2)\prime}\left(\Gamma_\infty(a_0+\delta_{SF})\right)}{\mathrm{H}_n^{(2)}\left(\Gamma_\infty(a_0+\delta_{SF})\right)}, \end{aligned} \tag{D.23}$$

with Γ_∞ and Γ_0 substituted with the expressions from eqs. (E.14) and (E.18) respectively.

The limits of the integral can be replaced by $(-1, 1)$ since the integrand will be exponentially small in the region $|\tau| > 1$ as $\bar{R} \to \infty$. This happens because when $|\tau| > 1$, Γ_∞ becomes imaginary and so the dependence on $\bar{r}$ is now through a modified Hankel function. This is

demonstrated by using the following expressions from Rienstra and Hirschberg (2004),

$$\mathrm{K}_n\left(z\right) = \frac{\pi(-\mathrm{i})^{n+1}}{2}\mathrm{H}_n^{(2)}\left(-\mathrm{i}z\right), \tag{D.24}$$

and the asymptotic behaviour for large argument,

$$\mathrm{K}_n\left(z\right) \sim \sqrt{\frac{\pi}{2z}}\mathrm{e}^{-z} \quad \text{as} \;\; z \to \infty. \tag{D.25}$$

Therefore when $|\tau| > 1$,

$$\begin{aligned} &\mathrm{H}_n^{(2)}\left(\Gamma_\infty \bar{R}\sin\bar{\theta}\right) = \mathrm{H}_n^{(2)}\left(-\mathrm{i}\gamma_\infty \bar{R}\sin\bar{\theta}\right) = \frac{2}{\pi(-\mathrm{i})^{n+1}}\mathrm{K}_n\left(\gamma_\infty \bar{R}\sin\bar{\theta}\right) \simeq \\ &\simeq \frac{2}{\pi(-\mathrm{i})^{n+1}}\sqrt{\frac{\pi}{2\gamma_\infty \bar{R}\sin\bar{\theta}}}\mathrm{e}^{-\gamma_\infty \bar{R}\sin\bar{\theta}} \to 0, \text{ as } \bar{R} \to \infty, \end{aligned} \tag{D.26}$$

since $\sin\bar{\theta}$, $\gamma_\infty > 0$ by default.
After this change of variables, the point where $\hat{\phi}'(c) = 0$ can easily be found by using eq.(D.21),

$$\hat{\phi}'(c) = 0 \Rightarrow c = \cos\hat{\theta}. \tag{D.27}$$

The quantity $\hat{\phi}''(c)$ is also required and can easily be evaluated as

$$\hat{\phi}''(c) = \frac{k_0}{\sigma_\infty \sin^2\hat{\theta}} > 0. \tag{D.28}$$

With all these quantities known, the integral from eq.(D.19) can be replaced using eq.(D.3),

$$I_n \;\sim\; \frac{1}{2\pi}g_n\left(c\right)\left(\frac{2\pi}{\hat{R}|\hat{\phi}''(c)|}\right)^{1/2} \mathrm{e}^{\mathrm{i}\hat{R}\hat{\phi}(c)+\mathrm{i}\pi/4}, \quad \text{as } \hat{R} \to \infty \tag{D.29}$$

where,

$$\begin{aligned} g_n\left(c\right) =& \frac{k_0}{\sigma_\infty^2}F_n\left(c,\omega_0\right)\Bigg[\mathrm{J}_{n-l}\left(\Gamma_{\infty c}b\right) \\ &+ \Bigg[\frac{2\mathrm{i}\,Y_n\left(\Gamma_{0c}\right)}{\pi(a_0+\delta_{SF})\,\mathrm{H}_n^{(2)}\left(\Gamma_{\infty c}(a_0+\delta_{SF})\right)k_0^2\left(1+\frac{(\cos\hat{\theta}+M_\infty)M_\infty}{\sigma_\infty^2}\right)^2 D_n\left(c,\omega_0\right)} \\ &- \mathrm{J}_n\left(\Gamma_{\infty c}(a_0+\delta_{SF})\right)\Bigg]\frac{\mathrm{H}_{n-l}^{(2)}\left(\Gamma_{\infty c}b\right)}{\mathrm{H}_n^{(2)}\left(\Gamma_{\infty c}(a_0+\delta_{SF})\right)}\Bigg]\sqrt{\frac{2}{\pi\frac{k_0}{\sigma_\infty}\sin^2\hat{\theta}\hat{R}}}\,\mathrm{e}^{\frac{1}{2}n\pi\mathrm{i}}\,\mathrm{e}^{\frac{1}{4}\pi\mathrm{i}}, \end{aligned} \tag{D.30}$$

and

$$\hat{\phi}(c) = -\frac{k_0}{\sigma_\infty}\sin^2\hat{\theta} - \frac{k_0}{\sigma_\infty}\cos^2\hat{\theta} - \frac{k_0}{\sigma_\infty}M_\infty\cos\hat{\theta} = -\frac{k_0}{\sigma_\infty}(1+M_\infty\cos\hat{\theta}). \tag{D.31}$$

Also the terms $\Gamma_{\infty c}$ and Γ_{0c} are the Γ_∞ and Γ_0 respectively, but evaluated using $\tau = c = \cos\hat{\theta}$,

$$\Gamma_{\infty c} = \frac{k_0}{\sigma_\infty}\sin\hat{\theta}, \tag{D.32}$$

and

$$\Gamma_{0c} = \frac{k_0}{\sigma_\infty}\sqrt{\sigma_\infty^2 + (\cos\hat{\theta}+M_\infty)\left[2M_0 - (\cos\hat{\theta}+M_\infty)\frac{\sigma_0^2}{\sigma_\infty^2}\right]}, \tag{D.33}$$

whereas the terms $F_n\left(c,\omega_0\right)$ and $D_n\left(c,\omega_0\right)$ are respectively,

$$F_n\left(c,\omega_0\right)=\pi^2\xi_{lq}P_{lq}\,\mathrm{e}^{-\mathrm{i}(l-n)\beta}\,k_0\left(1+\frac{(\cos\hat{\theta}+M_\infty)M_\infty}{\sigma_\infty^2}\right)\Psi_{lq}(\Gamma_{\infty c}), \tag{D.34}$$

and

$$\begin{aligned}D_n\left(c,\omega_0\right)=&\left[\mathrm{H}_n^{(2)\prime}\left(\Gamma_{0c}(a_0+\delta_{SF})\right)-\mathrm{J}_n'\left(\Gamma_{0c}(a_0+\delta_{SF})\right)\frac{\mathrm{H}_n^{(2)\prime}\left(\Gamma_{0c}a_0\right)}{\mathrm{J}_n'\left(\Gamma_{0c}a_0\right)}\right]\\&\times\frac{\sqrt{\sigma_\infty^2+(\cos\hat{\theta}+M_\infty)\left[2M_0-(\cos\hat{\theta}+M_\infty)\frac{\sigma_0^2}{\sigma_\infty^2}\right]}}{k_0\sigma_\infty\left(1+\frac{(\cos\hat{\theta}+M_\infty)M_0}{\sigma_\infty^2}\right)^2}\\&-\left[\mathrm{H}_n^{(2)}\left(\Gamma_{0c}(a_0+\delta_{SF})\right)-\mathrm{J}_n\left(\Gamma_{0c}(a_0+\delta_{SF})\right)\frac{\mathrm{H}_n^{(2)\prime}\left(\Gamma_{0c}a_0\right)}{\mathrm{J}_n'\left(\Gamma_{0c}a_0\right)}\right]\\&\times\frac{\sin\hat{\theta}}{k_0\sigma_\infty\left(1+\frac{(\cos\hat{\theta}+M_\infty)M_\infty}{\sigma_\infty^2}\right)^2}\frac{\mathrm{H}_n^{(2)\prime}\left(\Gamma_{\infty c}(a_0+\delta_{SF})\right)}{\mathrm{H}_n^{(2)}\left(\Gamma_{\infty c}(a_0+\delta_{SF})\right)}.\end{aligned} \tag{D.35}$$

Finally, considering that $\mathrm{e}^{\frac{1}{4}\pi\mathrm{i}}\,\mathrm{e}^{\frac{1}{4}\pi\mathrm{i}}=\mathrm{e}^{\frac{1}{2}\pi\mathrm{i}}=\mathrm{i}$, eq.(D.29) can be written

$$\begin{aligned}I_n=&\frac{\mathrm{i}\,F_n\left(c,\omega_0\right)}{\pi\,\hat{R}\,k_0}\frac{k_0}{\sigma_\infty}\Bigg[\mathrm{J}_{n-l}\left(\Gamma_{\infty c}b\right)\\&+\Bigg[\frac{2\mathrm{i}\,Y_n\left(\Gamma_{0c}\right)}{\pi(a_0+\delta_{SF})\,\mathrm{H}_n^{(2)}\left(\Gamma_{\infty c}(a_0+\delta_{SF})\right)k_0^2\left(1+\frac{(\cos\hat{\theta}+M_\infty)M_\infty}{\sigma_\infty^2}\right)^2D_n\left(c,\omega_0\right)}\\&-\mathrm{J}_n\left(\Gamma_{\infty c}(a_0+\delta_{SF})\right)\Bigg]\frac{\mathrm{H}_{n-l}^{(2)}\left(\Gamma_{\infty c}b\right)}{\mathrm{H}_n^{(2)}\left(\Gamma_{\infty c}(a_0+\delta_{SF})\right)}\Bigg]\mathrm{e}^{\frac{1}{2}n\pi\mathrm{i}}\mathrm{e}^{-\mathrm{i}\hat{R}\frac{k_0}{\sigma_\infty}(1+M_\infty\cos\hat{\theta})}.\end{aligned} \tag{D.36}$$

Now rewrite the expressions in the original coordinates,

$$\Delta_\infty\;=\;\Gamma_{\infty c}\;=\;\frac{k_0}{\sigma_\infty}\sin\hat{\theta}=\frac{k_0}{\sigma_\infty}\frac{\sigma_\infty\sin\bar{\theta}}{(1-M_\infty^2\sin^2\bar{\theta})^{1/2}}=\frac{k_0\sin\bar{\theta}}{(1-M_\infty^2\sin^2\bar{\theta})^{1/2}}, \tag{D.37}$$

and by setting $C\left(\bar{\theta}\right)=\frac{\cos\bar{\theta}+(1-M_\infty^2\sin^2\bar{\theta})^{1/2}M_\infty}{\sigma_\infty^2}$, the following is obtained

$$\Delta_0\;=\;\Gamma_{0c}=\frac{k_0}{(1-M_\infty^2\sin^2\bar{\theta})^{1/2}}\sqrt{(1-M_\infty^2\sin^2\bar{\theta})+C\left(\bar{\theta}\right)[2M_0(1-M_\infty^2\sin^2\bar{\theta})^{1/2}-C\left(\bar{\theta}\right)\sigma_0^2]}. \tag{D.38}$$

Also by setting $S\left(\bar{\theta}\right)\;=\;\frac{(1-M_\infty^2\sin^2\bar{\theta})^{1/2}+M_\infty\cos\bar{\theta}}{\sigma_\infty^2}$, the following is obtained

$$\frac{F_n\left(c,\omega_0\right)}{k_0}=\pi^2\xi_{lq}P_{lq}\,\mathrm{e}^{-\mathrm{i}(l-n)\beta}\,\frac{S\left(\bar{\theta}\right)}{(1-M_\infty^2\sin^2\bar{\theta})^{1/2}}\,\Psi_{lq}(\Delta_\infty). \tag{D.39}$$

Accordingly,

$$\begin{aligned}\frac{\mathrm{i}\,F_n\,(c,\omega_0)}{\pi\,\hat{R}\,k_0}\,\frac{k_0}{\sigma_\infty} =& \mathrm{i}\pi^2\xi_{lq}P_{lq}\,\mathrm{e}^{-\mathrm{i}(l-n)\beta}\,\frac{S\,(\bar{\theta})}{\pi\frac{\bar{R}}{\sigma_\infty}(1-M_\infty^2\sin^2\bar{\theta})^{1/2}(1-M_\infty^2\sin^2\bar{\theta})^{1/2}}\,\Psi_{lq}(\Delta_\infty)\frac{k_0}{\sigma_\infty} = \\ =& \mathrm{i}\pi\xi_{lq}P_{lq}\,k_0\,\mathrm{e}^{-\mathrm{i}(l-n)\beta}\,\frac{S\,(\bar{\theta})}{\bar{R}(1-M_\infty^2\sin^2\bar{\theta})}\,\Psi_{lq}(\Delta_\infty).\end{aligned} \tag{D.40}$$

Another term from eq.(D.36) that can take its final form is

$$\begin{aligned}&\mathrm{e}^{-\mathrm{i}\hat{R}\frac{k_0}{\sigma_\infty}(1+M_\infty\cos\hat{\theta})} = \mathrm{e}^{-\mathrm{i}\frac{\bar{R}}{\sigma_\infty}(1-M_\infty^2\sin^2\bar{\theta})^{1/2}\frac{k_0}{\sigma_\infty}(1+\frac{M_\infty\cos\bar{\theta}}{(1-M_\infty^2\sin^2\bar{\theta})^{1/2}})} = \\ &\mathrm{e}^{-\mathrm{i}\bar{R}k_0\frac{((1-M_\infty^2\sin^2\bar{\theta})^{1/2}+M_\infty\cos\bar{\theta})}{\sigma_\infty^2}} = \mathrm{e}^{-\mathrm{i}k_0\bar{R}S\,(\bar{\theta})}.\end{aligned} \tag{D.41}$$

Finally, the large bracket term from eq.(D.36) will become

$$\begin{aligned}&\Bigg[\mathrm{J}_{n-l}\,(\Gamma_{\infty c}b) \\ &+\Bigg[\frac{2\mathrm{i}\,Y_n\,(\Gamma_{0c})}{\pi(a_0+\delta_{SF})\,\mathrm{H}_n^{(2)}\,(\Gamma_{\infty c}(a_0+\delta_{SF}))\,k_0^2\,(1+\frac{(\cos\hat{\theta}+M_\infty)M_\infty}{\sigma_\infty^2})^2\,D_n\,(c,\omega_0)} \\ &-\mathrm{J}_n\,(\Gamma_{\infty c}(a_0+\delta_{SF}))\Bigg]\frac{\mathrm{H}_{n-l}^{(2)}\,(\Gamma_{\infty c}b)}{\mathrm{H}_n^{(2)}\,(\Gamma_{\infty c}(a_0+\delta_{SF}))}\Bigg] = \\ &=\Bigg[\mathrm{J}_{n-l}\,(\Delta_\infty b) \\ &+\Bigg[\frac{2\mathrm{i}\,(1-M_\infty^2\sin^2\bar{\theta})\,Y_n\,(\Delta_0)}{\pi(a_0+\delta_{SF})\,\mathrm{H}_n^{(2)}\,(\Delta_\infty(a_0+\delta_{SF}))\,k_0^2\,S^2\,(\bar{\theta})\,D_n\,(\Delta_\infty,\Delta_0)} \\ &-\mathrm{J}_n\,(\Delta_\infty(a_0+\delta_{SF}))\Bigg]\frac{\mathrm{H}_{n-l}^{(2)}\,(\Delta_\infty b)}{\mathrm{H}_n^{(2)}\,(\Delta_\infty(a_0+\delta_{SF}))}\Bigg],\end{aligned} \tag{D.42}$$

where

$$\begin{aligned}D_n\,(\Delta_\infty,\Delta_0) =& \Bigg[\mathrm{H}_n^{(2)\prime}\,(\Delta_0(a_0+\delta_{SF})) - \mathrm{J}_n'\,(\Delta_0(a_0+\delta_{SF}))\,\frac{\mathrm{H}_n^{(2)\prime}\,(\Delta_0 a_0)}{\mathrm{J}_n'\,(\Delta_0 a_0)}\Bigg] \\ &\times\frac{\Delta_0}{k_0^2(1+\frac{C\,(\bar{\theta})\,M_0}{(1-M_\infty^2\sin^2\bar{\theta})^{1/2}})^2} \\ &-\Bigg[\mathrm{H}_n^{(2)}\,(\Delta_0(a_0+\delta_{SF})) - \mathrm{J}_n\,(\Delta_0(a_0+\delta_{SF}))\,\frac{\mathrm{H}_n^{(2)\prime}\,(\Delta_0 a_0)}{\mathrm{J}_n'\,(\Delta_0 a_0)}\Bigg] \\ &\times\frac{\sin\bar{\theta}(1-M_\infty^2\sin^2\bar{\theta})^{1/2}}{k_0\,S^2\,(\bar{\theta})}\,\frac{\mathrm{H}_n^{(2)\prime}\,(\Delta_\infty(a_0+\delta_{SF}))}{\mathrm{H}_n^{(2)}\,(\Delta_\infty(a_0+\delta_{SF}))}.\end{aligned} \tag{D.43}$$

By inserting eqs. (D.40)-(D.43) into eq.(D.36) and since

$$p'_{t_{ff}}\,(\bar{R},\bar{\phi},\bar{\theta},t) \;=\; \frac{1}{2\pi}\sum_{n=-\infty}^{\infty} I_n\mathrm{e}^{-\mathrm{i}n\bar{\phi}}\,\mathrm{e}^{\mathrm{i}\omega_0 t}, \tag{D.44}$$

from eqs. (3.120) and (D.1), the total field in real space can finally be written

$$
\begin{aligned}
p'_{t_{ff}}\left(\bar{R},\bar{\phi},\bar{\theta},t\right) = & \frac{\mathrm{i}\xi_{lq}P_{lq}\,k_0\,\Psi_{lq}(\Delta_\infty)}{2\bar{R}}\,\frac{S\left(\bar{\theta}\right)}{\left(1-M_\infty^2\sin^2\bar{\theta}\right)}\,\mathrm{e}^{-\mathrm{i}k_0\bar{R}S(\bar{\theta})}\sum_{n=-\infty}^{\infty}\Bigg[\mathrm{J}_{n-l}\left(\Delta_\infty b\right) \\
& + \Bigg[\frac{2\mathrm{i}\left(1-M_\infty^2\sin^2\bar{\theta}\right)Y_n\left(\Delta_0\right)}{\pi(a_0+d)\,\mathrm{H}_n^{(2)}\left(\Delta_\infty(a_0+d)\right)k_0^2\,S^2\left(\bar{\theta}\right)D_n\left(\Delta_\infty,\Delta_0\right)} \\
& - \mathrm{J}_n\left(\Delta_\infty(a_0+d)\right)\Bigg]\frac{\mathrm{H}_{n-l}^{(2)}\left(\Delta_\infty b\right)}{\mathrm{H}_n^{(2)}\left(\Delta_\infty(a_0+d)\right)}\Bigg] \\
& \times \mathrm{e}^{\frac{1}{2}n\pi\mathrm{i}}\,\mathrm{e}^{\mathrm{i}(n-l)\beta}\,\mathrm{e}^{-\mathrm{i}n\bar{\phi}}\,\mathrm{e}^{\mathrm{i}\omega_0 t},
\end{aligned}
\tag{D.45}
$$

Equation (D.45) is the essential conclusion of this section. It describes the acoustic pressure in the far-field around the fuselage using spherical polar coordinates centered on the cylindrical fuselage.

Appendix E

Asymptotic Evaluation of the Integral using the Method of Steepest Descent for the Step-Function Boundary Layer Case

The integral in eq.(3.120) can also be evaluated using the method of steepest descent as in Gabard (2008). The method of steepest descent is more mathematically robust than the method of stationary phase since it incorporates the deformation of the integration path onto the complex plane avoiding the branch points (points along the k_z-axis where $\Gamma_\infty = 0$, see Fig. (3.4)). In contrast, in the stationary phase method the integration takes place along the real k_z-axis.

The steepest descent analysis presented here follows the procedure proposed by Gabard (2008). Firstly, the integral in question

$$I_n = \frac{1}{2\pi} \int_{-\infty}^{\infty} \overline{p'_{t_{nff}}} \left(\bar{r}, k_z\right) \mathrm{e}^{-\mathrm{i}k_z \bar{z}} \, \mathrm{d}k_z, \tag{E.1}$$

can be rewritten as

$$I_n = \frac{1}{2\pi} \int_{-\infty}^{\infty} \Lambda(k_z) \, \mathrm{H}_n^{(2)} \left(\Gamma_\infty \bar{r}\right) \mathrm{e}^{-\mathrm{i}k_z \bar{z}} \, \mathrm{d}k_z, \tag{E.2}$$

by using eq.(3.119) and setting

$$\begin{aligned} \Lambda(k_z) = & F_n \left(k_z, \omega_0\right) \Bigg[\mathrm{J}_{n-l} \left(\Gamma_\infty b\right) \\ & + \Bigg[\frac{2\mathrm{i} \, Y_n \left(\Gamma_0\right)}{\pi (a_0 + \delta_{SF}) \, \mathrm{H}_n^{(2)} \left(\Gamma_\infty (a_0 + \delta_{SF})\right) \left(k_0 + k_z M_\infty\right)^2 D_n \left(k_z, \omega_0\right)} \\ & - \mathrm{J}_n \left(\Gamma_\infty (a_0 + \delta_{SF})\right) \Bigg] \frac{\mathrm{H}_{n-l}^{(2)} \left(\Gamma_\infty b\right)}{\mathrm{H}_n^{(2)} \left(\Gamma_\infty (a_0 + \delta_{SF})\right)} \Bigg]. \end{aligned} \tag{E.3}$$

As is usually the case for far-field analysis, spherical polar coordinates $(\bar{R}, \bar{\theta}, \bar{\phi})$ are utilized and the integral is solved in the limit as $\bar{R} \to \infty$. First substitute

$$\bar{r} \;=\; \bar{R}\sin\bar{\theta} \quad \text{and} \quad \bar{z} \;=\; \bar{R}\cos\bar{\theta}. \tag{E.4}$$

Then the dependence of the function $\overline{p'_{t_{nff}}}(\bar{r}, k_z)$ on $\bar{r}$ is via the Hankel function

$$\mathrm{H}_n^{(2)}\left(\Gamma_\infty \bar{r}\right) \;=\; \mathrm{H}_n^{(2)}\left(\Gamma_\infty \bar{R}\sin\bar{\theta}\right) \;\sim\; \sqrt{\frac{2}{\pi\Gamma_\infty \bar{R}\sin\bar{\theta}}}\,\mathrm{e}^{\frac{1}{2}n\pi\mathrm{i}}\,\mathrm{e}^{\frac{1}{4}\pi\mathrm{i}}\,\mathrm{e}^{-\mathrm{i}\Gamma_\infty \bar{R}\sin\bar{\theta}} \quad \text{as} \;\; \bar{R}\to\infty. \tag{E.5}$$

Also, $\exp(-\mathrm{i}k_z\bar{z}) \to \exp(-\mathrm{i}k_z\bar{R}\cos\bar{\theta})$ so the integral in eq.(E.2) can be expressed in the form

$$I_n \;\sim\; \frac{1}{2\pi}\int_{-\infty}^{\infty}\Lambda(k_z)\sqrt{\frac{2}{\pi\Gamma_\infty \bar{R}\sin\bar{\theta}}}\,\mathrm{e}^{\frac{1}{2}n\pi\mathrm{i}}\,\mathrm{e}^{\frac{1}{4}\pi\mathrm{i}}\,\mathrm{e}^{-\mathrm{i}\Gamma_\infty \bar{R}\sin\bar{\theta}}\,\mathrm{e}^{-\mathrm{i}k_z\bar{R}\cos\bar{\theta}}\mathrm{d}k_z \quad \text{as} \;\; \bar{R}\to\infty. \tag{E.6}$$

Introduce the similarity variables following Chapman (2000)

$$(\bar{x}, \bar{y}, \bar{z}) \;=\; \left(\hat{R}\sin\hat{\theta}\cos\bar{\phi}, \hat{R}\sin\hat{\theta}\sin\bar{\phi}, \hat{R}\sigma_\infty\cos\hat{\theta}\right), \tag{E.7}$$

where

$$\sigma_\infty^2 \;=\; 1 - M_\infty^2, \tag{E.8}$$

$$\Theta \;=\; 1 - M_\infty^2\sin^2\bar{\theta}, \tag{E.9}$$

$$\hat{R} \;=\; \frac{\bar{R}}{\sigma_\infty}\Theta^{1/2}, \tag{E.10}$$

$$\cos\hat{\theta} \;=\; \frac{\cos\bar{\theta}}{\Theta^{1/2}}, \tag{E.11}$$

$$\sin\hat{\theta} \;=\; \frac{\sigma_\infty\sin\bar{\theta}}{\Theta^{1/2}}. \tag{E.12}$$

Also following Rienstra and Hirschberg (2004), introduce the variable τ

$$\tau \;=\; \sigma_\infty^2\frac{k_z}{k_0} - M_\infty, \tag{E.13}$$

which means that

$$\Gamma_\infty \;=\; \frac{k_0}{\sigma_\infty}(1-\tau^2)^{1/2}, \tag{E.14}$$

$$k_z \;=\; \frac{k_0}{\sigma_\infty^2}(\tau + M_\infty), \tag{E.15}$$

$$\mathrm{d}k_z \;=\; \frac{k_0}{\sigma_\infty^2}\mathrm{d}\tau. \tag{E.16}$$

Note that all the similarity variables are based on the free stream Mach number M_∞. However, in the case of the step-function boundary layer, unlike the case of uniform flow, there is one more term that needs to be rewritten in terms of the free stream similarity variables. This term is Γ_0 which is the only term that is dependent on the Mach number inside the boundary layer M_0. By introducing the following term for brevity purposes,

$$\sigma_0^2 \;=\; 1 - M_0^2, \tag{E.17}$$

Γ_0 can be rewritten in terms of the free stream similarity variables by using eq.(E.15),

$$\Gamma_0 = \frac{k_0}{\sigma_\infty}\sqrt{\sigma_\infty^2 + (\tau + M_\infty)\left[2M_0 - (\tau + M_\infty)\frac{\sigma_0^2}{\sigma_\infty^2}\right]}. \tag{E.18}$$

By introducing these similarity variables, the integral can be rewritten

$$I_n \sim \sqrt{\frac{k_0}{2\pi^3 \hat{R}\sin\hat{\theta}\sigma_\infty^3}}\, e^{\frac{1}{2}n\pi i}\, e^{\frac{1}{4}\pi i} e^{-i\frac{k_0\hat{R}}{\sigma_\infty}M_\infty\cos\hat{\theta}} \int_{-\infty}^{\infty} \frac{\Lambda(k_z(\tau))}{(1-\tau^2)^{1/4}} e^{\frac{k_0\hat{R}}{\sigma_\infty}q(\tau)} d\tau, \tag{E.19}$$

where

$$q(\tau) = -i(1-\tau^2)^{1/2}\sin\hat{\theta} - i\tau\cos\hat{\theta}. \tag{E.20}$$

When $\frac{k_0\hat{R}}{\sigma_\infty} \to \infty$, then the integral can be approximated using the method of steepest descent (see Chapter 4 of Felsen and Marcuvitz (1994)). As in Gabard (2008), the function q is analytic except for the branch cuts of the square root term $(1-\tau^2)^{1/2}$ which correspond to to the branch cuts of Γ_∞ (see Fig. (3.4) and Fig. (E.1)) and go from ± 1 to $\pm 1 \mp i\infty$ in the τ complex plane.

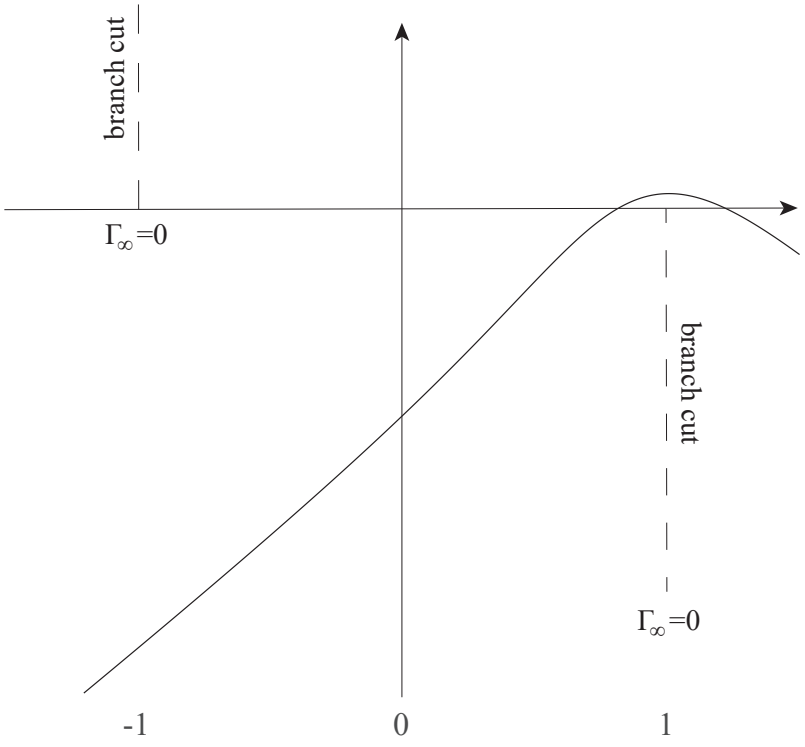

FIGURE E.1: Location of branch cuts in the complex τ plane. The thick solid line represents the deformed integration contour of steepest descent path (SDP). Note how the deformed contour avoids the branch points at $\tau = \pm 1$.

As in the case by Gabard (2008), the first order saddle point τ_s is found by setting

$$q'(\tau_s) = 0 \Rightarrow \tau_s = \cos\hat{\theta}. \tag{E.21}$$

This gives $q(\tau_s) = -\mathrm{i}$ and

$$q''(\tau_s) = \mathrm{i}(1-\cos^2\hat{\theta})^{-3/2}\cos\hat{\theta}\cos\hat{\theta}\sin\hat{\theta} + \mathrm{i}(1-\cos^2\hat{\theta})^{-1/2}\sin\hat{\theta} = \frac{\mathrm{i}}{\sin^2\hat{\theta}}. \tag{E.22}$$

Using that saddle point, a path of steepest descent is defined by $q(\tau) = q(\tau_s) - s^2$, where s is a real parameter as proposed by Gabard (2008). Solving for τ one can obtain the following parameterisation of the steepest descent path

$$\begin{aligned} &q(\tau) = q(\tau_s) - s^2 \Rightarrow -\mathrm{i}(1-\tau^2)^{1/2}\sin\hat{\theta} - \mathrm{i}\tau\cos\hat{\theta} = -\mathrm{i} - s^2 \Rightarrow \\ &\tau^2 - 2(1-\mathrm{i}s^2)\tau\cos\hat{\theta} + (1-\mathrm{i}s^2)^2 - \sin^2\hat{\theta} = 0. \end{aligned} \tag{E.23}$$

This quadratic equation yields a discriminant of $4\sin^2\hat{\theta}(1-(1-\mathrm{i}s^2)^2)$. This means that

$$\begin{aligned} &\tau = \frac{2\cos\hat{\theta}(1-\mathrm{i}s^2) \pm \sqrt{4\sin^2\hat{\theta}(1-(1-\mathrm{i}s^2)^2)}}{2} = \cos\hat{\theta}(1-\mathrm{i}s^2) \pm \sin\hat{\theta}\sqrt{(1-(1-\mathrm{i}s^2)^2)} \Rightarrow \\ &\tau = \cos(\hat{\theta} \mp \cos^{-1}(1-\mathrm{i}s^2)) \end{aligned} \tag{E.24}$$

As explained in Chapter 4 of Felsen and Marcuvitz (1994), on the path of steepest descent the integrand decays exponentially away from the saddle point, and thus only the contribution on that point is considered. Note that the saddle point coincides with the point of stationary phase. Therefore, the integral in eq.(E.19) can be evaluated as

$$\int_{\mathrm{SDP}} \frac{\Lambda(k_z(\tau))}{(1-\tau^2)^{1/4}} \mathrm{e}^{\frac{k_0\hat{R}}{\sigma_\infty}q(\tau)}\mathrm{d}\tau \sim \sqrt{\frac{-2\pi}{\frac{k_0\hat{R}}{\sigma_\infty}q''(\tau_s)}} \frac{\Lambda(k_z(\tau_s))}{(1-\tau_s^2)^{1/4}} \mathrm{e}^{\frac{k_0\hat{R}}{\sigma_\infty}q(\tau_s)}. \tag{E.25}$$

One must choose the argument of the square root as $\arg(\mathrm{d}\tau)_{\tau_s}$, where $\mathrm{d}\tau$ denotes an element at τ_s along the steepest descent path (see p. 382 of Felsen and Marcuvitz (1994)). Also, $\Lambda(k_z(\tau_s))$ is the term $\Lambda(k_z)$ evaluated at the saddle point. Thus, eq.(E.19) becomes,

$$I_n \sim \sqrt{\frac{k_0}{2\pi^3\hat{R}\sin\hat{\theta}\sigma_\infty^3}} \mathrm{e}^{\frac{1}{2}n\pi\mathrm{i}} \mathrm{e}^{\frac{1}{4}\pi\mathrm{i}} \mathrm{e}^{-\mathrm{i}\frac{k_0\hat{R}}{\sigma_\infty}M_\infty\cos\hat{\theta}} \sqrt{\frac{-2\pi}{\frac{k_0\hat{R}}{\sigma_\infty}\frac{\mathrm{i}}{\sin^2\hat{\theta}}}} \frac{\Lambda(k_z(\tau_s))}{\sqrt{\sin\hat{\theta}}} \mathrm{e}^{-\mathrm{i}\frac{k_0\hat{R}}{\sigma_\infty}}, \tag{E.26}$$

or

$$I_n \sim \frac{\mathrm{i}^{n+1}}{\pi\hat{R}\sigma_\infty}\Lambda(k_z(\tau_s))\,\mathrm{e}^{-\mathrm{i}\frac{k_0\hat{R}}{\sigma_\infty}(1+M_\infty\cos\hat{\theta})}. \tag{E.27}$$

By shifting back to the original coordinates

$$I_n \sim \frac{\mathrm{i}^{n+1}}{\pi\bar{R}\Theta^{1/2}}\Lambda(k_z(\tau_s))\,\mathrm{e}^{-\mathrm{i}\frac{k_0\frac{\bar{R}}{\sigma_\infty}\Theta^{1/2}}{\sigma_\infty}(1+M_\infty\frac{\cos\bar{\theta}}{\Theta^{1/2}})} = \frac{\mathrm{i}^{n+1}}{\pi\bar{R}\Theta^{1/2}}\Lambda(k_z(\tau_s))\,\mathrm{e}^{-\mathrm{i}k_0\bar{R}(\frac{\Theta^{1/2}+M_\infty\cos\bar{\theta}}{\sigma_\infty^2})}. \tag{E.28}$$

And by setting $S(\bar{\theta}) = \frac{\Theta^{1/2}+M_\infty\cos\bar{\theta}}{\sigma_\infty^2}$,

$$I_n \sim \frac{\mathrm{i}^{n+1}}{\pi\bar{R}\Theta^{1/2}}\Lambda(k_z(\tau_s))\,\mathrm{e}^{-\mathrm{i}k_0\bar{R}S(\bar{\theta})}. \tag{E.29}$$

Next the term $\Lambda(k_z(\tau_s))$ is evaluated,

$$\begin{aligned}\Lambda(k_z(\tau_s)) =& F_n(\tau_s)\Bigg[\mathrm{J}_{n-l}\left(\frac{k_0}{\sigma_\infty}\sqrt{1-\tau_s^2}b\right)\\ &+\Bigg[\frac{2\mathrm{i}\,Y_n\left(\Gamma_0(\tau_s)\right)}{\pi(a_0+\delta_{SF})\,\mathrm{H}_n^{(2)}\left(\frac{k_0}{\sigma_\infty}\sqrt{1-\tau_s^2}(a_0+\delta_{SF})\right)\left(k_0+\frac{k_0}{\sigma_\infty^2}(\tau_s+M_\infty)M_\infty\right)^2 D_n(\tau_s)}\\ &-\mathrm{J}_n\left(\frac{k_0}{\sigma_\infty}\sqrt{1-\tau_s^2}(a_0+\delta_{SF})\right)\Bigg]\frac{\mathrm{H}_{n-l}^{(2)}\left(\frac{k_0}{\sigma_\infty}\sqrt{1-\tau_s^2}b\right)}{\mathrm{H}_n^{(2)}\left(\frac{k_0}{\sigma_\infty}\sqrt{1-\tau_s^2}(a_0+\delta_{SF})\right)}\Bigg].\end{aligned} \tag{E.30}$$

The smaller terms become, by shifting back to original coordinates,

$$\Gamma_\infty(\tau_s)=\frac{k_0}{\sigma_\infty}\sqrt{1-\tau_s^2}=\frac{k_0}{\sigma_\infty}\sin\hat{\theta}=\frac{k_0\sin\bar{\theta}}{\Theta^{1/2}}=\Delta_\infty, \tag{E.31}$$

and,

$$\begin{aligned}F_n(\tau_s)&=\pi^2\xi_{lq}P_{lq}\,\mathrm{e}^{-\mathrm{i}(l-n)\beta}\left(k_0+\frac{k_0}{\sigma_\infty^2}(\tau_s+M_\infty)M_\infty\right)\Psi_{lq}(\Gamma_\infty(\tau_s))\Rightarrow\\ F_n(\tau_s)&=\pi^2\xi_{lq}P_{lq}\,\mathrm{e}^{-\mathrm{i}(l-n)\beta}k_0\frac{S(\bar{\theta})}{\Theta^{1/2}}\Psi_{lq}(\Delta_\infty)\end{aligned} \tag{E.32}$$

The radial wavenumber $\Gamma_0(\tau_s)$,

$$\begin{aligned}\Gamma_0(\tau_s)&=\frac{k_0}{\sigma_\infty}\sqrt{\sigma_\infty^2+(\tau_s+M_\infty)\left[2M_0-(\tau_s+M_\infty)\frac{\sigma_0^2}{\sigma_\infty^2}\right]}\Rightarrow\\ \Gamma_0(\tau_s)&=k_0\sqrt{1+\frac{\cos\bar{\theta}+M_\infty\Theta^{1/2}}{\sigma_\infty^2\Theta^{1/2}}\left[2M_0-\frac{\cos\bar{\theta}+M_\infty\Theta^{1/2}}{\sigma_\infty^2\Theta^{1/2}}\sigma_0^2\right]}.\end{aligned} \tag{E.33}$$

By setting $C(\bar{\theta})=\frac{\cos\bar{\theta}+\Theta^{1/2}M_\infty}{\sigma_\infty^2}$,

$$\begin{aligned}\Gamma_0(\tau_s)&=k_0\sqrt{1+\frac{C(\bar{\theta})}{\Theta^{1/2}}\left[2M_0-\frac{C(\bar{\theta})}{\Theta^{1/2}}\sigma_0^2\right]}\Rightarrow\\ \Gamma_0(\tau_s)&=\frac{k_0}{\Theta^{1/2}}\sqrt{\Theta+C(\bar{\theta})\left[2M_0\Theta^{1/2}-C(\bar{\theta})\sigma_0^2\right]}=\Delta_0.\end{aligned} \tag{E.34}$$

The term $Y_n\left(\Gamma_0(\tau_s)\right)$ is only dependent on $\Gamma_0(\tau_s)$ which means $Y_n\left(\Gamma_0(\tau_s)\right)=Y_n\left(\Delta_0\right)$. Another term that needs evaluating is the following

$$\left(k_0+\frac{k_0}{\sigma_\infty^2}(\tau_s+M_\infty)M_\infty\right)^2=\left(k_0+\frac{k_0}{\sigma_\infty^2}\left(\frac{\cos\bar{\theta}}{\Theta^{1/2}}+M_\infty\right)M_\infty\right)^2=k_0^2\frac{S^2(\bar{\theta})}{\Theta}. \tag{E.35}$$

The term $D_n(\tau_s)$ becomes

$$\begin{aligned} D_n\left(\Delta_\infty, \Delta_0\right) = & \left[\mathrm{H}_n^{(2)\prime}\left(\Delta_0(a_0+\delta_{SF})\right) - \mathrm{J}_n'\left(\Delta_0(a_0+\delta_{SF})\right)\frac{\mathrm{H}_n^{(2)\prime}\left(\Delta_0 a_0\right)}{\mathrm{J}_n'\left(\Delta_0 a_0\right)}\right]\frac{\Delta_0}{k_0^2\left(1+\frac{C(\bar{\theta})}{\Theta^{1/2}}M_0\right)^2} \\ & - \left[\mathrm{H}_n^{(2)}\left(\Delta_0(a_0+\delta_{SF})\right) - \mathrm{J}_n\left(\Delta_0(a_0+\delta_{SF})\right)\frac{\mathrm{H}_n^{(2)\prime}\left(\Delta_0 a_0\right)}{\mathrm{J}_n'\left(\Delta_0 a_0\right)}\right] \\ & \times \frac{\sin\bar{\theta}\,\Theta^{1/2}}{k_0 S^2(\bar{\theta})}\frac{\mathrm{H}_n^{(2)\prime}\left(\Delta_\infty(a_0+\delta_{SF})\right)}{\mathrm{H}_n^{(2)}\left(\Delta_\infty(a_0+\delta_{SF})\right)}. \end{aligned} \tag{E.36}$$

Therefore, by substituting eqs. (E.31)-(E.36) into eq.(E.30), $\Lambda(k_z(\tau_s))$ becomes

$$\begin{aligned} \Lambda(k_z(\tau_s)) = & \pi^2\xi_{lq}P_{lq}\,\mathrm{e}^{-\mathrm{i}(l-n)\beta}k_0\frac{S(\bar{\theta})}{\Theta^{1/2}}\,\Psi_{lq}(\Delta_\infty)\Bigg[\mathrm{J}_{n-l}\left(\Delta_\infty b\right) \\ & + \Bigg[\frac{2\mathrm{i}\,Y_n\left(\Delta_0\right)\Theta}{\pi(a_0+\delta_{SF})\,\mathrm{H}_n^{(2)}\left(\Delta_\infty(a_0+\delta_{SF})\right)k_0^2\,S^2(\bar{\theta})\,D_n(\Delta_\infty,\Delta_0)} \\ & - \mathrm{J}_n\left(\Delta_\infty(a_0+\delta_{SF})\right)\Bigg]\frac{\mathrm{H}_{n-l}^{(2)}\left(\Delta_\infty b\right)}{\mathrm{H}_n^{(2)}\left(\Delta_\infty(a_0+\delta_{SF})\right)}\Bigg]. \end{aligned} \tag{E.37}$$

Substituting eq.(E.37) into eq.(E.29)

$$\begin{aligned} I_n \sim & \frac{\mathrm{i}^{n+1}}{\pi\bar{R}\Theta^{1/2}}\pi^2\xi_{lq}P_{lq}\,\mathrm{e}^{-\mathrm{i}(l-n)\beta}k_0\frac{S(\bar{\theta})}{\Theta^{1/2}}\,\Psi_{lq}(\Delta_\infty)\Bigg[\mathrm{J}_{n-l}\left(\Delta_\infty b\right) \\ & + \Bigg[\frac{2\mathrm{i}\,Y_n\left(\Delta_0\right)\Theta}{\pi(a_0+\delta_{SF})\,\mathrm{H}_n^{(2)}\left(\Delta_\infty(a_0+\delta_{SF})\right)k_0^2\,S^2(\bar{\theta})\,D_n(\Delta_\infty,\Delta_0)} \\ & - \mathrm{J}_n\left(\Delta_\infty(a_0+\delta_{SF})\right)\Bigg]\frac{\mathrm{H}_{n-l}^{(2)}\left(\Delta_\infty b\right)}{\mathrm{H}_n^{(2)}\left(\Delta_\infty(a_0+\delta_{SF})\right)}\Bigg]\mathrm{e}^{-\mathrm{i}k_0\bar{R}S(\bar{\theta})}, \end{aligned} \tag{E.38}$$

or

$$I_n \sim \frac{\mathrm{i}^{n+1}\pi\xi_{lq}P_{lq}k_0}{\bar{R}}\frac{S(\bar{\theta})}{\Theta}\,\Psi_{lq}(\Delta_\infty)\mathfrak{D}_n(\bar{\theta})\mathrm{e}^{-\mathrm{i}k_0\bar{R}S(\bar{\theta})}\mathrm{e}^{-\mathrm{i}(l-n)\beta}, \tag{E.39}$$

where

$$\begin{aligned} \mathfrak{D}_n(\bar{\theta}) = & \Bigg[\mathrm{J}_{n-l}\left(\Delta_\infty b\right) \\ & + \Bigg[\frac{2\mathrm{i}\,Y_n\left(\Delta_0\right)\Theta}{\pi(a_0+\delta_{SF})\,\mathrm{H}_n^{(2)}\left(\Delta_\infty(a_0+\delta_{SF})\right)k_0^2\,S^2(\bar{\theta})\,D_n(\Delta_\infty,\Delta_0)} \\ & - \mathrm{J}_n\left(\Delta_\infty(a_0+\delta_{SF})\right)\Bigg]\frac{\mathrm{H}_{n-l}^{(2)}\left(\Delta_\infty b\right)}{\mathrm{H}_n^{(2)}\left(\Delta_\infty(a_0+\delta_{SF})\right)}\Bigg]. \end{aligned} \tag{E.40}$$

And since

$$p'_{t_{ff}}\left(\bar{R},\bar{\phi},\bar{\theta},t\right) = \frac{1}{2\pi}\sum_{n=-\infty}^{\infty} I_n\,\mathrm{e}^{-\mathrm{i}n\bar{\phi}}\,\mathrm{e}^{\mathrm{i}\omega_0 t}, \tag{E.41}$$

then

$$p'_{t_{ff}}(\bar{R},\bar{\phi},\bar{\theta},t) = \frac{1}{2\pi}\sum_{n=-\infty}^{\infty}\frac{\mathrm{i}^{n+1}\pi\xi_{lq}P_{lq}k_0}{\bar{R}}\frac{S(\bar{\theta})}{\Theta}\,\Psi_{lq}(\Delta_\infty)\mathfrak{D}_n(\bar{\theta})\mathrm{e}^{-\mathrm{i}k_0\bar{R}S(\bar{\theta})}\mathrm{e}^{-\mathrm{i}(l-n)\beta}\,\mathrm{e}^{-\mathrm{i}n\bar{\phi}}\,\mathrm{e}^{\mathrm{i}\omega_0 t}, \tag{E.42}$$

which becomes

$$p'_{t_{ff}}(\bar{R},\bar{\phi},\bar{\theta},t) = \frac{\mathrm{i}\xi_{lq}P_{lq}k_0}{2\bar{R}}\frac{S(\bar{\theta})}{\Theta}\,\Psi_{lq}(\Delta_\infty)\,\mathrm{e}^{-\mathrm{i}k_0\bar{R}S(\bar{\theta})}\sum_{n=-\infty}^{\infty}\mathfrak{D}_n(\bar{\theta})\mathrm{i}^n\mathrm{e}^{-\mathrm{i}(l-n)\beta}\,\mathrm{e}^{-\mathrm{i}n\bar{\phi}}\,\mathrm{e}^{\mathrm{i}\omega_0 t}. \tag{E.43}$$

However $\mathrm{i}^n = (\mathrm{e}^{\mathrm{i}\frac{\pi}{2}})^n = \mathrm{e}^{\frac{1}{2}n\pi\mathrm{i}}$, which means that eq.(E.43) can finally be rewritten as

$$p'_{t_{ff}}(\bar{R},\bar{\phi},\bar{\theta},t) = \frac{\mathrm{i}\xi_{lq}P_{lq}k_0}{2\bar{R}}\frac{S(\bar{\theta})}{\Theta}\,\Psi_{lq}(\Delta_\infty)\,\mathrm{e}^{-\mathrm{i}k_0\bar{R}S(\bar{\theta})}\sum_{n=-\infty}^{\infty}\mathfrak{D}_n(\bar{\theta})\mathrm{e}^{\frac{1}{2}n\pi\mathrm{i}}\mathrm{e}^{-\mathrm{i}(l-n)\beta}\mathrm{e}^{-\mathrm{i}n\bar{\phi}}\,\mathrm{e}^{\mathrm{i}\omega_0 t}. \tag{E.44}$$

It is important to note that this expression is exactly the same as the final expression derived using the stationary phase method in appendix D.

Appendix F

Asymptotic Evaluation of the Integral using the Method of Stationary Phase for the Linear Boundary Layer Case

The integral in eq.(3.211) is in a suitable form to be solved using the method of stationery phase following the same procedure as in the case of uniform flow, which was presented in section 3.1.4.1. More specifically, the integral

$$I_n \;=\; \frac{1}{2\pi}\int_{-\infty}^{\infty} \overline{p'_{t_{nff}}}\,(\bar{r},k_z)\,\mathrm{e}^{-\mathrm{i}k_z\bar{z}}\,\mathrm{d}k_z. \tag{F.1}$$

is in the appropriate form to be evaluated by the method of stationary phase as presented in McAlpine and Kingan (2012). Define $I(x)$ such that

$$I(x) \;=\; \int_a^b f(t)\mathrm{e}^{\mathrm{i}x\phi(t)}\mathrm{d}t, \quad \text{as } x\to\infty. \tag{F.2}$$

Then, according to the method of stationery phase, if there is a single point $a \le c \le b$ such that $\phi'(c) = 0$, provided that $\phi''(c) \neq 0$, then

$$I(x) \;\sim\; f(c)\left(\frac{2\pi}{x|\phi''(c)|}\right)^{1/2}\; \mathrm{e}^{\mathrm{i}x\phi(c)\pm\mathrm{i}\pi/4}, \quad \text{as } x\to\infty. \tag{F.3}$$

As is usually the case for far-field analysis, spherical polar coordinates $(\bar{R},\bar{\theta},\bar{\phi})$ are utilized and the integral is solved in the limit as $\bar{R}\to\infty$. First substitute

$$\bar{r} \;=\; \bar{R}\sin\bar{\theta} \quad \text{and} \quad \bar{z} \;=\; \bar{R}\cos\bar{\theta} \tag{F.4}$$

Then the dependence of the function $\overline{p'_{t_{nff}}}(\bar{r}, k_z)$ on $\bar{r}$ is through the Hankel function

$$\mathrm{H}_n^{(2)}(\Gamma_\infty \bar{r}) = \mathrm{H}_n^{(2)}(\Gamma_\infty \bar{R}\sin\bar{\theta}) \sim \sqrt{\frac{2}{\pi\Gamma_\infty \bar{R}\sin\bar{\theta}}}\, \mathrm{e}^{\frac{1}{2}n\pi\mathrm{i}}\, \mathrm{e}^{\frac{1}{4}\pi\mathrm{i}}\, \mathrm{e}^{-\mathrm{i}\Gamma_\infty \bar{R}\sin\bar{\theta}} \quad \text{as} \quad \bar{R}\to\infty. \tag{F.5}$$

Also, $\exp(-\mathrm{i}k_z\bar{z}) \to \exp(-\mathrm{i}k_z\bar{R}\cos\bar{\theta})$ so the integral in eq.(F.1) can be expressed in the form

$$I_n \sim \frac{1}{2\pi}\int_{-\infty}^{\infty} f_n(k_z, \bar{R}, \bar{\theta})\, \mathrm{e}^{-\mathrm{i}\bar{R}(\Gamma_\infty \sin\bar{\theta} + k_z\cos\bar{\theta})}\, \mathrm{d}k_z \quad \text{as} \quad \bar{R}\to\infty, \tag{F.6}$$

where

$$\begin{aligned} f_n(k_z, \bar{R}, \bar{\theta}) = F_n(k_z, \omega_0) \Bigg[& \mathrm{J}_{n-l}(\Gamma_\infty b) \\ & + \mathrm{H}_{n-l}^{(2)}(\Gamma_\infty b) \\ & \times \frac{\left[\mathrm{J}'_n(\Gamma_\infty(a_0+\delta_L)) - \frac{R}{G}\frac{\varepsilon}{\Gamma_\infty a_0}(1+KM_\infty)^2\mathrm{J}_n(\Gamma_\infty(a_0+\delta_L))\right]}{\left[\frac{R}{G}\frac{\varepsilon}{\Gamma_\infty a_0}(1+KM_\infty)^2\mathrm{H}_n^{(2)}(\Gamma_\infty(a_0+\delta_L)) - \mathrm{H}_n^{(2)\prime}(\Gamma_\infty(a_0+\delta_L))\right]} \Bigg] \\ & \times \sqrt{\frac{2}{\pi\Gamma_\infty \bar{R}\sin\bar{\theta}}}\, \mathrm{e}^{\frac{1}{2}n\pi\mathrm{i}}\, \mathrm{e}^{\frac{1}{4}\pi\mathrm{i}}. \end{aligned} \tag{F.7}$$

Introduce the similarity variables following Chapman (2000)

$$(\bar{x}, \bar{y}, \bar{z}) = \left(\hat{R}\sin\hat{\theta}\cos\bar{\phi}, \hat{R}\sin\hat{\theta}\sin\bar{\phi}, \hat{R}\sigma_0\cos\hat{\theta}\right), \tag{F.8}$$

where

$$\sigma_\infty^2 = 1 - M_\infty^2, \tag{F.9}$$

$$\hat{R} = \frac{\bar{R}}{\sigma_\infty}(1 - M_\infty^2\sin^2\bar{\theta})^{1/2} = \frac{\bar{R}}{\sigma_\infty}\Theta^{1/2}, \tag{F.10}$$

$$\cos\hat{\theta} = \frac{\cos\bar{\theta}}{(1 - M_\infty^2\sin^2\bar{\theta})^{1/2}} = \frac{\cos\bar{\theta}}{\Theta^{1/2}}, \tag{F.11}$$

$$\sin\hat{\theta} = \frac{\sigma_\infty\sin\bar{\theta}}{(1 - M_\infty^2\sin^2\bar{\theta})^{1/2}} = \frac{\sigma_\infty\sin\bar{\theta}}{\Theta^{1/2}}, \tag{F.12}$$

And following Rienstra and Hirschberg (2004), introduce the variable τ

$$\tau = \sigma_\infty^2\frac{k_z}{k_0} - M_\infty, \tag{F.13}$$

which means that

$$\Gamma_\infty = \frac{k_0}{\sigma_\infty}(1-\tau^2)^{1/2}, \tag{F.14}$$

$$k_z = \frac{k_0}{\sigma_\infty^2}(\tau + M_\infty), \tag{F.15}$$

$$\mathrm{d}k_z = \frac{k_0}{\sigma_\infty^2}\mathrm{d}\tau. \tag{F.16}$$

The next step is to substitute these variables into the integrand. This process will be presented term by term to facilitate legibility. Firstly, the $F_n(k_z, \omega_0)$ term,

$$F_n(\tau, \omega_0) = \pi^2 \xi_{lq} P_{lq}\, k_0 \Big(1 + \frac{(\tau + M_\infty) M_\infty}{\sigma_\infty^2}\Big)\, \Psi_{lq}\, \mathrm{e}^{-\mathrm{i}(l-n)\beta}. \tag{F.17}$$

Then

$$K(\tau) = \frac{\tau + M_\infty}{\sigma_\infty^2}, \tag{F.18}$$

$$\mu(\tau) = \nu \Big(\frac{\tau + M_\infty}{\sigma_\infty^2}\Big)^2 + n^2, \tag{F.19}$$

$$s(\tau) = \frac{(\tau + M_\infty)}{\sigma_\infty^2}(M_\infty - M_w), \tag{F.20}$$

and

$$g(\tau) = \Big(\frac{(\tau + M_\infty)}{\sigma_\infty^2}\Big)^2 (M_\infty - M_w)\Big(\frac{\sigma_\infty^2}{\tau + M_\infty} + M_w\Big). \tag{F.21}$$

Now the large bracketed terms. Firstly, the R term,

$$\begin{aligned} R(\tau) = &\Bigg\{ \mu(\tau)\Big(\frac{1}{g(\tau)} - \frac{1}{(s^2(\tau) + g(\tau))}\Big) - \nu \\ &- \varepsilon \Bigg[\frac{(2n^2 - \mu(\tau))}{s^2(\tau)} \ln\Big(\frac{s^2(\tau)}{g(\tau)} + 1\Big) - \frac{2n^2}{s^2(\tau) + g(\tau)} + \frac{\mu(\tau)}{g(\tau)} - \frac{\nu}{2} \Bigg] \Bigg\}, \end{aligned} \tag{F.22}$$

which finally becomes

$$\begin{aligned} R(\tau) = &\Bigg\{ \nu \Bigg[\frac{1}{\Big[\frac{\sigma_\infty^2}{\tau + M_\infty} + M_w\Big]\Big[M_\infty + \frac{\sigma_\infty^2}{(\tau + M_\infty)}\Big]} - 1 \Bigg] \\ &+ \frac{n^2}{\Big[1 + \frac{(\tau + M_\infty)}{\sigma_\infty^2} M_w\Big]\Big[\frac{(\tau + M_\infty)}{\sigma_\infty^2} M_\infty + 1\Big]} \\ &- \varepsilon \Bigg[\frac{n^2}{\Big(\frac{(\tau + M_\infty)}{\sigma_\infty^2}\Big)^2 (M_\infty - M_w)} \Big[\frac{1}{\Big[\frac{\sigma_\infty^2}{\tau + M_\infty} + M_w\Big]} - \frac{2}{\Big[M_\infty + \frac{\sigma_\infty^2}{(\tau + M_\infty)}\Big]} \\ &+ \frac{1}{(M_\infty - M_w)} \ln\Big(\frac{\Big(\frac{\sigma_0^2}{\tau + M_\infty} + M_\infty\Big)}{\Big(\frac{\sigma_\infty^2}{\tau + M_\infty} + M_w\Big)} \Big) \Big] \\ &+ \frac{\nu}{(M_\infty - M_w)} \Big[\frac{1}{\Big(\frac{\sigma_\infty^2}{\tau + M_\infty} + M_w\Big)} - \frac{(M_\infty - M_w)}{2} - \frac{1}{(M_\infty - M_w)} \ln\Big(\frac{\Big(\frac{\sigma_\infty^2}{\tau + M_\infty} + M_\infty\Big)}{\Big(\frac{\sigma_\infty^2}{\tau + M_\infty} + M_w\Big)} \Big) \Big] \Bigg] \Bigg\}. \end{aligned} \tag{F.23}$$

Similarly, the other bracketed term

$$G(\tau) = \Bigg\{ 1 + \varepsilon^2 \Bigg[\mu(\tau)\Big(\frac{s^2(\tau)}{3g(\tau)} + \frac{1}{2}\Big) - \nu\Big(\frac{s^2(\tau)}{4} + \frac{2}{3} g(\tau) + \frac{1}{2}\frac{g^2(\tau)}{s^2(\tau)}\Big) \Bigg] \Bigg\}, \tag{F.24}$$

which eventually becomes

$$G(\tau) = \Bigg\{1 + \varepsilon^2 \Bigg[n^2 \Big[\frac{M_\infty - M_w}{3\Big(\frac{\sigma_\infty^2}{\tau + M_\infty} + M_w\Big)} + \frac{1}{2} \Big] + \nu \Big(\frac{\tau + M_\infty}{\sigma_\infty^2} \Big)^2 \Big[\frac{M_\infty - M_w}{3\Big(\frac{\sigma_\infty^2}{\tau + M_\infty} + M_w\Big)} + \frac{1}{2} - \frac{(M_\infty - M_w)^2}{4} - \frac{2}{3}(M_\infty - M_w)\Big(\frac{\sigma_\infty^2}{\tau + M_\infty} + M_w\Big) - \frac{1}{2}\Big(\frac{\sigma_\infty^2}{\tau + M_\infty} + M_w\Big)^2 \Big] \Bigg] \Bigg\}. \tag{F.25}$$

Also, another term that needs evaluating is

$$\frac{\varepsilon}{\Gamma_\infty(\tau) a_0}(1 + K(\tau) M_\infty)^2 = \frac{\varepsilon}{\frac{k_0}{\sigma_\infty}(1 - \tau^2)^{1/2} a_0} \Big(\frac{\tau + M_\infty}{\sigma_\infty^2} \Big)^2 \Big(\frac{\sigma_\infty^2}{\tau + M_\infty} + M_\infty \Big)^2. \tag{F.26}$$

By introducing these similarity variables and taking into account that

$$\bar{R} \sin \bar{\theta} = \hat{R} \frac{\sigma_\infty}{(1 - M_\infty^2 \sin^2 \bar{\theta})^{1/2}} \sin \hat{\theta} \frac{(1 - M_\infty^2 \sin^2 \bar{\theta})^{1/2}}{\sigma_\infty} = \hat{R} \sin \hat{\theta}, \tag{F.27}$$

and

$$\bar{R} \cos \bar{\theta} = \hat{R} \frac{\sigma_\infty}{(1 - M_\infty^2 \sin^2 \bar{\theta})^{1/2}} \cos \hat{\theta} \, (1 - M_\infty^2 \sin^2 \bar{\theta})^{1/2} = \hat{R} \sigma_\infty \cos \hat{\theta}, \tag{F.28}$$

the integral can be rewritten

$$I_n \sim \frac{1}{2\pi} \int_{-\infty}^{\infty} g_n(\tau, \hat{R}, \hat{\theta}) \, \mathrm{e}^{\mathrm{i} \hat{R} \hat{\phi}(\tau)} \, \mathrm{d}\tau \tag{F.29}$$

where

$$\begin{aligned} g_n(\tau, \hat{R}, \hat{\theta}) = & \frac{k_0}{\sigma_\infty^2} F_n(\tau, \omega_0) \Bigg[\mathrm{J}_{n-l}(\Gamma_\infty(\tau) b) \\ & + \mathrm{H}_{n-l}^{(2)}(\Gamma_\infty(\tau) b) \\ & \times \frac{\Big[\mathrm{J}_n'(\Gamma_0(\tau)(a_0 + \delta_L)) - \frac{R(\tau)}{G(\tau)} \frac{\varepsilon}{\frac{k_0}{\sigma_\infty}(1-\tau^2)^{1/2} a_0} \Big(\frac{\tau + M_\infty}{\sigma_\infty^2} \Big)^2 \Big(\frac{\sigma_\infty^2}{\tau + M_\infty} + M_\infty \Big)^2 \mathrm{J}_n(\Gamma_\infty(\tau)(a_0 + \delta_L)) \Big]}{\Big[\frac{R(\tau)}{G(\tau)} \frac{\varepsilon}{\frac{k_0}{\sigma_\infty}(1-\tau^2)^{1/2} a_0} \Big(\frac{\tau + M_\infty}{\sigma_\infty^2} \Big)^2 \Big(\frac{\sigma_\infty^2}{\tau + M_\infty} + M_\infty \Big)^2 \mathrm{H}_n^{(2)}(\Gamma_\infty(\tau)(a_0 + \delta_L)) - \mathrm{H}_n^{(2)\prime}(\Gamma_\infty(\tau)(a_0 + \delta_L)) \Big]} \Bigg] \\ & \times \sqrt{\frac{2}{\pi \frac{k_0}{\sigma_\infty}(1 - \tau^2)^{1/2} \hat{R} \sin \hat{\theta}}} \, \mathrm{e}^{\frac{1}{2} n \pi \mathrm{i}} \, \mathrm{e}^{\frac{1}{4} \pi \mathrm{i}}, \end{aligned} \tag{F.30}$$

and

$$\hat{\phi}(\tau) = -\frac{k_0}{\sigma_\infty}(1 - \tau^2)^{1/2} \sin \hat{\theta} - \frac{k_0}{\sigma_\infty}(\tau + M_\infty) \cos \hat{\theta}. \tag{F.31}$$

The limits of the integral can be replaced by $(-1, 1)$ since the integrand will be exponentially small in the region $|\tau| > 1$ as $\bar{R} \to \infty$, as explained in appendix D.

After this change of variables, the point where $\hat{\phi}'(c) = 0$ can easily be found by using eq.(F.31),

$$\hat{\phi}'(c) = 0 \Rightarrow \frac{k_0}{\sigma_\infty}(1 - c^2)^{-1/2} c \sin \hat{\theta} - \frac{k_0}{\sigma_\infty} \cos \hat{\theta} = 0 \Rightarrow c = \cos \hat{\theta}. \tag{F.32}$$

The quantity $\hat{\phi}''(c)$ is also required and can easily be evaluated,

$$\begin{aligned}\hat{\phi}''(\tau) &= \frac{k_0}{\sigma_\infty}(1-\tau^2)^{-3/2}\tau^2\sin\hat{\theta} + \frac{k_0}{\sigma_\infty}(1-\tau^2)^{-1/2}\sin\hat{\theta} \rightarrow \\ \hat{\phi}''(c) &= \frac{k_0}{\sigma_\infty}\sin^{-3}\hat{\theta}\cos^2\hat{\theta}\sin\hat{\theta} + \frac{k_0}{\sigma_\infty} = \frac{k_0}{\sigma_\infty}\left(\frac{\cos^2\hat{\theta}}{\sin^2\hat{\theta}}+1\right) = \frac{k_0}{\sigma_\infty\sin^2\hat{\theta}}.\end{aligned} \tag{F.33}$$

With all these quantities known, the integral from eq.(F.29) can be replaced using eq.(F.3),

$$I_n \sim \frac{1}{2\pi}g_n(c)\left(\frac{2\pi}{\hat{R}|\hat{\phi}''(c)|}\right)^{1/2} \mathrm{e}^{\mathrm{i}\hat{R}\hat{\phi}(c)+\mathrm{i}\pi/4}, \quad \text{as } \hat{R}\rightarrow\infty \tag{F.34}$$

or

$$\begin{aligned}I_n = \frac{1}{2\pi}\frac{k_0}{\sigma_\infty^2}F_n(c,\omega_0)\Bigg[&\mathrm{J}_{n-l}(\Gamma_\infty(c)b) \\ &+ \mathrm{H}^{(2)}_{n-l}(\Gamma_\infty(c)b) \\ &\times \frac{\left[\mathrm{J}'_n(\Gamma_\infty(c)(a_0+\delta_L)) - \frac{R(c)}{G(c)}\frac{\varepsilon}{\frac{k_0}{\sigma_\infty}\sin\hat{\theta}\,a_0}\left(\frac{c+M_\infty}{\sigma_\infty^2}\right)^2\left(\frac{\sigma_\infty^2}{c+M_\infty}+M_\infty\right)^2\mathrm{J}_n(\Gamma_\infty(c)(a_0+\delta_L))\right]}{\left[\frac{R(c)}{G(c)}\frac{\varepsilon}{\frac{k_0}{\sigma_\infty}\sin\hat{\theta}\,a_0}\left(\frac{c+M_\infty}{\sigma_\infty^2}\right)^2\left(\frac{\sigma_\infty^2}{c+M_\infty}+M_\infty\right)^2\mathrm{H}^{(2)}_n(\Gamma_\infty(c)(a_0+\delta_L)) - \mathrm{H}^{(2)\prime}_n(\Gamma_\infty(c)(a_0+\delta_L))\right]}\Bigg] \\ &\times \sqrt{\frac{2}{\pi\frac{k_0}{\sigma_\infty}\sin^2\hat{\theta}\,\hat{R}}}\,\mathrm{e}^{\frac{1}{2}n\pi\mathrm{i}}\,\mathrm{e}^{\frac{1}{4}\pi\mathrm{i}}\sqrt{\frac{2\pi}{\hat{R}\frac{k_0}{\sigma_\infty\sin^2\hat{\theta}}}} \\ &\times \mathrm{e}^{\mathrm{i}\hat{R}\left(-\frac{k_0}{\sigma_\infty}\sin^2\hat{\theta}-\frac{k_0}{\sigma_\infty}\cos^2\hat{\theta}-\frac{k_0}{\sigma_\infty}M_\infty\cos\hat{\theta}\right)}\mathrm{e}^{\mathrm{i}\pi/4}.\end{aligned} \tag{F.35}$$

Bearing in mind that,

$$\Gamma_0(c) = \frac{k_0}{\sigma_\infty}\sin\hat{\theta}, \tag{F.36}$$

also

$$\mathrm{e}^{\mathrm{i}\pi/4}\mathrm{e}^{\frac{1}{4}\pi\mathrm{i}} = \mathrm{e}^{\frac{1}{2}\pi\mathrm{i}} = \cos\frac{\pi}{2} + \mathrm{i}\sin\frac{\pi}{2} = \mathrm{i}, \tag{F.37}$$

$$F_n(c,\omega_0) = \pi^2\xi_{lq}P_{lq}\,k_0\left(\frac{1+M_\infty\cos\hat{\theta}}{\sigma_\infty^2}\right)\Psi_{lq}(\Gamma_\infty(c)\mathrm{e}^{-\mathrm{i}(l-n)\beta}. \tag{F.38}$$

Also, for the sake of brevity the large bracketed term is replaced with

$$\begin{aligned}\mathfrak{L}(c) = \Bigg[&\mathrm{J}_{n-l}(\Gamma_\infty(c)b) \\ &+ \mathrm{H}^{(2)}_{n-l}(\Gamma_\infty(c)b) \\ &\times \frac{\left[\mathrm{J}'_n(\Gamma_\infty(c)(a_0+\delta_L)) - \frac{R(c)}{G(c)}\frac{\varepsilon}{\frac{k_0}{\sigma_\infty}\sin\hat{\theta}\,a_0}\left(\frac{c+M_\infty}{\sigma_\infty^2}\right)^2\left(\frac{\sigma_\infty^2}{c+M_\infty}+M_\infty\right)^2\mathrm{J}_n(\Gamma_\infty(c)(a_0+\delta_L))\right]}{\left[\frac{R(c)}{G(c)}\frac{\varepsilon}{\frac{k_0}{\sigma_\infty}\sin\hat{\theta}\,a_0}\left(\frac{c+M_\infty}{\sigma_\infty^2}\right)^2\left(\frac{\sigma_\infty^2}{c+M_\infty}+M_\infty\right)^2\mathrm{H}^{(2)}_n(\Gamma_\infty(c)(a_0+\delta_L)) - \mathrm{H}^{(2)\prime}_n(\Gamma_\infty(c)(a_0+\delta_L))\right]}\Bigg].\end{aligned} \tag{F.39}$$

So eq.(F.35) becomes

$$I_n = \frac{\mathrm{i}F_n\,(c,\omega_0)}{\pi\sigma_\infty\hat{R}}\mathfrak{L}(c)\mathrm{e}^{-\mathrm{i}\hat{R}\frac{k_0}{\sigma_\infty}(1+M_\infty\cos\hat{\theta})}\mathrm{e}^{\frac{1}{2}n\pi\mathrm{i}}. \tag{F.40}$$

Going back now to the original coordinates,

$$\Delta_\infty \;=\; \Gamma_\infty(c) = \;\frac{k_0}{\sigma_\infty}\sin\hat{\theta} = \frac{k_0\sin\bar{\theta}}{\Theta^{1/2}}. \tag{F.41}$$

Also,

$$\frac{\mathrm{i}F_n\,(c,\omega_0)}{\pi\sigma_\infty\hat{R}} = \frac{\mathrm{i}\pi\xi_{lq}P_{lq}k_0\mathrm{e}^{-\mathrm{i}(l-n)\beta}}{\bar{R}}\frac{\left(\Theta^{1/2}+M_\infty\cos\bar{\theta}\right)}{\sigma_\infty^2\Theta}\,\Psi_{lq}(\Delta_\infty) \tag{F.42}$$

and with

$$S(\bar{\theta}) = \frac{\left(\Theta^{1/2}+M_\infty\cos\bar{\theta}\right)}{\sigma_\infty^2}, \tag{F.43}$$

eq.(F.42) becomes

$$\frac{\mathrm{i}F_n\,(c,\omega_0)}{\pi\sigma_\infty\hat{R}} = \frac{\mathrm{i}\pi\xi_{lq}P_{lq}k_0\mathrm{e}^{-\mathrm{i}(l-n)\beta}}{\bar{R}}\frac{S(\bar{\theta})}{\Theta}\,\Psi_{lq}(\Delta_\infty). \tag{F.44}$$

The exponent term will become

$$\mathrm{e}^{-\mathrm{i}\hat{R}\frac{k_0}{\sigma_\infty}(1+M_\infty\cos\hat{\theta})} = \mathrm{e}^{-\mathrm{i}\frac{\bar{R}}{\sigma_\infty}\Theta^{1/2}\frac{k_0}{\sigma_\infty}(1+M_\infty\frac{\cos\bar{\theta}}{\Theta^{1/2}})} = \mathrm{e}^{-\mathrm{i}\bar{R}k_0(\frac{\Theta^{1/2}+M_\infty\cos\bar{\theta}}{\sigma_\infty^2})} = \mathrm{e}^{-\mathrm{i}k_0\bar{R}S(\bar{\theta})}. \tag{F.45}$$

Finally the bracketed term must be evaluated. Firstly, the terms inside the bracket are considered. The R term

$$\begin{aligned}
R(c) =& \Bigg\{\nu\left[\frac{1}{\left[\frac{\sigma_\infty^2}{c+M_\infty}+M_w\right]\left[M_\infty+\frac{\sigma_\infty^2}{(c+M_\infty)}\right]}-1\right] \\
&+\frac{n^2}{\left[1+\frac{(c+M_\infty)}{\sigma_\infty^2}M_w\right]\left[\frac{(c+M_\infty)}{\sigma_\infty^2}M_\infty+1\right]} \\
&-\varepsilon\Bigg[\frac{n^2}{\left(\frac{(c+M_\infty)}{\sigma_\infty^2}\right)^2(M_\infty-M_w)}\Big[\frac{1}{\left[\frac{\sigma_\infty^2}{c+M_\infty}+M_w\right]}-\frac{2}{\left[M_\infty+\frac{\sigma_\infty^2}{(c+M_\infty)}\right]} \\
&+\frac{1}{(M_\infty-M_w)}\ln\left(\frac{\left(\frac{\sigma_\infty^2}{c+M_\infty}+M_\infty\right)}{\left(\frac{\sigma_\infty^2}{c+M_\infty}+M_w\right)}\right)\Big] \\
&+\frac{\nu}{(M_\infty-M_w)}\Big[\frac{1}{\left(\frac{\sigma_\infty^2}{c+M_\infty}+M_w\right)}-\frac{(M_\infty-M_w)}{2}-\frac{1}{(M_\infty-M_w)}\ln\left(\frac{\left(\frac{\sigma_\infty^2}{c+M_\infty}+M_\infty\right)}{\left(\frac{\sigma_\infty^2}{c+M_\infty}+M_w\right)}\right)\Big]\Bigg]\Bigg\}.
\end{aligned} \tag{F.46}$$

The most common term involving c will become

$$\frac{\sigma_\infty^2}{c+M_\infty} = \frac{\sigma_\infty^2}{\cos\hat{\theta}+M_\infty} = \frac{\sigma_\infty^2}{\frac{\cos\bar{\theta}}{\Theta^{1/2}}+M_\infty} = \frac{\sigma_\infty^2\Theta^{1/2}}{\cos\bar{\theta}+M_\infty\Theta^{1/2}}, \tag{F.47}$$

and by setting

$$C(\bar{\theta}) = \frac{\left(\cos\bar{\theta}+M_\infty\Theta^{1/2}\right)}{\sigma_\infty^2}, \tag{F.48}$$

the common term will become

$$\frac{\sigma_\infty^2}{c+M_\infty} = \frac{\Theta^{1/2}}{C(\bar{\theta})}. \tag{F.49}$$

This means that the logarithm's argument will be

$$\frac{\left(\frac{\sigma_\infty^2}{c+M_\infty}+M_\infty\right)}{\left(\frac{\sigma_\infty^2}{c+M_\infty}+M_w\right)} = \frac{\frac{\Theta^{1/2}}{C(\bar{\theta})}+M_\infty}{\frac{\Theta^{1/2}}{C(\bar{\theta})}+M_w} = \frac{\Theta^{1/2}+M_\infty C(\bar{\theta})}{\Theta^{1/2}+M_w C(\bar{\theta})}. \tag{F.50}$$

With these terms known, the $R(c)$ term will become

$$\begin{aligned} R(\bar{\theta}) = &\left\{ \frac{\nu C^2(\bar{\theta})+n^2\Theta}{\left(\Theta^{1/2}+M_w C(\bar{\theta})\right)\left(\Theta^{1/2}+M_\infty C(\bar{\theta})\right)} - \nu \right. \\ &- \varepsilon\left[\frac{n^2\Theta}{C^2(\bar{\theta})(M_\infty-M_w)}\left[C(\bar{\theta})\left(\frac{C(\bar{\theta})(M_\infty-2M_w)-\Theta^{1/2}}{\left(\Theta^{1/2}+M_w C(\bar{\theta})\right)\left(\Theta^{1/2}+M_\infty C(\bar{\theta})\right)}\right)\right. \\ &\left.+\frac{1}{(M_\infty-M_w)}\ln\left(\frac{\Theta^{1/2}+M_\infty C(\bar{\theta})}{\Theta^{1/2}+M_w C(\bar{\theta})}\right)\right] \\ &\left.+\frac{\nu}{(M_\infty-M_w)}\left[\frac{C(\bar{\theta})}{\left(\Theta^{1/2}+M_w C(\bar{\theta})\right)}-\frac{(M_\infty-M_w)}{2}-\frac{1}{(M_\infty-M_w)}\ln\left(\frac{\Theta^{1/2}+M_\infty C(\bar{\theta})}{\Theta^{1/2}+M_w C(\bar{\theta})}\right)\right]\right\}. \end{aligned} \tag{F.51}$$

As for the $G(c)$ term,

$$\begin{aligned} G(c) = &\left\{1+\varepsilon^2\left[n^2\left[\frac{M_\infty-M_w}{3\left(\frac{\sigma_\infty^2}{c+M_\infty}+M_w\right)}+\frac{1}{2}\right]+\nu\left(\frac{c+M_\infty}{\sigma_\infty^2}\right)^2\left[\frac{M_\infty-M_w}{3\left(\frac{\sigma_\infty^2}{c+M_\infty}+M_w\right)}+\frac{1}{2}\right.\right. \\ &\left.\left.-\frac{(M_\infty-M_w)^2}{4}-\frac{2}{3}(M_\infty-M_w)\left(\frac{\sigma_\infty^2}{c+M_\infty}+M_w\right)-\frac{1}{2}\left(\frac{\sigma_\infty^2}{c+M_\infty}+M_w\right)^2\right]\right]\right\}, \end{aligned} \tag{F.52}$$

or

$$\begin{aligned} G(\bar{\theta}) = &\left\{1+\varepsilon^2\left[\left(n^2+\nu\frac{C^2(\bar{\theta})}{\Theta}\right)\left[\frac{C(\bar{\theta})(2M_\infty+M_w)+3\Theta^{1/2}}{6\left(\Theta^{1/2}+M_w C(\bar{\theta})\right)}\right]\right.\right. \\ &\left.\left.-\frac{\nu}{\Theta}\left[\frac{C^2(\bar{\theta})(M_\infty-M_w)^2}{4}+\left(\Theta^{1/2}+M_w C(\bar{\theta})\right)\left(C(\bar{\theta})(\frac{2}{3}M_\infty-\frac{1}{6}M_w)+\frac{1}{2}\Theta^{1/2}\right)\right]\right]\right\}. \end{aligned} \tag{F.53}$$

Finally the last term inside the bracket $\mathfrak{L}$ that needs evaluating

$$\begin{aligned} &\frac{\varepsilon}{\frac{k_0}{\sigma_\infty}\sin\hat{\theta}\,a_0}\left(\frac{c+M_\infty}{\sigma_\infty^2}\right)^2\left(\frac{\sigma_\infty^2}{c+M_\infty}+M_\infty\right)^2 = \frac{\varepsilon}{\frac{k_0}{\sigma_\infty}\frac{\sigma_\infty\sin\bar{\theta}}{\Theta^{1/2}}a_0}\frac{C^2(\bar{\theta})}{\Theta}\frac{(\Theta^{1/2}+M_\infty C(\bar{\theta}))^2}{C^2(\bar{\theta})} \\ &= \frac{\varepsilon(\Theta^{1/2}+M_\infty C(\bar{\theta}))^2}{k_0 a_0\sin\bar{\theta}\Theta^{1/2}}. \end{aligned} \tag{F.54}$$

So, finally substituting all those terms into eq.(F.40),

$$I_n = \frac{\mathrm{i}\pi\xi_{lq}P_{lq}k_0\mathrm{e}^{-\mathrm{i}(l-n)\beta}}{\bar{R}}\frac{S(\bar{\theta})}{\Theta}\,\Psi_{lq}(\Delta_\infty)\mathfrak{L}(\bar{\theta})\mathrm{e}^{-\mathrm{i}k_0\bar{R}S(\bar{\theta})}\mathrm{e}^{\frac{1}{2}n\pi\mathrm{i}}, \tag{F.55}$$

where

$$\begin{aligned}\mathfrak{L}(\bar{\theta}) = \Bigg[&\mathrm{J}_{n-l}\left(\Delta_\infty b\right)\\ &+\mathrm{H}^{(2)}_{n-l}\left(\Delta_\infty b\right)\\ &\times\frac{\left[\mathrm{J}'_n\left(\Delta_\infty(a_0+\delta_L)\right)-\frac{R(\bar{\theta})}{G(\bar{\theta})}\frac{\varepsilon(\Theta^{1/2}+M_\infty C(\bar{\theta}))^2}{k_0a_0\sin\bar{\theta}\Theta^{1/2}}\mathrm{J}_n\left(\Delta_\infty(a_0+\delta_L)\right)\right]}{\left[\frac{R(\bar{\theta})}{G(\bar{\theta})}\frac{\varepsilon(\Theta^{1/2}+M_\infty C(\bar{\theta}))^2}{k_0a_0\sin\bar{\theta}\Theta^{1/2}}\mathrm{H}^{(2)}_n\left(\Delta_\infty(a_0+\delta_L)\right)-\mathrm{H}^{(2)\prime}_n\left(\Delta_\infty(a_0+\delta_L)\right)\right]}\Bigg],\end{aligned} \tag{F.56}$$

with $R(\bar{\theta})$ and $G(\bar{\theta})$ given in eqs. (F.51) and (F.53).

Finally, the far-field pressure in real space is given by eq.(3.211)

$$p'_{t_{ff}}\left(\bar{r},\bar{\phi},\bar{z},t\right) = \frac{1}{(2\pi)^2}\sum_{n=-\infty}^{\infty}\int_{-\infty}^{\infty}\overline{p'_{t_{nff}}}\left(\bar{r},k_z\right)\mathrm{e}^{-\mathrm{i}k_z\bar{z}}\,\mathrm{d}k_z\,\mathrm{e}^{-\mathrm{i}n\bar{\phi}}\,\mathrm{e}^{\mathrm{i}\omega_0 t}, \tag{F.57}$$

or

$$p'_{t_{ff}}\left(\bar{r},\bar{\phi},\bar{z},t\right) = \frac{1}{(2\pi)}\sum_{n=-\infty}^{\infty}\frac{1}{(2\pi)}\int_{-\infty}^{\infty}\overline{p'_{t_{nff}}}\left(\bar{r},k_z\right)\mathrm{e}^{-\mathrm{i}k_z\bar{z}}\,\mathrm{d}k_z\,\mathrm{e}^{-\mathrm{i}n\bar{\phi}}\,\mathrm{e}^{\mathrm{i}\omega_0 t}, \tag{F.58}$$

or from eq.(F.1)

$$p'_{t_{ff}}\left(\bar{r},\bar{\phi},\bar{z},t\right) = \frac{1}{(2\pi)}\sum_{n=-\infty}^{\infty}I_n\,\mathrm{e}^{-\mathrm{i}n\bar{\phi}}\,\mathrm{e}^{\mathrm{i}\omega_0 t}, \tag{F.59}$$

and inserting eq.(F.55)

$$p'_{t_{ff}}\left(\bar{r},\bar{\phi},\bar{z},t\right) = \frac{\mathrm{i}\xi_{lq}P_{lq}k_0}{2\bar{R}}\frac{S(\bar{\theta})}{\Theta}\Psi_{lq}(\Delta_\infty)\mathrm{e}^{-\mathrm{i}k_0\bar{R}S(\bar{\theta})}\mathrm{e}^{\mathrm{i}\omega_0 t}\sum_{n=-\infty}^{\infty}\mathfrak{L}(\bar{\theta})\mathrm{e}^{-\mathrm{i}(l-n)\beta}\mathrm{e}^{\frac{1}{2}n\pi\mathrm{i}}\mathrm{e}^{-\mathrm{i}n\bar{\phi}}. \tag{F.60}$$

Equation (F.60) is the essential conclusion of this section. It describes the acoustic pressure in the far-field around the fuselage using spherical polar coordinates centered on the cylindrical fuselage.

Bibliography

M. Abramowitz and I. Stegun. *Handbook of Mathematical Functions*. Dover Publications, Inc., New York, 1965.

ACARE. European aeronautics: A vision for 2020, 2001.

I. Achunche, J. Astley, R. Sugimoto, and A. Kempton. Prediction of forward fan noise propagation and radiation from intakes. *Proceedings of the 15th AIAA/CEAS Aeroacoustics Conference*, number AIAA 2009-3239, 2009.

A. Agarwal, A.P. Dowling, H.-C. Shin, and W. Graham. Ray-tracing approach to calculate acoustic shielding by a flying wing airframe. *AIAA Journal*, 45(5):1080–1090, 2007.

Airbus. Airbus global market forecast 2018-2037, 2019.

R.K. Amiet. Refraction of sound by a shear layer. *Journal of Sound and Vibration*, 58(4):467–482, 1978.

R.J. Astley. Can technology deliver acceptable levels of aircraft noise? *Proceedings of Internoise Conference Melbourne, Australia*, pages 369–382, 2014.

N. Atalla and S.A.L. Glegg. Ray-acoustics approach to fuselage scattering of rotor noise. *American Helicopter Society, 47th Annual Forum Proceedings*, pages 841–853, 1991.

I.V. Belyaev. The effect of an aircraft's boundary layer on propeller noise. *Acoustical Physics*, 58 (4):387–395, 2012.

Boeing. Commercial market outlook 2018-2037, 2019.

J.J. Bowman, T.B.A. Senior, and P.L.E. Uslenghi. *Electromagnetic and Acoustic Scattering by Simple Shapes*. North-Holland Publishing Co., 1969.

E.J. Brambley, M.Darau, and S.W. Rienstra. The critical layer in sheared flow. *Proceedings of the 17th AIAA/CEAS Aeroacoustics Conference*, number AIAA 2011-2806, 2011.

E.J. Brambley, M.Darau, and S.W. Rienstra. The critical layer in linear-shear boundary layers over acoustic linings. *Journal of Fluid Mechanics*, 710:545–568, 2012.

H.H. Brouwer. The scattering of open rotor tones by a cylindrical fuselage and its boundary layer. *Proceedings of the 22nd AIAA/CEAS Aeroacoustics Conference*, number AIAA 2016-2741, 2016.

D. Burd and W. Eversman. Inlet acoustic treatment for interior noise control. *Proceedings of the 13th AIAA/CEAS Aeroacoustics Conference*, number AIAA 2007-3526, 2007.

O. Bychkov and G. Faranosov. An experimental study and theoretical simulation of jet-wing interaction noise. *Acoustical Physics*, 64(4):437–453, 2018.

O. Bychkov, G. Faranosov, S. Denisov, and N. Ostrikov. Theoretical modeling of the excess noise due to jet-wing interaction. *Proceedings of the 22nd AIAA/CEAS Aeroacoustics Conference*, number AIAA 2016-2932, 2016.

L.M.B.C. Campos. On the singularities and solutions of the extended hypergeometric equation. *Integral Transforms and Special Functions*, 9(2):99–120, 2000.

L.M.B.C. Campos and M.H. Kobayashi. On the reflection and transmission of sound in a thick shear layer. *Journal of Fluid Mechanics*, 424:303–326, 2000.

L.M.B.C. Campos and M.H. Kobayashi. On the propagation of sound in a high-speed non-isothermal shear flow. *International Journal of Aeroacoustics*, 8(3):199–230, 2009.

L.M.B.C. Campos and M.H. Kobayashi. Sound transmission from a source outside a nonisothermal boundary layer. *AIAA Journal*, 48(5):878–892, 2010.

L.M.B.C. Campos and P.G.T.A. Serrao. On the acoustics of an exponential boundary layer. *Philosophical Transactions of the Royal Society of London, Series A: Mathematical and Physical Sciences*, 356(1746):2335–2379, 1998.

L.M.B.C. Campos, J.M.G.S. Oliveira, and M.H. Kobayashi. On sound propagation in a linear shear flow. *Journal of Sound and Vibration*, 219(5):739–770, 1999.

S.M. Candel, A. Guedel, and A. Julienne. Refraction and scattering of sound in an open wind tunnel flow. *Proceedings of the 6th International Congress on Instrumentation in Aerospace Simulation Facilities*, pages 288–299, 1975.

S.M. Candel, A. Julienne, and M. Julliand. Shielding and scattering by a jet flow. *Proceedings of the 3rd AIAA Aero-acoustics Conference*, number AIAA 76-545, 1976.

C.J. Chapman. Similarity variables for sound radiation in a uniform flow. *Journal of Sound and Vibration*, 233(2):157–164, 2000.

European Commission. Flightpath 2050-europe's vision for aviation, 2011.

J. Dierke, R. Ewert, J. Delfs, C. Stohr, and M. Rose. The effect of a boundary layer on engine noise propagating to the fuselage at flight conditions. *Proceedings of the 19th AIAA/CEAS Aeroacoustics Conference*, number AIAA 2013-2006, 2013.

J.H. Dittmar and D.G. Hall. The effect of swirl recovery vanes on the cruise noise of an advanced propeller. *Proceedings of the 13th AIAA Aeroacoustics Conference*, number AIAA 90-3932, 1990.

W. Eversman. Effect of boundary layer on the transmission and attenuation of sound in an acoustically treated circular duct. *Journal of the Acoustical Society of America*, 49(5):1372–1380, 1970.

W. Eversman. Approximation for thin boundary layers in the sheared flow duct transmission problem. *Journal of the Acoustical Society of America*, 53(5):1346–1350, 1972.

W. Eversman and R.J. Beckemeyer. Transmission of sound in ducts with thin shear layers-convergence to the uniform flow case. *Journal of the Acoustical Society of America*, 52(1): 216–220, 1972.

R. Ewert, O. Konrow, J.W. Delfs, J. Yin, T. Rober, and M. Rose. A caa approach to tone haystacking. *Proceedings of the 15th AIAA/CEAS Aeroacoustics Conference*, number AIAA 2009-3217, 2009.

L.B. Felsen and N. Marcuvitz. *Radiation and Scattering of Waves*. IEEE Press, New York, 1994.

C.R. Fuller. Free-field correction factor for spherical acoustic waves impinging on cylinders. *American Institute of Aeronautics and Astronautics Journal*, 27(12):1722–1726, 1989.

G. Gabard. Near- to far-field characteristics of acoustic radiation through plug flow jets. *Journal of the Acoustical Society of America*, 124(5):2755–42766, 2008.

J. Gaffney. *Theoretical Methods to Predict Near-field Fuselage Installation Effects due to Inlet Fan Tones*. Ph.D. thesis, University of Southampton, 2016.

J. Gaffney and A. McAlpine. Fuselage boundary-layer refraction of fan tones radiated from an installed turbofan aero-engine. *Journal of Acoustical Society of America*, 141(3):1653–1663, 2017.

J. Gaffney and A. McAlpine. A theoretical model of fuselage pressure levels due to fan tones radiated from the intake of an installed turbofan aero-engine. *Journal of Acoustical Society of America*, 143(6):3394–3405, 2018.

S. Glegg and W. Devenport. *Aeroacoustics of Low Mach Number Flows*. Academic Press, 2017.

M. Goldstein and E. Rice. Effect of shear on duct wall impedance. *Journal of Sound and Vibration*, 30(1):79–84, 1973.

I.S. Gradshteyn and I.M. Ryzhik. *Table of Integrals, Series and Products*. Academic Press, 7th Edition, 2007.

D.B. Hanson. Shielding of prop-fan noise by the fuselage boundary layer. *Journal of Sound and Vibration*, 92(4):591–598, 1984.

D.B. Hanson. Near-field frequency-domain theory for propeller noise. *American Institute of Aeronautics and Astronautics Journal*, 23(4):499–504, 1985.

D.B. Hanson and B. Magliozzi. Propagation of propeller tone noise through a fuselage boundary layer. *Journal of Aircraft*, 22(1):63–70, 1985.

Volume 1: Aircraft noise International Civil Aviation Organisation. Annex 16 to the convention on international civil aviation: Environmental protection, 5th edition, 2008.

D.S. Jones. The scattering of sound by a simple shear layer. *Philosophical Transactions of the Royal Society*, 284(1323):287–328, 1977.

S.-H. Ko. Sound attenuation in acoustically lined circular ducts in the presence of uniform flow and shear flow. *Journal of Sound and Vibration*, 22(2):193–210, 1972.

R.E. Langer. On the connection formulas and the solutions of the wave equation. *Physical Review*, 51:669–676, 1937.

J. Lawrence. *Aeroacoustic Interactions of Installed Subsonic Round Jets*. Ph.D. thesis, University of Southampton, 2014.

M.J. Lighthill. On sound generated aerodynamically: 1 general theory. *Proceedings of the Royal Society of London A: Mathematical, Physical and Engineering Sciences*, A:564–578, a.

M.J. Lighthill. On sound generated aerodynamically: 2 turbulence as a source of sound. *Proceedings of the Royal Society of London A: Mathematical, Physical and Engineering Sciences*, 37 (2):145–153, b.

G. Lilley. The prediction of airframe noise and comparison with experiment. *Journal of Sound and Vibration*, 239(4):849–859, 2001.

H.Y. Lu. Fuselage boundary-layer effects on sound propagation and scattering. *American Institute of Aeronautics and Astronautics Journal*, 28(7):1180–1186, 1990.

S. Mariano. Effect of wall shear layers on the sound attenuation in acoustically lined rectangular ducts. *Journal of Sound and Vibration*, 19(3):261–275, 1971.

S. Mayoral and D. Papamoschou. Prediction of jet noise shielding with forward flight effects. *Proceedings of the 51st AIAA Aerospace Sciences Meeting*, number AIAA 2013-0010, 2013.

A. McAlpine and M.J. Kingan. Far-field sound radiation due to an installed open rotor. *International Journal of Aeroacoustics*, 11(2):213–245, 2012.

A. McAlpine, J. Gaffney, and M.J. Kingan. Near-field sound radiation of fan tones from an installed turbofan aero-engine. *Journal of Acoustical Society of America*, 138(3):1313–1324, 2015.

G.L. McAninch. A note on propagation through a realistic boundary layer. *Journal of Sound and Vibration*, 88(2):271–274, 1983.

C.J. Mead and P.J.R. Strange. Under-wing installation effects on jet noise at sideline. *Proceedings of the 4th AIAA/CEAS Aeroacoustics Conference*, number AIAA 98-2207, 1998.

J.M. Miles. On the disturbed motion of a vortex sheet. *Journal of Fluid Mechanics*, 4:538–554, 1958.

P. Mungur and G.M.L. Gladwell. Acoustic wave propagation in a sheared fluid contained in a duct. *Journal of Sound and Vibration*, 9(1):28–48, 1969.

P. Mungur and H.E. Plumblee. Propagation and attenuation of sound in a soft-walled annular duct containing a sheared flow. *NASA SP-207*, pages 305–327, 1969.

International Coordinating Council of Aerospace Industries Associations. Technology continues to play important role in reduscing noise around airports, 2004.

N.N. Ostrikov. Sound radiation by distributed quadrupole sources near rigid bodies. *Acoustical Physics*, 58(4):481–489, 2012.

D. Papamoschou. Imaging of directional distributed noise sources. *Journal of Sound and Vibration*, 330(10):2265–2280, 2012.

Rolls-Royce plc. Ultrafan. URL https://www.rolls-royce.com/media/our-stories/innovation/2016/advance-and-ultrafan.

D.C. Pridmore-Brown. Sound propagation in a fluid flowing through an attenuating duct. *Journal of Fluid Dynamics*, 4:393–406, 1958.

E.J. Rice, M.F. Heidmann, and T.G. Sofrin. Modal propagation angles in a cylindrical duct with flow and their relation to sound radiation. *Proceedings of the 17th Aerospace Sciences Meeting*, number AIAA 79-0183, 1979.

S. Rienstra. Sound transmission in slowly varying circular and annular lined ducts with flow. *Journal of Fluid Mechanics*, 380:279–296, 1998.

S. Rienstra. Sound propagation in slowly varying lined flow ducts of arbitrary cross-section. *Journal of Fluid Mechanics*, 495:157–173, 2003.

S.W. Rienstra and A. Hirschberg. *An Introduction to Aeroacoustics*. 2004.

D-M. Rouvas and A. McAlpine. Theoretical methods for the prediction of near-field and far-field dound radiation of fan tones scattered by a cylindrical fuselage. *Proceedings of the AIAA Aviation 2021*, AIAA 2021-2300, 2021. .

D-M. Rouvas and A. McAlpine. An analytical model of sound refraction by the fuselage boundary-layer for fan tone radiation from a turbofan aero-engine. *Proceedings of the 28th AIAA/CEAS Aeroacoustics Conference*, AIAA 2022-3059, 2022a. .

D-M. Rouvas and A. McAlpine. Prediction of fan tone radiation scattered by a cylindrical fuselage. *Proceedings of the 11th EASN Conference*, 1226(012050), 2022b. .

P.J.G. Schwaller, B.J. Tester, and D.G. Henshaw. The effects of fan noise of inlet steady flow distortion. *Proceedings of the 3rd AIAA/CEAS Aeroacoustics Conference*, number AIAA 97-1590, 1997.

P.J.G. Schwaller, N.J. Baker, JD. Tomlinson, P. Sijtsma, and R. Hennings. Noise validation of model fan rig with engine. *Proceedings of the 12th AIAA/CEAS Aeroacoustics Conference*, number AIAA 2006-2479, 2006.

J.N. Scott. Propagation of sound waves through a linear shear layer. *AIAA Journal*, 17(3): 237–244, 1979.

R.H. Self. *"Asymptotic Expansion of Integrals" in Lecture Notes on the Mathematics of Acoustics, edited by M.C.M. Wright*. Imperial College Press, 2005.

P.N. Shankar. On acoustic refraction by duct shear layers. *Journal of Fluid Mechanics*, 47(1): 81–91, 1971.

M. Siefert and J. Delfs. Refraction and scattering in high mach number boundary layers. *Proceedings of the 17th AIAA/CEAS Aeroacoustics Conference*, number AIAA 2011-2847, 2011.

M.J.T. Smith. *Aircraft Noise*. Cambridge Press, 1989.

D. Stanescu, M.Y. Hussaini, and F. Farassat. Aircraft engine noise scattering by fuselage and wings: a computational approach. *Journal of Sound and Vibration*, 263(5):319–333, 2002.

C.K.W. Tam and P.J. Morris. The radiation of sound by the instability waves of a compressible plane turbulent shear layer. *Journal of Fluid Mechanics*, 98(2):349–381, 1980.

J.M. Tyler and T.G. Sofrin. Axial flow compressor noise studies. *SAE Technical Paper*, 70: 309–332, 1962.

T.Q. Wang and S. Zhou. Investigation on sound field model of propeller aircraft - the effect of vibrating fuselage boundary. *Journal of Sound and Vibration*, 209(2):299–316, 1998.